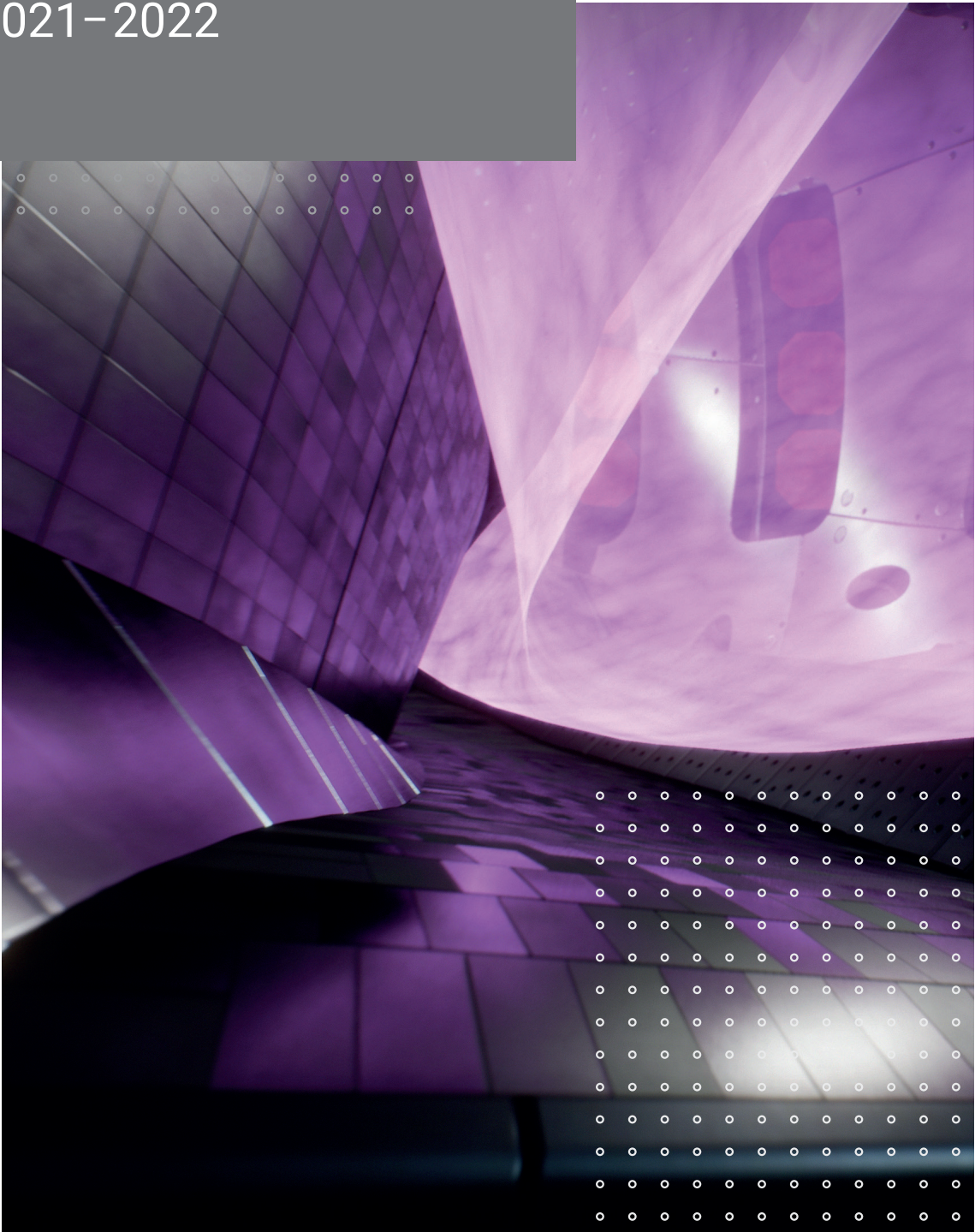




SCIENTIFIC REPORT
2021–2022





SCIENTIFIC REPORT

January 2021 – September 2022

The Max Planck Institute
for Plasma Physics is an
institute of the Max Planck
Gesellschaft and part of the
European Fusion Programme



This report gives an overview of the scientific work of IPP from January 2021 to September 2022.

The goal of the superconducting optimized stellarator Wendelstein 7-X is to demonstrate high-power long-pulse operation under reactor relevant conditions. After the very successful first experiment campaigns, which ended in 2018, Wendelstein 7-X went into its completion phase, which prepared the device for high performance long-pulse operation. Extensive and labour-intensive new installations include active cooling of all in-vessel components, an elaborate actively cooled high-heat-flux divertor consisting of ten divertor modules, each equipped with a cryo-pump, and many other new or upgraded systems, ranging from more and more advanced diagnostics to more heating power to extend the operational space. After some delay due to the COVID pandemic, the work was successfully completed end of 2021. The commission of Wendelstein 7-X is now in full swing with first plasma operation and the start of the scientific exploitation expected in the last quarter of 2022.

The break in Wendelstein 7-X operation was also used to further analyse the scientific results of the first campaigns, essentially confirming initial conclusions. While in typical gas fuelled ECRH plasmas, transport is dominated by anomalous losses, in cases of pellet injection or other fuelling methods with centrally peaked density profiles, the confinement properties are considerably improved. These special plasma conditions were also used to demonstrate neo-classical transport optimization underlying the Wendelstein 7-X design. Published in the Journal "Nature" in 2021, this result attracted worldwide attention. More recent evaluations show – maybe not surprisingly – that the challenge will be to extend the duration of such a regime of improved confinement and to find a balance between good energy confinement and sufficiently high impurity transport.

In parallel to Wendelstein 7-X completion, a strategy process was established, developing a plan for the further long-term upgrades of the device and its components. A central element is the extension of the heating power, which is required for achieving higher plasma beta values. The other important aspect is the conversion of Wendelstein 7-X to a full-metal device. For this purpose, a project was implemented for developing a design of a new tungsten divertor. While an extension of the ECRH power has already begun, the concrete realization of more neutral beam heating power and, in particular, the tungsten divertor still requires the results from the upcoming campaigns.

The ASDEX Upgrade experimental program is devoted to the preparation of ITER operation and improvement of the physics basis for DEMO. In the 2021 and 2022, ASDEX Upgrade operated for about 16 months, with an average 60:40 distribution IPP-internal:EUROfusion. A major enhancement was the installation of a Shattered Pellet Injector (SPI) and its dedicated diagnostics in cooperation with the ITER organization. About 20 % of the 2022 campaign was devoted to SPI studies, planned and conducted in collaboration of ITER, EUROfusion and IPP. The key scenario is a double injection, first with a deuterium pellet for dilutive cooling followed by an impurity doped pellet for radiative termination. Concerning development of advanced tokamak scenarios concentrated on implementation and exploitation of predictive tools for scenario development, including transport and safety factor modelling. Furthermore, the reason for the previously observed large scatter in confinement in the hybrid scenario could be ascribed to a variation in separatrix density and fueling.

Increasing efforts were devoted to the development of no-ELM scenarios focused on ITER and DEMO. Due to their relatively broad parameter space and compatibility to benign power exhaust, EDA H-mode and the QCE regime were extensively investigated. Regarding RMP ELM suppression additional safety factor windows for its existence were found as well as a clear upper limit of hydrogen fraction in the fuel gas. Concerning the effect of RMPs on the L-H threshold power, an increase with perturbation amplitude was found, in contrast to previous studies with lower amplitude. The effect is largest when edge plasma response is maximized and can be modelled very well with an offset-linear threshold. The onset of the increase is connected to reversal of the poloidal $E \times B$ velocity inside the separatrix from electron to ion direction.

In combination with experiments on feedback controlled formation of an X-point radiator (XPR) by seed impurities, the compact radiative divertor regime (CRD) has been developed. It combines benign power exhaust with no-ELM conditions, at moderately reduced energy confinement. The physics of the XPR could be well described by SOLPS modelling, using divertor Thomson scattering data for validation, and a simple analytical model. A new approach for the characterization of the ASDEX Upgrade operational space using separatrix parameters and analytical theory proved successful in describing L-mode density limit and H-L transition. A key element is the transition from dominant drift wave to interchange turbulent transport. An important outcome of the model is the experimentally verified prediction that in a clean machine, large separatrix densities can be obtained in sufficiently heated H-mode.

IPP's collaborations with JET, JT-60SA, ITER and other devices of the public and private sector appearing on the horizon were re-organized in a single project called 'International Tokamak Collaboration'. After several years of preparation, experiments with deuterium-tritium at JET could demonstrate the compatibility of sustained high fusion power production with the metal ITER-like wall. The 59 MJ of fusion energy achieved is a new world record. This breakthrough was accomplished in so-called 'hybrid' plasmas that have been co-developed by IPP scientists.

IPP's two test facilities, ELISE and BATMAN Upgrade, provide valuable input for both the commissioning and operation of the Neutral Beam Test Facility in Padova as well as for the preparation of the ITER beam lines. With the new CW power supply an extracted negative ion current of 190 A/m^2 was achieved in a 1000 s hydrogen beam. Both ITER diagnostics in development at IPP, namely the pressure gauges and the port-mounted bolometer cameras, have made significant further progress and approach their final design review in 2023. The final design review for the ITER PCS for the first plasma operation phase was successfully finished. A follow-up contract for the first non-active pre-fusion power operation phase has been awarded to IPP. For JT-60SA, the successor of JET, IPP is preparing a pellet injection system as well as a massive gas injection system for disruption mitigation. IPP is also contributing to the preparation of future ITER and JT-60SA operation with simulations and theoretical studies. Billions of dollars were invested recently in fusion start-ups, mainly in the US, but recently also in Germany. IPP has made initial contact with a few of these fusion start-ups.

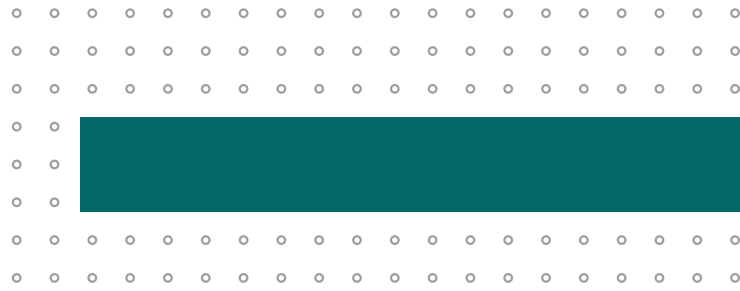
There has been substantial progress in our theoretical divisions. As mentioned above, it was shown that without the neoclassical optimization underlying the design of the device the record energy confinement achieved in Wendelstein 7-X could not have been attained. In addition, the physical mechanism by which turbulent transport is reduced in these plasmas has also been identified. In tokamak theory, in an effort to complement and connect increasingly sophisticated non-linear gyrokinetic simulations with reduced models, a global transport code for energetic ions (ATEP) was developed based on the general transport theory of phase space zonal structures. Furthermore, in order to build predictive capabilities for the most dangerous disruptive events for ITER, so-called hot vertical displacement events, dedicated experiments and non-linear MHD simulations were conducted and found to agree well in terms of key parameters like electromagnetic forces.



Scientific Director Sibylle Günter

Content

Tokamak Research	
ASDEX Upgrade	9
International Tokamak Collaborations	
International Tokamak Collaborations	41
Stellarator Research	
Wendelstein 7-X Construction and Operations	57
Wendelstein 7-X Science	63
DEMO	
DEMO Design Activities	81
Plasma-Wall Interactions and Materials	
Plasma-Wall Interaction	85
Plasma Theory	
Theoretical Plasma Physics	93
Max Planck Princeton Cooperation	
Max Planck Princeton Research Center for Plasma Physics	119
Plasmas beyond Fusion	
Plasma for Gas Conversion	123
Astrophysical Plasmas	125
Electron-Positron Plasmas	127
Publications, Figures and References	
Publications	131
Figures	132
References	133
Appendix	
How to reach IPP in Garching	142
How to reach Greifswald Branch Institute of IPP	143
IPP in Figures	144



Tokamak Research

ASDEX Upgrade

Head: Prof. Dr. Arne Kallenbach

The ASDEX Upgrade experimental program is devoted to the preparation of ITER operation, research for basic physics understanding and the design of a prototype fusion reactor, DEMO. In the 2021 and 2022 campaigns, ASDEX Upgrade operated about 16 months, with an averaged 60:40 distribution between IPP-internal and the EUROfusion WP-TE programs.

1 Introduction

1.1 Overview

ASDEX Upgrade (AUG) operated from December 2020 till July 2021 and from December 2021 till July 2022. Thanks to the hygiene concept developed in April 2020, the standard operational cycle of 5 days in 2 weeks could be fully reinstated in the 2021 and 2022 campaigns. The EUROfusion fraction of the program was 35 % in 2021 and 43 % in 2022. Both campaigns were technically very successful, with 1146 and 1260 shots executed for proposals. Almost all actuators and major diagnostics were fully available, except ECRH gyrotron 7 (sent for repair in summer 2021, then stuck in Russia, back in summer 2022), NBI source 7 (water leak in ion dump in restart Dec 2021), and the lower divertor Thomson scattering system (in-vessel mirror out of adjustment in April 2022). Due to the Covid-19 pandemic, planning and experiment participation by scientific coordinators had to be done largely via remote participation. On-site operation of special diagnostics by external collaborators has been fully resumed from spring 2022. In parallel to the campaigns, preparation work was ongoing for the upgrade of ASDEX Upgrade with an alternative upper divertor (EUROfusion PEX project). In addition, working groups have been started to develop ideas for ASDEX Upgrade modifications and plans till the early 2030s. This process is currently ongoing and led to a number of refurbishing activities aimed at a prolonged tokamak lifetime. These activities will be done prior and parallel to the PEX Upgrade, taking advantage of work synergies. As a result, the whole vent will last about 2 years, but collect also other activities which require a large down-time, like a refurbishment of the EZ2 motor generator and an upgrade of NBI box I from arc to RF sources.

1.2 Machine Enhancements

The major enhancements in the period of report were the installation of the shattered pellet injector (SPI) and its dedicated diagnostics in cooperation with the ITER organization and the new high current power supply Group 7, providing a more efficient and flexible supply for poloidal field coils, an extension of available power and energy, and a back-up for potential failure of aged power supplies. The NBI source 5 has been upgraded with a variable gap, enabling a decoupling of acceleration voltage and power. This allowed transport studies with, e.g., different acceleration voltages at the same injection power. Another application is the increase of the heating power at low densities, where the NBI shine-through limits the beam energy and with a fixed gap thus also

the power. Following the success of the source 5 modification, it was decided to upgrade the remaining three sources from injector II to variable gaps in the upcoming vent. A number of new diagnostics contributed to improved physics understanding, like the divertor Thomson scattering and several microwave turbulence diagnostics.

1.3 Major Physics Results

Substantial progress could be achieved in regimes with an X-point radiator, disruption mitigation studies with the newly installed shattered pellet injector (SPI) as well as with massive gas injection (MGI), the development of advanced tokamak scenarios, no-ELM scenarios and turbulence studies. A strong focus of the 2022 campaign was on disruption mitigation studies with the shattered pellet injector (SPI). The injector was installed at ASDEX Upgrade after its characterization in the lab and delivered first pellets into plasma in December 2021. Subsequently, 230 ASDEX Upgrade discharges were performed for SPI studies, about 20 % of the 2022 campaign. The experiments were planned and conducted in collaboration of the ITER DMS task force, EUROfusion and IPP staff. Data were collected for different injection geometries, pellet species and plasma parameters. The key scenario is a double injection, first with a deuterium pellet for dilutive cooling followed by an impurity (doped) pellet for radiative plasma termination. The SPI experiments were complemented by experiments on control and benign termination of runaway beams, using double massive gas injection of deuterium and impurities.

Increasing efforts were devoted to the development of no-ELM scenarios with perspectives focused on ITER and DEMO. Due to their relatively broad parameter space and compatibility to benign power exhaust, EDA H-mode and the QCE regime were extensively investigated. Interesting physics results regarding the RMP ELM suppressed H-mode were additional safety factor windows for its existence and a clear upper limit of hydrogen fraction in the fuel gas for the occurrence of ELM suppression. In combination with experiments with controlled formation of an X-point radiator (XPR) by seed impurities, the compact radiative divertor regime (CRD) has been developed. This regime combines benign power exhaust with no-ELM conditions, at moderately reduced energy confinement. Due to the closeness of the X-point to the divertor target, the CRD regime provides a larger plasma volume, which may compensate a reduced confinement. The physics of the X-point radiator could be well described by SOLPS modeling, using divertor Thomson scattering data for validation, and a simple analytical model.

The development of advanced tokamak scenarios concentrated on the implementation and exploitation of predictive tools for scenario development, including transport and safety factor modelling. This allowed the determination of the beta limit in dependence of, e.g., the safety factor profile.

In the context of scenarios with RMP ELM suppression, the effect of the magnetic perturbations on the L-H threshold power were investigated.

In contrast to previous studies with lower relative perturbation amplitude, an increase of the threshold power with perturbation was found. The response of the threshold is largest when the edge plasma response is maximized and could be modelled very well with an offset-linear threshold approach. The onset of the power threshold increase is connected to a reversal of the poloidal $E \times B$ velocity inside the separatrix from electron to ion drift direction.

The experimental studies were complemented by transport modeling of L-modes, no-ELM regimes and H-modes with ASTRA-TGLF as well as gyrokinetic simulations. For H-mode conditions with a pedestal, the IMEP workflow was successfully applied, specifying realistic boundary conditions for the core transport model.

A new approach for the characterization of the ASDEX Upgrade operational space using separatrix parameters and analytical theoretical descriptions proved highly successful in predicting the L-H power threshold, the L-mode density limit and the H-L transition. A key element of the separatrix operational space is the transition from dominant drift wave to interchange turbulent transport. An important outcome of the model is the experimentally verified prediction that in a clean (tungsten wall) machine, large separatrix densities can be obtained in H-mode provided the heating power is sufficiently high.

1.4 Major Vent for the Installation of the Alternative Upper Divertor and Beyond

From August 2022, ASDEX Upgrade has started a major vent scheduled till July 2024. Main objectives are the installation of an alternative upper divertor, including a cryo-pump and two in-vessel coils capable to produce snowflake and X-divertor configurations. In addition, new diagnostics will be installed like, e.g., an upper divertor Thomson scattering system. With the refurbishment of a large number of vacuum seals and other components, the EZ2 generator, the NBI box 1, and installation of a new ICRF generator 6, ASDEX Upgrade is expected to be well prepared for further experimental campaigns till the early 2030s.

2 AUG Machine Status

2.1 Introduction

During the report period, two experimental campaigns with in total 2612 successful plasma shots were carried out.

The maximum heating power and energy applied in single discharges was $P_{\text{heat}} = 25$ MW and $E_{\text{heat}} = 114$ MJ, respectively. The integral heating energy deposited into the plasma and received by the in-vessel components is $E_{\text{heat},20,22} = 80$ GJ. Two scheduled small shut downs were used for small repairs of in-vessel components and for installation of new diagnostics as indicated in figure 1. The opening that has just begun will last for two years during which a comprehensive repair of the vessel components will be carried out together with the installation of the new upper divertor.

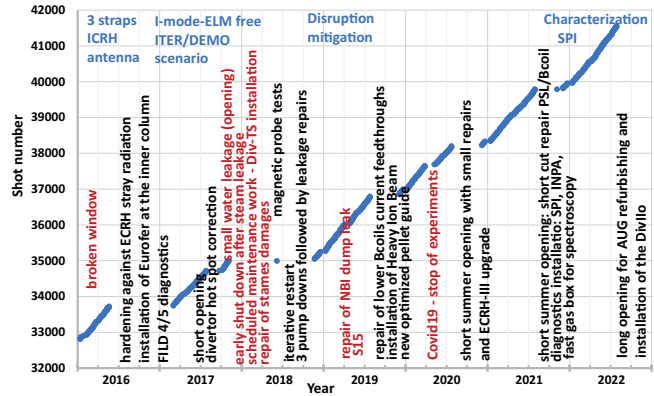


Figure 1. Shot history of the report period 2016–2022. Unscheduled interruptions are marked in red.

2.2 Upgrade of AUG with New Diagnostics

2.2.1 SPI

A great effort was made to install in the 2021 shut down the Shattered Pellet Injection (SPI) on time to allow the study of disruption mitigation and runaway suppression. Along with the SPI, its diagnostics were implemented: a) two fast cameras with different views and, b) bolometry was widely extended from 384 (just 2 sectors) to 596 channels in 5 sectors, implementing 9 new cameras. The latter allows to measure toroidal radiation asymmetries in unprecedented precision and, thus, allows to answer one of the main questions for SPI: If the induced radiation is too localized and would lead to local melting. The high spatial resolution allows to follow pellet clouds around the torus.

2.2.2 Reflectometry

A new forward model for O-mode reflectometry enables its implementation into integrated data analysis, where joint analysis with other diagnostics resolves the initialisation problem. The mathematical benefits of the new model allow for fast and reliable determination of the density profile, outperforming established methods [1]. The combination of a corresponding inversion technique with Bayesian sampling methods provides real-time suited stand-alone analysis with error propagation.

2.2.3 iHIBP – First Signals

After a development and commissioning phase of three years, the imaging heavy ion beam probe (i-HIBP) [2] measured the first signals on the scintillator detector on 26th of November 2021. Although the collimation of the probing beam was not optimized, the signals clearly showed a strong dependence of the plasma current and the fluctuating intensity pattern could be related to filaments in the scrape-off layer. Further optimization of the hardware, especially the beam collimation is planned, with the goal of measurement of the edge current density with the i-HIBP.

2.2.4 Divertor Helium Beam

A further thermal helium beam consisting of a piezo valve and an optical head was installed in the lower divertor of AUG. It allows highly resolved measurements of the electron temperature and density. With this new diagnostic, detachment physics and turbulent transport processes as filaments motion can be investigated in 2D.

2.2.5 Comb Reflectometer

A fully tunable multi-frequency comb W-band Doppler backscattering system has been developed, tested, and deployed in AUG. It measures the back-scattered power from 7 channels simultaneously with a variable central sampling frequency anywhere inside the W-band and variable inter-frequency spacing. The system enables the simultaneous measurement of turbulence properties at seven radial positions. This allows for the investigation of fast timescales during L-H transitions, I-phases, I-mode bursts, transients during heat wave propagation, etc.

2.2.6 Second CECE

In collaboration with the MIT, the Correlation Electron Cyclotron Emission (CECE) diagnostic for T_e fluctuation measurements was further extended in March 2021 with a second RF receiver unit installed in sector 11. Together, the two units provided a radially localized measurement of the long-range-correlation properties of, amongst others, the I-mode edge QC-mode. The CECE diagnostic suite was further extended in early 2022 with the installation of the 2nd CECE receiver in sector 5 together with a W-band reflectometer for simultaneous α_{IT} measurements. The sector 9 CECE receiver was also extended from 24 to 32 radial channels.

2.2.7 Imaging Neutral Particle Analyser (iNPA)

In collaboration with European research center and Spanish university, the Imaging Neutral Particle Analyser (iNPA) has been designed and installed in 2021 to measure the fast neutrals escaping after charge exchange reactions. The final design of the diagnostic features an energy resolution of 12 keV for 100 keV ions and a radial resolution below 8 cm at the low field side of AUG, with a temporal response of 1 kHz. In the last campaign the commissioning of iNPA has been successfully completed [3].

2.3 Preliminary Study of the In-vessel Articulated Robotarm

As part of a master's thesis [4], it was studied how an articulated arm could be implemented in AUG. The In-vessel Articulated Robotarm (IVAR) would help in shortening the downtime of AUG, allowing the inspection and removal of small broken components inside the vacuum vessel. The need for an inspection arm became evident some campaign ago, during which a minor damage led to two weeks of operation interruption to access AUG for repair/removal. IVAR is planned in the midplane manipulator port, enclosed in a vacuum barrier in

a linear slide. Its length allows to reach all positions in the vessel, thanks to its seven rotation degrees of freedom (DOF) and one translational DOF. IVAR design is cable-driven, with an hyper-redundant, cantilevered arm consisting extremely light modular elements in order to reduce stresses. A successful demonstrator, with few modular elements and simple control system, was developed proving the design principles.

2.4 Ongoing Divllo

A new upper divertor (Divllo) with two integrated coils, has been designed and will be installed in the next long shutdown. The aim of the Divllo is to realize alternative magnetic configurations, to spread the parallel heat flux in a wider divertor area. The design of the Divllo has been concluded and the procurement of the components is ongoing. It consists of 7 cryo-pump segments with active charcoal, the inner divertor, the outer divertor, which at the same time will be the casing of the two concentric coils (4 turns each). The Divllo is protected with graphite tiles coated with tungsten. The coils are powered in opposite direction, only a small imbalanced current is allowed, due to force limitations, and the maximum current is 52 kAt. In 2020, an ad-hoc co-axial Tefzel Insulated Conductor (TIC) was manufactured and delivered in IPP. The conductor consists of an oxygen-free copper pipe with a center bore for water cooling. The electrical insulation Tefzel has a thickness of 2.5 mm and a stainless-steel jacket provides the vacuum compatibility and the requested safety against winding short cut. The manufacturing of the main Divllo components is in progress: the welded casings of the cryo-pumps are ready, while Chevron baffles are about to be completed. The other components are in good progress and they will be ready for assembly at the beginning of the year. To increase the operation safety, the in-vessel coils are designed without electrical joints, this implies, that the coils will be entirely wound inside the vessel. A conductor reel placed outside the vessel will be progressively unwound by means of a despooler. At the top of the despooler, a straightening machine will plastically bend the conductor that will be inserted into the vessel via a middle port. An in-vessel bending machine will bend the conductor to get the four turns of the coils. The procedure will be automatically executed by a control system, but the execution of the coil terminations requires manual work, difficult to implement due to severe space limitation. Several manual bending machines have been realized, to be used depending on the space available. The in-vessel bending machine with its ancillary's system, the straightening machine, the despooler and the joggle tool, which are the larger tools that will be used during the winding operations, were delivered early this summer, together with the control system. The remaining components required for the lifting of both the bending machine and the coils will be delivered in a couple of months. The vacuum feedthrough design is completed and its prototype has been successfully tested: a repair strategy of it will be executed in the next months.

2.4.1 AUG Twin

In the framework of the activities carried out for the installation of the new upper divertor DivIlo, it has been built an AUG twin in the ITZ hall. Its purpose is to test, refine and practice all the procedures, sequences and complex manoeuvres required for the winding of the in-vessel coils, thus saving valuable AUG operational time. A closed frame made of aluminum profiles is built around the octant prototype of AUG vacuum vessel, reconstructing the overall dimensions within AUG. On this frame, all the supporting elements of the in-vessel components are connected. The positioning of which is accurately measured to within a tenth of mm, reproducing the mounting condition in AUG. The assembly of the stainless-steel coil housings (part of the outer divertor) was successfully tested on the test stand and now they are ready for installation in AUG. To decouple the assembly in the AUG from the ITZ Hall, aluminum dummies of the coil casings were manufactured and are now installed in the ITZ Hall. The preassembly in the test facility started with some of the delivered components: the transport frame designed for the insertion of the bending machine has already been assembled and tested by simulating the removal of the A-port (middle port); the despoiler is in mounting phase. In the test facility, also the graphite tiles will be mounted to check the assembly tolerances, along with all the diagnostics required for the new DivIlo. By end of February 2023, two coils will be bent in the AUG twin, one of which can be electrically tested.

2.5 Vacuum and Conditioning

After the renewal and adoption of the pumping- and boronization system a phase of debugging and optimization was started. Especially for the boronization system hardware adoptions were needed for reliable operation, i.e. a fresh coating every 3 weeks. The WinCC control programs had been improved to enable safe, reliable and almost automatic operation of standard routines as cryo pump regeneration, glow discharges, change of operation gases or even boronization. This requires communication of the individual control systems. The cooling water calorimetry, a unique system which includes almost all in-vessel components has been substantially refurbished. After exchanging the measuring transformer to commercially available ones, the sensitivity was enhanced by a factor of almost ten. This allows to use the data to study the power flux to the plasma facing components (PFC) [5, 6]. To enhance the accuracy of the gas feed, especially for low fluxes, the communication with the DCS system had been adopted. Additionally, the gas monitor diagnostic UVS was transferred to Phyton and extended by other gas inlets as He beam diagnostic and killer gas. Preparation of the new upper divertor required the development of test procedures, qualification of materials and components. Vacuum test of first delivered parts had been done successfully. To ensure safe operation the hardware and control of many components as e.g. the glow discharge gas inlet, killer gas valve gas fed, pressure gauges of the TPS, dust dropper system, He feed at the hall had been renewed.

2.6 ICRF

A large fraction of the preparation work for the new ICRF generator 6, to be delivered to IPP in 2024 (delayed due to COVID-19), was completed. The future generator location next to the AUG ICRF generators 1–4 was prepared with the infrastructure as e.g. cooling water. A concept of coaxial connections and switches was elaborated taking advantage of existing 3 dB hybrids to connect either to 2-strap or to 3-strap antennas in case generator 5 is offline.

A step-by-step hardware renewal for timer and interlock control was started. A power controller upgrade enabled automatic gentle generator power ramps including those after safety switch-off due to arcing. This and adding pre-load resistors in the driver stage will extend the vacuum tube lifetime. Reduction of arc switch-off time from 50 to 25 ms (with potential for further future reductions) improved the power delivery to the plasma. Additional grid overvoltage protection was installed in AUG generator 1 to avoid possible damage of the driver socket capacitor in case of a vacuum tube failure with internal short circuit. Such an incident had happened in 2021 and a replacement of socket capacitor was kindly provided by the DIII-D colleagues.

ICRF power was integrated in the AUG actuator management helped by real-time information exchange between the ICRF and AUG fast control systems. Automatic ICRF power replacement of the antenna pairs and further integration in the AUG real-time control algorithms became possible.

2.7 ECRH

In the 2020 report the completion of the ECRH-3 system was described. In the last two years the system proved to be highly reliable. Only the launcher mechanics, which is a modified version of the ECRH-1 setup, showed some need for improvement in the actual 2 year shut-down. The clamping of the glass-fiber rods for torque transfer was not slip-proof, leading to wrong poloidal launcher settings for launcher 4 and a loss of several discharges in the 2020 campaign. In the 2021 and 2022 campaigns small ball bearings on launchers 2 (toroidal, 2 defects) and 3 (poloidal) were damaged by arcs. Since this did not happen during 20 years of ECRH-1 operation, it is probably due to changes in the insulation structure to suppress halo currents, which obviously needs revisiting and improvement.

As also described in the previous report, power limitations due to arcing in the systems have successfully been removed, allowing to use the full available gyrotron power to inject up to 6 MW into the plasma. This power is in tendency decreasing on a time scale of years as the ECRH-2 gyrotrons are aging. In 2021, gyrotron 7 had to stop operation completely after a significant loss of beam current in spite of significantly increased heater power, indicating strongly asymmetric emission. GYCOM and IPP agreed on inspection and repair and mid-February 2022 the repaired gyrotron was ready for shipment to IPP, just as the Ukraine-conflict started. This delayed the delivery, which was finally realized with strong efforts and trust on both sides.

In July 2022 the gyrotron was accepted at IPP and delivered more than 800 kW into the plasma during the last week of plasma operation.

2.8 NBI

One of the Neutral Beam Injection's eight sources was upgraded with an extraction system with a novel in-situ variable acceleration gap developed in house. With the usual fixed gap NBI an ion source must be operated at constant perveance, causing a strong dependence of the beam power on the beam energy (black line in figure 2). The variable gap widens the operational space, enabling higher powers at lower beam energies and therefore reduced shine through, as well as reduced power at higher beam energy. A prototype was successfully tested in 2022 and the upgrade of the remaining three sources on the same injector will follow in 2023/24.

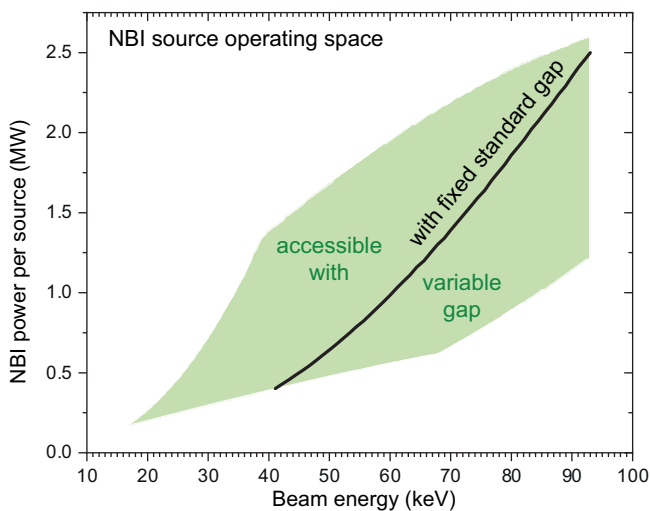


Figure 2. Operational space of an injector 2 ion source in the beam energy – neutral beam power plane with standard fixed acceleration gap (black line) and variable gap (green shaded area).

The 2022–24 maintenance break will also be used to replace the arc sources of injector 1 with RF-driven sources like those in use on injector 2. This source type offers significant advantages regarding reliability and behaviour in pulsed operation.

2.9 Pellet Injection with Impurity Doped Pellets

Impurity doped pellets have the potential for faster and more efficient radiative cooling in the outer part of the plasma. The AUG pellet injection system was extended to accommodate mixtures of D with N_2 , Ne, Ar, Kr and Xe [7]. The additional pellet weight and mechanical properties result in a limit for the impurity content in order to protect the stop cylinder from mechanical damage. A de-enrichment of the impurity in the pellet compared to the gas mixture has been observed, which amounts typically to a factor of about 10. The injection of impurity doped

pellets leads to immediate radiation spikes, as shown in figure 3 for the case of D pellets doped with about 0.1 atom % Ar. The immediate radiation amounts to 2.5 kJ per pellet, followed by radiation of the deposited Ar in the outer plasma and subsequent Ar recycling. The radiation spike is a factor of 4 more intense compared to an estimate based on the Ar radiative potential, suggesting modifications of the Ar ionization balance during pellet ablation [8].

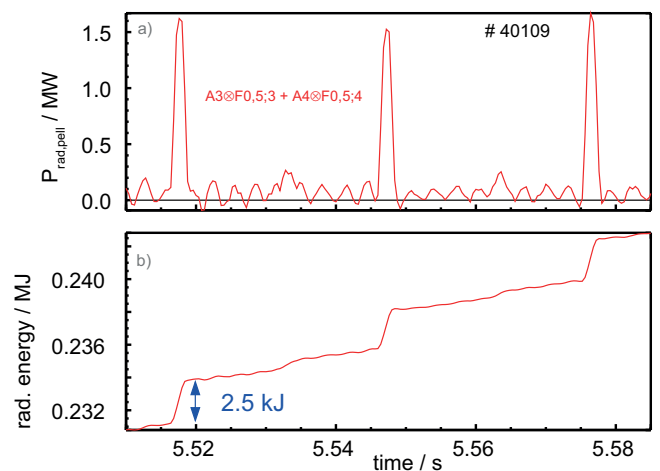


Figure 3. Total incremental radiated power and energy during Ar doped D pellet injection.

3 AUG Operation

3.1 Introduction

Both, the 2021 and 2022 AUG campaigns were technically very successful (from now on, 2021 numbers are given in brackets). The commissioning phase started on November 26th 2021 (2020/11/11th) and it was planned for 9 (7) days of operation. Finally, in the 2022 campaign there were performed 6 commissioning days, 3 days were lost for repairs on the NBI. The scientific program started on December 16th 2021 (2020/12/15th) and ended on July 27th 2022 (2021/07/28th) after 77 (72) days of operation. 6 (2) days were so called “technical shot days” for calibration of diagnostics, commissioning and repair. These days (and the commissioning phase) are not counted for the average numbers given here. There were 1669 (1499) shots performed in total. 1319 (1214) were useful from scientific point of view (“green shots”), 133 (92) technical shots to verify magnetic probes, coil's power supply operation, calibrate diagnostics or tests of technical modifications of essential systems. The shot days with highest number of useful plasma discharges were performed on March 24th for the ITER SPI program with 34 shots and on January 27th (2021/03/4th) for mixed physical program with 27 (24) shots. In average, there were 18.6 (17.3) useful shots per day performed. We lost 3.3 (2.4) shots per day and we performed 1.4 (1.3) technical shots per day. The evolution of shots over both campaigns is shown in figure 4.

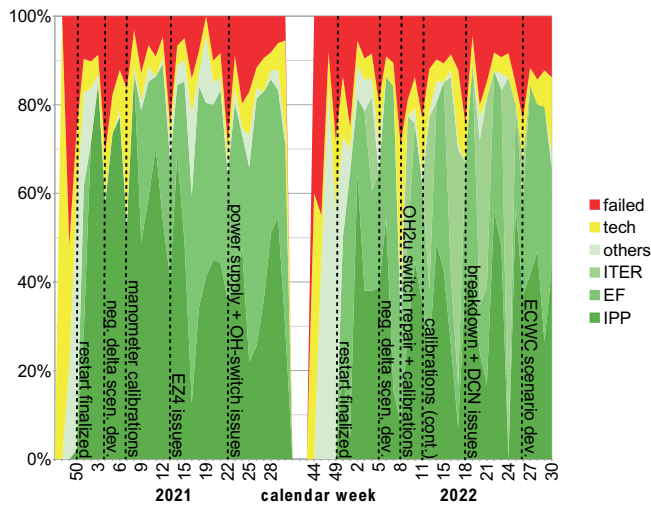


Figure 4. Evolution of useful (green), technical (yellow) and lost shots (red) over all weeks of operation of both campaigns.

3.2 Experimental Power Supply

During Corona pandemic, chains of transmission could be avoided by restrictive precautions. Thus, operation of the generators, high current and high voltage power plants could be guaranteed for ASDEX Upgrade and the various test plants. Operation was essentially smooth, without major disruptions. Nevertheless, increased failures and malfunctions of individual electronic assemblies show the importance to successively upgrade or renew the systems, some of which are more than 40 years old. A medium-term investment plan has been drawn up for better planning. This includes the progressive modernization or renewal of outdated facilities highly relevant to the operation of ASDEX Upgrade and beyond.

3.2.1 New Switchgear Group F

In 2021, the uncovered switchgear Group F was renewed. The switchgear, which dates back to 1965, no longer corresponded to the state of the art in terms of fault arc safety and personal protection. The renovation was also necessary in order to reliably supply the new high-voltage installations (Batman Upgrade, Elise PSM, NBI RF sources). In 2022, an additional switchgear Group C was built for the future supply of the new semiconductor laboratory of the Max Planck Society (HLL), including a new transformer station with two mains transformers for the L5 / L5E buildings.

3.2.2 EZ2 Flywheel Generator

The regular revision of flywheel generator EZ2 proved again to be urgently needed. A balancing ring of the motor was loose and had to be re-welded. At the shaft generator a bad contact of the winding was determined. A temporary continuation of operation was considered possible.

Therefore, the repair could be postponed until the next break. During the overhaul the winding support wedges of the generator stator were replaced in order to maintain short-circuit strength. Thereby a winding rod was damaged, but could be replaced by a spare one. In a meta-study, the lifespan of the EZ2 flywheel was investigated and found to be non-critical. In parallel to the experimental operation, the specification for the renewal of the drive converter, the main excitation and several auxiliary converters of EZ2 was prepared and the tendering and awarding process was carried out. This is intended to upgrade the flywheel generator for another 20 years of operation.

3.2.3 High Current Power Supply Group 7

In May 2021, after a successful short-circuit test, the two converter transformers for the new thyristor converter Group 7 were delivered and installed. Immediately afterwards, the commissioning started and was successfully completed in February 2022. This included remote operation and thyristor crowbar overvoltage protection. The converter extends the pulsed power capabilities of ASDEX Upgrade and ensures a certain redundancy for the magnet coils supply. In the remaining six months of ASDEX Upgrade operation, the converter was successively tested in all possible configurations on all OH and vertical coils. Minor errors that had not been noticed during dummy load commissioning could be corrected.

3.2.4 High Voltage Power Supply OCEM PSM

Installation of the new ELISE c/w high-voltage power supply was completed in early 2021. After successful commissioning on a resistive dummy load ELISE was transferred from the former pulsed HV power supply to the new pulse step modulator (PSM) system. So far, the goal of 1000 s pulses has been achieved and the maximum high voltage power was 1334 kW for 469 s with 10.0 kV / 37.4 A from the extraction grid power supply (EGPS) and 44.5 kV / 21.6 A from the acceleration grid power supply (AGPS).

3.2.5 Renovation of ICRF Driving Amplifiers

For the upgrade of the ICRF driving amplifier, a control module of the Sinamics DC Master series was purchased. This solution makes it possible to maintain the principle of a three-phase a.c. controller (W3C). After initial tests with a function generator, the module was successfully tested at the 100 Hz generator network including frequency drift during an ASDEX Upgrade pulse. So far, three 150 W light bulbs have been used as a dummy load. In the next step, the original 16 kV output transformer will be connected and control will be further improved.

3.3 CODAC

3.3.1 IT Infrastructure

In 2020 a new group "IT infrastructure and security" has been established within IPP's Garching site, therefore the ASDEX Upgrade IT group could hand over the responsibility for general IT services like

office IT equipment, office network, WiFi, printers, remote computer access, etc. to this new group. The equipment of workstations for the ASDEX Upgrade departments, both in hardware and software, is now provided by the new local IT group, in close cooperation with the ASDEX Upgrade IT group.

The responsibility for all IT systems involved in the acquisition of data from measurements at ASDEX Upgrade and their direct processing, as well as software development for storing, retrieving and processing data from ASDEX Upgrade, remains with the ASDEX Upgrade IT group.

3.3.2 AUG Data Acquisition

Data acquisition at ASDEX Upgrade ran routinely and reliably during the last campaigns. The average amount of data collected during one shot has increased again from 50 GB in the 2020 campaign to 53 GB in 2021, and to 61 GB in 2022, which resulted in a total amount of measured raw data of 72 TB in 2022, furthermore 9 TB of evaluated data and about 10 TB of video data.

The underlying file system for all data from ASDEX Upgrade, both measured and evaluated data, since nearly 3 decades is the Andrew file system (AFS), hosted jointly by the AUG IT group and MPCDF. Since this file system is not a viable option for the future due to its decreasing support, a new and modern file system is now being installed by the local IT group. Preparations for the transfer of all data, about 1 PB, to the new file system have been started. While the API for writing and retrieving of the shot data will be adapted to the new system, so that the changeover is transparent to the end-user, at the same time the opportunity is taken to add more metadata to the data from the experiments in order to improve their quality in terms of 'FAIR data' (findable, accessible, interoperable, reusable), and to expand the existing data retrieval API for a future offering of 'open data'.

For a number of new and existing diagnostics, the data acquisition systems have either been newly commissioned or upgraded, most of them based on the approved in-house developed standard "SIO2" [9]. Where necessary, legacy Solaris host servers have been replaced by recent Linux systems. In order to assist both the diagnostic operators and the electronics groups, a new set of tools has been developed to provide direct online insight into the data collected by a SIO2 system, helping to speed up the commissioning and troubleshooting process for new and existing diagnostic systems. Furthermore the software for running SIO2 data acquisition systems has been modernized and improved, e.g. changes in the configuration of a diagnostic can now easily be accomplished on a short timescale without the need to re-compile any driver.

Among the newly built diagnostics especially worth mentioning is the data acquisition for the new Comb reflectometer diagnostic for measurements of turbulence properties (see section 2.2). With data acquisition at a rate of 20 MHz for up to 18 channels, it is currently one of the largest data acquisition systems at ASDEX Upgrade, having a data throughput of 700 MB/s and so producing a total of 6.5 GB of data per

shot. The data acquisition system for this diagnostic, based on "SIO2", has been built and commissioned successfully and is running very reliably. Therefore, it will be loaned to W7-X during the reconstruction phase of ASDEX Upgrade and is currently being implemented at W7-X. The current standard data acquisition system used at ASDEX Upgrade, "SIO2" and its predecessors, has been developed at IPP since some time ago, because no commercial systems were available previously which fulfilled the high demands for diagnostic systems at ASDEX Upgrade. Nowadays, powerful commercial off-the shelf (COTS) products for data acquisition are available on the market. Therefore, such systems are being evaluated as alternative for the data acquisition of future diagnostics. Currently, for a new portable Helium-beam diagnostic, which will not only be used at ASDEX Upgrade, but also at W7-X and TCV, the data acquisition is being built based on COTS systems, using MicroTCA components (an open and modular standard for building high performance switched fabric computer systems in a small form factor).

3.4 Special Topics

3.4.1 Divllo Power Supplies

For the future supply of the new Divllo in-vessel coils two additional power supplies including cabling, disconnectors, earthing switches, current measurement, overcurrent and overvoltage protection are required. During the past year, the design was refined and most of the components have been ordered. The existing thyristor converter Group 3 will be used for common (13 kA / 500 V) and differential (± 3 kA / 500 V) coils supply.

A critical point is the supply of water and electricity to the TIC coils. The ends of the conductor are only a few centimeters out of the vacuum flanges. Special connectors with and without MULTILAM lamellas have been designed and tested. The final design fulfills the requirements for good current conduction and did not show any degradation over time and under overload conditions. The connections will be further qualified at the Divllo mockup.

Another challenge is the overvoltage protection of the connected power supplies during a plasma disruption. It was analyzed by help of FEM calculations that the induced voltage from coil side can reach amplitudes of about 5 kV in the millisecond time scale [10]. Without counteractions, this would destroy the power supplies (operating at 340 V) and risk the mechanical integrity of the divertor coils due to Lorentz forces caused by uncontrolled short-circuit currents. The typical protection methods cannot be used, here, due to strict coil force limitations. Therefore, the development of a new kind of so called "ripping crowbar" was initiated in house. First experimental results are promising and will be published, soon. The concept is already published and discussed [11].

3.4.2 Ultracaps as an Alternative for Flywheel

A PhD was initiated in 2019 having the goal to find alternatives to fly-wheel generators as pulsed energy source of high power and energy.

Flywheels of required size are not available on the free market, anymore. The biggest AUG flywheel EZ2 provides an energy of about 2 GJ while the biggest commercial system used for grid stabilization application is of 200 MJ size. The concept of Modular Multilevel Converters (MMC) with integrated Ultracaps was identified as a potential candidate to fulfill the needs of AUG and future fusion-based power plants like DEMO.

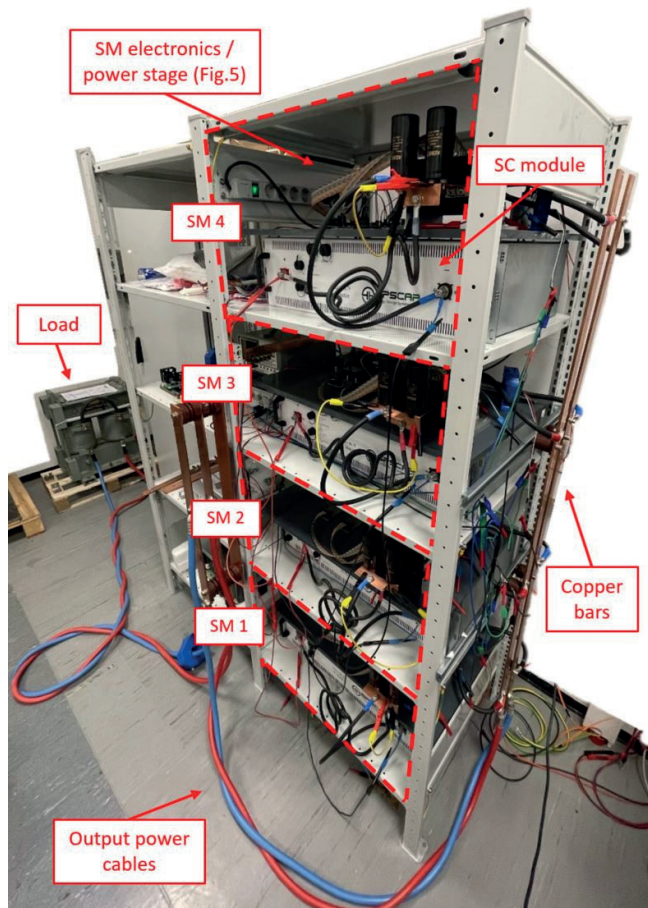


Figure 5. Demonstrator for the Ultracap-based energy storage consisting of 4 modules.

In cooperation with the Technical University of Darmstadt (TUD) a demonstrator consisting of 4 Ultracap modules (see figure 5) with integrated power stage was developed, realized and intensively tested to proof scalability up to very big matrices consisting of thousands of modules. To replace EZ2 it was calculated that about 2400 modules are required. The advantages of the concept are (i.) scalability of storage capacity and power stage by solely adding modules to an existing matrix, (ii.) high safety against destructive faults due to distributed and redundant power stages able to decouple single modules from the matrix, (iii.) high tolerance for lost modules (the others continue normal

operation), (iv.) wide range of topologies for different applications realizable with the same fundamental modules (DC-, 3-phase-, high voltage serial, high current parallel operation, etc.). The thesis is almost finalized. The results were published and presented [12, 13, 14]. Public/ industrial partners have to be found for finalizing the development and mass production of the modules. Financing needs to be organized.

3.4.3 Low Voltage Varistors for In-vessel Use

In 2020 there was initiated a cooperation project with Fraunhofer Institute for Ceramic Technologies and Systems (IKTS) with the goal to develop new kind of ceramics showing “varistor behaviour” for in-vessel use in present and future fusion devices. The applications are (i.) electric insulation with intrinsic voltage balancing capability, (ii.) arc protection and (iii.) voltage dependent activation of components (e.g. in-vessel coils). Varistor materials have a comparable electric characteristic as (better known) Zener diodes, this means, they behave like isolators for small voltage and conductors for voltages exceeding a specific threshold, the breakdown voltage VBD (or breakdown electric field EBD as a parameter independent from component’s dimensions). In contrast to diodes, the electric behaviour is based on the countless microscopic contacts (up to 10^6 1/mm³) between the grains of the ceramic. This could provide high tolerance to microscopic damage e.g. caused by neutron radiation. Another advantage is the high absorbable energy (100 kJ/kg), high current capability (>1 kA/cm²) and high reaction speed (>1 kA/μs). Unfortunately, commercially available varistors have EBD in the range of 1 kV/cm. This is factor 10 too high for vacuum in-vessel use, where arcing typically starts for electric fields >0.1 kV/cm. Thus, a study was started to proof feasibility of low-voltage varistors. First results are promising, reaching EBD<0.2 kV/cm [15]. Further research has to be done to optimize the electric behaviour and to qualify for fusion applications.

3.4.4 Outage of Essential Systems

During 2022 campaign, for the first time, the operation of AUG was analyzed from technical and organizational point of view on a daily basis. The database was manually updated after each shot day and shared with the whole team for corrections. Further sources considered are the AUG journal, updated by the session leaders and the AUG technical logbook accessible by the whole technical staff for detailed description of fault scenarios. As a result, the outage from and the failures, issues and delays caused by “essential systems” could be visualized by bargraphs. Because of the manual update of the database, the given numbers can only be taken as minimal values.

In the 2022 campaign, there was identified a total outage time of essential systems of 59 shot days but finally there were lost only 3.2 days of operation. This was possible by clever project management, using available redundancies and adapting the physical program to new technical limitations. In total, 242 shots were lost (interrupted before reaching the plasma current flat top). Main causes were:

(i.) plasma current breakdown or ramp-up issues (46 shots), (ii.) integration of the new thyristor group 7 (44 shots), (iii.) technical issues of our main RT density measurement (28 shots), (iv.) simple faults in the discharge program overlooked by the proponent and the session leader like coil current requests exceeding range limits (28 shots). Also delays caused by essential systems were noted, but this is very incomplete and will not be discussed in detail. In total, there were about 2700 minutes waiting time collected, which is equivalent to approx. 2 shots per day. Possible counteractions were discussed on the yearly AUG program seminar.

4 Scenarios

4.1 Negative Triangularity Plasmas

A dedicated effort on negative triangularity (NT) plasmas was launched already in 2019 and will be continued beyond 2022 [16]. In the last two years, more extreme shapes have been developed and investigated approaching upper triangularities of -0.45 at 600 kA plasma current (cf. figure 6). As can be seen in the depicted time traces, the density control is limited, as the density rises to values in the range of the Greenwald density due to the non-matching shape at the lower divertor. Still, at high heating powers considerable electron (~ 4 keV) and ion temperatures (~ 5.5 keV) could be reached, while the density is reduced. Those plasmas were expected to stay in L-mode even at high heating powers, while globally offering the confinement quality of H-modes. However, the discharges were clearly transitioning into H-mode at power thresholds typical also for standard shapes.

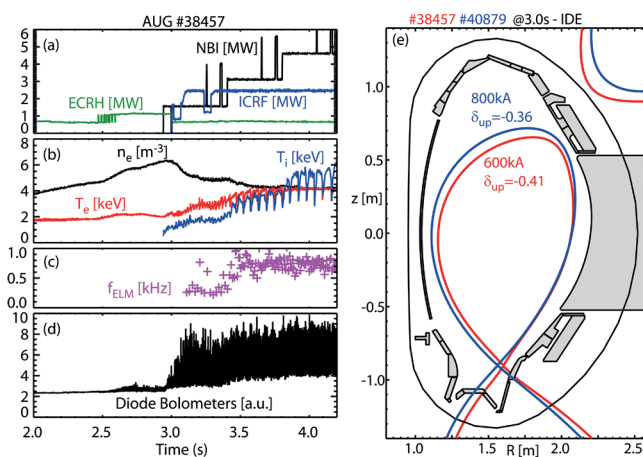


Figure 6. (a)-(d): Time traces of #38457 featuring a plasma shape with NT at 600 kA, (e): Most extreme NT plasma shapes for 600 kA and 800 kA discharges (equilibrium reconstruction with pressure constraints).

This is documented via various diagnostics including bolometry (see figure 6d) and Doppler reflectometry measurements of the radial

electric field (E_r). The plasma edge features low pedestal stability – as expected for the NT shape – resulting in low pedestal pressure, high ELM frequencies and reduced densities. As a result, the global thermal confinement is about 15 % below that of the $H_{98(y,2)}$ scaling for H-mode. Further effort was put into plasmas in unfavorable drift configuration preventing H-mode. Those discharges indeed stay in L-mode judging from E_r -measurements, however they still feature ELM-like instabilities. Their global confinement $H_{98(y,2)} \sim 0.75$ suggests confinement superior to L-mode, but not quite at H-mode level. In most recent experiments slightly reduced NT shapes at 800 kA plasma current were developed for better reactor relevance. The analysis for these cases is underway. It is foreseen to address the influence of shaping on the confinement on a more local level analyzing temperature gradients and modeling the turbulence via gyrokinetic calculations.

4.2 ITER Baseline Scenario in AUG

Investigations in support of the ITER baseline scenario (IBS) are ongoing in AUG. In the last two years emphasis was put on understanding the apparent confinement gap observed during flattop in AUG, the stability of the LH transition and the ramp-down phase.

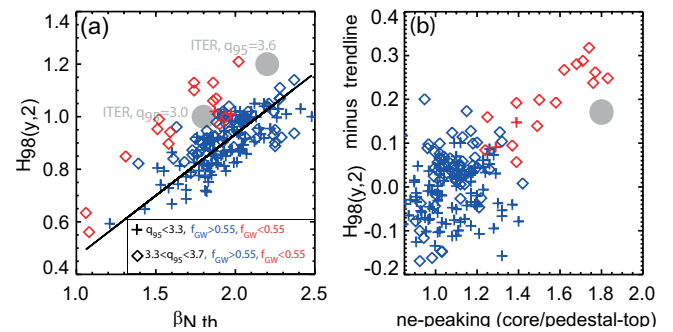


Figure 7. (a) The database of IBS performed in AUG. Data in the plane $H_{98(y,2)}$ vs β_N are depicted and a trendline for high density data is identified. On the right, the correlation between the deviations of $H_{98(y,2)}$ from this trendline vs. density peaking are presented.

In Figure 7, data from an IBS database are depicted. IBS discharges with high Greenwald fractions ($f_{GW} > 0.55$, blue data) turn out to follow a trend in the $H_{98(y,2)}$ vs. β_N plane (cf. figure 7(b)), which features too small confinement at the IBS design point indicated via the gray spot. This is independent of using the full current IBS ($q_{95} = 3$) or the IBS with reduced current (i.e. $q_{95} = 3.6$) for which operational boundary conditions are simpler.

Earlier fueling effects at the edge pedestal were investigated as possible effect on confinement. However, these effects turned out to be unimportant. Therefore, the focus was moved towards core transport.

According to figure 7(a), a simple remedy for recovering $H_{98(y,2)}$ seems to be a reduction of density (red data), while figure 7(b) demonstrates that the reduction of density goes along with density peaking. These observations are consistent with transport analyses guided by TGLF. Thus, there is hope that in ITER the confinement gap observed in AUG is irrelevant as there the density peaking will concomitantly exist with high Greenwald fractions. Also, doubts are in order on whether these dependencies are correctly mimicked by scalings such as $H_{98(y,2)}$. Investigations on the stability of the LH-transition for the IBS allowed for the establishment of a stability map. At auxiliary heating power (P_{aux}) twice or three times that of the LH threshold power (P_{LH}), stable H-mode entry can be reproduced at gas fueling levels which are typical for stable flat-top phases. For smaller gas flux levels the ELM frequency decreases and density and radiation rises resulting in a collapse of the plasma. The plasma behaves similarly if the gas fueling level is maintained, but rather the heating power is slightly reduced. Surprisingly, a stable regime is found at P_{aux} close to P_{LH} featuring a small ELM regime, which due to the existence of the so-called quasi-coherent mode is identified to be an EDA H-mode. In order to reliably obtain an EDA H-mode P_{aux} must not be too large and the gas fueling must be approximately twice or three times as large as the fueling levels necessary to maintain stable type-I ELM H-modes. For higher P_{aux} , it was demonstrated that the injection of Ar and Kr can enable the EDA H-mode. Similar investigations have been performed for ramp-down experiments. However, the small ELM regime often shows up naturally during ramp-downs due to an abundance of gas and a reduction of heating power. The vertical control of the plasma can be ensured by controlling the internal inductance (I_i). Various strategies have been investigated, showing that controlled plasma shaping and the ramp rate of the plasma current are the most powerful means of influencing I_i .

4.3 Non-inductive Tokamak Operation

This direction of scenario development bundles the efforts to sustain a large fraction of the plasma current by bootstrap current and external current drive under reactor relevant conditions, i.e. $T_i \sim T_e$, q_{95} close to the values actually envisaged for DEMO ($q_{95} = 3.0 - 3.93$ [17]) and ITER (scenario 4, non-inductive, $q_{95} = 4.5 - 5.0$ [18]). The related questions concern dynamo effects on the current profile (flux pumping), effects of the current profile on transport and MHD stability, combined with the effects of high beta also on flux pumping, transport and MHD stability. Additionally, changes in transport do modify the bootstrap current and external current drive profiles. In the last progress report from 2020 significant progress has been reported (mainly based on data from the 2018/19 campaign after the large steam event). Analyzing the 2020 data, it turned out that the 2019 data were hardly reproducible, most obvious from the need for significantly more heating to reach the same beta (i.e. significantly poorer confinement). These striking differences led to a prioritization of these studies in terms of allocated discharges (in 2021 essentially all proposed shots were allocated, in 2022 at least

still 50%). It turned out that the recycling fluxes in the machine have a strong effect on plasma confinement also at such values, at least an order of magnitude lower than at the H-mode density limit. This is illustrated in figure 8 and [17].

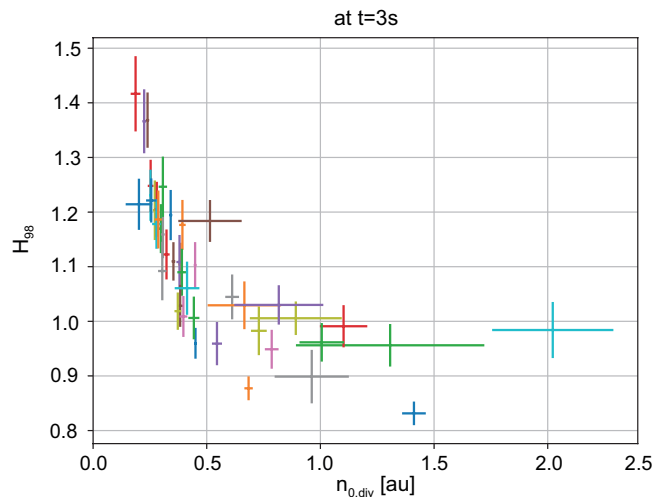


Figure 8. Increase of plasma confinement (here H-factor $H_{98(y,2)}$) for very low recycling fluxes (here divertor gauge F04).

It turned out that the effect can be explained in a similar way as the confinement degradation close to the H-mode density limit, i.e. by changes in the edge profiles of density and temperature, leading to changes in the pressure profiles which modify the peeling-ballooning stability [19]. Based on these results it seems very likely that the exceptionally good results from 2019 were due to the thoroughly cleaning of the whole interior of the device in 2018 after the heavy steam leak late in 2017. In the subsequent campaigns (2020–22) much more control effort was necessary to achieve low values of the recycling flux. Inevitably, such a subtle control scheme is rather sensitive to actuator or sensor failures as they happened in particular in 2022 (no NBI7, HST issues with NBI8, delayed coil OH2s, loss of calibration of manometer, DCN laser and detector issues, short term issues on ECRH and NBI systems). In the 2022 campaign the concept of model based ramp-up optimization was successfully applied, in order to reach high beta phases with $T_i \sim T_e$ (as for example described in [20]) early in the discharge to allow studies of these plasma states on several current diffusion times. Details on this and other topics are still under investigation.

An open topic was the importance of the $E \times B$ shear on the peaking of the T_i . In [21] it is described that a replacement of a toroidally inclined NBI beam by ICRH did not change that peaking although the $E \times B$ shear was significantly changed. Since also the fast particle population was changed, it remained unclear in how far both changes were important. This has been clarified using GENE simulations [22],

which allowed to reproduce the experimental findings within the uncertainties. Parameter variations around the operational points indicate that the $E \times B$ shear plays a minor role, while it is crucial to capture ICRF modifications to the fast ion populations (H^+ and D^+) [23].

5 3D Physics

ASDEX Upgrade is equipped with a set of 16 in-vessel saddle coils (dubbed "B-coils") to produce a small, non-axisymmetric magnetic perturbation (MP) of the otherwise axisymmetric tokamak field. This capability has been used to study the plasma response to resonant and non-resonant MPs, and to mitigate or suppress Edge Localised Modes (ELMs) in H-mode plasmas.

5.1 Effect of Resonant Magnetic Perturbations on the L-H Power Threshold

For ELM suppression from the beginning of the H-mode on, it may be desirable to switch on the MP field before the L-mode to H-mode (L-H) transition, which may affect the L-H power threshold. In a previous study [24], using moderate MP field and medium to high plasma densities only a weak effect was found. This work has now been extended to lower densities and higher MP amplitude [25]. Figure 9 shows the L-H power threshold for a scan of $n = 2$ MP field strength, which can be measured, e.g. by the amplitude of the poloidal $m = 10$, 11, or 12 components of the vacuum field at the $q = 5$ plasma surface. The L-H power threshold remains constant at low MP amplitudes and increases at high MP amplitudes.

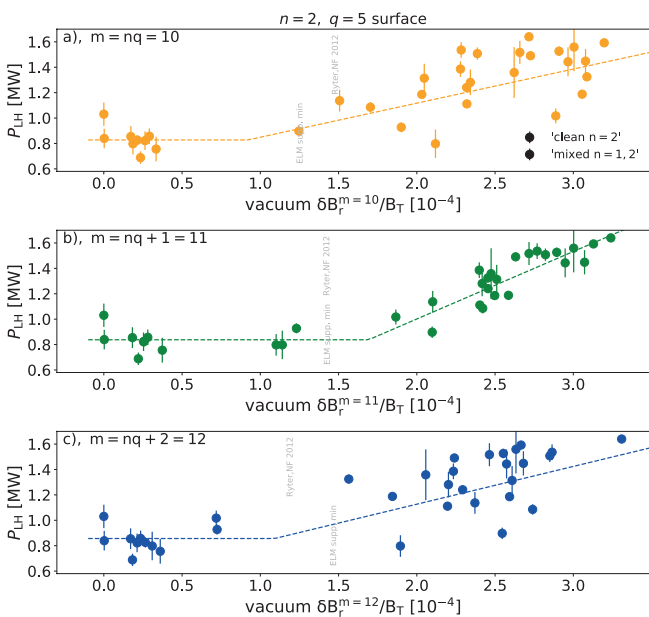


Figure 9. L-H power threshold as a function of the vacuum MP amplitude for poloidal modes $m = 10$, $m = 11$, and $m = 12$, calculated at the $q = 5$ surface.

As indicated in the figure, the transition region is about at the MP levels of reference [24], and at the level required for ELM suppression. The existence of two poloidally separated rows of B-coils allows to vary the phase difference $\Delta\varphi_{UL}$ between the current patterns in the upper and lower toroidal coil sets, and thereby to vary the poloidal mode spectrum of the generated MP. In figure 10, this technique is applied to scan the resonant field component ($m = 10$ at the $q = 5$ plasma surface, blue dashed curves in arbitrary units) at constant coil current amplitude. The L-H power threshold (black points) increases with increasing resonant total MP component, i.e. when the plasma response is included (blue solid line), but both quantities are not proportional. Instead, a threshold in the resonant component of the MP field has to be exceeded for the L-H power threshold to increase (red curve). This observation suggests that the L-H transition is affected by the resonant plasma response, and one can speculate that the threshold behaviour originates from its non-linear effect on plasma parameters that govern the MP shielding such as perpendicular plasma flows and/or the radial electrical field.

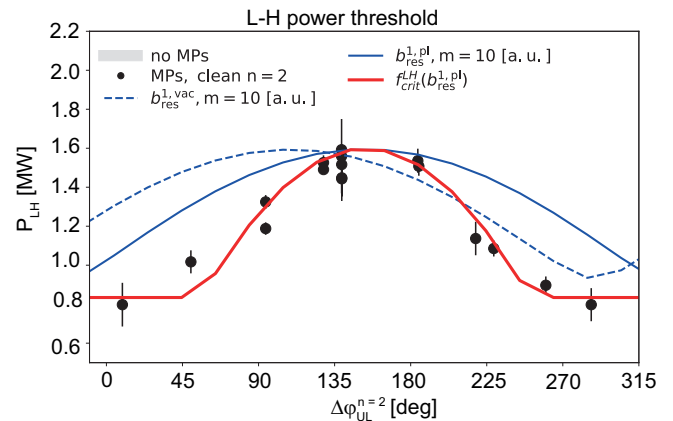


Figure 10. Measured L-H power threshold (black points) as a function of differential phase $\Delta\varphi_{UL}$ between upper and lower B-coil MP field. $\Delta\varphi_{UL} = 150^\circ$ corresponds to the maximum resonant total MP field (blue solid line).

5.2 ELM Suppression in Hydrogen Plasmas

For the initial pre-fusion operation phase of ITER in hydrogen or helium, it is planned to commission H-mode plasmas which likely produce ELMs and hence may need ELM mitigation techniques in place. Access to ELM suppression has been tested in ASDEX Upgrade in hydrogen plasmas with parameters similar to those in deuterium ELM suppression plasmas. A large degree of ELM mitigation was obtained, but no full suppression. Figure 11 shows time traces of two H-mode plasmas, shot 38168 in hydrogen, and shot 34826 in deuterium with similar heating power, similar pedestal density (below the empirical density maximum for ELM suppression in both cases) and similar q_{95} (inside the empirical window around $q_{95} = 3.7$). While the deuterium discharge shows complete ELM suppression, small mitigated ELMs persist in the case of hydrogen.

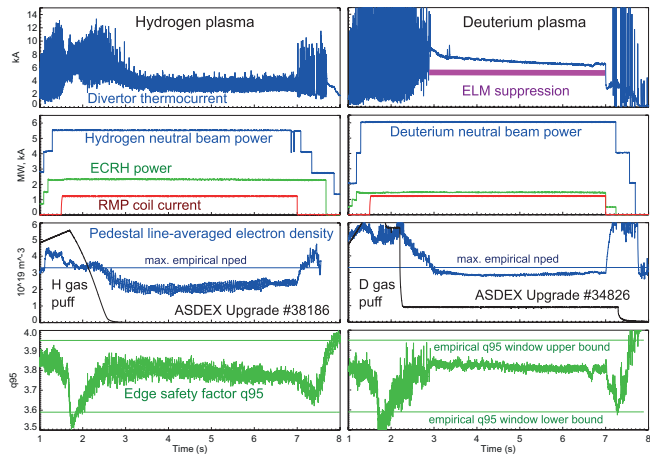


Figure 11. Time traces of H-mode discharges in hydrogen (left) and deuterium (right), matching all known critical parameters for ELM suppression. While ELMs are suppressed in the case of deuterium, they are only mitigated in the hydrogen plasma.

In a hydrogen fueling scan, a critical maximum relative concentration of hydrogen of $H/(H+D) = 38\%$ for ELM suppression has been measured. The underlying reason for this mass dependence has not yet been identified. It should be noted that the pedestal parameters measured in these hydrogen plasmas fall well into the region populated by deuterium ELM suppressed plasmas, so pedestal collisionality and beta are matching well, while the mass change implies a difference of the normalised gyroradius, ρ^* . A true identity experiment that matches all three parameters has not yet been carried out in AUG, but is a possibility for the future.

5.3 Access to ELM Suppression

In AUG it was previously found that ELM suppression requires the edge safety factor to be in a window $q_{95} = 3.59\text{--}3.95$ [26]. Additional effort was spent to extend this range towards higher q_{95} , for the benefit of ITER scenarios at reduced plasma current. These studies made use of the maximum RMP current amplitude, and differential phase $\Delta\Phi$ adapted to the q_{95} trajectories as to obtain maximum resonant field amplitude. Time traces of one successful discharge are shown in figure 12. In a q_{95} ramp upwards, three ELM suppression windows are detected, the first (known window) up to $q_{95} \sim 3.95$, a second at $q_{95} = 4.0$ to $q_{95} \sim 4.2$ and a third window at $q_{95} \sim 4.25$ to $q_{95} = 4.4$. The narrow intervals between these windows are filled with miniscule ELMs. Above $q_{95} = 4.4$, fairly large ELMs return. Even though ELM suppression is lost, the plasma density drops after $t \sim 4.6$ s, indicating an intact “pump-out” effect due to a significant resonant magnetic perturbation. An interesting but open question is the origin of the q_{95} windows. If the locations of resonant surfaces with respect to the pedestal top are important for ELM suppression,

as has been proposed e.g. in reference [27], then one would expect a q_{95} spacing of ELM suppression thresholds of $\Delta q = 0.5$ (for the $n = 2$ MP used here). Instead, the observed spacing between upper thresholds of neighbouring pairs of windows is much smaller, $\Delta q = 4.4 - 4.25 \sim 0.15$ and $\Delta q = 4.2 - 3.95 \sim 0.25$.

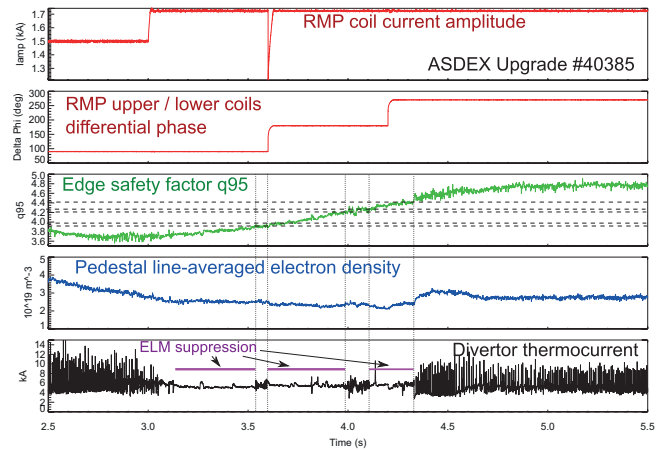


Figure 12. Edge safety factor q_{95} scan to identify windows for ELM suppression at $q_{95} > 3.95$.

Another apparent phenomenon is the requirement of a minimum upper plasma triangularity δ_u , where ELM suppression was obtained at $\delta_u = 0.23$ and not at $\delta_u = 0.05$ [28]. In new experiments, the lower triangularity was raised and ELM suppression was found in the range of $\delta_l = 0.38 - 0.5$ (upper triangularity $\delta_u = 0.23$). With high shaping, the q_{95} window at $q_{95} = 3.59\text{--}3.95$ seems to persist. However, no significant increase of the pedestal pressure was found when increasing δ_l . This result is maybe expected, since without ELMs, the ELM stability limit may become irrelevant for the pedestal parameters, and this role is taken over by the transport mechanism that produces the observed density reduction.

It has been noted in reference [26] that for high pedestal T_e (figure 15 in reference [26]) ELMs may re-appear, and it was hypothesized that this could be an effect of the total pressure reaching the perturbed ELM stability limit. However, there may also be effects of the T_e/T_i ratio. This has been addressed in a heating mix scan, where the ratio of NBI and ECR heating power was varied. Due to low pedestal collisionality electron and ion temperature are somewhat decoupled on the entire plasma radius, out to the pedestal top. As an example, figure 13 shows time traces of pulse 38900 where with increasing ECRH power (while NBI power is kept constant) the T_e/T_i ratio approaches unity and small, grassy ELMs reappear ($t = 4.7 - 5.2$ s). Interestingly, T_i , plasma rotation and plasma density remain practically unchanged so the question is how the T_e/T_i ratio affects the ELM behaviour without changing pedestal transport significantly.

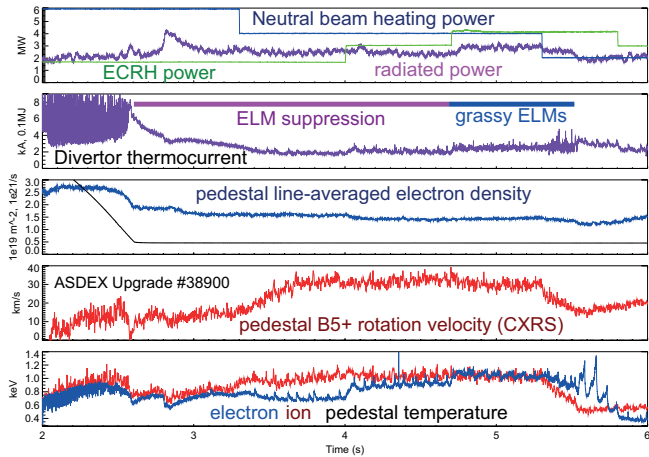


Figure 13. Time traces of shot 38900, where minute grassy ELMs re-appear at $t=4.7-5.2$ s with increased electron heating and pedestal T_e/T_i approaching unity.

6 MHD

MHD stability studies on AUG address both fundamental MHD phenomena such as reconnection physics as well as the analysis of performance limiting MHD modes with the aim to avoid them (see also section 8) or mitigate their consequences. For the latter, the new Shattered Pellet Injection system, which was installed on AUG in a joint project with ITER, was operated in the 2021/22 campaign.

6.1 Sawtooth Reconnection Physics

A better understanding of sawtooth reconnection physics is beneficial to both fusion research (sawteeth may trigger neoclassical tearing modes, which deteriorate the plasma confinement and may lead to disruption) and magnetic reconnection research (as the reconnection has similar nature in space and laboratory plasmas).

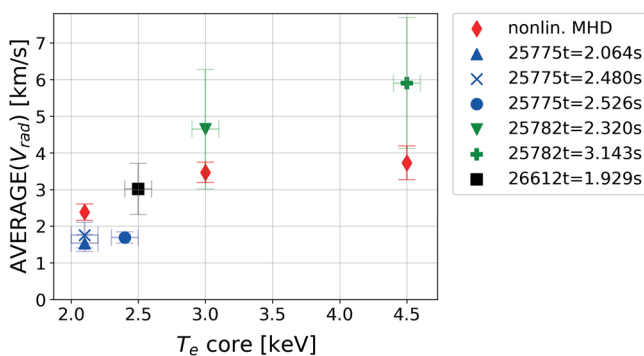


Figure 14. The dependence of the averaged radial velocity of the plasma core on the core electron temperature T_e during sawtooth crash phases.

Radial velocities V_{rad} of the plasma core during the sawtooth crash phase have been measured with the electron cyclotron emission imaging (ECEI) diagnostic diagnostic in AUG [29]. These measurements introduce a novel approach for studying magnetic reconnection during sawteeth since the radial velocity characterizes the rate of the reconnection. The radial velocities and their average values $AVG(V_{rad})$ have been compared to nonlinear two-fluid simulations using the TM1 code [30]. The comparison has shown good qualitative and quantitative agreement of the results (see figure 14). The variations of $AVG(V_{rad})$ and observed crash durations are explained by the finite ion-sound Larmor $\rho_s \sim \sqrt{T_e}$ effect (a contribution of the electron pressure gradient term in the generalized Ohm's law).

Additionally, the observed crash durations have been compared to the time scaling of the Kadomtsev model (which is a Sweet-Parker type magnetic reconnection in a collisional plasma) in figure 15.

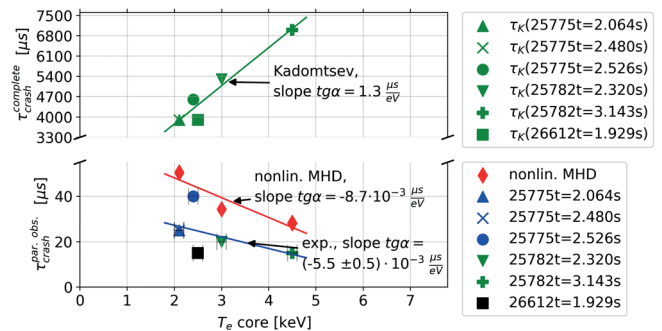


Figure 15. The dependence of the duration of partially observed sawtooth crashes on the plasma core electron temperature. Kadomtsev times of complete crashes are calculated using the experimental parameters from the six crashes. Straight lines represent a linear fit to the data.

The predictions based on the Kadomtsev model gave wrong dependencies and two orders of magnitude difference for the crash time compared to the experiment. The latter is a confirmation that a two-fluid description, which contains electron pressure gradient and electron inertia effects, is required to correctly model magnetic reconnection during the sawtooth crash.

6.2 Locked Mode Analysis

Tearing modes with toroidal mode number $n=1$ are often observed to be disruption precursors, especially when they are locked to the vessel. Therefore, it is important to clarify the role of the coupling of modes with different poloidal mode numbers and their locking to the wall before a disruption.

While the structure of sufficiently fast rotating modes can be analyzed by Mirnov coils measuring the time derivative of the poloidal magnetic perturbation field, for locked modes the radial magnetic perturbation field must be determined by integrating the voltage induced in saddle coils.

The locked-mode detector at AUG is a set of saddle coils positioned at the high-field side midplane. In order to resolve the poloidal locked mode structure, the B-coils (cf. section 5) above and below the midplane on the low-field side in front of the Passive Stabilization Loop (PSL) can be used in addition when they are not active [31]. Since the radial magnetic perturbation field is reduced by mirror currents in nearby conducting structures, the saddle coils, in particular the B-coils, are only suitable for a frequency range below ~ 5 kHz. For mode analysis in terms of amplitude and phase, a 3-D finite element model of AUG has been developed based on [32]. This program predicts all magnetic measurements of a rotating perturbation current at the resonant surface (cf. figure 16), including the frequency-dependent influence of the PSL and a simplified representation of the vacuum vessel. By superposition of modes with different poloidal mode numbers and fitting the simulated to the measured data, the complex mode amplitudes can be determined for arbitrarily low mode frequencies, so that the poloidal mode structure of even locked modes can be analyzed. This is the prerequisite to study mode coupling on the route towards a disruption.

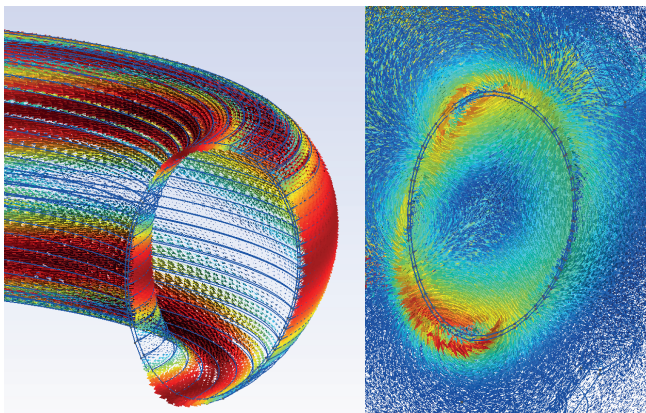


Figure 16. (right). The absolute values of the amplitudes are colour coded with red the maximal value. The direction is indicated as arrows, partly distinguishable.

To best represent the real geometry and conductivity of the vacuum vessel, the remaining free parameters of the model have to be adjusted. Dedicated experiments with tailored mode behavior have been designed with the aim that the mode frequency covers the range that allows simultaneous mode observation by the Mirnov coils, the locked-mode detector and the B-coils. This has been achieved by heating power and torque input variation during an existing $n = 1$ (dominant $m = 2$) tearing mode. This new simulation tool, optimized with dedicated experiments, allows to study the mode behavior before disruptions, in particular the changes in mode composition and complex mode amplitudes during the locked phase.

6.3 Error Field Correction Experiments

The $n = 1$ error fields (EFs) in AUG are very small, less than 10^{-5} of the primary magnetic field for the resonant EF components. This allows tokamak operation in most regimes in L and H-modes without any correction of the EFs. The situation changes in high beta plasmas with the central safety factor profile slightly above one as is typical for the improved H-mode (hybrid) scenario in AUG. In this case, even a small EF can be amplified by the plasma, and EF correction becomes important and helps to improve the overall performance. The required correction currents are small (about 10 % of the maximal B-coil currents). During the 2022 campaign, two variants of the EF corrections were tested, as shown in figure 17.

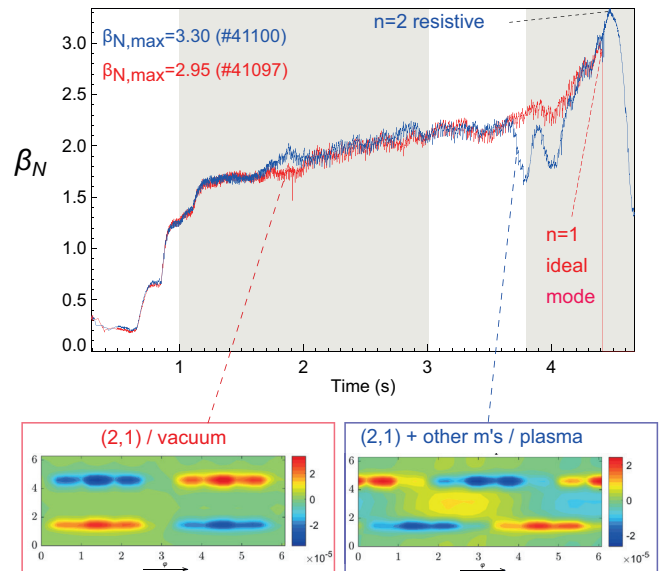


Figure 17. Time traces of two experiments with different error field correction strategies (upper panel). The corresponding correction patterns are shown in maps of poloidal versus toroidal angle in the lower panels.

In the first case, the dominant vacuum (2,1) component of the EF was canceled with the B-coils and $\beta_{N,max} = 2.95$ was achieved (red trace in figure 17). The plasma was limited by an ideal $n=1$ kink mode, which is a clear indication of the ideal beta limit. This correction was calculated assuming a pure electromagnetic model of the EF in the CAFÉ code. The second variant takes into account the plasma response to external perturbations and reached $\beta_{N,max} = 3.3$ (blue trace in figure 17) and the limit was resistive. In this case, the results of the electromagnetic simulations were combined with linear MHD calculations from the MARS code to reduce the dominant EF in the presence of the plasma. The shaded areas on the figure indicate the time when the EF correction was applied. The magnetic fields applied by the B-coils at the $q = 2$ surface are shown in figure 17.

6.4 Disruption Mitigation by SPI

ITER selected Shattered Pellet Injection (SPI) as its primary disruption mitigation actuator [33]. SPI offers the possibility to smoothly bridge between massive gas injection, where material penetration does not scale favorably for large devices; and (impurity) pellet injection, where ablating the necessary amount of material from a single pellet is difficult.

In SPI, a single large pellet is formed, launched towards the plasma, and broken into smaller pieces just before reaching the plasma edge. With a careful selection of pellet speed, material, and impact geometry it is possible to control the size- and speed distribution of the resulting frozen material spray (and residual gas), allowing to optimize the disruption mitigation characteristics of a given injection recipe. The relationship between pellet parameters and spray quantifiers, and those to disruption mitigation efficacy, is however highly complicated, requiring major research effort.

Mid-2020 ITER IO decided to fully finance the development and installation of a state-of-the-art SPI injector on AUG. The goal of the project is to explore the relationship between these aforementioned parameters, and to give direct input for the design of the ITER Disruption Mitigation System (DMS), in particular on the choice of shatter geometries, desired pellet compositions, and speeds. For this reason, the AUG SPI was designed to be uniquely flexible: it has 3 cold cells, which can independently generate 3 pellets from $D_2(H_2)$, Ar, Ne, and mixtures of Ne + $D_2(H_2)$. Each cold cell can vary the pellet diameter between 1–8 mm, the pellet length between 2–11 mm, and the pellet speed between 60–900 m/s (note, that not any arbitrary combination is possible). The system features shatter heads which are relatively easy to exchange.

After assembly and basic commissioning in late spring 2021, the SPI team has engaged in several months of laboratory characterization. This has served three main purposes:

- i. Development of a large array of reliable and reproducible pellet recipes (combinations of the above parameters);
- ii. Collection of pellet shatter data for more than 1400 cases with the help of ultra-high-speed video cameras;
- iii. Selection of the shatter heads to be installed in AUG.



Figure 18. Shatter spray of an 8 mm diameter, N_e pellet (250 m/s, 25 deg).

About a dozen different geometries were tested (see figure 18 for an example). Based on the results of the laboratory testing, the three shatter heads installed inside AUG for the 2022 campaign are a 25°, 78 mm long, 21 × 21 mm rectangular head, a 25°, 46 mm long, 16 mm diameter circular head, and a 12.5°, 78 mm long, 21 × 21 mm rectangular head. This trio provides the largest coverage of spray distributions, and also allows the comparison of similar size distributions at different penetration speeds.

Analysis conducted on a subset of the pellet shatter videos suggests that the currently available pellet break-up models cannot describe the observations. The mean fragment size as function of normal impact velocity drops exponentially in the data (whereas it is linear in present theory), while the number of fragments is a linear function in the data, but grows exponentially in theory [34]. Further work is necessary to understand the implications of these observations on SPI simulations, which require an input of shard distributions.

The installation of the SPI injector was accompanied by two large diagnostic extensions. Two views were equipped with high-resolution ultra-high-speed cameras, providing a two-axis view of pellet injection, ablation, and subsequent plasma evolution. Furthermore, 5 new foil bolometer arrays (4 channels each) and four new AXUV diode arrays (48 channels each) were installed, providing AUG with the most detailed bolometer coverage of any tokamak for disruption studies.

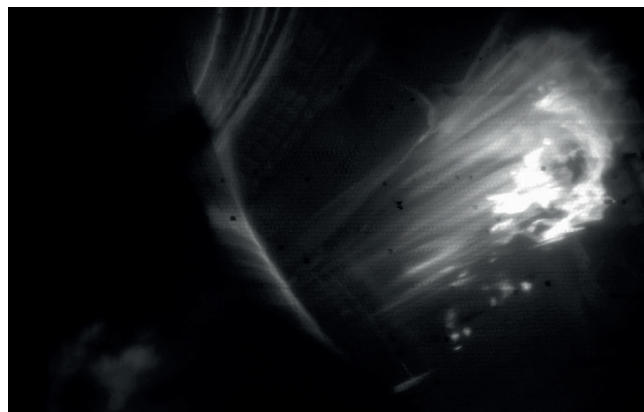


Figure 19. Double D-SPI injection in AUG #40789.

The first pellets were fired into AUG plasmas in late-2021, 18 months after the contract signature with ITER. The AUG SPI experiments are organized within the triple collaboration of the ITER DMS Task Force, EUROfusion, and IPP; with the latter two providing a significant shot budget. During the course of 2022, 12 sessions (219 discharges) were dedicated to study the impact of different pellet parameter combinations on disruption mitigation characteristics. Multiple target plasmas were investigated, to understand the impact of e.g. plasma thermal energy, safety factor profile, or pedestal temperature on pellet assimilation. Single and multi-pellet injection schemes were tested.

Several discharges were dedicated to understand the efficacy of SPI mitigation of SPI fired into an already collapsing plasma. Timing of the Thomson scattering diagnostic with respect to the injection was adjusted to provide density measurements at the most impactful time points of pellet assimilation. An example of a dual SPI injection is shown in figure 19.

Early analysis of the AUG data suggests that both the pre-thermal-quench time (pre-TQ) and the current quench time drop exponentially with neon fraction for D_2 -Ne mixture pellets, i.e., even as low as less than 0.1 % of Ne doping in an otherwise pure D_2 pellet led to a significantly different disruption than pure D_2 injection.

The data analyzed so far suggests that the 12.5° shatter head offers better assimilation than the alternatives: shorter pre-TQ, faster density rise, and faster current quench. A smaller shatter angle is easier for the ITER DMS design, and provides a smaller dependence on pellet velocity, an advantage for robustness. However, a short pre-TQ is more constraining for multi-injection strategies, a disadvantage for staggered injection schemes. There are some indications that a wider spread of the fragment plume may be beneficial (in AUG provided by the circular shatter head), however, as in this case the effective shatter angle is also a function of lateral position within the shatter head, the circular cross-section poses challenges for reproducibility.

7 Transport

At AUG, more accurate evaluations of the experimental thermal stored energies and confinement times, an important element in the assessment of confinement regimes and discharge scenarios, are now routinely obtained with the application of the RABBIT code, which calculates the beam ion energy content and losses [35].

The achievement of stable H-mode confinement without ELMs is an urgent research priority. Stationary ELM free conditions obtained just below the H-mode threshold, using feedback on the radiated power via seeded Ar impurity, have been investigated [36]. The resulting highpower L-modes exhibit confinement significantly higher than usual L-modes. Reduced pedestal pressures are compensated by increased profiles gradients in the peripheral region, caused by ITG turbulence reduction through impurity dilution. This limits the relevance of this scenario to a reactor. More strongly radiating impurities like Xe could have more favorable effects. Research on ELM-free regimes has also been performed by exploring the I-mode in non-deuterium plasmas [37]. The existence of the I-mode in hydrogen and helium plasmas has been demonstrated. Hydrogen features a higher power threshold than deuterium to enter I-mode, but also a 2–3 times broader power window, as well as a higher electron edge pressure at the L- to I-mode transition, always featuring pedestal relaxation events (PRE). These properties allowed a better characterization of PRE and their differentiation from type-III ELMs. Helium I-modes feature similar properties to deuterium I-modes. The analysis also shows

a correlation between the edge radial electric field minimum, the increasing net input power, with a dominant role of the edge ion temperature. L-mode confinement is the starting condition for any transition to high confinement regimes. AUG dedicated experiments and an intense related modelling activity have been dedicated to the understanding of the L-mode confinement [38] and edge turbulence [39, 40]. The ASTRA code and the quasi-linear turbulent transport model TGLF–SAT2 have been applied with boundary conditions at the separatrix [38]. Separatrix values are set with simplified models independent from profile measurements, with the experimental particle content matched in feed-back in the simulations. The sensitivity of the full-radius L-mode profile predictions to these assumptions is found to be very limited. Comparisons with experimental results covered variations ECRH power in both hydrogen and deuterium plasmas, plasma current at fixed magnetic field, with both ECRH and NBI heating, plasma density at constant ECRH power in hydrogen plasmas, as well as variations of the fraction of electron and ion heating. The ASTRA–TGLF predictions have been found to reproduce all of the experimentally explored dependencies with relatively good accuracy, demonstrating that the main L-mode confinement properties can be reproduced by full-radius simulations with a quasi-linear turbulent transport model. Some disagreement is only found at high electron heating power, with underpredicted ion thermal stored energy, and in the current dependence of confinement, which, in electron heated conditions, is predicted to be weaker than in the experiment. L-mode edge turbulence is investigated with nonlinear gyrokinetic simulations based on dedicated experimental results from AUG and JET-ILW, also with different hydrogen isotopes [39]. Analysis of the measured edge logarithmic gradients with increasing input power reveal that the ion temperature profile plays the dominant role in the radial electric field evolution. Larger input power and ion heat flux are needed in hydrogen to obtain values of T_i and R/L_{Ti} similar to the ones observed in deuterium. As a consequence, more power is needed in hydrogen to develop values of the edge radial electric field similar to those of deuterium plasmas. These observations point to a key role of the edge turbulence dependence on the main ion mass in determining the different L–H power thresholds with different isotopes. This change in transport is found in gyrokinetic simulations to be connected to the parallel electron dynamics, with stronger nonadiabatic response at low main ion mass. The gyrokinetic simulations demonstrate different roles of temperature and density gradients in driving or stabilizing the edge turbulence at different wavelengths and a strong stabilizing role of the external flow shear at large scales, destabilized by the R/L_{Ti} drive and the electromagnetic effects. When all of the experimental parameters are included in the nonlinear GENE gyrokinetic simulations from L- to H-mode, experimental values of electron and ion heat fluxes are matched within uncertainties [40], as shown in figure 18 for the ion heat flux. Nonlinear simulations of a stationary ELM-free H-mode phase also reveal a very strong effect of the mean $E \times B$ shear

reaching transport levels in the experimental range, thereby compatible with the confinement transition. Building on the good performance of the TGLF model in the prediction of L-mode edge transport and in the comparison with the GENE predicted impact of the $E \times B$ shearing, L-H transitions in full-radius ASTRA-TGLF transport simulations with self-consistent evolution of the radial electric field have been obtained with increasing heating power (see figure 20). The predicted L-H transition power is experimentally realistic, but also sensitive to the assumed conditions at the separatrix.

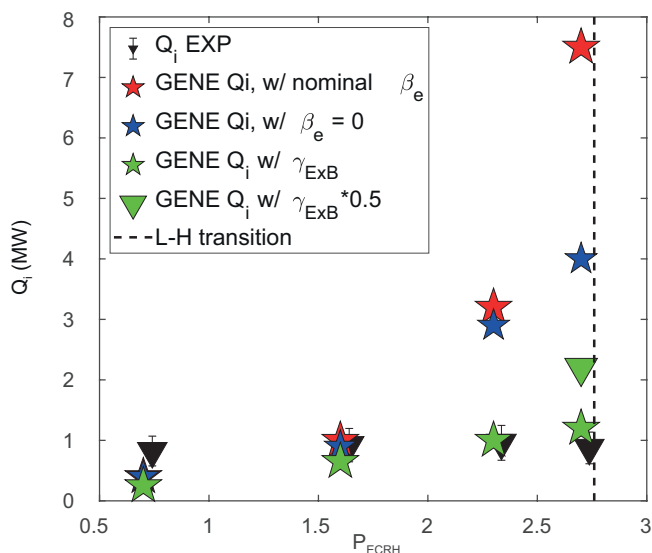


Figure 20. Ion heat flux at $\rho=0.95$ from an AUG ECRH power scan in a H plasma and corresponding GENE nonlinear gyrokinetic results, singling out different ingredients in the modelling as described in the legend.

Specific studies are also dedicated to the comparison of AUG plasmas in hydrogen and deuterium disentangling pedestal and core effects by matching the pedestal pressure with increased triangularity in hydrogen [41]. The beam ion content, larger in deuterium than in hydrogen, is identified as the main ingredient which increases the core confinement in deuterium. These observations are quantitatively consistent with nonlinear gyrokinetic simulations, but are not reproduced by quasilinear models when fast particle fractions are large [41]. An increased inter-ELM transport in the pedestal region in hydrogen as compared to deuterium is consistent with the above described L-mode edge studies, as well as by enhanced inter-ELM density fluctuation levels in hydrogen, measured by Doppler reflectometry. The pedestal is found to set below the peeling-ballooning limit, consistent with the dominance of transport effects. Isotope studies in AUG have been recently reviewed [42].

H-mode confinement and full-radius profiles are successfully predicted with the IMEP workflow (integrated model based on engineering parameters) [43]. ASTRA simulations, combining TGLF or QuaLiKiz

with an empirical pedestal transport model and an extended two-point model for the SOL, are integrated with MISHKA peeling-ballooning stability calculations. After the successful validation on a large database of AUG H-modes [43], a dimensionless form of the pedestal transport model is successfully applied to C-Mod and JET-ILW plasmas and compared with the EPED model [44]. IMEP predictions often show that the pedestal is better described than the core. A dedicated validation of the TGLF and QuaLiKiz models is performed on dedicated AUG experiments on core ion heat transport stiffness [45]. TGLF predicts stiffness which is closer to the experiment, however without the nonlinear fast particle stabilization, which is significant in nonlinear gyrokinetic simulations. QuaLiKiz is in better agreement with the experimental values of the electron heat flux. Here, a new collision operator improves predictions with central electron heating. AUG has also contributed to a recent multi-device study, with related multi-scale nonlinear gyrokinetic simulations, on the impact of the ETG turbulence [46, 47].

The tokamak flight simulator FENIX [48] couples the tokamak control system with a computationally fast, still enough realistic, plasma model [49]. A distinguishing feature of this tool is that it only requires the pulse schedule (PS) as input. The output is a virtual realization of the full discharge, which allows one to verify if the PS fulfils the control and physics goals. Emphasis is dedicated to the development of fast physics models which combine computational speed and physical realism [49]. For the core, physics-based analytical formulae, including explicit regressions on the TGLF model, are derived. These are applied to the full-radius in L-mode, whereas in H-mode a model for edge localized modes and pedestal pressure is included. In the scrape-off layer, in addition to the 2-point model, a multi-species and multi-region particle balance model is implemented. An analytical model which describes both banana-plateau and Pfirsch-Schlüter impurity transport is developed to closely reproduce the NEO drift-kinetic code results [50]. It is extended to include rotational effects, also at low collisionality. FENIX applications are dedicated to AUG and EU-DEMO [51]. On AUG, FENIX is applied to physics model validation and to the control system interactions with the plasma to predict the full system behavior. For EU-DEMO, kinetic control using realistic actuator behavior (e.g. the pellet injector) can be optimized to avoid undesired oscillations in the fusion power or loss of detachment due to density perturbations.

8 Plasma Control

Plasma Control at ASDEX Upgrade serves two main purposes, providing a reliable and robust fundament with high availability to execute experiments, and developing novel approaches and control functions to open and extend operational domains by improved real-time plasma state measurement, stabilizing feedback loops, comprehensive monitoring and sophisticated decision taking. Participation

in the development of the ITER (see section "International Tokamak Collaboration Project") and DEMO (see section "DEMO Design_Activities") control systems in addition widens the view for advanced control requirements and generalization of use cases.

Various measures have been taken to further enhance the stability and availability of the control system. Real-time, as well as non-real-time services of the Discharge Control System (DCS) have been packaged into Docker containers leading to a minimization of external dependencies and allowing for quick and safe roll-back, in case errors in newly deployed functions should be detected despite the extensive checks preceding every release. Moreover, the non-real-time services are now executed in a virtual environment, simplifying installation and maintenance. Currently, operating system updates to RockyLinux 8 (non-real-time) and RedHawk 8 (real-time) are being prepared.

The operational requests in the past campaigns have been challenging regarding the DCS configuration. In particular, negative triangularity experiments (see section 4.1) required high flexibility in the allocation of power supplies to coils regarding current polarity and the subsequent combined limits for control and protection monitoring. In order to minimize potential configuration errors this configuration process has been automated as far as possible.

A further protection component is the real-time video diagnostic. The previous system was bound to a dedicated very aged version, could not be upgraded and had therefore to be replaced to stay maintainable and extensible. The successor system now adheres to the modern DCS Satellite standard and is highly configurable. The new diagnostic focuses on image analysis to identify hotspots, while protective actions are now exclusively configured and taken by the control system.

The versatile dynamic decision taking capabilities of the DCS have been exploited to make major progress on the field of disruption avoidance and overall shot performance. Dynamic rule-based discharge planning considers limit proximity to HDL and MARFES in order to insert avoidance or recovery segments repairing otherwise severe degradation or even disruptive conditions. This capability is a powerful instrument to boost the robustness and effectiveness of discharge exploitation and will be developed further. Advancing control performance is to a large extent dependent on the precision and reliability of measurements and reconstructions. Accurate magnetic and kinetic profiles, for instance, are essential for current profile control. In a new approach, these profiles are calculated from measurements of magnetic fields, flux, T_e , n_e , but also from control-oriented models using the control system's actuation commands as inputs and aligning their predictions with the measurements. After the Janet code base for magnetic equilibrium had been migrated to C++ and sped up by \sim factor of 10 to \sim 100 microseconds per iteration, a major effort was taken to couple it with the RAPTOR observer accounting for plasma current diffusion and pressure profile. This is expected to be completed next year and will open the possibility of the current profile control.

Even more precise profile measurements can be obtained, when the

power deposition profiles for heating and current drive actuators are taken into account. In preparation of this future step, the real-time Torbeam algorithm has been modernized and adapted to the DCS Satellite standard. The real-time code now offers full Torbeam capabilities without simplifying assumptions, without penalties of the real-time performance. The improved accuracy of reconstructed profiles will facilitate the development of an advanced q-profile shaping scenario with fast ramp-up and a profile-dependent ECH timing.

Another example, where control can develop new operational ranges is the feedback control of the X-point radiator location (see section 13.1). It cannot only be used to control the detachment status, which is otherwise hard to measure, but also to avoid or reduce instabilities like MARFES and ELMs.

Developing and safely applying advanced and sophisticated control methods in regular operation is only possible with powerful design tools. For the validation of discharge programs, the design of new discharge scenarios and control strategies the FENIX flight simulator is being developed, which combines a plasma physics model (ASTRA) with a model of the plasma control system and is configured using genuine discharge program and DCS configuration data. A beta release is about to be released, soon followed by a first public release, that will support scenario and control development also during the enhancement phase (see section 1.4). Likewise, a modernized implementation of the Discharge Program Editor (DPE) has been developed, featuring high responsiveness, a novel user interface and a streamlined internal structure, that eases future extensions, in particular dedicated topical panels, validation and consistency checks and decision logic editors. The beta-version of the new DPE will be released together with FENIX and can already be used to prepare discharge programs for simulation.

9 ICRF Physics

The fast ion content associated with ICRF power was characterized with FIDA, neutrons and NPAs to validate and improve ICRF modeling codes. A focus was put on the comparison between $n = 2$ and $n = 3$ D-beam ion acceleration, with intriguing result that neutron signals (sensitive to high energies) are stronger for $n = 3$, while FIDA signals (sensitive to mid-range energies) are stronger for $n = 2$. Simulations were started to investigate this trend, particularly with TRANSP-NUBEAM-TORIC including an RF kick operator revised by PPPL colleagues to ensure the consistency of the applied model. FIDA signals have been collected for the first time for "pure" hydrogen minority heating with H-NBI instead of D-NBI (low absorption at $n = 2$ D). First TRANSP-NUBEAM calculations indicate a good agreement in the core plasma. Scans of phasing of the full 5-strap antenna array (phase-locked 2-strap and 3-strap antennas) have been carried out and show clear variations of FIDA and neutron signals. Effects of the low k_{\parallel} fraction in H minority with D-NBI ($n = 2$ D) and at $n = 3$ D will be modeled in the next future.

More data on the ^4He -(^3He)-H 3-ion heating scheme were collected. Experimental studies of the ITG stabilization by the ICRF-accelerated fast hydrogen ions in the plasma core and the effect on the T_i profile steepening [52] were continued. The roles of the central electron heating, the hydrogen concentration and the core MHD (controlled by tailoring q -profile) were investigated.

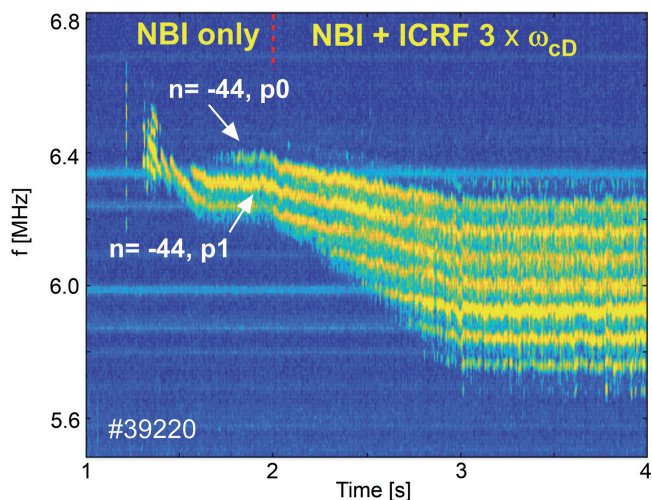


Figure 21. Evolution of spectrum of hf AEs with resolved mode numbers excited by NBI and by further acceleration via ICRF at $n = 3 D$.

The Ion Cyclotron Emission (ICE) spectrum and mode number measurements on AUG [53] reveal a variety of high frequency Alfvénic eigenmodes (hf AEs) driven by NBI. The hf AEs are strongly modified when NBI fast ions are accelerated by ICRF at $n = 3 D$ (see figure 21) and fast ion anisotropy is increased. Observations are supported by fast ion modelling codes TRANSP and ASCOT. The frequency response of the modified hf AEs is consistent with the fast ion evolution during the ICRF acceleration.

A new diagnostic for fast density (n_e) measurements at the edge, the Microwave Intensity refractometer in the Limiter Shadow (MILS) [54] located on an ICRF antenna, is developed and in operation at AUG, supported by the full-wave calculations to reconstruct the n_e distribution. Benchmarks with Li-BES, He-BES and Langmuir probes showed good agreement for the far SOL n_e . MILS also provides n_e values in the limiter shadow, scarcely covered by other diagnostics. The data is used in edge physics studies, e.g. ICRF local n_e modifications, EC wall conditioning, SOL properties of ELMs and of density filaments.

The density filaments in the SOL were rarely considered for ICRF power deposition so far: they are much smaller than radial wavelength of the fast wave, and not much power scattering is expected. However, the much shorter slow wave plays a larger role near the steep density gradient at the filament surface. Conditions were identified under which this gives rise to the excitation of surface wave modes that propagate

along the filaments, and the amount of power lost thereto was quantified [55]. These conditions match those under which large ICRF edge losses occurred on NSTX, an observation that had no convincing explanation for over 10 years. Favoring high harmonics, low k_{\parallel} , and high edge densities, these wave modes are unlikely to exist on AUG or other machines with conventional ICRF antennas including the future ones such as ITER, SPARC and DEMO.

Another important topic was to study experimentally the direct launching of the unwanted slow wave into the SOL by ICRF antenna (e.g. by image currents on the limiters), since particularly for ITER and DEMO the expected plasma density at the ICRF antenna can be very low. As a part of a PhD thesis, elements of the AUG ICRF antenna periphery were modified, in order to launch ICRF signals and study their propagation in the real SOL conditions with intermittent plasma density. Special AUG scenarios were used to expand the low-density SOL region across the ICRF antenna limiters. It was possible to detect low-density localized signals by electrostatic probes on the AUG midplane manipulator, at a distance of up to several meters from the source. Results of the experiments indicate that the injected signals indeed propagate through the low-density SOL following characteristics of the slow wave.

When lacking the ability to couple ICRF antenna codes to a core code, perfect absorbers, Perfectly Matched Layers (PMLs), are used to mimic good single-pass absorption in the antenna simulations. The edge density gradient is also partly replaced by a discontinuous jump from vacuum to plasma, in an attempt to avoid numerical issues associated with the lower hybrid resonance. Numerical surface wave modes were identified [56] that propagate along this density discontinuity and cannot be absorbed by the PMLs. The conditions were determined when these modes do not affect the results of antenna simulations.

In order to put constraints on theoretical descriptions of the RF sheath boundary condition, a feasibility study of local electric field measurement with spectroscopic methods at ICRF antenna was performed in the frameworks of another PhD thesis [57]. An optimized experimental configuration with spatially-resolved sheath measurements and a polarizer was first tested on the linear IPP device IShTAR. The measurements indicated that electric fields across the RF sheath at the IShTAR ICRF antenna are higher when the latter is powered during a helicon discharge, although the interpretation of the results is hindered by the presence of the RF waves from the helicon antenna. First experimental tests of the developed Stark spectrometry setup in AUG have provided insights for the next steps needed to apply the method on a tokamak.

10 Spectroscopy

10.1 Impurity Transport

A non-parametric inference of impurity transport coefficients by using charge exchange recombination spectroscopy (CXRS) measurements of Ne X, Ne VIII, O VIII, and C VI lines has been developed.

Due to their close atomic numbers, neon, oxygen and carbon impurity ions were assumed to have the same diffusion coefficient D and convection velocity v . Unlike conventional techniques that modulate or perturb the impurity concentrations, a quasi-stationary plasma with static impurity profiles was employed. Since the ratio of v to D only describes the equilibrated profile of the sum of all impurity charge states, steady-state measurements can still decouple D and v if different charge states are simultaneously observed. The analysis framework based on Bayesian probability theory was formulated and applied to a type III ELMy H-mode plasma. The charge exchange reactions with the background neutrals, which are known to affect the impurity charge state balance, were taken into account by introducing additional free parameters. While D at the pedestal is close to the neoclassical level ($1 \text{ m}^2\text{s}^{-1}$), a large diffusion coefficient and a strong outward convection are inferred inside the pedestal top [58].

Fully stripped boron transport was also studied by means of perturbation experiments using the ICRH antennae as actuators and the CXRS diagnostics to measure the boron density response. Using this technique it was possible to separate the diffusive and convective contributions to the B particle flux and create a database of transport coefficients covering a wide range of plasma parameters [59]. This database shows that the normalized ion temperature gradient (R/L_{Ti}) is the strongest organizing parameter and hollow B density profiles only occur for $R/L_{Ti} > 6$. This can be seen in figure 22, which shows the measured diffusion and convection coefficients as a function of R/L_{Ti} at mid-radius. The database also shows that large changes in NBI heating have only a small impact on low-Z impurity transport while even low levels of ECRH power dramatically increase both the diffusive and convective fluxes, resulting in peaked impurity density profiles. The measured impurity transport coefficients are well reproduced by a combination of neoclassical and gyro-kinetic modeling, with the exception of the hollow B density profiles, for which the sign of the measured convection is not captured. This data-set also demonstrates a non-monotonic dependence of the experimentally measured ratio of B diffusivity to ion heat conductivity (D/χ_i) in qualitative agreement with theoretical predictions.

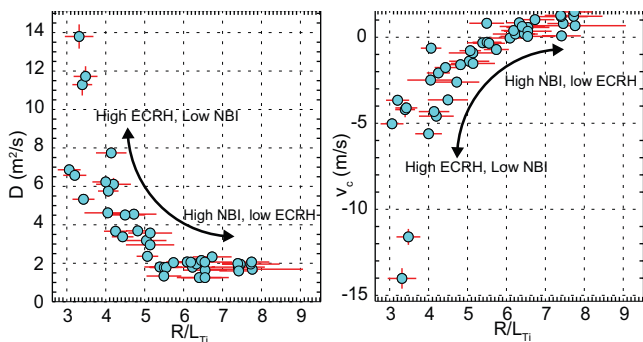


Figure 22. Boron particle diffusion and convection coefficients measured at mid-radius as a function of the normalized ion temperature gradient.

A new method was developed to model the neutral population produced by the gas puff-based charge exchange recombination spectroscopy systems. With this method, the edge impurity density on the high field side (HFS) and low field side (LFS) can be obtained without the need to apply a neutral beam injection system. The neutral penetration needed for the calculation of the impurity density is obtained with a new gas puff module implemented in the FIDASIM code. The impurity density profile evaluated with the new gas puff module matches the impurity density calculated with standard beam-based charge exchange diagnostics. Edge impurity toroidal and poloidal flows show asymmetric structures. In H-mode, the edge impurity density at the HFS is around 2–3 times higher than at the LFS. These asymmetries are in agreement with the measured poloidal velocities. In L-mode, there is no density asymmetry [60].

10.2 Edge Investigations

The thermal helium beam diagnostic at ASDEX Upgrade is used to infer the electron density n_e and temperature T_e in the scrape-off layer and the pedestal region from the emission of visible lines of the locally injected helium. The link between n_e and T_e and the emission is provided by a collisional radiative model, which delivers the evolution of the populations of the relevant excited states as the He atoms travel through the plasma. A computationally efficient method with just three effective states is shown to provide a good approximation of the population dynamics. It removes an artificial rise of T_e at the plasma edge when using a simple static model. Furthermore, the re-absorption of the vacuum ultra-violet resonance lines has been introduced as an additional excitation mechanism and is mainly important in the region close to the injection point. This extra excitation leads to a much better fit of the measured line ratios in this region for larger puff rates [61]. A new correlation analysis technique for the thermal helium beam diagnostics has been applied. Instead of directly evaluating line ratios from fluctuating time series, arithmetic operations to all available He I lines were applied and time series with desired dependencies on the plasma parameters have been constructed. By cross-correlating those quantities and by evaluating ensemble averages, uncorrelated noise contributions can be removed. Through the synthetic data analysis, the analysis technique is capable of providing the power spectral densities of meaningful plasma parameters, such as the electron density and the electron temperature, even under low-photon-count conditions. The analysis technique was applied to the experimental data obtained in ASDEX Upgrade and successfully resolved the electron density and temperature fluctuations up to 90 kHz [62].

A novel diagnostic has been developed based on the active spectroscopy of singly ionized helium to measure the radial electric field (E_r) at the outer mid-plane across the separatrix in all confinement regimes. This new spectroscopic system has been characterized by means of a forward model and bench-marked against other E_r measurements and the different diagnostics show overall good agreement [63].

Using these techniques, the formation of the edge E_r and its evolution prior to the L-H transition has been systematically investigated in favorable (ion ∇B -drift towards active X-point) and unfavorable (ion ∇B -drift away from active X-point) drift configuration plasmas in AUG [64]. It was found that in both drift configurations in L-mode the measured upstream E_r in the scrape-off layer (SOL) can be described by divertor measurements together with a simple 1D model. In the confined plasma the different contributions from the ion profiles determining E_r are of the same size, but they can have competing roles. Thus, the evolution of E_r in L-mode depends sensitively on the evolution of these individual contributions. Comparisons of L-modes in the two different drift configurations at matched plasma parameters have shown that the SOL- E_r profiles are the same between the configurations, whereas the E_r well in the confined plasma edge is shallower in unfavorable compared to favorable drift configuration. Neoclassical calculations cannot reproduce these observed differences in E_r , which indicates that non-neoclassical effects can play a role in setting the edge E_r in L-mode. The resulting weaker E_r gradients in unfavorable compared to favorable drift configuration L-modes at matched plasma parameters could be a possible explanation for the increased H-mode power threshold in unfavorable compared to favorable drift configuration. Comparisons of the E_r profiles at the H-mode onset additionally show that the E_r gradients can be very different between the two drift configurations. This indirectly indicates that differences in the turbulence characteristics might be present between the two configurations, which would be an additional element in explaining the different H-mode power thresholds in the two configurations.

The interplay between fast-ion transport induced by externally applied magnetic perturbations (MPs) and toroidal rotation (v_{tor}) has been studied in two low collisionality H-mode plasmas [65]. The study combines the analysis of experimental data with fast-ion modeling with the ASCOT orbit following code. The $j \times B$ fast-ion driven torque was evaluated with ASCOT simulations, using both the vacuum and the plasma response approach, in a high and low q_{95} equilibrium. The impact of MPs on fast-ion torque deposition was linked to v_{tor} changes via the momentum balance equation. The experimentally observed reduction in v_{tor} has been reproduced with high accuracy for the low q_{95} discharge, for which plasma response leads to amplification of the MP. For the high q_{95} case, the v_{tor} reduction is over-predicted in the pedestal region, which may be related to a stronger shielding of the MP than that predicted by the plasma response model. The analysis of the experimental data shows that the correlation between the measured fast-ion losses and v_{tor} is strongly dependent on the pitch angle of the lost fast-ions, which is in line with fast-ion redistribution due to MPs being resonant and thus strongly dependent on the ion orbit topology. These results highlight the importance of calculating fast-ion driven torques in full 3D magnetic fields when studying neoclassical toroidal viscous torques and the need for accurate models for the calculation of the plasma response.

The modeling tools developed in this work may enable the joint optimization of ELM control, fast-ion transport, and toroidal rotation drive in future fusion devices by optimizing the combination of the poloidal spectrum of the MP and q-profile of the axis-symmetric equilibrium.

11 Plasma Edge Physics

11.1 News on EDA H-mode and Quasi-continuous Exhaust (QCE) Scenarios

The EDA H-mode, first discovered and named at Alcator C-mod in 1997/99, is a stationary ELM-free H-mode scenario, now also developed at ASDEX Upgrade, that replaces the ELMy edge transport with a quasi-coherent mode (QCM). This mode is visible in several edge diagnostic systems such as reflectometry, ECE and the thermal He-beam diagnostic [66].

The quasi-continuous exhaust (QCE) scenario is also a scenario without type-I ELMs. Here the edge transport is replaced by type-II ELMs. The type-II ELMs are interpreted as ballooning modes at the pedestal foot, sometimes their signature is also visible at similar frequencies as the above mentioned QCM, but with lower coherency.

Both regimes have a wider parameter space at highly shaped plasmas, because the high shaping shifts the instability boundary of large type-I ELMs to higher gradients. The EDA H-mode is more easily achieved with pure or dominant wave-heating at low normalized pressure β , the QCE scenario can be optimized for high heating powers and high β . At low heating powers it is possible to transition from an EDA H-mode into a QCE scenario by gradually increasing both heating power and density. No discrete transition but rather a continuous change was observed.

Measurement of the Correlation ECE diagnostic in both EDA H-mode and QCE regimes shows a coherent mode being the strongest across the steep gradient region ($\rho_{\text{pol}} = 0.96 - 1$). In the QCE regime, the broadband turbulence dominates the pedestal top and outer core region.

The following efforts were undertaken to identify the dominant physical mechanisms in both scenarios and further analysis is still ongoing.

11.1.1 EDA H-modes

Besides a minimum fueling level required to access the regime, higher gas puff leads to a small density increase and allows the application of more power. Some scenarios were developed with a special focus on diagnostics, for example lower current plasmas that allow better and deeper QCM measurements due to the lower density pedestal. Taking advantage of such scenarios, the midplane manipulator was used with the high-heat-flux ball-pen probe to cross the separatrix of the EDA H-mode and directly measure several key QCM properties. These include cross-phases, wavenumber, phase velocity, and showed that the QCM drives significant cross-field transport, thereby confirming its important role in the regime.

In order to determine a key fingerprint of the underlying instability, the poloidal wave number k_{pol} and the radial wave number k_r of the QCM were estimated by means of a 5×5 grid of detection points of the thermal helium beam. Normalized to the drift scale ρ_s , the poloidal wave number is in the range of $k_{\text{pol}} \rho_s = 0.06$ and scales with the square root of the pressure, while $k_r \rho_s = 0$. These properties of the QCM point towards a kinetic or resistive ballooning mode, which is being confirmed in a direct comparison to non-linear MHD and turbulence simulations. The visco-resistive MHD code JOREK is being used to probe the non-linear stability of the EDA H-mode by taking the experimental equilibrium reconstruction of an EDA H-mode discharge as initial conditions. Simulations with realistic resistivity and parallel conductivity that include diamagnetic drifts show non-axisymmetric perturbations with toroidal mode numbers of 5–9 being linearly unstable and growing to limit the build-up of the edge pedestal and, therefore, act as a mechanism to prevent the onset of type-I ELMs. GENE analysis of EDA H-mode with Ar seeding reveals dominant ITG turbulence in the core region, TEM at the pedestal top and cannot conclude on the QCM. One of the most serious limitations of these gyrokinetic studies is the high radial resolution that would be necessary to implement a realistic flow shear profile [67].

11.1.2 QCE Scenario

The successful experimental decoupling of pedestal top and pedestal foot led to the hypothesis that small ELMs are caused by ballooning modes sitting at the pedestal foot [68]. This hypothesis is supported by a detailed analysis of the influence of different stabilizing mechanisms, namely local magnetic shear, connection length to the stabilizing high field side and radial electric field induced shear flow [69].

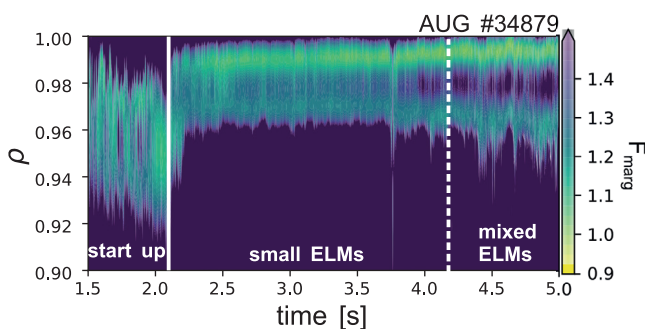


Figure 23. Temporal development of the normalized pedestal pressure expressed as ratio to the ballooning stability threshold, $F_{\text{marg}} = \alpha_{\text{exp}}/\alpha_{\text{crit}}$. A ballooning unstable region is identified at the pedestal foot in the small-ELM-scenario.

Also the ideal ballooning analysis of the transition from type-I ELMy H-modes to the ELM-free QCE scenario confirms that the pedestal foot becomes ballooning unstable. Figure 23 shows the closeness to the ballooning stability threshold expressed by F_{marg} across the pedestal.

QCE discharges with edge profiles that are ballooning unstable across the whole pedestal show a low confinement of H_{98} around 0.8, while edge profiles that are ballooning stable in the pedestal middle (second stability) have a good energy confinement with H_{98} around 1 [70].

The non-linear MHD code JOREK was used to simulate the transition from small ELMs to type-I ELMs by either reducing the separatrix density or increasing the input heating power. The stabilizing factors that play a role in the suppression of the small ELMs are also investigated by analyzing the simulations, and the importance of including diamagnetic effects in the simulations is highlighted. The underlying instabilities were identified as resistive peeling-ballooning modes [71].

11.2 Gas Puff Modulation Experiments

The reaction of the plasma edge to fuelling modulation has been investigated with dedicated experiments in L-modes and H-modes with and without type-I ELMs. The piezo valves which are situated close to the plasma allow short opening and closing times. The fast edge diagnostics installed at ASDEX Upgrade are ideally suited to provide fast measurements of electron density and temperature and, in case heating beams are applied, also ion temperature. The analysis of the pedestal region is conducted with the 1.5-dimensional transport code ASTRA, with the plasma heating profiles, the equilibrium and the measured kinetic profiles as input and the transport coefficients for heat and particle transport as output. The particle transport coefficients in the edge form a set of solutions together with the assumed neutral particle flux at the outer boundary, i.e. the separatrix [72]. In all cases, the edge transport coefficients react sensitively to fueling changes which makes the use of modulation experiments for the separation of particle diffusion and particle pinch impossible. Nevertheless, the experiments provide a wealth of information about the dependence of the dominant transport mechanism on changes to the electron density in the different regions of the pedestal. Transport at the pedestal foot increases in all investigated scenarios after fuelling is increased leading to a flattening of the density gradient.

Inside of the pedestal top the plasma reacts in different ways depending on the scenario: in L-mode and in QCE discharges transport reacts delayed or only weakly and we observe a pronounced increase in density at the pedestal top and further inside.

Figure 24 shows the gas puff modulation in the top panel and below the increase of the electron density (blue) in the edge interferometer channel together with the increase of the electron heat diffusivity (orange) at the position $\rho_{\text{pol}} = 0.95$. The data are averaged over 18 modulation cycles in a QCE discharge. At $t = 0$ the valve is opened, 2 ms later the density starts to increase and 8 ms later the heat diffusivity is increasing. After the closure of the valve it also takes some time until the diffusivity drops to its average value.

In EDA H-modes on the other hand, transport increases rapidly after fuelling is increased, flushing the fueled particles from the confined region and limiting the density increase due to fuelling.

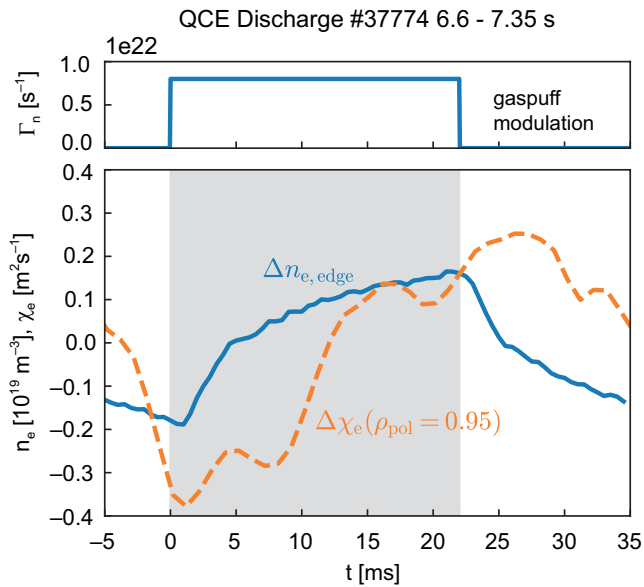


Figure 24. top panel: Neutral gas flux with modulation period of 22 ms, main panel: change of edge density (interferometer H-5, blue) and change of electron heat diffusivity (orange) at the position $\rho_{\text{pol}} = 0.95$ derived from ASTRA.

The experimental data were also used as input to linear GENE runs to determine the dominant turbulent transport mechanism in both the steep gradient region and the region inside the pedestal top. In the analyzed QCE discharge the steep gradient region is dominated by KBM/RBM modes at large scales, being consistent with the experimentally determined increase of transport with higher fueling. Inside the pedestal top all discharges are dominated by ITG at large scales and ETG at small scales.

11.3 Estimation and Role of the SOL Electric Field

The electric field in the Scrape-off Layer (SOL) of fusion devices is a key quantity affecting the plasma transport and possibly also the overall plasma confinement. To understand the transport in the edge and SOL region and extrapolate it to future devices, it is therefore essential to test physics models for the electric field by comparing them to experimental measurements. However, due to the complex measurements and analysis, such comparisons are scarce and have not been very successful so far.

In ASDEX Upgrade a systematic experimental analysis of the electric field in L-mode discharges at different plasma currents, densities and heating powers was now carried out. The analysis shows that the maximum of the radial electric field E_r in the outer midplane SOL measured by Doppler reflectometry decreases with the edge Greenwald density (see figure 25). Further analysis and a comparison to Ohm's law showed that E_r at the outer midplane is mainly determined by the outer target conditions. Based on the relation between the

electric field and the target conditions, a model to estimate the maximum of E_r in the SOL in terms of upstream parameters was developed.

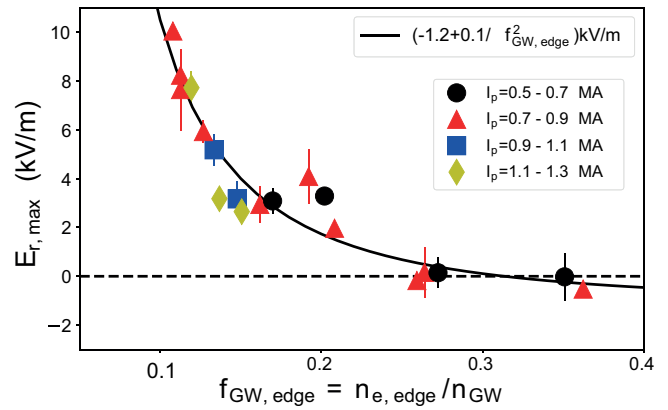


Figure 25. Dependence of maximum of the radial electric field in the SOL in dependence of the edge Greenwald density for different plasma currents I_p .

The findings of this study can contribute to the understanding of $E \times B$ flows and the toroidal rotation in the edge and SOL. Furthermore, the results will be applied to understand the role of turbulence suppression due to the E_r shear close to the separatrix and its role in confinement transitions.

11.4 Turbulent SOL transport measured by new dedicated probes

Radial transport in the plasma edge and Scrape-off Layer of tokamaks is widely controlled by turbulence that arises from the nonlinear saturation of micro instabilities driven by steep gradients across the separatrix. Therefore, understanding turbulence in tokamaks is fundamental since it ultimately impacts plasma confinement, as well as a broad range of phenomena and effects, such as the effective area for power exhaustion on the divertor. Experimentally, characterizing turbulence requires measuring fluctuations with high temporal and spatial resolution. Plasma quantities such as density and electron temperature are of great importance, although the most relevant quantity is perhaps the plasma potential since the radial motion of turbulent plasma occurs via $E \times B$ drift. A probe head installed on the midplane manipulator of ASDEX Upgrade capable of simultaneously measuring plasma potential, density, and electron temperature has been used to characterize turbulence in the SOL and plasma edge in various plasma regimes such as L-mode, ELMy H-mode, and EDA H-mode. Important insights about the nature of turbulent transport in this region were achieved. Particularly, the interplay between fluctuations and mean profiles, as plasma evolves towards the density limit in L-mode, shows that the rise of the collisionality and the relaxation of the radial electric field favor the growth of interchange turbulence and intermittent (blobby) transport across the entire SOL.

11.5 Separatrix Operational Space

The operational space for safe and efficient operation of a tokamak is limited by several constraints. Of high interest is the Greenwald density limit for L-mode, accessibility of high confinement, H-mode and loss of high confinement at about a Greenwald density fraction of unity [73]. The technically feasible operational range of tokamaks is also limited due to power exhaust requirements. The power exhaust capabilities of a magnetic confinement fusion device vastly depend on the plasma conditions around the separatrix. In previous work, we characterized the plasma conditions at the separatrix based on global turbulence parameters introduced by Rogers, Drake, Zeiler (RDZ) and Scott. In [74], an increase in the plasma decay lengths around the separatrix was shown to be correlated with the turbulence parameter α . Here, we present three boundary lines describing the L–H (H–L) transition, L-mode density limit and ideal ballooning mode limit for the plasma edge ($n_{e,sep} - T_{e,sep}$) space just inside the separatrix. The presented model equations have been developed on the basis of a dedicated and carefully established experimental database in conjunction with heuristic techniques to derive these equations from the complex drift-Alfvén (DALF) model.

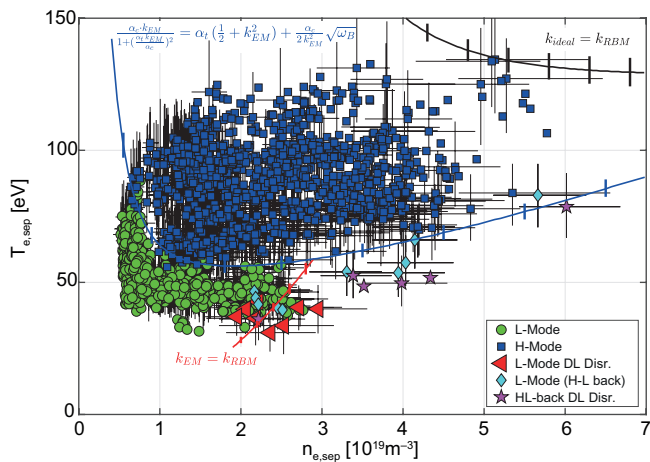


Figure 26. Separatrix operational space of ASDEX Upgrade in terms of electron density and temperature. Different operation regimes are indicated by different symbols. Red line shows boundary of the L-mode density limit (equation (3)). Blue line indicates the L–H–L transition (equation (8)). Black line indicates the ideal MHD boundary (equation (12)). Error bars are plotted only for a subset of the data for clarity in the figure.

12 Plasma-Wall Interaction

The ASDEX Upgrade divertor manipulator offers the unique capability of exposing samples up to a size of two standard target tiles to a dedicated series of discharges with samples installed and retrieved via an airlock system without breaking the vessel vacuum. The main focus of recent experiments was firstly on investigations of tungsten melt

motion during repeated transient surface melting by ELMs, which is a potential risk for large scale tokamaks equipped with a tungsten divertor. Further experiments aimed at the quantification of predicted power flux to geometrically shadowed side faces of toroidal gaps in divertor mono block structures. This mechanism was predicted to be of concern for ELMs in large scale tokamaks such as ITER because the corresponding particle pulses are expected to arrive at the divertor retaining almost their full upstream pedestal temperature with correspondingly large ion gyro radii. Because of that it is impossible to shield all leading edges simultaneously by appropriate surface shaping.

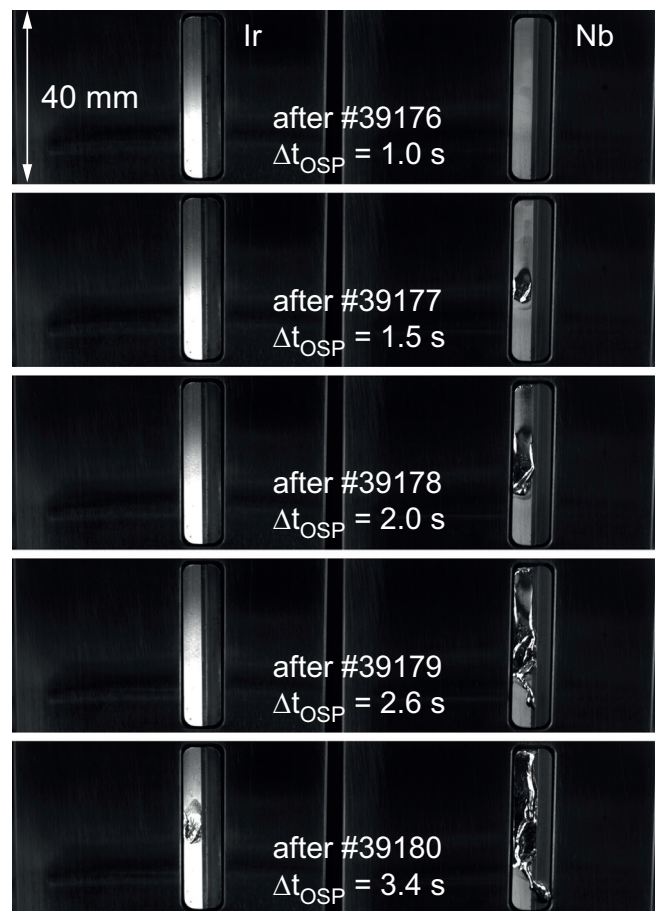


Figure 27. Images of the Ir and Nb samples acquired after each discharge by an inspection camera at a view port of the divertor manipulator air lock. Despite almost identical melt temperature, the melt volumes of both metals under identical exposure conditions differ because of different heat capacities and heat conductivities.

In the melt studies the importance of thermionic electron emission as main driver of melt motion was investigated in detail by comparing in one experiment transient melt motion triggered by ELMs on two samples at the same poloidal position with one sample at vessel

potential and the other sample insulated [75]. In a second experiment melt motion at two samples made of proxy metals niobium and iridium with strongly different electron work function was compared under similar conditions (see figure 27). The outcome of both experiments was interpreted by detailed simulations [76] using the MEMOS melt motion code [77]. The experimental results confirmed the implemented physics models in the code and greatly increased confidence in predictive simulations for the ITER tokamak.

Penetration of ELM-related ions into toroidal gaps of mono-block structures was investigated by exposing dedicated gap structures with mirror polished internal side faces which had been coated with a thin platinum marker layer. The thickness of this layer was characterised before and after exposure by detailed optical and electron microscopy as well as by ion beam analysis using micro-beams for high spatial resolution. This way, both the erosion of the platinum marker and the deposition of intrinsic impurities (tungsten and carbon) could be quantitatively measured. It turned out that the erosion/deposition pattern from the gap entrance further down along the gap side face had exactly the shape and dependency on gyro orbit orientation as expected for ELM-related ions arriving at pedestal temperature of O(keV). The experiments provided for the first time direct experimental evidence for this effect [78] and served to quantitatively validate ion orbit and PIC simulation codes used for predicting the effect of connected power flux to toroidal mono-blocks in ITER.

Most recently the efficacy of boron powder injection as a means for in-situ wall conditioning during plasma discharges was investigated by exposure of witness samples using the manipulator systems at both the divertor and outer mid-plane and measuring the amount and spatial distribution of isotope enriched injected boron [79] after series of dedicated discharges.

13 Power Exhaust Physics

13.1 X-Point Radiator

With the full detachment of the outer divertor, the development of a strongly localized radiation zone close to the X-point is observed. Behind the radiating zone, the electron temperature is reduced to only a few electron volts, while pressure along the closed flux surfaces is conserved, i.e. the density increased [80]. The height of this X-point radiator (XPR) above the X-point can be controlled via the gas puff or heating power [81]. The real-time detection of the XPR, which is based on the AXUV diagnostic, is also used for the avoidance of density limit disruptions (see section 8). In almost the complete operational range of AUG at high density or high collisionality the XPR was observed after the injection of a sufficient amount of nitrogen. The confinement with respect to the ITER $H_{98(y,2)}$ scaling is in the range of 0.8 to 1.1, i.e. the presence of an XPR leads to only a small reduction of the confinement. An X-point radiator is also observed at JET and TCV, showing that this feature is independent of the machine size or wall material [82].

If the XPR moves significantly inside the confined region, ELMs are disappearing. The ELMs are suppressed due to a reduction of the pedestal pressure gradients. In this regime, the line averaged electron density is reduced by about 15% and the stored energy by about 10%, while the confinement factor H_{98} stays about constant. The ELM suppression is generally observed if the XPR is more than 7 cm above the X-point, and this regime is accessible in all tested configurations ($P_{\text{heat}} = 1.7\text{--}17.5$ MW, $I_p = 0.8\text{--}1.2$ MA, $q_{95} = 3.7\text{--}6$). As this ELM suppressed regime comes inherently with an exhaust solution and only with a small reduction in confinement, it is a viable scenario also for future tokamaks [83].

The X-point radiator is also used as a tool to achieve a detached LH transition. During the transition from L- to H-mode, the heat flux in the SOL changes drastically, by increased heating power, narrowing of the heat flux channel or changes in the stored energy. If the XPR is placed and controlled inside the confined region, it acts as a buffer for the changing heat fluxes. The slower active control of the height by nitrogen seeding ensures to avoid re-attachment or over-seeding. With this scheme it was possible to achieve a discharge (AUG #40333, [84]) which remains detached from power ramp up to power and current ramp down. In the present discharge, the flattop is hold for 1.5 s, but could be expanded for any other need. The active control adjusts the reduced seeding requirement to maintain detachment through the power ramp down, HL transition and current ramp down. Since the requested XPR height during the flattop was above the threshold for the ELM suppression, the whole discharge was ELM-free except for a few benign ELMs during the ramp up.

A new divertor concept is also applying the XPR as a tool to mitigate heat fluxes: the compact radiative divertor (CRD) [85]. In this configuration, the divertor volume is minimized by moving the X-point close to the divertor targets (see figure 28).

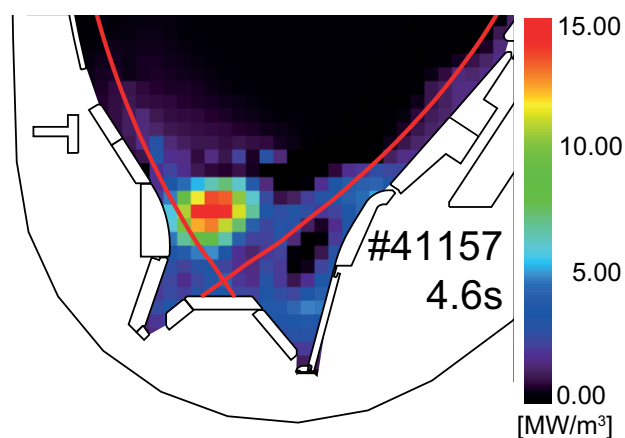


Figure 28. Radiation distribution in discharge #41157 with a compact radiative divertor. The divertor volume is minimized, the overloading of the target materials is avoided by the X-point radiator.

This is usually omitted, as the shallow inclination angle of the magnetic field lines on the target ($\ll 3^\circ$) would lead to immediate overheating at any leading edge. In case of the CRD, the heat fluxes are dissipated by the XPR before reaching the target. Experiments in upper and lower single null configuration showed that this is sufficient to avoid overheating and reduce the target loads to benign levels [85].

This new concept would highly reduce the construction complexity of a divertor, reduce forces on shaping coils, increase vertical stability of the scenarios and would allow to make more efficient use of the magnetic volume, as the divertor volume is strongly reduced. However, it has to be proven that such a scenario is also accessible in a reactor scale device, that re-attachment can fully be avoided and that the heat load by radiation are below material limits. The experiments of the detached LH transition show a possible way to access a CRD configuration, but need to be further validated.

13.2 X-Point Radiator Modelling

To improve the physical understanding of processes that determine the occurrence and evolution of an XPR, both an analytical model was developed and SOLPS-ITER simulations were performed. Based on particle and energy balances, a reduced model [86] describes the occurrence of stable and unstable XPR. Prior to the development of an XPR, the neutral deuterium density near the X-point plays a key role in reducing the temperature due to ionization and charge exchange energy losses. This results in a stable power-balance solution at a high temperature above the main impurity radiation peak. A second solution, at temperatures of a few eV, is associated with the XPR. The access to it via a radiation collapse is blocked as long as the high temperature solution exists. This condition was expressed in terms of an access parameter XA , with parameter dependencies consistent with experiment and with SOLPS-ITER simulations ([87], see below). Accordingly, XPRs occur at high values of XA , i.e., at high safety factors, separatrix and neutral densities, and at low separatrix temperatures or heating powers. A large flux expansion at the X-point is a prerequisite for the occurrence; impurities must be present, but their density does not enter into XA .

With an exponential increase of the recombination rate at low temperature, the XPR becomes MHD unstable, leading to a MARFE and, possibly, to a disruption. A critical density for MARFE occurrence is formulated with the upstream density and safety factor as leading parameters, as in the experiment. From a combined power-particle balance, an edge plasma parameter domain for MARFE occurrence was derived which resembles that used for active MARFE avoidance schemes [88]. Figure 29 shows, that MARFE formation can happen through two different routes. If an XPR is already present, MARFEs occur along route (i). This process mainly depends on the plasma edge density. Along route (ii), MARFE occurrence underlies the criterion for XPR access. Here, a gas puff, increasing the neutral density,

or a loss of heating power, reducing the temperature, may produce a fast and uncontrollable transition to a MARFE. MARFEs are predicted to be more likely in carbon devices than in impurity-seeded plasmas of tungsten devices.

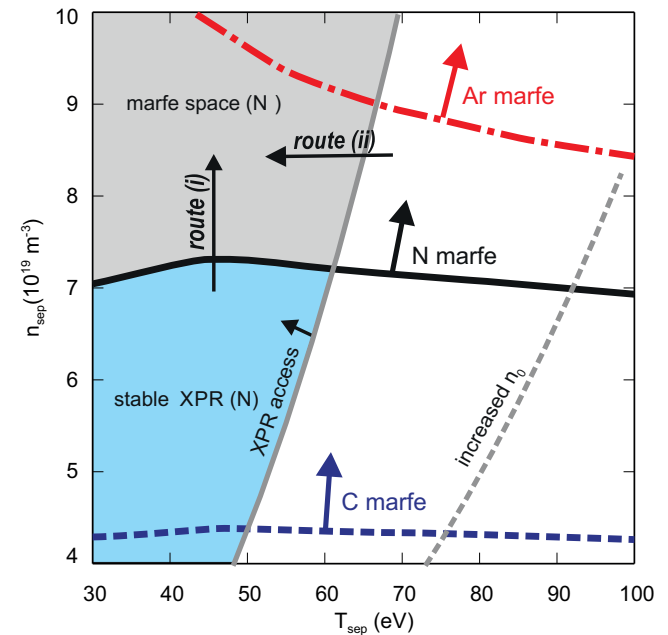


Figure 29. Separatrix density-temperature landscape indicating where stable XPRs can be found (blue) and the limits to the marfe space (grey). The boundaries apply to the nitrogen impurity, they change for carbon or argon impurities and at higher neutral density as indicated. There is only a small parameter window where stable XPR can exist. Two routes to a marfe and potentially a disruption are indicated, a controllable one (i) and a fast one (ii).

SOLPS-ITER was applied to study the XPR phenomenon in AUG. As shown in figure 30(a), the simulation with drifts is able to reproduce the profiles of electron density and temperature measured by divertor Thomson scattering. In the confined region near the X-point, a cold XPR core with a temperature lower than 5 eV was found, surrounded by a highly radiative band (see figure 30(b)).

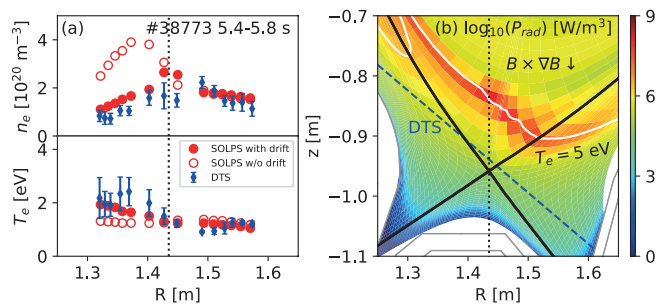


Figure 30. (a) Electron density and temperature along the LOS of DTS. (b) Cross section of line radiation density.

By analyzing the power, particle and momentum balances in the simulations, a simple sketch of an XPR can be depicted. With sufficient impurity seeding, the divertor region is cooled down by line radiation, which decreases the opacity for neutrals. As a result, more neutrals are able to penetrate the confined region near the X-point and be ionized there. Plasma density and pressure increase in the highly ionizing zone, leading to a radial diffusive transport towards the inner confined region and a parallel convective particle flux from the ionizing zone towards the upstream position. The X-point temperature is reduced further by ionization losses. When the temperature at the X-point reaches around 1 eV, the volumetric recombination rate increases substantially. With drifts in a favorable field direction, the cold and dense region of the XPR expands towards the upstream position on the high-field side.

Consistent with the reduced model [86] a threshold of the access parameter was found for the generation of an XPR in the simulations. The threshold is robust for different flux tubes at various radii and for different toroidal magnetic field strengths, indicating that the reduced model already contains the most important physics for initiating an XPR.

13.3 I-Mode Power Exhaust

I-mode is an attractive operational regime for a fusion power plant (FPP) due to its H-mode-like energy confinement, its L-mode-like particle confinement, and the absence of type-I ELMs. However, under some conditions I-mode plasmas do exhibit pedestal relaxation events (PREs) that transiently enhance the energy reaching the divertor target plates [89]. This energy is an important quantity to predict, as it needs to be compared to divertor material limits. A considerable step forward in understanding the compatibility of I-mode PREs with the strict requirements of a FPP was recently achieved by analyzing data from two tokamaks: ASDEX Upgrade and Alcator C-Mod [90]. It was found that the PRE divertor energy fluence (ϵ PRE) scales with the pedestal top electron pressure, similarly to type-I ELMs [74]. However, for the same pedestal top pressure, the PRE energy fluence is lower than that of type-I ELMs, approximately by a factor of three. Nonetheless, projections of ϵ PRE to DEMO-like devices are still found to be of concern. In addition, this multi-device study revealed that PREs occur only in a subset of I-mode discharges, mainly when the plasma is close to the H-mode transition. Therefore, PREs could be avoided by keeping the plasma away from the H-mode transition. Also, they could be used to monitor the proximity to H-mode, and hence to avoid the plasma entering an undesired ELMy H-mode.

13.4 Energy Load on First Wall Elements

The AUG cooling water calorimetry (CWC) is able to detect heat loads of in-vessel components in a robust manner. The diagnostic consists of 88 cooling units covering the tokamak almost entirely in poloidal and toroidal direction. Exploiting this diagnostic, a set of

dedicated shots with constant heating power have been executed using a highly shaped small ELM magnetic geometry in order to investigate the differences on heat loads at the AUG first wall. The flattop fueling has been varied on a shot-to-shot basis while keeping constant all the other parameters, exploring a large range of the density operational space of AUG. Reducing the fueling rate allows a gradual transition from small ELM regime at high density into a type-I ELMy H-mode. Additionally, the safety factor q has been varied. With the lowest flattop fueling, reaching a type-I ELMy H-mode, a fraction of $\sim 6\%$ of energy loads at the first wall normalized against the entire energy has been recorded, whereas in the highest fueling case, being in small ELM scenario, the first wall heat loads are increased up to 16%. Considering all cases reveal an almost linear trend between the fraction of energy deposited at the first wall and the turbulence control parameter α_t [74]. This observation is consistent with an enhancement of the filamentary activity at higher turbulence levels.

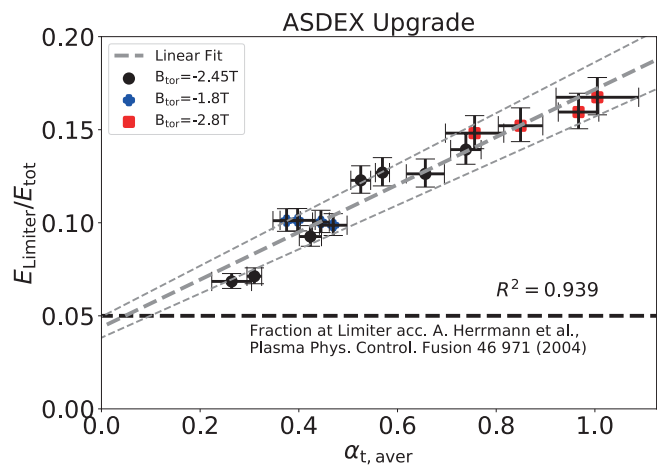


Figure 31. The CWC measurements reveal a linear increase of the first wall energy load with the turbulence parameter due to enhanced filamentary transport through the SOL.

14 Turbulence Studies

A significant step forward has been made in the validation of a high-level turbulence code based on global and microscopic turbulence parameters. Detailed kinetic profile and fluctuation data were collected for two L-mode plasma scenarios with steep and flat electron temperature gradients. The electron temperature profile was shaped by using ECRH at two off-axis deposition radii; one neutral beam was injected to induce plasma rotation for a clearer separation of the Doppler reflectometry (DR) peak. The core density profile steepens when the inner heating power is increased. Linear GENE simulations based on the experimental profiles show the dominance of ITG turbulence with an increasing importance of TEM and ETG in the steep gradient scenario.

Two Doppler reflectometers in O-mode and one in X-mode provided detailed information on density fluctuation wavenumber (k) spectra, radial correlation lengths, eddy tilt angle and turbulent propagation velocity, while a correlation ECE (CECE) diagnostic was used for measuring electron temperature fluctuations, their correlation lengths and, in combination with a reflectometer, density-temperature fluctuation crossphases.

For a realistic comparison of experimental data with non-linear GENE simulations [92], a synthetic diagnostic response is computed based on the simulated density and temperature fluctuations, for which extensive IPF-FD3D full-wave code [93] analyses were performed.

As a test of the reliability of the DR measurements, the poloidal symmetry of the turbulent propagation velocity was investigated in great detail. This study was also motivated by reports from TEXTOR, Tore Supra and TJ-II on poloidal asymmetries, an unexpected finding since the turbulent phase velocity is known to be small compared with the poloidal $E \times B$ flow and the latter is set by the constant plasma potential on the flux surfaces. Therefore, the DR flow measurements, which provide the sum of $E \times B$ and phase velocity, should be poloidally symmetric. On AUG, this was indeed found in a careful experiment [94, 95] and later confirmed in the validation discharges from above [96] (see figure 32). The small residual asymmetries at low k values, i.e. small poloidal angles θ , are attributed to a non-linear diagnostic response.

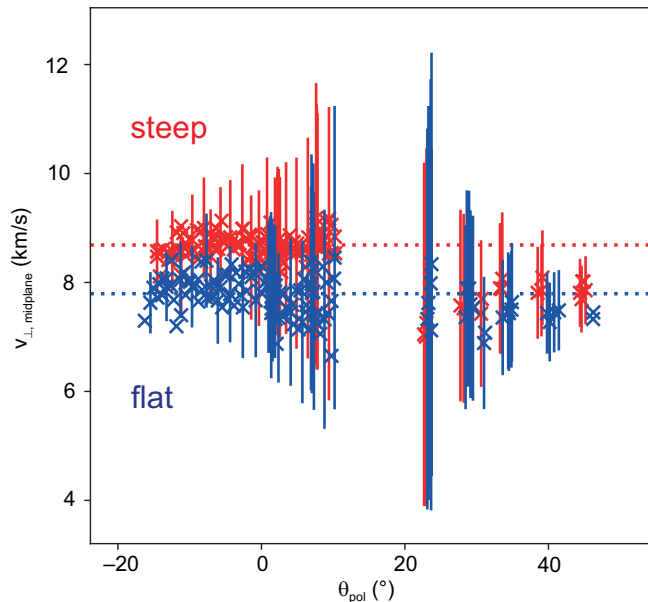


Figure 32. Perpendicular velocity of electron density fluctuations mapped to the midplane for various poloidal angles, measured with X-mode Doppler reflectometry in both scenarios.

On the background of experimental kinetic profiles, GENE runs were carried out for two radial positions within the experimental measure-

ment interval. GENE reproduces the ion heat flux well, which changed by less than 5% from the flat to the steep gradient scenario. The increase in electron heat transport by a factor of 2.5 was also reproduced, although the absolute values in both scenarios are overestimated by a factor of about two. GENE runs with different impurity fractions are currently being performed to clarify this discrepancy. Still, the gyrokinetic simulations reproduce many features of the fluctuation data.

As previously reported [97], GENE reproduces the shape of the Doppler k spectra for both O and X-mode polarization via aforementioned synthetic diagnostic analysis. As figure 34 confirms for the validation experiments, the agreement is only achieved after application of the synthetic diagnostics which leads to individual modifications for the two wave polarizations [98]. Note an arbitrary vertical offset has been introduced for better visibility. In the recent study, the amplitudes of density fluctuations were smaller in the steep scenario than in the flat one. This was unexpected, because the density scale length was shorter in the flat scenario. It is a remarkable result that GENE reproduces this trend in excellent agreement with the experiment.

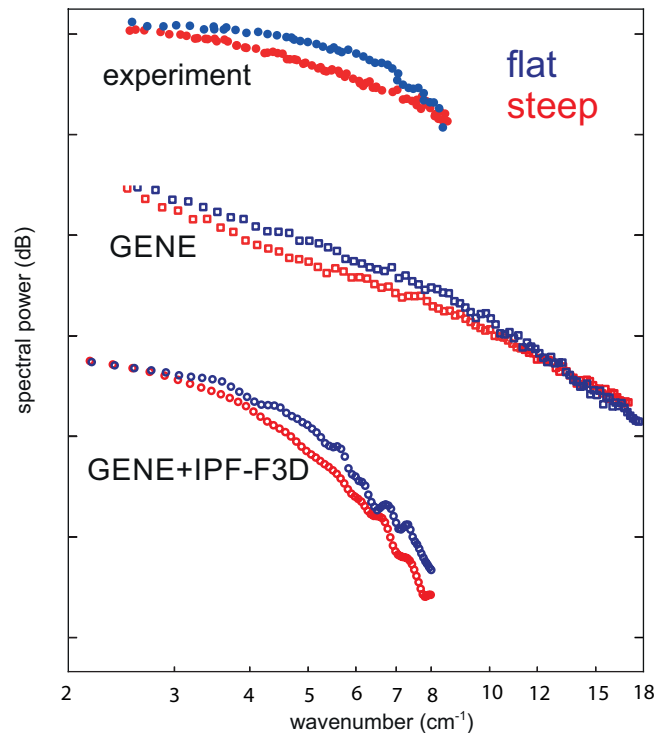


Figure 33. Comparison of k spectra from the DR in O-mode, GENE raw data and modelled with IPF-FD3D for flat and steep scenarios

On the other hand, the electron temperature fluctuation amplitude of the steep scenario exceeded that of the flat scenario by a factor of two.

GENE also reproduces this trend and provides power spectra with a similar shape and amplitude as the experiment.

The radial correlation length of turbulent eddies is an important parameter for estimating transport. It was studied for both electron temperature and density fluctuations based on correlation analyses of neighboring ECE and DR channels, respectively. The DR measures density fluctuations for a specific k_{\perp} , i.e. for a poloidal scale length which can be steered by a movable mirror. It was found, that the radial and poloidal scale lengths increase concurrently, which was to be expected. Furthermore, the flat scenario exhibited a smaller correlation length than the steep scenario, which is in line with the broader k spectrum in the flat scenario and the diagnostic effect of the DR. The GENE simulation results in conjunction with the full-wave calculations are remarkably consistent with these experimental observations. This is the first comparison of correlation lengths using IPF-FD3D on GENE. For the steep scenario, the radial correlation lengths of the electron temperature fluctuations at $k_{\perp} \gg 0$ derived from the CECE diagnostics agree well with those of the density.

The cross-phase between electron density and temperature fluctuations bears information on the turbulence drive. Experimentally it is determined from a correlation analyses of DR and ECE channels which measure in the same plasma volume. This was already successfully done on AUG [99] and was also applied to the validation discharges. In the cross phase, there was no change between flat and steep scenarios. The absolute value of the cross-phase could not yet be determined because it shows a dependence on frequency. This effect is attributed to a slight shift of the volumes in which the two diagnostics measure.

In summary, these efforts have resulted in an unprecedentedly comprehensive experiment-code comparison for two well-diagnosed discharge scenarios in which a high degree of agreement has been observed.

Scientific Staff

Tokamak Scenario Development (E1): F. Albers, C. Angioni, N. Arden, K. Bald, M. Bauer, N. Berger, H. Blank, V. Bobkov, A. Bock, N. Bonanomi, A. Buhler, A. Burckhart, D. Carlton, P. David, M. Dibon, M. Dunne, T. Eberl, H. Eixenberger, E. Fable, D. Fajardo Jimenez, H. Faugel, J. C. Fuchs, H. Fünfgelder, L. Gianonne, I. Girka, O. Girka, I. Goldstein, I. Gomez, A. Gräter, A. Gude, K. Hegele, J. Hobirk, I. Hofer-Maksymiw, V. Igochine, F. Janky, A. Kallenbach, A. Kappatou, C.-P. Käsemann, B. Klesper, M. Koleva, A. Kostic, A. Kreuzeder, O. Kudlacek, P. T. Lang, P. Leitenstern, C. Li, L. Liu, T. Luda di Cortemiglia, A. Magnanimo, M. Maraschek, P. de Marne, R. Merkel, M. Muraca, R. Ochoukov, F. Paulus, M. Peglau, B. Petzold, B. Plöckl, T. Pütterich, G. Raupp, M. Reich, M. Reisner, V. Rohde, M. Rott, F. Ryter, O. Samoylov, G. Schall, M. Schandrud, A. B. Schmidt, P. A. Schneider, R. Schramm, G. Schrepfer, M. Schubert, K.-H. Schuhbeck, J. Schweinzer, O. Seibold-Benjak, A. Seiler, G. Sellmair, B. Sieglin, A. Sigalov, D. Silvagni, M. Sochor, F. Stelzer, J. Stober, G. Suarez Lopez,

W. Suttrop, G. Tardini, M. Teschke, W. Tierens, W. Treutterer, M. Uhlmann, M. Usoltseva, T. Vierle, S. Vorbrugg, D. Wagner, M. Weiland, M. Willensdorfer, B. Wiringer, I. Zammuto, T. Zehetbauer, M. Zilker, H. Zohm

Plasma Edge and Wall (E2M): M. Balden, M. Bernert, G. Birkenmeier, L. Bock, B. Böswirth, D. Brida, L. Chen, G. Conway, S. Denk, R. Dux, T. Eich, S. Elgeti, M. Faitsch, R. Fischer, T. Gleiter, S. Glöggler, H. Greuner, M. Griener, O. Grover, G. Guedes Grenfell, T. Happel, F. Hitzler, T. Höschen, K. Hunger, J. Kalis, K. Krieger, B. Kurzan, T. Lunt, H. Maier, M. Mayer, R. McDermott, P. Molina Cabrera, R. Neu, T. Nishizawa, O. Pan, I. Paradelo Perez, U. Plank, J. Riesch, K. Schmid, C. Schuster, F. Sciortino, D. Stieglitz, U. Stroth, B. Tál, E. Trier, G. Vogel, D. Wendler, M. Wischmeier, E. Wolfrum, A. Zito
Tokamak Physics Division (TOK): V. Artigues, A. Banon Navarro, A. Bergmann, M. Bergmann, R. Bilato, T. Body, A. Bottino, A. Chankin, D. Coster, A. Di Siena, T. Görler, F. Jenko, O. Linder, J. Martin Collar, F. Matos, I. Novikau, G. Papp, G. Pautasso, E. Poli, B. Rettino, A. Stegmeier, K. Stimmel, D. Told, P. Ubl, W. Zholobenko

Magneto-hydrodynamics and Energetic Particle Physics Group (MHD-Group): F. J. Artola Such, F. Atour, V. Bandaru, A. Cathey Cevallos, S. Günter, T. Hayward-Schneider, F. Holderied, M. Hölzl, K. Lackner, P. Lauber, A. Lieber, Z. Lu, G. Meng, V. Mitterauer, N. Nikulsin, V.-A. Popa, R. Ramasamy, K. Särkimäki, N. Schwarz, E. Strumberger, W. Tang, F. Vannini, X. Wang, F. Wiescholke, Q. Yu

Numerical Methods in Plasma Physics (NMPP): O. Maj

IT Infrastructure and Security: D. Beckert, V. Bludov, O. Dragicevic, H. Fafard, A. Jahn, M. Kölbl, A. Lenz

ITER Technology & Diagnostics (ITED): U. Fantz, M. Fröschle, N. de Harder, B. Heinemann, C. Hopf, C. Martens, H. Meister, R. Nocentini, G. Orozco, R. Riedl, J. Thalhammer

Integrated Technical Center (ITZ): R. Blokker, J. Böning, R. Gliga, N. Jaksic, R. Jung, M. Kircher, H. Köhnlein, G. Lexa, B. Mendelevitch, R. Stadler, H. Pirsch, J. Tretter, M. Weißgerber

Max Planck Computing and Data Facility, Garching (MPCDF): K. Desinger, C. Guggenberger, C. Hanke, F. Hinterland, J. Kennedy, E. Laure, K. Lehnberger, M. Panea-Doblado, J. Reetz, M. Rampp, K. Reuter, R. Ritz, A. Schmidt, A. Schott, E. Summer, K. Zilker

IPP Greifswald, DE: G. Fuchert, D. Gradic, D. Kulla, F. Reimold

University of Greifswald, DE: P. Manz

Technical University of Munich, DE: K. Höfler

Forschungszentrum Jülich (FZJ), DE: A. Huber, A. Krämer-Flecken, L. Li, D. Reiser

Karlsruhe Institute of Technology (KIT), Karlsruhe, DE: C. Day, V. Hauer, S. Varoutis

IGVP, University of Stuttgart, DE: B. Plaum, M. Ramisch

Institute of Theoretical and Computational Physics, Graz, AT: M. Heyn, S. Kasilov, W. Kernbichler, P. Lainer, M. Markl

ÖAW, University of Innsbruck, AT: S. Costea, C. Ionita-Schrittwieser, A. Kendl, R. Schrittwieser

ÖAW, IAP, Vienna University of Technology, AT: G. Harrer, L. Radovanovic

- LPP-ERM-KMS, TEC Partner, Brussels, BE:** Y. Kazakov, E. Lerche, V. Maquet
- Ghent University, Ghent, BE:** V. Klevarova, A. Shabbir
- IPP CAS, Prague, CZ:** M. Farnik, O. Ficker, F. Jaulmes, M. Komm
- Department of Physics, Technical University of Denmark, Kgs. Lyngby, DK:** J. H. Holm, T. Jensen, J. Madsen, V. Naulin, R. D. Nem, A. H. Nielsen, S. K. Nielsen, J. Olsen, J. Rasmussen, M. Salewski, M. Stejner, T. Verdier
- Department of Applied Physics, Aalto University, FI:** A. Salmi, S. Sipilä, A. Snicker
- VTT Technical Research Centre, Espoo, FI:** A. H. Hakola, T. Tala
- Modeling Group, École supérieure d'ingénieurs Léonard-de-Vinci, Courbevoie, FR:** A. Biancalani
- Aix-Marseille University, CNRS, Marseille, FR:** Y. Camenen
- Institut Jean Lamour, CNRS, University of Nancy, FR:** F. Brochard, S. Heuraux, A. Houben
- Laboratoire de Physique des Plasmas, Ecole Polytechnique, Palaiseau, FR:** P. Hennequin
- CEA/IRFM, Saint Paul Lez Durance, FR:** E. Joffrin
- Centre for Energy Research, Budapest, HU:** G. Cseh, D. Dunai, G. Kocsis, G. Pokol, D. Réfy, T. Szepesi, S. Zoletnik
- Department of Physics, National University of Ireland, Cork, IE:** P. J. McCarthy
- Department of Electrical and Electronic Engineering, University of Cagliari, IT:** B. Cannas, G. Sias
- ENEA, Centro Ricerche Frascati, IT:** B. Esposito, E. Giovannozzi, G. Rocchi
- ENEA, University of Milano-Bicocca, Milano, IT:** M. Cavedon, A. Dal Molin, G. Gorini, M. Nocente
- ENEA, IPST, Milan, IT:** E. Alessi, G. Croci, S. Garavaglia, G. Granucci, A. Mancini, P. Mantica, S. Nowak, D. Ricci, C. Sozzi, M. Tardocchi
- ENEA, Consorzio CREATE, Naples, IT:** O. D'Arcangelo
- ENEA Consorzio RFX, Padova, IT:** A. Murari, C. Piron, G. Spizzo, M. Spolaore, D. Terranova, G. Trevisan, M. Valisa, N. Vianello
- Department of Industrial Engineering, University of Rome, Rome, IT:** E. Peluso
- ISC-CNR and Politecnico di Torino, Torino, IT:** C. Marchetto, D. Milanesio
- Università degli Studi della Tuscia, DEIM Dept., Viterbo, IT:** A. Redl
- Eindhoven University of Technology, Eindhoven, NL:** G. Ronchi, J. Scholte
- Institute of Plasma Physics and Laser Microfusion, Warsaw, PL:** A. Chomiczewska, K. Galazka, I. Ivanova-Stanik, R. Zagórski
- Instituto de Plasmas e Fusão Nuclear, IST, Universidade de Lisboa, PT:** L. Gil, D. Hachmeister, V. Plyusnin, J. Santos, E. Seliunin, A. Silva, C. Silva, P. Varela, J. Vicente
- National Institute for Laser, Plasma and Radiation Physics, Magurele-Bucharest, RO:** T. Craciunescu
- Barcelona Supercomputing Center-Centro Nacional de Supercomputación, Barcelona, ES:** M. Mantsinen
- Laboratorio Nacional de Fusión, CIEMAT, Madrid, ES:** G. Ratta, E. Solano
- University of Seville, Seville, ES:** P. Cano Megias, D. J. Cruz Zabala, J. J. Dominguez Palacios Durán, J. Galdon-Quiroga, M. Garcia Muñoz, J. Gonzalez Martin, A. Jansen van Vuuren, P. Oyola, J. F. Rivero Rodriguez, L. Sanchis Sanchez, E. Viezzer
- Department of Physics, Chalmers Univ. of Technology, Gothenburg, SE:** K. Insulander Björk
- KTH Royal Institute of Technology, Stockholm, SE:** L. Frassinetti, P. Petersson, S. Ratynskaia, M. Rubel, E. Thorén
- Swiss Plasma Center, Lausanne, CH:** S. Coda, B. P. Duval, F. Felici, T. Goodman, B. Labit, A. Merle, A. Pau, L. Porte, O. Sauter, A. Shalpegin, U. Sheikh, C. Sommariva
- CCFE Fusion Association, Culham Science Centre, UK:** S. Henderson, D. A. Ryan, S. Saarelma, S. Sharapov, J. Simpson, M. Valovic, I. Voitsekhoitch
- Department of Physics, Durham University, UK:** S. Gibson
- University of York, York Plasma Institute, UK:** L. Horvath, B. Lipschultz
- Kharkov Institute of Physics and Technology, Kharkiv, UA:** M. Dreval
- MIT Plasma Science and Fusion Center, Cambridge, MA, USA:** R. Bielajew, A. J. Creely, A. Hubbard, P. Rodriguez-Fernandez, B. Vanovac, A. E. White, C. You
- University of California, Davis, CA, USA:** N. C. Luhmann
- University of Wisconsin, Madison, USA:** T. Cote, B. Geiger, O. Schmitz
- Columbia University, New York City, USA:** N. Leuthold, C. Paz-Soldan
- Princeton Plasma Physics Laboratory, Princeton, N.J., USA:** F. Laggner, R. Maingi, R. Nazikian
- General Atomics, San Diego, CA, USA:** T. Hellsten, Y. Liu, M. van Zeeland
- Institute of Plasma Physics, Chinese Academy of Sciences, Hefei, CN:** Q. Yang, W. Zhang
- Ioffe Institute, St. Petersburg, RU:** M. Iliasova, E. Khilkevitch, A. Shevelev



International Tokamak Collaborations

International Tokamak Collaborations

Heads: Dr. Hans Meister, Dr. Philip Schneider, Dr. Josef Schweinzer

All activities concerning IPP's collaborations with tokamaks worldwide have been merged into a new project. At JET with its ITER-like wall, the development of the hybrid scenario with significant contributions from IPP, led in the JET DT campaign to a world record for the achieved fusion energy. While IPP's contributions to ITER and JT-60SA are continuing successfully, collaborations with new devices both of the public and private sector appear on the horizon.

1 Introduction

At the end of 2021, IPP decided to initiate a new internal project for IPP's collaborations with tokamak experiments worldwide. In the short term, this 'International Tokamak Collaborations' (ITC) project also includes the participation in JET campaigns until the foreseen end of operation in 2023, but in the medium and long term, it primarily means collaboration with JT-60SA, ITER and with other future devices both of the public and private sector.

The aim of the ITC project is to influence the scientific program of these machines in the future and to play an important role in the scientific exploitation and technical operation. In doing so, IPP aims to verify its ideas and methods developed at ASDEX Upgrade on future (and larger) tokamaks to make these concepts fit for the ultimate use in fusion reactors. In support of this goal, IPP is also developing technologies (heating methods, plasma diagnostics, plasma control system) for the operation of these machines. For the analysis and interpretation of later results, scientific software packages are prepared and have been made available in particular to the ITER project.

Besides continuing the exploitation of the inhouse experiment ASDEX Upgrade, strengthening the pillar of collaboration (experiment, modeling and simulation) with upcoming reactor-relevant devices is of major importance for the future of the Garching site. Although the scientific attractiveness of ASDEX Upgrade can certainly be ensured by selective improvements of the hardware until at least 2030, for the time after that, the aforementioned next-generation machines will increasingly come into focus. These devices are emerging in particular in the private fusion energy sector which is developing at the moment with impressive speed.

The ITC project might therefore be seen as one element of IPP's long-term strategy to shape the further development of fusion as an energy source at the forefront not only in collaboration with government-funded labs, but also together with private companies of the fusion energy sector.

2 JET

After several years of preparation, experiments with deuterium-tritium (D-T) plasmas were conducted in the fall of 2021. The main goal of these DT2 experiments, to demonstrate a plasma stationary over 5 s with a high fusion power, was fulfilled. The obtained fusion energy of

59 MJ is a new world record and is twice that achieved in the 1997 JET DT1 campaign.

The record fusion energy was produced in so-called "hybrid" plasmas that have been co-developed by IPP staff for several years and are planned for ITER as a scenario at lower plasma current. A key aspect of the new experiments is that in JET the first wall is no longer made of carbon – as it was in 1997 – but of beryllium (main chamber) and tungsten (divertor). These wall materials are also foreseen in ITER (ITER like wall, ILW) and have a strong impact on tokamak operation and plasma control.

The fundamentals gathered during the operation of JET with the ILW, but also previously in ASDEX Upgrade with a full tungsten wall, have contributed decisively to this success.

IPP scientists have significantly contributed to this achievement which has attracted worldwide attention even outside the fusion community and to other experimental and theoretical studies which are presented in the following.

2.1 Hybrid Scenario for High Fusion Performance in DT

Deuterium-tritium experiments were performed at JET at the end of 2021, for the first time after the initial D-T experiments in 1997. One of the main goals of the recent D-T campaigns was to demonstrate sustained high fusion power production, compatible with the JET ITER-like wall.

One of the plasma scenarios prepared for the JET D-T campaign was the 'hybrid' scenario ('hybrid' plasmas operate at lower current and higher β_p than 'baseline' scenario plasmas). The scenario was further developed and successfully optimized in deuterium in recent years, leading to significantly extended duration of high performance [1, 2]. In particular, a reduction in the tungsten content due to temperature gradient screening was achieved, as high ion temperature at the pedestal top resulted in outward neoclassical convection, enhanced by the high rotation in the low collisionality regime of these plasmas. Furthermore, deleterious MHD activity was successfully avoided [3]. A detailed analysis of the JET 'hybrid' scenario confinement dependence on plasma β and power has shown that the power degradation follows the IPB98(y,2) scaling, but higher plasma β leads to better plasma confinement [4].

The deuterium experiments were followed by experiments in pure tritium, meant to provide experience in navigating the isotope effects and their impact on plasma performance. For example, as predicted by modelling, increased core impurity radiation during the current ramp up was observed in tritium, which had to be counteracted by increasing the density. The access to the H-mode phase had to be accordingly adjusted by fine-tuning the heating power and fueling rate. The lessons learned in tritium allowed rapid progress in D-T where similar adjustments had to be made.

The 'hybrid' scenario plasmas, which were operated for the first time in D-T, were very successful; sustained high D-T fusion power was

produced in such plasmas with $I_p = 2.3$ MA and a current overshoot [2], $B_t = 3.45$ T, $\beta_p > 1$, $q_0 \geq 1$ and $n_D \sim n_T$ fuel mixture, with the maximum fusion power produced averaged over 5 s reaching ~ 8.3 MW. Fusion power production higher than 10 MW was sustained for more than three α -particle slowing-down times. The fusion power and gain achieved with this scenario in the JET ITER-like wall exceeded those of the steady ELMy H-mode plasmas performed in the 1997 JET D-T campaign with the carbon wall. The confinement level is at or above the $H_{98(y,2)}$ scaling.

The record fusion energy produced in a ‘hybrid’ plasma with $n_D \sim n_T$ was 45.8 MJ [2]. This was finally further increased to the worldwide record of ~ 59 MJ (see figure 1) in T-rich ‘hybrid’ plasmas operated at higher magnetic field, in order to optimize the non-thermal contribution to the fusion power [1].

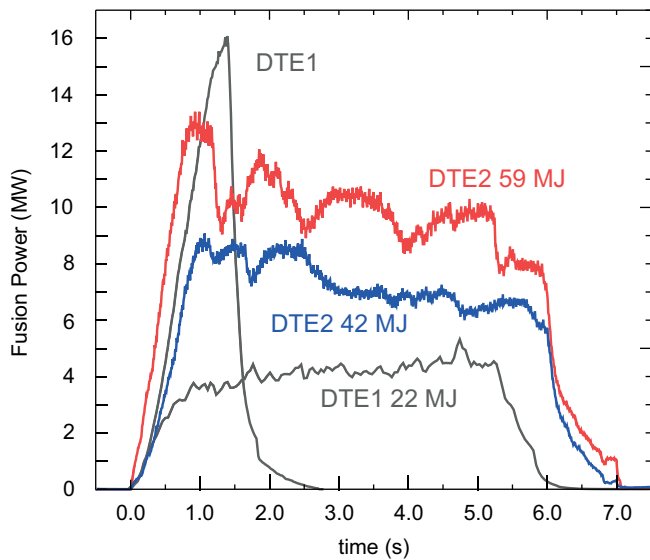


Figure 1. Sustained fusion power produced with the ‘hybrid’ scenario in the recent JET D-T experiments (DTE2) with $n_D \sim n_T$ (blue) and $n_T \gg n_D$ (red), in comparison to the fusion power production achieved in the previous JET D-T campaign in 1997 (DTE1, grey).

The D, T and D-T ‘hybrid’ scenario experiments were supported by extensive modelling of the isotope and impurity transport, both interpretatively and predictively. The experimental data collected in D-T plasmas with high performance and confinement in D-T will provide an unique opportunity to validate models and extrapolate these results to prepare the D-T operation of ITER and other future devices [1].

2.2 The L-H Power Threshold of Tritium-containing Plasmas

During the experimental campaign of JET from December 2020 till the end of 2021, tritium was used as plasma fuel in order to study pure tritium plasmas and isotope mixtures containing tritium including

the reactor relevant mixture of deuterium-tritium (D-T). This was the first opportunity to study the transition from low confinement to high confinement mode (L-H transition) of tritium-containing plasmas in metallic wall conditions, i.e. the ITER-like wall (ILW).

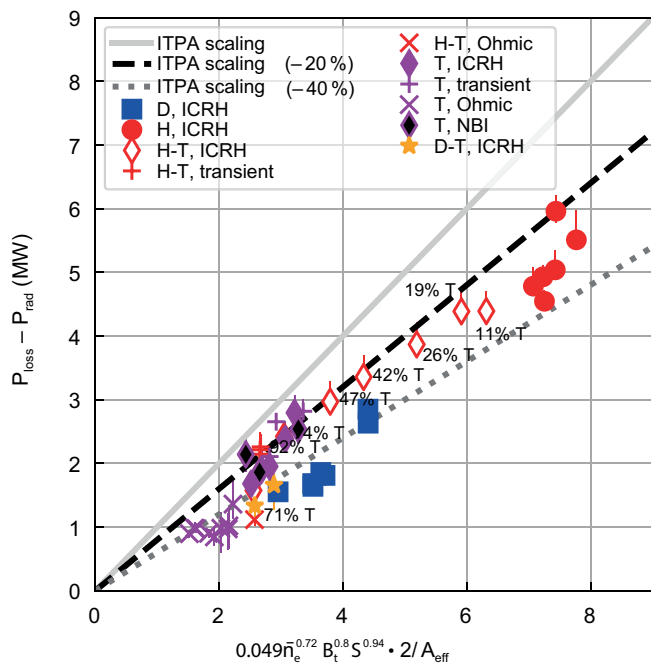


Figure 2. Measured L-H power threshold, $P_{\text{loss}} - P_{\text{rad}}$, corrected by the radiated power from the bulk plasma, P_{rad} , for different main ion plasma isotopes at a magnetic field of $B_t = 1.8$ T and a plasma current of $I_p = 1.7$ MA compared to the isotope dependent ITPA scaling (x-axis).

Previous tritium experiments in the late nineties [5], which were performed in JET with plasma facing components made of carbon (graphite tiles), suggested that the L-H power threshold, i.e. the necessary input power to access the high confinement regime (H-mode), scales inversely proportional to the effective isotope mass A_{eff} . In plasmas of different hydrogenic isotope mixtures i.e. pure hydrogen (H), pure deuterium (D), pure tritium (T), and the isotope mixtures H-T and D-T, we could confirm the same trend of lower L-H transition power, P_{loss} , with increasing isotope mass in JET with the ILW for a data set at a toroidal magnetic field of $B_t = 1.8$ T and a plasma current of $I_p = 1.7$ MA [6]. In comparison to the ITPA scaling of the L-H power threshold [7], which was derived from a multi-machine database of D plasmas, the new T-containing data is about 25 % lower than the scaling (even up to 40 % lower, when the bulk radiation is subtracted as shown in figure 2). Furthermore, it was found that the electron temperature profiles at the edge are very similar for all isotopes at the L-H transition, and that the heat transport in L-mode determines the necessary power to access the H-mode [8].

2.3 Transport Properties of Plasmas with Different Main Ion Masses H, D, T

Knowing the isotope mass dependence of confinement is a key prerequisite for accurate predictions of the performance of D-T fusion plasmas. During JET tritium operation in 2021 the experimental database was extended by pure T and mixed D-T plasmas. It was confirmed again that in the edge and core of ELMy H-modes different physics govern the ion mass dependence which was previously reported for H and D plasmas [9]. In the edge pedestal T plasmas follow the trend observed in H and D plasmas. The pedestal top density increases with isotope mass for similar gas fuelling rates. The degradation of the pedestal pressure observed with increasing gas puffing is very pronounced in H plasmas, less severe in D plasmas and nonexistent in T. Meaning in T plasmas the density can be increased with gas puffing at constant pressure.

The energy confinement in the plasma core shows a strong dependence on the pedestal energy. In H and D the core confinement is comparable when the pedestal pressure is matched (see figure 3). This is possible because for the investigated scenario with 1.4 MA and 1.7 T the fast-ion content is too low and differences due to the mass dependence in the fast-ion slowing down time do not cause a major impact on heat transport [10]. The T plasmas, however, show a deviation from the trend observed in H and D. While the core energy confinement in T is similar to H and D at medium pedestal pressure it is significantly improved at higher pedestal pressure. This increase in core confinement is also observed in D-T plasmas.

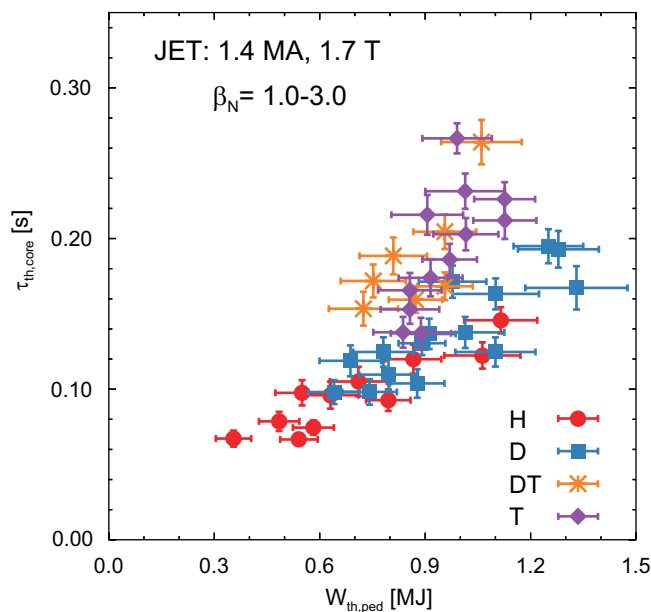


Figure 3. Confinement time calculated from the core stored energy compared to the pedestal stored energy for plasmas with different main ion mass.

The quasilinear model TGLF-Sat2 was used within ASTRA for flux driven simulations to predict the core transport with a fixed pedestal as boundary condition. It was found that TGLF-Sat2 does overpredict the heat transport, in particular for the plasmas with higher pedestal pressures. The reason for this discrepancy is currently under investigation.

2.4 Divertor Heat Flux Measurements

The divertor heat flux is still one of the main challenges towards a safe operation of next step devices. Especially the impact of large transients, like type-I ELMs, needs to be understood and potentially avoided. In recent years the ELM energy fluence onto the outer divertor target in deuterium was shown to scale with the pedestal top pressure for many devices, e.g. ASDEX Upgrade, JET and MAST.

Building on this knowledge, new experiments in an optimized plasma shape for infrared thermography were conducted at JET allowing measurements not only at the outer divertor target but also on the inner one. This allows to challenge state-of-the-art simplified predictions as well as 3D modelling of ELMs. Furthermore, the tritium campaign gave the unique opportunity for divertor heat flux studies investigating the influence of the main ion species.

2.5 Coupled KIPP-EDGE2D Modelling of Parallel Transport in the SOL and Divertor

The Kinetic code for Plasma Periphery (KIPP) models the parallel (along magnetic field lines) propagation of charged particles in the scrape-off layer (SOL) and divertor. An iterative coupling between KIPP and EDGE2D-EIRENE was used to achieve converged solutions in the main SOL region. These results reveal a substantial increase in maximum T_e and T_i along field lines due to the kinetic effect of the heat flux limit caused by the non-local transport of super-thermal charged particles from the 'main SOL' to the divertor and target plates. On the divertor targets, at the same time, no significant contribution to the total target power loads attributed to kinetic effects was found, in a comparison with the total, conductive plus convective, ion plus electron power flux predicted by the EDGE2D-EIRENE alone. Also, no 'burnthrough' of detachment by kinetic effects was found in coupled cases on field lines where partial detachment was predicted by EDGE2D-EIRENE.

2.6 Full-plasma Integrated Modelling with IMEP

The design of future fusion reactors requires an accurate prediction of the plasma confinement and of the plasma density and temperature profiles, as these determine the fusion performance. For this purpose IMEP was recently developed as an integrated model for AUG plasmas. IMEP combines core, pedestal and scrape-off layer physics [11, 12] and has now been extended to Alcator C-Mod and JET-ILW plasmas, in order to test it on devices with a large variation in plasma size. The validation has been carried out on a database containing 55 stationary JET-ILW ELMy H-mode phases, featuring scans in heating

power, fuelling rate, triangularity, plasma current, magnetic field, and divertor configurations. The results show that IMEP can accurately predict the pedestal width. The pedestal top pressure is accurately predicted for cases which are found to be close to the ideal peeling ballooning (PB) stability boundary. Cases far from the PB boundary, however, are strongly overpredicted and one explanation is that they require a resistive MHD code for a more realistic prediction, what at present is not included in IMEP.

2.7 Validation of Quasi-linear Turbulent Transport Models against Plasmas with Dominant Electron Heating

The TGLF transport model is applied in the ASTRA code and tested against an extensive set of experimental results from AUG and JET-ILW to assess its reliability for plasma conditions similar to those expected in the ITER pre-fusion power operation phase 1 (PFPO-1) [13]. Here kinetic profile predictions require high accuracy in the central electron temperatures to be applied to the calculation of third harmonic electron cyclotron absorption. Moreover, correctly predicting the transition from L-mode to H-mode requires precise estimates of the ion heat flux in the periphery of the plasma, completely determined by the thermal exchange between auxiliary heated electrons and ions. Electron and ion temperature profiles obtained with TGLF-SAT1geo show good agreement with the experimental profiles in general, also with a sufficiently accurate prediction of the ion heat fluxes at the edge. There is a slight tendency to under-predict central T_e and particularly T_i at high ratios T_e/T_i .

3 ITER

The IPP continued to support ITER in the reporting period through different channels. IPP scientists are represented in all Topical Groups of the ITPA, either as regular members, or as experts or in two cases as well in a leading role as chair or deputy chair. In addition, IPP scientists act as ITER Science Fellows in five different areas such as fuel retention management (improvement of WallDYN predictions), plasma control (ITER flight simulator, plasma initiation with ECRH), microwave diagnostics and turbulence and last but not least disruption and runaway electron mitigation.

Also the experimental programme of ASDEX Upgrade has always been focused on scientific issues relevant to ITER. In 2021, a framework agreement was signed between four partners to design, construct, install and operate ITER relevant Shattered Pellet Injection (SPI) hardware on ASDEX Upgrade, DIII-D, KSTAR and JET. The goal is to test the concept of SPI for mitigation of disruptions and avoidance / mitigation of runaway electrons during the current quench. Further details and results on the experiments conducted at ASDEX Upgrade in 2022 can be found in the respective chapter of this report.

As an in-kind contribution, IPP provided 14 software packages (ASTRA, B2.5, CLISTE, CVIEW, EMC3, IDA, LIGKA, RABBIT, STARWALL,

TORBEAM, TRIDYN, TESSIM, TORIC and WALLDYN) to ITER. The access, use and further development of these codes by ITER Organization (IO) and Members of the ITER Agreement will be conducted via a central repository hosted by ITER.

In addition to direct contributions to the IO, IPP is working on ITER relevant topics in the framework of the EUROfusion work package WPPriO. For more extensive activities, contracts exist with IO and Fusion for Energy (F4E). These include mainly the development of the ITER Plasma Control System (PCS), negative ion sources for neutral beam heating and the design of two ITER diagnostics.

3.1 Development of RF Driven Negative Hydrogen Ion Sources

The two test facilities at IPP, ELISE (equipped with a half-size ITER source) and BATMAN Upgrade (with the IPP prototype source), both using RF driven ion sources, are part of the European roadmap towards the ITER NNBI (Negative ion based Neutral Beam Injection) systems. The activities on both test facilities are supported within the scope of a direct agreement between ITER and IPP via EUROfusion in the period 2020–2025. Since the beginning of 2022 additionally a bilateral framework agreement exists for the collaboration between IPP and Consorzio RFX, Padova, Italy, host of the Neutral Beam Test Facility (NBTF).

ELISE and BATMAN Upgrade provide valuable input both for commissioning and operation of the NBTF and for preparation of the ITER beam lines. The investigations at IPP are supported by fundamental experiments and diagnostic developments conducted at the 'AG Experimentelle Plasmaphysik (EPP)', University of Augsburg.

One of the main goals of ELISE is to demonstrate the ITER requirements with respect to the extracted negative ion density ($286 \text{ A/m}^2 \text{ D}^-$, $329 \text{ A/m}^2 \text{ H}^-$) at an electron-ion ratio below one, a source pressure of 0.3 Pa and a global beam homogeneity better than 90 % for 1 h in deuterium and 1000 s in hydrogen. In 2018, the target values for hydrogen were demonstrated for 1000 s plasma on time with pulsed extraction ($\approx 10 \text{ s}$ beam extraction each $\approx 150 \text{ s}$) and using additional biased surfaces, the 'potential rods' [14]. For deuterium, 60 % of the target value was achieved in long pulses [15]. A better performance in deuterium is limited by a higher co-extracted electron current compared to hydrogen accompanied by a stronger vertical asymmetry and a stronger increase with time. The latter is attributed to a degradation of the low convertor surface work function, caused by the interaction with the plasma.

Consequently, the focus at ELISE was on identifying measures to stabilize the co-extracted electrons during long deuterium pulses, preferably without the potential rods as they are not foreseen for ITER NBI. Modifying the potential of the window-frame bias plate surrounding the plasma grid that in its standard setup is connected to the source vessel, turned out to be a promising alternative [16]. In fact, using a floating bias plate, an extracted negative ion current density of 256 A/m^2 ,

i.e. 90 % of the ITER target value could be achieved in short deuterium pulses (20 s plasma on time, ≈ 10 s beam extraction) at a pressure of 0.3 Pa. Compared to the operation with potential rods the co-extracted electron current is reduced in the two grid segments such that the magnetic filter field strength, which is usually higher than in hydrogen, could be reduced as well. As a consequence, the vertical plasma drift is smaller and the vertical symmetry of the co-extracted electrons is improved. In addition, a lower beam divergence is obtained, showing the relevance of the interplay of magnetic filter field and biasing of surfaces.

In order to overcome the limitation of pulsed extraction at ELISE, the test facility was converted to full steady state operation. Steady beam operation is required because the release of caesium by back-streaming of positive ions contribute significantly to the caesium dynamics. A new CW power supply for beam extraction and acceleration, was installed and commissioned in spring 2022 [17]. Furthermore, a new CW capable beam calorimeter was designed for both test facilities, simultaneously allowing beam power measurements by water calorimetry and beam profile measurements by IR imaging the blackened back side with a resolution of 2 cm \times 3 cm (ELISE) and 2 cm \times 2 cm (BATMAN Upgrade) [18, 19]. With an actively cooled plasma grid and bias plate, BATMAN Upgrade will also convert to full steady state operation at the end of 2022.

Figure 4 shows the extracted negative ion current and the co-extracted electron currents for the top and bottom beam segment measured during one of the very first 1000 s hydrogen beam pulses at ELISE using the CW power supply and the CW calorimeter: after a short caesium redistribution phase (≈ 100 s) the extracted negative ion current is stable above 190 A/m² at an electron-ion ratio below one.

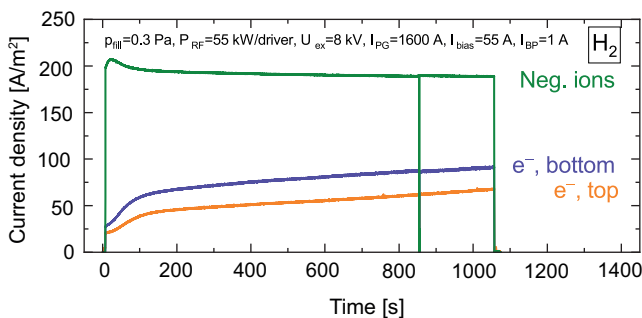


Figure 4. Extracted negative ion current and co-extracted electron current (top and bottom segment) for a 1000 s ELISE pulse with the new CW high voltage power supply and the CW calorimeter.

With the new CW calorimeter at BATMAN Upgrade steady state operation up to ≈ 100 s became possible, limited by the heating up of the uncooled plasma grid insert. Additional caesium evaporation was tested by means of a caesium shower loop mounted around the

beamlets to counteract the temporal instability of the co-extracted electron current. The increase of the co-extracted electron current could be stabilized, demonstrating the relevance of providing sufficient flux of neutral caesium particles to the plasma grid [16]. Further concept improvements regard the uniformity of the evaporation from the caesium loop before designing a system for ELISE.

A key focus at BATMAN Upgrade is the investigation of the beam optics, in particular divergence and deflection of the total beam as well as of the individual beamlets. In collaboration with ITER, a MITICA-like extraction system has been installed with the additional asymmetric deflection compensation magnets (pioneered by Consorzio RFX) embedded in the upper half of the extraction grid in order to compensate the row-wise horizontal zig-zag deflection, caused by the alternating polarity of the co-extracted electron suppression magnets [20]. Figure 5 shows (a) the simulation for the two beamlet groups together with (b) the beam measured in about 85 cm distance from the grounded grid on a 1D Carbon Fiber Composite tile and (c) the beam divergence measured by Beam Emission Spectroscopy (BES).

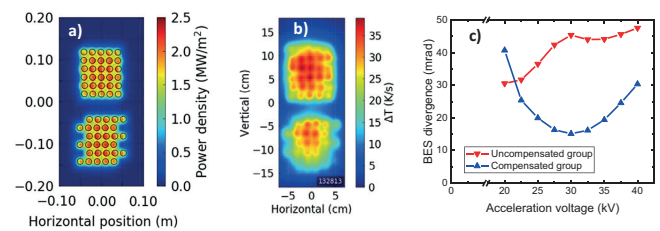


Figure 5. (a) Simulated power density of the beam from BATMAN Upgrade on the CFC calorimeter. The upper grid half is equipped with additional deflection compensation magnets; the central two rows are masked. (b) Measured temperature increase on the CFC calorimeter. (c) Measured horizontal divergence by Beam Emission Spectroscopy for the upper and lower beamlet group.

The BES signal from the compensated group shows a clear optimum of divergence with changing acceleration voltage and a much lower divergence than the uncompensated group. A robust zig-zag compensation in a wide parameter range could be demonstrated as well [21].

The experimental investigations of the beam optics are accompanied by modelling activities for which the extraction of negative ions and electrons from a plasma simulated by the 3D Monte Carlo PIC code ONIX [22] has been coupled [23] to the IBSimu beam code. This allows, for the first time, to take surface produced negative ions into account for beam optics calculations. This reveals that directly extracted negative ions contribute to the formation of a halo depending on the temperature of the negative ions. Furthermore, the plasma sheath together with the complex 3D magnetic field structure could be identified to play an important role for accumulation of electrons at the meniscus and consequently for the co-extracted electron current.

Here, first insights for the larger co-extracted electron current in deuterium than in hydrogen could be gained.

The parameters which determine the formation of negative ions at the convertor surface are the particle fluxes of atomic hydrogen and positive hydrogen ions together with the work function of the caesiated surface. In addition to routinely measuring the positive ions by Langmuir probes, a direct measurement of the atomic hydrogen species using the two-photon-absorption-laser-induced-fluorescence (TALIF) diagnostic was successfully applied for the very first time at such an ion source [24]. Moreover, to measure the work function in-situ in the ion source between pulses, a very sensitive photocurrent measurement technique was set up at BATMAN Upgrade. First results indicate the presence of a work function lower than the one of bulk caesium and confirm results of systematic investigations from the laboratory setup at University of Augsburg [25].

Based on the IPP developments in the past, improvements like solid-state RF generators are now foreseen to be implemented at the NBTF facilities and ITER NBI. Other examples concern the electric separation of the grid segments to measure the symmetry of co-extracted electrons, or the planned implementation of the floating bias plate for SPIDER.

An example for close collaborations among the ITER NBI team, NBTF team and F4E is the development of reliable molybdenum coating techniques for the large source components together with industrial partners. IPP is also strongly involved in the beam divergence task force set up by IO.

A close collaboration was furthermore established (and supported by ITER) with NIFS, Toki Japan, for a comparison of the extracted beam properties between the NIFS arc sources and IPP RF sources. For this purpose, a prototype RF source from IPP has been transferred to NIFS and is currently under installation there.

3.2 Development of ITER Diagnostics

Since 2013 IPP leads the consortia for the development of the ITER bolometer diagnostic and the Diagnostic Pressure Gauges (DPG) for ITER within Framework Partnership Agreements (FPA) with F4E and accomplished conceptual and preliminary design phases combined with prototype testing for the evaluation of concepts and sensors. At the beginning of this reporting period DPGs closed their Preliminary Design Review (PDR) successfully and bolometers prepared the PDR for the port mounted cameras and the sensor, while the development of divertor and vacuum-vessel (VV) mounted cameras is followed on lower priority due to the staged approach.

3.2.1 Bolometers

In autumn 2020 and January 2021 the final sensor prototypes from both manufacturers (Fraunhofer-IMM, Germany; CSEM, Switzerland) chosen by F4E have been received. IMM successfully manufactured the supported membrane (SM) sensor types (20 μm Au-absorbers

on a 3 μm SiN membrane supported by a Si-frame) as well as self-supported (SS) membrane type sensors (20 μm Au-absorbers on a 20 μm ZrO₂-substrate), see figure 6. Manufacturing succeeded within the required very tight tolerances. Before delivery all samples were five times thermally cycled up to 400 °C. CSEM successfully manufactured the SS membrane type sensors with the same mechanical stability, general parameters and accuracy and additionally provided samples of a SM type sensor. The latter was a development that could not be completed fully which resulted in samples stable up to 300 °C only.



Figure 6. Sensor prototypes (view from meander side): 4 single channels SM type from IMM, 4-channel sensor SS type from IMM, 5-channel sensor SS type from CSEM, one single channel SS type from CSEM (from left to right).

IPP tested these prototypes in the IBOVAC test facility, a vacuum oven at IPP that can heat bolometer sensors up to 450 °C while simultaneously performing calibration measurements. This facility has been extended by sensor holders featuring wire-bonded contacts to the sensors, thus eliminating any uncertainties at high temperatures due to the spring-loaded contacts used previously. Figure 7 summarizes the main results [26].

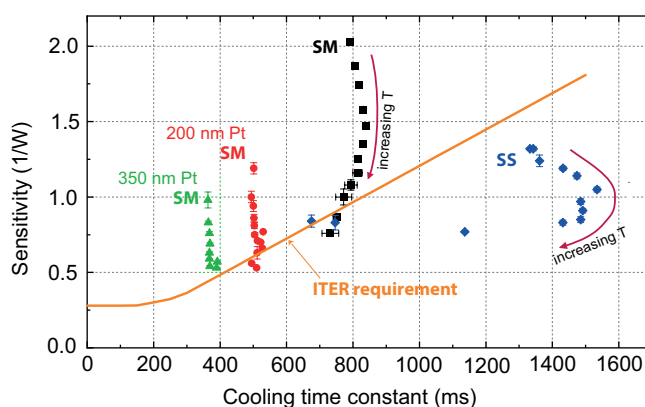


Figure 7. Results for bolometer sensor characterization of supported membrane (SM) and self-supported membrane (SS) sensor types with various thicknesses of heat conduction layers and at varying temperatures.

The ITER measurement requirement is defined as a combination of sensitivity S and cooling time constant τ at an operating temperature of 200 °C (orange line in figure 7). The measurement pairs of S and τ

align mostly in vertical lines as τ is almost independent of temperature, but it varies with the thickness of the heat conduction layer (indicated as material and thickness in figure 7). SM type sensors fulfil the requirement, values below the orange curve have been measured at temperatures above 300 °C. For the SS membrane type sensors, τ decreases from about 150 °C onwards, indicating a change in the properties of the sensor. This sensor type is therefore rated incompatible for measurements at higher temperatures, despite that it successfully survived thermal cycling tests without applied voltage.

In collaboration with KIT the sensors have also been exposed to steam, simulating the event of a loss of coolant in ITER. All sensor types passed this test. Further sensor tests at IPP are in preparation: 25 thermal cycles up to 350 °C to validate the assumptions for life-time, a pressure wave onto the membrane as well as an intense light flash to verify the mechanical resistance in case of disruption mitigation measures. Significant effort has been invested to prepare irradiation testing of these sensors in collaboration with F4E and its suppliers. IPP manufactured sensor holders and installed sensor samples connected by wire bonding. Dedicated electronics have been developed to implement a simplified calibration measurement that can be run on demand during the irradiation exposure. All these components have been delivered to F4E's subcontractor for integration into the irradiation rig. The actual irradiation exposure will be done in 2023 and provide the last piece of information on which a decision on the sensors to be used in ITER can be taken.

To quantify the thermal attachment of bolometer cameras, thermal interlayers have been prototyped and their thermal and mechanical properties have been measured. This extensive test campaign demonstrated that Sigraflex® graphite sheets provide high thermal transfer coefficients of at least 850 W/m²K as well as a relatively high electrical resistivity of 700 $\mu\Omega$ m perpendicular to its surface, which reduces the impact of halo currents and thus the EM forces on the cameras [27].

While the construction of ITER is steadily progressing, the first bolometer components, in particular the bosses to attach VV cameras, will soon be installed in Sector 6 on the VV. To support this task, a boss installation tool has been designed by IPP, its manufacturing commissioned by F4E and delivered to IO in autumn 2021. Next to be installed is the so-called cable installation template (CIT), which will attach the VV cables for bolometer cameras on their dedicated location and protect them during first plasma until the final VV bolometer camera will be installed during the second assembly phase [28]. This component has been designed by IPP and passed its final design review (FDR) in April 2021. Since then, manufacturing is handled by F4E and IPP supports both F4E and IO in the final adjustments of the CIT.

The design of divertor mounted cameras resulted in a generic camera model that has been distributed to all locations in the divertor cassettes, including the connections to the cable loom as well as to the cooling water circuit following a re-design of the outlets initiated by IO.

The design and analysis activities for the port mounted cameras were focused on passing the PDR in January 2022. The EM analysis revealed that forces up to 100 kN in the vertical direction have to be considered. To cope with these loads, a dedicated attachment scheme using wedges to lock the camera in place and relieve the bolts from shear stresses has been developed. It could be applied to all port mounted cameras and was endorsed during the PDR. Since then additional design improvements have been implemented to reduce loads as well as to avoid stress concentrations in the camera housing. The revised design is now being analysed. Additionally, critical internal camera components have been detailed and are being prototyped. The specifications for prototyping the MI cable holder have been done and procurement of components has started. The sensor holder prototypes have already been manufactured and first steps in the assembly sequence could be validated: welding of camera internal signal wires and wire bonding of the sensor [29]. Thermal cycling and vibration testing of the assembly are planned.

3.2.2 Diagnostic Neutral Pressure Gauges (DPG)

The main outcome of the PDR for the ITER DPGs was the insufficient lifetime of the emitter in the sensor due to creep and the deterioration of the coating used to enhance electron emission. Thus, IPP proposed the concept of an indirectly heated emitter, similar to the LaB6 crystal pressure gauges at W7-X. After successful initial tests a new baseline design with an emitter stack consisting of a sintered ZrC slab was chosen, indirectly heated by pyrolytic graphite and thermally isolated from the frame by ZrO₂ blocks (figure 8) [30].

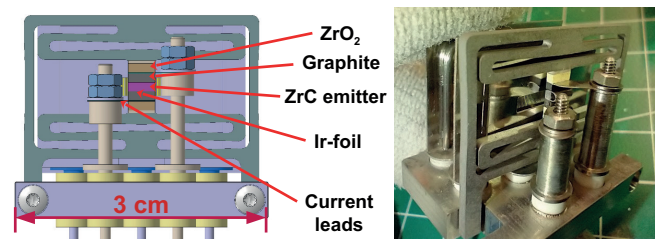


Figure 8. Design of the sensor head for DPG with a ZrC emitter (left) and picture of a prototype (right).

Several prototypes of this new design have been produced and thoroughly tested. Initial tests at various pressures in H₂-atmosphere, but without magnetic field demonstrated a good reproducibility and low measurement uncertainty (figure 9, left). Tests on reproducibility and measurement uncertainty with B-field are ongoing. A dedicated measurement campaign has been conducted in the test facility D-Mag in Greifswald to characterize the ZrC emitters at high B-fields and various pressures in H₂, D₂ and He. Stable operation during 30 minutes operation time at B = 6 T could be demonstrated for all cases.

This meets typical operational requirements in ITER, only some gauge locations on the high-field side will be at up to 8 T.

Figure 9 shows on the right the summary plot for the measurements taken in H_2 , demonstrating that the complete range for ITER neutral pressures in the boundary can be covered [31]. Also, completely assembled gauge heads as well as an individual emitter stack successfully passed a steam ingress test. Furthermore, an investigation on irregular, fast jumps of the ion current in collaboration with ASDEX Upgrade identified ranges of the grid potentials that can suppress these jumps [32].

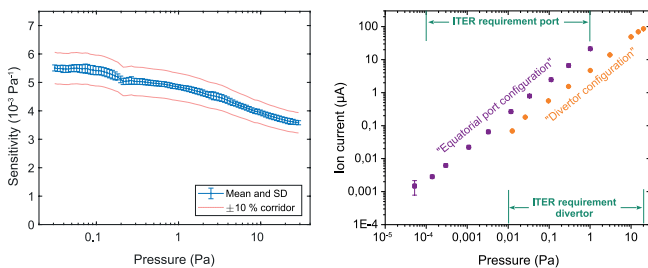


Figure 9. 3000 on-/off-cycles for the DPG with crystal emitter at various pressures in H_2 -atmosphere without B-field (left) and measurements for two configurations at various pressures in H_2 -atmosphere at 6 T demonstrating the achievement of the ITER requirements (right).

This first operation of the ZrC emitter for many hours indicated erosion effects on the pyrolytic graphite. Life-time tests at 20 Pa H_2 for 340 h operating time revealed a total erosion of $\sim 500 \mu\text{m}$ on the graphite block corresponding to an erosion rate of $1.5 \mu\text{m}/\text{h}$. As the erosion is more pronounced at the surface between graphite and ZrC and not visible on the outer surfaces of the graphite blocks, a strong temperature dependence and a diffusive process is presumed. These tests have been repeated with adding a W-foil or an Ir-foil of $50 \mu\text{m}$ or $100 \mu\text{m}$ thickness as interlayer between graphite and ZrC. With the $100 \mu\text{m}$ thick Ir-foil the erosion rate could be reduced to $0.4 \mu\text{m}/\text{h}$ (figure 10). This is an encouraging result but might not yet be sufficient to meet the ITER life-time requirement for the gauges, which would demand operation of 1500 h according to current reliability analyses (RAMI). The preparations for the upcoming FDR include the investigation of other interlayer materials (Mo and Ta) to better suppress C-diffusion. Also, vibration tests in collaboration with F4E are in preparation to evaluate the resilience of the (partially eroded) emitter stack against mechanical loads in ITER as well as to re-run the RAMI analysis with less demanding assumptions on the life-time of the gauges.

With the change of the baseline for the sensor head, the design of the diagnostic components for integration in ITER had to be updated, too. Furthermore, an independent assessment of the manufacturing and assembly feasibility recommended minor design improvements.

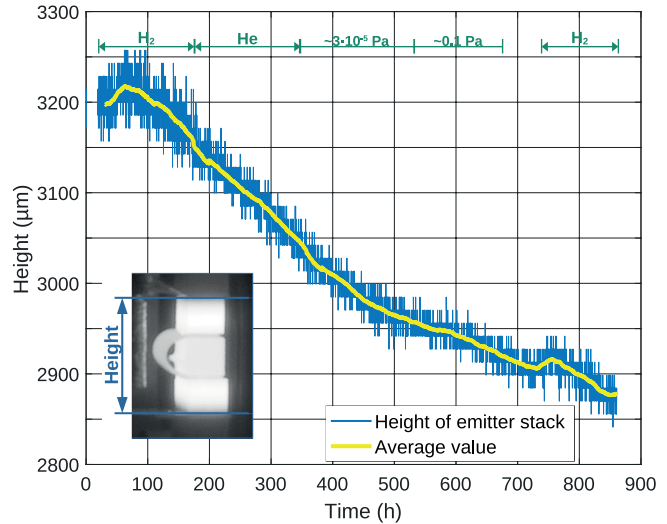


Figure 10. Evolution of the height of the emitter stack based on automatic picture evaluation (see insert) during a total operating time of 851 h, out of which 274 h in 20 Pa H_2 atmosphere, 160 h in 20 Pa He and the rest at various pressures of the residual gas.

All diagnostic components have been implemented in ITER's design database and published for final review by F4E and IO. They are also the basis for the final structural assessment of the diagnostic components, which is being performed by analysts of F4E.

An ongoing discussion with IO (without impact on the structural assessment) is still the design and distribution of the first junction boxes for DPG signal cables (IO responsibility), that might impact the signal quality. Furthermore, based on experience from ASDEX Upgrade proposals have been made for the routing and bundling of DPG signal cables outside the VV in order to retain an as high as possible signal quality. A final conclusion on this topic is pending.

The electronics for DPGs have been developed by IPP and now further improved based on the test results obtained. The final prototype test was the operation of the electronics together with an ITER-like control system. This so called mini-CODAC has been provided by F4E. In a first round few improvements have been implemented. The second part of the test then confirmed the successful coupling of the prototype DPG electronics with the ITER mini-CODAC and measurements on a DPG head prototype at the neutral gas lab at IPP were recorded. Several measurements were done for different pressures of hydrogen, with and without a magnetic field, demonstrating that the developed electronics operate as specified.

3.2.3 Prospects of ITER Diagnostic Development at IPP

Both diagnostics developed for ITER at IPP approach their FDR, for the DPG this is planned for January 2023, for the port-mounted bolometer cameras this is planned for July 2023. After the successful

completion of the FDR, F4E uses the results to procure the diagnostic components from industry as well as to place external contracts for the completion of additional subsystems. In particular, this includes the development of data acquisition hardware and operating software, but also bolometer subsystems. For the latter IPP was unable to provide sufficient engineering resources within the contractual and funding conditions of the FPA to complete their development within the timeframe prescribed by the schedule agreed between IO and F4E. Notably, these are the VV and divertor mounted bolometer cameras, which currently are nearing their PDR.

IPP expects that a significant amount of expertise from IPP's diagnostic teams will be required between FDR and operation in ITER and intends to support this phase with the required know-how. As contracts between F4E and industry for these tasks are still in preparation, it is not yet clear how IPP's involvement will look like. Options range from service provider via F4E over a subcontractor to industry up to participating in industrially led consortia. In any case IPP's future participation will depend on continuous and sufficient funding of these activities in order to keep non-permanent personnel at the institute and thus sustain IPP's competence in these fields.

3.3 Development of the Plasma Control System (PCS)

Since the Conceptual Design phase starting in 2012 the IPP has been contributing to the ITER PCS design as a partner in an international team. Starting with the Preliminary Design in 2014, the IPP is acting as the consortium lead. The last contract on the Final Design for First Plasma Operation from 2017 to 2020 was successfully finished without major chits. In February 2021 the ITER Organization published a follow-up call for tender for a new contract on the Final Design of the ITER PCS for the Pre-Fusion Plasma Operation-1. The call comprised a wide spectrum of design tasks from magnetic, fueling, H-mode, NTM, heat load and disruption control to exception handling. These tasks were complemented by a number of integration tasks, where the responsibility would be taken by IO itself. In response to this call, the IPP, its previous partners CREATE, Critiware, CEA and CCFE together with RFX as a new party formed a bidder team. The team elaborated an offer with detailed work breakdown, task descriptions, risk and dependency analysis, as well as effort estimates with a total work effort of 3700 full working days broken down in 7 design tasks and an agile project management. The project management, as well as three of the seven contracted tasks would be coordinated by the IPP: Disruption and runaway control, Exception Handling and Control Integration. This amounts to an effort of 880 working days or 24 % share for the IPP. The offer was placed by end of July 2021 and accepted by ITER in November 2021, such that the design project could start in January 2022, again with the IPP as consortium lead.

The agile approach introduces a staged, iterative workflow, the continuous interaction between developers and the IO stakeholders, as

well as frequent and quick feedback on the project evolution. For this purpose, the IPP has set up a Kanban project with about 650 work items, which is deployed as a Jira project and accessible to all team members including the IO. As the agile management takes a holistic project view, the Kanban project manages not only the consortium contributions, but also the work items under ITER responsibility. A Kanban board visualizes the current execution status of each activity by placing Kanban cards in dedicated columns. Developers can move the cards from one column to the next to indicate work progress and thus make it instantly visible for the entire team. The IPP organizes monthly status update meetings with participation of task coordinators, IO stakeholder representatives and the project management to monitor the project execution and possibly discuss and adjust the project plan. In order to keep trace of inter-task dependencies also in case of project adaptation, the work breakdown structure elaborated during the tendering is continuously kept up to date.

The first project phase until June 2022 dealt with elaborating detailed task specifications, analyzing system requirements, identifying potential off-normal use cases, refining design concepts and considering design integration aspects. Subsequently, control function development work has been started and is still ongoing. A major difference between current fusion control systems and the projected ITER PCS is the strict separation of the ITER control in the PCS from the investment protection in the separate Advanced Protection System (APS) and Central Interlock System (CIS). The APS and the CIS must be self-reliant and thus shall not make use of internal PCS calculations. This has a significant impact on the design of PCS and APS monitoring functions, both of which are in the responsibility of the design team, such that two – often different – solutions must be developed. In particular the Disruption Control design led by the IPP is affected by this architectural choice. The first function to be developed in its scope is a VDE detector. While VDE detection at ASDEX Upgrade can be easily accomplished by monitoring the control error of the vertical position feedback controller, the APS monitoring function on ITER must rely on different indicators, mainly the absolute vertical position and the vertical velocity. A second function under development is a current quench detector.

The ITER PCS must be prepared to robustly and reliably respond to unplanned situations which may be caused by failures or plasma events. This "Exception Handling" must be built into the individual control system components, as well as into a central PCS Pulse Supervision Controller that coordinates the activities of the entire system. The IPP Exception Handling task develops the central component. In addition, it supports the control function designers of other tasks with the collection of relevant events, their classification regarding probability, detectability and severity, as well as with adequate generalization in order to identify simple but efficient handling policies. Conducting and evaluating an initial Failure Mode Effect Analysis (FMEA) in collaboration with the other design tasks was

therefore the main focus of the initial development work and has meanwhile been concluded.

Finally, all developed controllers in the PCS will be coupled by the physics of the plasma behavior. It is therefore not sufficient to develop feedback controllers and exception handling functions independently. Instead, the combination of these components must yield a consistent integrated behavior. The purpose of the IPP control integration task is to promote the compliance of control solutions and to provide architecture elements that support integrated solutions. In the scope of this contract, the IPP is in charge of developing a re-usable generic base for Actuator Management. The purpose of Actuator Management is to resolve the inflexible direct allocation of controllers to actuators and replace it with a function, which dynamically selects appropriate actuators out of a resource pool. That way, it is not only possible to replace on-the-fly tripped actuators, but also to aggregate several actuators to a more powerful resource, or to prioritize the allocation of scarce actuator resources to a multitude of controllers. The ITER PCS will apply Actuator Management for gas and pellet fueling, as well as for electron cyclotron heating and current drive. The IPP can exploit its expertise in Actuator Management for heating systems in the ASDEX Upgrade Discharge Control system. Moreover, the ITER application poses an additional challenge, as the pellet and EC launching systems will also be adjustable in realtime such that e.g. a gyrotron can be used for either central heating or profile control depending on its mirror position or launcher selection. A first artefact of Actuator Management development will be a Virtual Actuator component, which provides a rule-based selection of actuators in a pool for a dedicated control purpose, however yet without consideration of dynamic launcher configurations.

3.4 Modelling of ITER ICRH Antennas

A set of simulations was performed on optimizations of ITER ICRH antennas in the framework of a contract between the ITER Organization and IPP.

The beneficial effect of using the Gas Pipe Orifices (GPOs), to be located close to the ITER ICRH antennas, on the ICRH performance was examined by calculating 3D plasma density (n_e) distributions using the EMC3-Eirene edge plasma fluid and neutral particle transport code, with a large variety of input parameters. The increase of the Scrape-Off-Layer (SOL) n_e and ICRH coupling resistance calculated using spatially averaged 1D n_e profiles, favours higher values of gas puff rate, separatrix density and transport diffusion coefficient. Nevertheless, for all the scanned parameters, a significant coupling improvement (and a decrease of near-fields, see below) was predicted for the antenna GPOs compared to the divertor gas puff, reaffirming the use of the local gas puff strategy.

In order to provide Radio Frequency (RF) simulations for the characterization of coupling and near-fields properties independently

of the TOPICA code, a full ITER ICRH full-size antenna model was thoroughly prepared, meshed and combined with adapted perfectly matched layer boundary conditions in the RAPLICASOL code. This code is based on 'COMSOL Multiphysics' and can cope with full 3D n_e distributions. Antenna RF properties calculated by RAPLICASOL agreed excellently with TOPICA on a large set of input parameters with poloidally and toroidally homogenous n_e (based on 1D n_e profiles). Extending the simulations to more realistic 3D n_e distributions, RAPLICASOL predicts a slightly reduced coupled power (by up to 10 %) compared to the 1D cases.

The near-field assessment was performed using TOPICA and RAPLICASOL outputs and assuming the parallel electric field component E_{\parallel} on the lateral sides of the antenna plasma facing components as a figure of merit to minimize RF sheaths which can lead to increased impurity release and heat loads. Similar analysis of E_{\parallel} describes well the experimental observations on ASDEX Upgrade and JET. The analysis of the power balance for the ITER antenna shows that an excellent minimization of E_{\parallel} can be obtained in $[0, \pi, 0, \pi]$ toroidal strap phasing by launching power predominantly from the central straps, but at reduced coupled power. Still a very good optimization is achievable using $[0, \pi, \pi, 0]$ without drawbacks on the coupled power. In terms of poloidal phasing, $[0, \pi]$ shows more preferable behaviour than $[0, -\pi/2]$.

Both with poloidally/toroidally homogenous n_e (TOPICA and RAPLICASOL) and with full 3D n_e (RAPLICASOL), the optimization is effective, with spatially averaged E_{\parallel} lower in 3D n_e except in $[0, \pi, 0, \pi]$ with very low E_{\parallel} .

Increased SOL density by using local GPOs decreases the near-fields when normalized to the coupled power in most cases, except cases at high n_e in $[0, \pi, 0, \pi]$ with very low E_{\parallel} . Future work will include analysis of high resolution full n_e -profile RAPLICASOL simulations which indicates that the propagative slow wave can modify the near-fields at the PFCs in the low coupling cases.

3.5 Disruption Physics: Runaway Electron Fluid Modelling

Uncontrolled termination of post-disruption relativistic runaway electron (RE) current can cause deep localized melting of the plasma facing components and poses a serious challenge to the successful operation of fusion grade tokamaks, including ITER. While RE deconfinement depends on the timescale of flux surface reformation, the magnetohydrodynamic (MHD) plasma stability itself is affected by the runaway current. Therefore, the interaction between REs and MHD is highly non-linear and determines the eventual impact-profile of REs on the components. This is the motivation of the present work, aimed at studying RE-MHD co-evolution in ITER disruptions using the non-linear 3D MHD code JOREK [33, 34] (see also chapter 6). The REs are modeled as a separate fluid species [35], subjected to field-parallel and drift transport along with an avalanche source including the effect of partially-ionized impurities [36]. The back-reaction of REs on

MHD is treated via current-coupling, while the impurities are assumed to be in coronal-equilibrium. Electrically conducting structures such as the vacuum-vessel and coils are included via coupling to STARWALL.

Starting with a 15 MA elongated free-boundary X-point plasma equilibrium, a pseudo thermal-quench followed by the first injection of Ne+D causes a current-quench and the subsequent vertical motion along with a multi-MA RE beam formation. Through axisymmetric simulations, we investigate the effect of first injection quantities, current-profile flattening, Neon 2nd injection and Neon-flushout in case of Deuterium 2nd injection. Within the constraint for the current-quench time for ITER ($50 \text{ ms} < t_{\text{CQ}} < 150 \text{ ms}$), our simulations predict a multi-MA RE beam for any combination of Ne/D injection scenarios, with the RE beam current increasing up to $I_{\text{RE}} \sim 9.5 \text{ MA}$ with the injected Neon quantity. This is in qualitative agreement with 1D code GO [37]. The 2nd injection of Neon causes both a faster decay of RE current, and a correspondingly faster vertical plasma motion towards the wall. However, 2nd injection of Neon is found to be ineffective in reducing the undissipated component of RE energy deposited onto the wall. Commensurate increase in the poloidal magnetic energy channeled to REs (due to the bound-electrons of Neon acting as additional avalanche targets), is seen to offset the additional dissipation of RE energy. In general, vertical motion and scrape-off of the plasma causes a net decrease in the edge safety factor ($q_{95} \sim a^2/I_p$). For ITER major disruptions, it is predicted that $q_{95} = 2$ occurs after the formation of a full RE beam. Full 3D simulations in the RE plateau phase show that such a regime can trigger fast growth of MHD instabilities leading to magnetic stochasticization which might potentially allow for a benign RE beam termination due to distributed RE losses on the wall. The JOREK disruption mitigation models will soon also be validated in detail against ASDEX Upgrade experimental data in direct collaboration with ITER.

3.6 Integrated Data Analysis

Scientific exploitation of fusion devices crucially depends on the reliability of measurements and their interpretation. Typically, a large number of redundant and complementary diagnostics allows for a detailed exploration of plasma scenarios. Redundant diagnostics for the same physical quantities allow to improve the reliability of estimated physical parameters and help to identify and quantify diagnostics inconsistencies. Complementary diagnostics provide valuable mutual information for their analysis as the interpretation of heterogeneous measurements is regularly highly correlated. A combined probabilistic analysis of all available diagnostics profits from the parametric dependencies and a thorough uncertainty quantification of all measured data, calibration and modelling parameters.

A group within the AUG team is playing a leading role in contributing advanced data analysis techniques to next generation tokamaks through the ITPA and by participating in the EUROfusion Workprogramme.

In 2020 an Integrated Data Analysis and Validation (IDAV) specialist working group (SWG) was founded within the ITPA Diagnostics Topical Group with the goal to develop a generic and open-source IDA-code package [38]. Its primary goal is to support ITER data analysis with an IDA framework. A first ITER IDA implementation combining the Thomson scattering (TS), the electron cyclotron emission (ECE) and the toroidal interferometer and polarimeter (TIP) diagnostics demonstrated the benefits of a combined analysis. The IDA framework is designed for highest modularity with standardized interfaces for any set of heterogeneous diagnostics. Various forward models for a diagnostic allows for low- to high-fidelity data modelling depending on the necessary interpretation depths and numerical requirements.

A set of likelihoods addressing all relevant uncertainty distributions, such as Student's t for robust outlier estimation, allows for a comprehensive uncertainty quantification. Measured data can optionally be augmented with independent physics modelling including their uncertainties allowing to constrain the correlated parameter space to physically reasonable solutions.

Multi-fidelity parameter estimation routines, e.g. maximum-a-posteriori and Markov chain Monte Carlo methods, are included. The appropriate, but not exclusively used, interface for data access and storage is given by the Integrated Modelling & Analysis Suite (IMAS) based on Interface Data Structures (IDS) designed for high modularity and flexibility to be suitable for any fusion device.

An additional activity (contractual basis: Implementing Agreement No. 5) at IPP's branch in Greifswald aims to develop synthetic spectroscopy models for studying both the expected performance of spectroscopy measurements by ITER diagnostics as well as to investigate novel methods for IDA of spectroscopic data. In order to verify the effectiveness of such synthetic models and analysis methods, they have not only to be developed for ITER diagnostics, but also for W7-X diagnostics, such that these results can be compared to actual measurement data of plasma discharges in the W7-X stellarator.

One of three agreed working packages concerns the Bayesian inference of the effective ion charge Z_{eff} in ITER plasmas. A Bayesian model has been developed in the MINERVA framework, which can predict bremsstrahlung of ITER reference plasmas observed with the 55.E6 Visible Spectroscopy Reference System (VSRS). The diagnostic comprises several interference filter based measurements at selected wavelengths as well as one spectrally resolved measurement sampling the plasma emission along a single line of sight passing the plasma core. The inference of Z_{eff} has been validated using synthetic data. Given a short time of a single posterior distribution evaluation of approx. 1.5 ms, a method has been proposed for a fast (approx. 2.5 ms) inference of Z_{eff} which will be implemented in the real-time feedback control system of ITER. In the case of a failure of the interferometer density measurement this method can be used to deliver the electron density n_e instead of Z_{eff} for plasma control purposes.

4 JT-60SA

The Japanese-European tokamak project JT-60SA was initiated in 2007 as part of the “Broader Approach” agreement between the EU and Japan for the fastest possible track to realize fusion energy. The JT-60SA is considered to be the successor of JET. It is intended to support ITER in answering the open physical questions for the design of a DEMO reactor. The focus is on research projects complementary to ITER with the focus of developing a DEMO design allowing fully noninductive, steady-state operation.

Construction of the machine at Naka, Japan, was completed in 2020. Commissioning is currently underway. The JT-60SA research plan, developed in conjunction with ITER, covers a facility lifetime of ~ 20 years. IPP is helping to prepare this large-scale plant with the following activities via EUROfusion’s WPSA.

4.1 Pellets

The construction of a new pellet launching system (PLS) for the JT-60SA device is currently in progress. Design and layout of this system has been developed and is part of the step ladder approach system evolution, composed by the steps ASDEX Upgrade -> JT-60SA -> DEMO. The design of the JT-60SA system is based on the well-established one of AUG, where efficient core particle fuelling is achieved by pellet injection from the torus vessel inboard side. Pellets arrive in the plasma predictably and precisely in time, launched by a centrifuge accelerator and transferred through a well-optimised guiding system. In line with the AUG PLS, also the JT-60SA one foresees a stop cylinder type centrifuge accelerator. Despite the engineering challenges for the realisation of this option integrated in an upgraded version of the PLS, it is considered as an optimal solution for the control of the pellet.

While the AUG system is restricted to a prefixed pellet size and composition from a limited reservoir, the JT-60SA design is extended for long pulse operation up to 100 s and simultaneous delivery of pellets with different sizes and compositions. Different pellet types can be produced into a single train serving simultaneously for different purposes: large pellets are needed for an efficient core particle fuelling and small pellets for ELM frequency pacing. A dedicated algorithm takes care that these control tasks are efficiently covered minimising cross talk [39]. Two high throughput hydrogen ice extruders are developed, to provide both pellet species as need and capable to yield a steady continuous ice flow producing an unlimited string of pellets. Furthermore, simultaneous extrusion of a twin ice rod is foreseen for one extruder, to reach the challenging requirement of 20 Hz rate for fuelling. Operation with both stable hydrogen isotopes is enabled in both extruders; on request, even isotopic mixtures can be produced for the fuelling pellets.

The current PLS layout allows for a further upgrade: the inclusion of a third extruder which would serve to reach higher fuelling fluxes or ELM pacing beyond 50 Hz. This is also achievable since the centrifuge design foresees a pellet repetition rates up to 100 Hz. On demand,

an upgraded option for a maximum of 200 Hz is possible. The third extruder could also be exploited for the delivery of seeding gases, by adding them into the pellets. The technical and physics feasibility of this approach had been demonstrated at ASDEX Upgrade: small amounts of nitrogen, argon or xenon were deposited in the plasma core via doped pellets, showing advanced performance in comparison to impurity gas puffing (see section 2.9 in chapter ‘ASDEX Upgrade’). This approach has been found highly relevant for DEMO. Hence, the new JT-60SA PLS represents already a potential prototype for a viable DEMO system covering almost all reactor needs – yet just leaving the ultimate pulse duration extension and operation with tritium as remaining issues.

IPP pellet experts have also been deeply committed in the preparation of the necessary infrastructures and the set-up of their laboratory, where the PLS will be assembled, tested and commissioned.

4.2 Massive Gas Injection for Disruption Mitigation

Disruption mitigation is a key task in the research plan of JT-60SA. Therefore, JT-60SA will be equipped with a MGI system for fast delivery of gaseous medium-Z impurities. The MGI system consists of two MGI valves, two vacuum feed throughs, the gas preparation system and the control system. The MGI valves are mounted inside the vacuum vessel behind the stabilizing plate in upper oblique position in sectors P09 and P18. Tubes from the MGI valves, which penetrate the stabilizing plate, guide the gas to the plasma.

The MGI valves are based on the design of the ASDEX Upgrade spring-driven MGI valves [40]. The valves have an internal gas reservoir of 815 cm³ and can be filled with mitigation gas up to a pressure of 6.5 MPa. The opening time of the valves is below 2 ms and CFD simulations show that up to 90 % of the mitigation gas is released within 10 ms. The MGI valves were designed according to the Japanese High Pressure Gas Law and the design has been accepted by the Ibaraki Prefectural Office in October 2021. The gas preparation system is used for mixing the mitigation gases, supplying the compressed air and pumping the MGI system. Mitigation gases can be mixed from up to four different gases with an accuracy of 20 kPa. This can be done either manually or with an automated mixing procedure for increased reliability and reproducibility. The MGI valves require 1.8 MPa of compressed air pressure to be closed. For this, the 0.7 MPa compressed air from the plant is fed into a mechanical pressure booster, which is built into the gas preparation system. A roughing pump, which is connected to the gas preparation system, can evacuate the gas system and the MGI valves to a pressure below 10 Pa.

The control system consists of the central PLC, the valve trigger electronics and the trigger signal selection electronics, all located in the electronics room, as well as the peripheral PLC at the gas preparation system.

The complete MGI system is being built and tested at IPP Garching in 2022 and will be shipped to Naka site early in 2023.

4.3 Energetic Particles

In order to predict and interpret the neutral beam driven (NBI) instabilities on JT-60SA and to extrapolate to ITER, global kinetic models are mandatory. The LIGKA/HAGIS package provides a gyro-kinetic, non-linear hybrid description that determines linear stability thresholds and the non-linear energetic particle (EP) redistribution. The objective of this work is to use a fully automated workflow to explore various JT-60SA-relevant scenarios, both in the ramp-up and the flat top phases. The linear and quasi-linear properties given by this workflow will be used in reduced transport models currently under development in order to assess and optimise the energetic particle properties in various operating scenarios. So far two scenarios crucially important for the main mission of JT-60SA were analysed in detail: a standard high- β scenario based on a transport code simulation (JINTRAC, IMAS shot number 70000,419) and a non-inductive high- β steady-state scenario.

In the flat top phase of the standard scenario, all toroidicity induced Alfvén eigenmodes (TAEs) investigated so far (toroidal mode numbers from 1-15) are strongly damped ($\gamma/\omega > 6\%$). It is not expected that the NBI drive will overcome the damping in this case. Also, the positive EP gradient introduced by the off-axis heating beams will not destabilise TAEs. However, higher frequency modes (EAEs) are expected to be close to the instability threshold. Sensitivity scans facilitated by the workflow capabilities will allow us to further determine their importance for the EP transport during the flat top. As soon as the time dependent equilibrium and profile data will be available, the more problematic ramp-up phase will be looked at.

The ramp-up phase has been already investigated for the non-inductive scenario [41]. Here, not only the TAEs are less damped, but also the beta-induced Alfvén eigenmodes (BAEs) and the related Alfvénic ITG branch are found to be unstable at intermediate toroidal mode numbers, contrary to present day experiments. This can be understood when comparing the BAE frequencies to the Alfvén frequency. Whereas for present day machines this ratio ($f_{\text{GAM}} / f_{\text{Alfvén}}$) is only a small fraction, at the high beta scenarios this ratio reaches almost 0.5 which is in the TAE frequency range. Therefore, a strong modification and destabilisation of the kinetic Alfvén continuum and to some extent also the TAE gap structure can be expected. In addition, the steep gradients lead to a large diamagnetic frequency, even for low poloidal mode numbers. Since the large EP particle orbits width also favours low toroidal modes numbers, the role of global (or at least meso-scale) modes becomes more prominent under these conditions. Beta-induced Alfvén Acoustic modes and low-frequency Alfvén eigenmodes are expected to be stable.

The very recent implementation of IMAS interfaces connecting the EP workflow to realistic NBI distributions will allow us to conclude the linear analysis and tackle the quasi-linear and non-linear EP transport aspects of JT-60SA.

4.4 Integrated Data Analysis

For JT-60SA the adaptation of the generic IDA code package has been specified with support by EUROfusion's WPSA. An application to the JT-60SA PO-1 commissioning diagnostics like interferometer, soft-X ray and visible spectroscopy, augmented with the PO-2 diagnostics Thomson Scattering and ECE was proposed for estimating the electron kinetic profiles and the effective ion charge. Using the same IDA code package for both, ITER (see section 3.6) and JT-60SA, highly benefits from experience exchange and might trigger mutual developments for similar diagnostics on both devices.

5 DTT

The Divertor Tokamak Test (DTT) facility in Frascati is an Italian high-field tokamak project with super-conducting coils with the aim to find a solution for the DEMO exhaust challenge. The device is supposed to start operation in 2028. IPP has been involved so far in the integrated transport modelling of DTT scenarios and via EUROfusion's WPDIV in the elaboration of divertor concepts. The DTT project has recently started to establish its research plan involving in this process also EU partners including IPP scientists.

5.1 Transport Modelling

Integrated transport modelling of DTT scenarios is required for several applications, such as the design of the diagnostic systems, the definition of the heating mixes, as well as the estimate of the fast particle losses and the neutron yields and the design of the neutron shields. The simulations are performed with the ASTRA transport code and model the time evolution of the DTT full power scenario at 5.85 T and 5.5 MA covering both the L- and the H-mode phases, starting from 0.65 s up to 36.0 s of the discharge evolution [42]. Profiles over the entire minor radius are predicted with the TGLF [43] transport model in the L-mode phase up to the L-H transition. Once entered H-mode, the IMEP [44] workflow is applied for the calculation of the pedestals, that are then imposed outside the normalized toroidal radius of 0.9. The time evolution of the magnetic equilibrium is taken from the CREATE free-boundary reconstruction and imposed as time dependent prescribed boundary in ASTRA. The current ramp follows the foreseen rate of 200 kA/s and the plasma shape moves from circular limited in the early phase to elongated and lower single null diverted in the later phase. Argon and tungsten are also included in the modelling, with a combination of neoclassical and turbulent transport models. Their concentration is tuned to match the prescribed value of the effective charge. The heating power time traces and profiles are consistently computed in ASTRA with the TORBEAM code for ECRH, the RABBIT code for the NBI heating. Geometries of the ECRH and NBI heating systems of DTT have been included in TORBEAM and RABBIT, coupled to ASTRA. The additional ICRF heating power density profiles have been prescribed from the output of external calculations.

The ramp of the heating power is followed according to the scheduled trajectory [45] exceeding 20 MW before the L-H transition. The foreseen full power current flat top phase has 45 MW of total heating power. The time evolution of the plasma density, with line averaged density which increases from 2 to $15 \cdot 10^{19} \text{ m}^{-3}$, is followed by adjusting the neutral influx in the simulation with feedback on the prescribed density value. No actual scrape-off layer model for the plasma density is yet included, whereas the two-point model is applied for the electron temperature. The central electron and ion temperatures are shown to increase from about 1 keV at 1.0 s to 10 keV and 6 keV respectively just before the L-H transition. Current work is dedicated to test the impact of different boundary conditions on the profiles, particularly directly after the L-H transition when IMEP is called. An upgrade of the scrape-off layer model is also planned.

6 Outlook

The newly founded project 'International Tokamak Collaborations' aims at co-ordinating the collaborative activities of IPP in the area of tokamak physics towards the development of a fusion power plant. Two main upcoming devices for collaboration will be JT-60SA and ITER. Large investments have been made recently all over the world for the foundation of nuclear fusion start-ups – a sign that corporate investors are taking more and more notice of this clean nuclear energy source. Developing and integrating the technologies together with the scientific knowledge needed to form a working and economical fusion power plant is probably beyond the current scope of one company or a publicly funded lab. Therefore, the next phase on the route to commercial fusion energy will most probably be public–private partnerships between the government-funded sector and emerging companies, in which cost and risk are shared. In this context possibilities for IPP concerning such new types of exciting collaborations might become a reality. The IPP has made initial contact with a few of these fusion start-ups. A good example is the US company Commonwealth Fusion Systems (CFS), which pursues the basic idea to develop on the fastest possible track a compact, high-field tokamak fusion reactor using well-established plasma physics concepts together with a new magnet technology based on high-temperature superconductor tapes. On this route the SPARC project is a major enterprise in CFS's strategy to demonstrate that their ideas are a realistic and quick path to economical fusion energy.

In the current design phase of SPARC IPP staff has been involved in review meetings on systems like the divertor, plasma facing components, the boronization system, techniques for massive gas injection, bolometer and spectroscopic diagnostics and finally the ICRF heating system.

These activities can be regarded as the starting point for an intensified collaboration not only with CFS, but also with other companies which follow an approach that fits to the expertise of IPP.

Scientific Staff

JET: C. Angioni, G. Birkenmeier, W. Bobkov, N. Bonanomi, A. Chankin, D. Coster, M. Dunne, M. Faitsch, J. Hobirk, A. Kappatou, T. Luda, G. Pautasso, P. Schneider, W. Tierens

JT-60SA: D. Coster, M. Dibon, U. Fantz, R. Fischer, T. Hayward-Schneider, K. Krieger, P. Lang, Ph. Lauber, R. Neu, C. Piccinni, B. Plöckl, V.-A. Popa, D. Stieglitz

ITER: V. Bandaru, R. Bilato, W. Bobkov, G. Conway, D. Coster, E. Fable, U. Fantz, H. Faugel, Y. Feng, R. Fischer, I. Gomez, M. Hölzl, O. Kulacek, M. Krychowiak, Ph. Lauber, P. McCarthy, H. Meister, R. McDermott, A. Mutzke, R. Ochoukov, G. Papp, G. Pautasso, E. Poli, G. Raupp, M. Reich, K. Schmid, D. Stieglitz, J. Stober, W. Tierens, W. Treutterer, M. Usoltseva, M. Weiland, W. Zhang

ITER-Bolo: H. Eixenberger, L. Flicker, B. Glasauer, S. Jahanbakhsh, N. Jaksic, A. Kampke, M. Majewski, H. Meister, A. Pataki, F. Penzel, A. Seiler, S. Schmitt (IMM)

ITER-DPG: A. Arkipov, W. Asad, H. Eixenberger, B. Glasauer, S. Jahanbakhsh, J. Koll, F. Mackel, H. Meister, A. Pataki, A. Seiler

ITER-NNBI: M. Barnes, F. Bonomo, R. Bergmayr, J. Berner, S. Briefi, S. Cristofaro, U. Fantz, M. Fröschle, N. den Harder, A. Heiler, B. Heinemann, C. Hopf, A. Hurlbatt, W. Kraus, M. Lindqvist, I. Mario, F. Merk, A. Mimo, R. Nocentini, G. Orozco, R. Riedl, G. Starnella, C. Wimmer, D. Wunderlich, D. Yordanov, G. Zadviitskiy, D. Zielke

DTT: C. Angioni, N. Bonanomi, A. Kallenbach, T. Luda, R. Neu, G. Tardini, M. Weiland, M. Wischmeier

SPARC: W. Bobkov, M. Dibon, R. Dux, A. Herrmann, H. Meister



Stellarator Research

Wendelstein 7-X Construction and Operations

Heads: Prof. Dr. Thomas Klinger, Prof. Dr. Hans-Stephan Bosch

Since the end of 2018, the final completion steps of the W7-X experiment towards long pulse operation were performed. Large and complex components have been assembled, in particular the high-heat flux divertor, cryo pumps and the ex-vessel and in-vessel water cooling circuits of all plasma-facing components. For cryo-pump operation, the cryo supply had to be substantially extended. The restart of W7-X began in early January 2022 with the technical commissioning, which was successfully concluded in September 2022. No major technical issues occurred, including the high-risk area of ultra-high vacuum leak tightness of the cooling system.

1 Wendelstein 7-X Completion

Head: Prof. Dr. Thomas Klinger

1.1 Introduction

The project "Wendelstein 7-X Completion" was successfully accomplished on 24th January 2022 by closing the W7-X plasma and outer vessels for vacuum pumping and subsequent commissioning and plasma operation. Between November 2018 and January 2022, an extensive upgrade of Wendelstein 7-X had been undertaken to prepare the device for demonstration of high-power long-pulse operation. For this purpose, the installation of active water cooling of all plasma-facing components was required. Divertor target plates, heat shields and wall panels had to be connected to the water-cooling system and each of the ten divertor elements was equipped with a cryopump. 85 ports had to be equipped with actively cooled port liners. In total, about 600 water cooling circuits and a complex cryo-feed system had to be installed. Naturally, diagnostic and heating enhancements were also implemented to prepare for the envisaged long pulse operation. Subsequently, a more detailed account is given on the project activities between September 2020 and September 2022.

1.2 Organization

To cope with the massive challenges and to manage schedule and budget, the dedicated project ("Wendelstein 7-X/C", set up in 2015) to a large extent continued to co-ordinate and decide on all activities related to the completion of the machine even beyond January 2022. The reason for this measure was twofold: Firstly, in January 2022 a complex first time commissioning of the ca. 600 cooling circuits induced a challenging new critical path in a very dense schedule. Secondly, a number of project activities, such as the final insulation of the cooling circuits and final diagnostic installations, had to run in parallel to OP2.1 commissioning for technological reasons. Both work packages required a well-drilled organization and communication set up and profited enormously from the extended use of the W7-X/C management set up.

The project organization was described in detail in the previous report [1]. In January 2022 at the end of the main completion phase, the

project organization was adapted to a more institutional character in preparation of the future scientific exploitation of W7-X. However, the longstanding project management set-up stayed in place at least until the end of the W7-commissioning phase in September 2022.

1.3 Plasma Vessel Components

The installation of an actively cooled high heat flux (HHF) divertor, its subcomponents such as cryo pump (CVP), pumping gap panels, bulkheads and baffle upgrades and the corresponding expansion of the associated cooling circuits were at the heart of the plasma vessel upgrades. Experience gained during the installation of the first 70 kg divertor target modules proved reliable until the installation of the last module: The deviation between neighbouring modules (e.g. creation of unwanted steps) did not exceed the specified assembly limit of 0.2 mm thereby fulfilling the specification set by the physics departments. Another formidable assembly challenge was posed by the connections of HHF modules to cooling pipes. The extremely tight installation space behind the divertor required the complicated adaption of hundreds of small pipes, supports, and interfaces. The final flange connection could only be tightened using space-saving tools and careful procedures developed in an extensive preparation program using a.o. a 1:1 "mock-up" of a plasma vessel sector. To minimize the risk of water leaks all connections were leak-tested at 10^{-9} mbar l/s, in some particular critical cases even at Helium overpressure of 29 bar. Overall, the assembly of the ten HHF divertor modules was completed largely according to plan within ca 45 weeks.

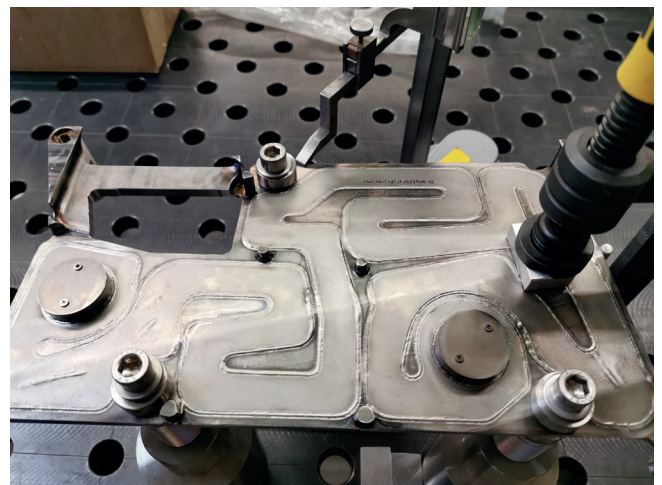


Figure 1. Pumping gap panel after most critical manufacturing step: precise e-beam welding of 3D shaped cutouts onto pre-milled cooling channel.

High precision electron beam welding was required to produce the 60 water-cooled so-called pumping gap panels (figure 1). They cover the gap between the horizontal and vertical divertor targets to protect

the plasma vessel wall from excessive radiation loads. In order to optimize the cryopump operation, ca. 700 individual steel sheets had to be designed, fabricated and installed in well sequenced procedures to seal bulkhead-like the space behind the divertor and the baffles. The sealing was complemented by the industrial procurement and installation of ca. 4000 gap protection grids made of copper steel compound to close pumping gaps between adjacent baffle tiles (figure 2). The grids fulfil a double function: In addition to sealing the divertor region, they limit the plasma radiation shine through on to another layer of in-vessel components or the plasma vessel wall. To back this up, almost 300 critical locations were identified in the baffle and heat shield regions and subsequently equipped with thermocouples (TC). The TC are now available to monitor heat sink temperatures on these locations. Furthermore, the TC signals will be used to provide an interlock with a defined temperature threshold as part of the central fast interlock system (cFIS) for first wall protection during plasma operation. In addition, 130 TC have been installed on water return lines of individual target fingers to assess the thermal loads on the target surfaces (calorimetry).

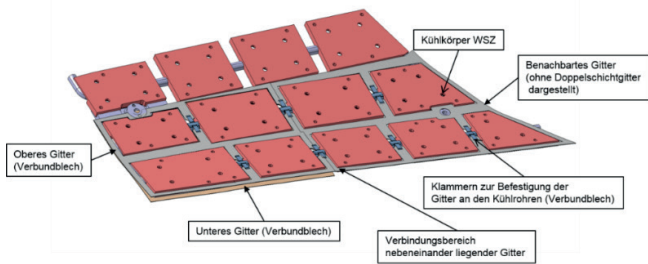


Figure 2. Sketch of typical double-layered gap protection grid made of copper-steel compound to close pumping gaps between adjacent heat sinks.

Essential thermal hardening and protection measures were extended to diagnostic port equipment, too. The ports themselves and diagnostic port inserts (e.g. plug-ins, immersion tubes) underwent a systematic cooling needs analysis. Selected ports were fitted with protection sets (port liners, bellows protection sheets) tailored to the locally expected plasma and ECRH stray radiation loads. The diagnostic inserts were equipped with water-cooled metal or graphite plasma facing heads, of which the former profited from the rapid maturing development of 3D metal printing methods. The relatively small plasma facing diagnostic fronts will eventually have to withstand radiation loads of up to 100 kW/m^2 over 1800 s. Conventional front-end fabrication with cooling pipe coils welded or brazed to copper-coated front plates does not always ensure the needed dense packaging of optical, electrical and other media channels within the available space. 3D-printing is a game changer in this field, as cooling channels can be sized and positioned for optimum cooling performance without compromising the diagnostic functionalities.

Figure 3 shows two development stages of a 3D-printed front for the IR thermography diagnostic, in particular the optimized cooling channel design and a functionality prototype test. Overall, 16 3D printed fronts will now be in operation, providing valuable experience for future thermomechanical designs under cramped conditions.

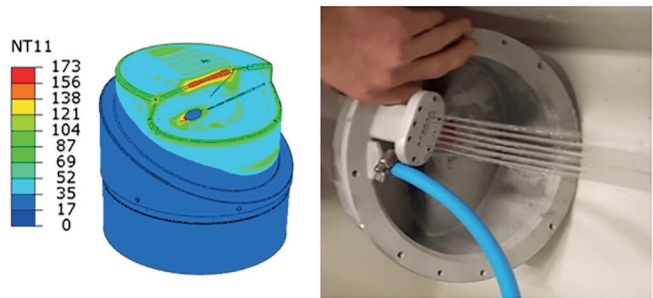


Figure 3. Thermomechanical design analysis of water-cooled head for IR thermography (left); cooling flow test on 3D printed head (right).

Finally, yet importantly, for completing the first wall, ca. 4500 graphite tiles had to be re-designed, position optimised, fabricated and installed. The accomplishment of this task made partial use of scan data of positions of already installed components and could naturally only take place in the final phase of the in-vessel schedule. Among those 4500 were the first ca 20 TZM (titanium-zirconium-molybdenum) tiles with sophisticated surface profiles to dampen ECRH stray light levels. Also, the first 40 tungsten tiles had to be installed to improve the thermal protection vertical baffle areas close to the divertor, after OP1.2 results had shown unexpectedly high heat loads in these locations.

1.4 Operating and Scientific Equipment

The completion of both, the cryogenic (LN₂ and LHe) and the large water-cooling networks were at the centre of operation plant upgrades accomplished during completion (W7-X/C). The complex design, manufacturing and installation of the vacuum-insulated transfer lines and the cryo valve box (CVB), acting as the central cryo distribution and control tool for the planned CVP operation, were procured from German and Dutch industries. The longstanding IPP experiences of contract monitoring and quality assurance paid off and in April 2021, final leakage and pressure tests were successfully completed jointly with the 10 CVP tests. The installation of the CVP triggered the procurement of the final jigsaw piece for the W7-X cryo plant: a capacity enhancement of the LN₂ cooling circuit for the CVP to deliver the required LN₂ over the maximum pulse length of 1800 s. The procurement has been conducted on the basis of a European call for tender and includes a valve box, a sub-cooler box with LN₂-bath, an LN₂-pump, and vacuum-insulated transfer lines. The contract with the Dutch company Demaco is running largely according to plan and the LN₂ network is expected to go into operation in 2023.

To complement this project a second purpose built storage tank was ordered, delivered and commissioned.

The more than 600 subcircuits for cooling the vessel components and the scientific equipment were designed and manufactured largely in-house. This was indispensable since design, fabrication and assembly took place amid increasing constrictions of available space around the torus. Figure 4 gives an impression of the extremely space-optimised cooling network, accommodating also close to 550 volume flow and temperature sensors as well as thermal insulation of all pipes to aid efficient W7-X baking operation. Not surprisingly, the completion of the W7-X cooling system was as critical for the overall project schedule as the installation of the HHF divertor has been. Moreover, first time commissioning of these large cooling circuits induced an additional five months in the pre-operation schedule as it required thorough leak and pressure testing, filling, hydraulic balancing and functional testing of each subcircuit with limited chances to parallelise activities. OP2.1 cooling circuit commissioning was concluded successfully on 15th July 2022.

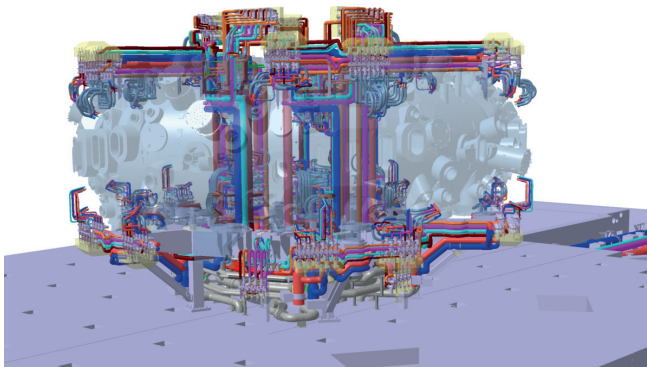


Figure 4. Water cooling and cryo line networks. The water cooling supplies target, baffle and wall circuits, portliners, and diagnostics. Indicated in gray is existing, in colour-code new pipe work..

Details of the ca. 40 diagnostic and heating enhancements during the final phase of W7-X/C are described in the scientific sections of this report. Here, only a short summary is given on the overall project management challenges to steer all enhancements to operational readiness by September 2022. The core task was the design, fabrication, testing and installation of about 100 water cooled diagnostic port inserts, ¾ of which had to be newly manufactured for OP2.1. The different development pace between design and procurement of diagnostic plasma facing components – in order to keep the in-vessel assembly schedule – and the development of the peripheral diagnostic parts presented another particular challenge during W7-X/C. The well-established systematic W7-X design review procedure turned out to be a very effective tool to prevent or mitigate detrimental quality effects from the schedule-dictated diagnostic fabrication process.

In case of important operation diagnostics (e.g. IR thermography units of divertor, divertor gas inlets and NBI heat shield thermography units) extremely close monitoring was necessary to ensure timely installation. A highlight of well-organised logistics amid limited personnel resources was the series vacuum hot leak testing of 35 diagnostic units, accomplished in-time in October 2021. In anticipation of the congested project end phase two test tanks had been converted and assembled from unused W7-X ports.

Last but not least, a third diboran decomposition device was pre-assembled in house and installed in-time to improve the boronization capabilities of the upcoming W7-X operation phases.

2 Wendelstein 7-X Commissioning and Operations

Head: Prof. Dr. Hans-Stephan Bosch

2.1 Vacuum

In MP2.1 the vacuum team supported intensively the assembly of in-vessel-components and diagnostics by performing leak tests. Approximately 4500 seals and joints of pipes and flanges have been checked. Special focus has been laid on approx. 500 CF vacuum joints, which are assembled inside of the vessel and will be operated at pressures of up to 26 bar and temperatures of up to 150 °C.

Pump down of plasma vessel (PV) and cryostat started end of January 2022. No major leaks at the cryostat occurred. After repair of some leaks, commissioning of PV and cryostat could be completed on begin of March 2022 with achieving a final pressure of less than 1e-6 mbar in the PV and approx. 2e-4 mbar in the cryostat.

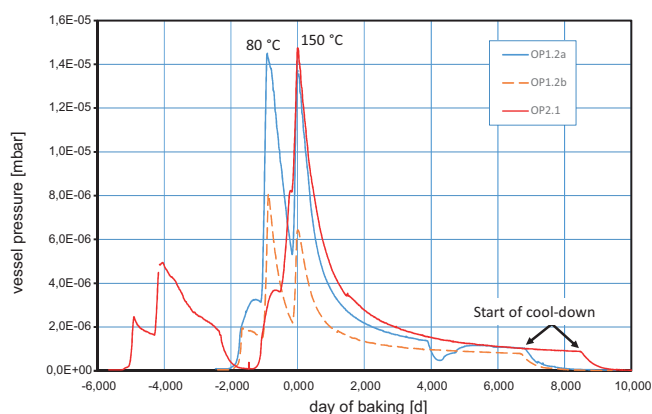


Figure 5. Pressure of Plasma Vessel during baking. The baking period of seven or more days starts with reaching 150 °C inside the Vessel (indicated by the red bar). The pressure at the end of baking is very similar for all commissioning processes, independent of the number of new installed components inside the VV.

Baking of the PV has been successfully performed in August 2022 (for PV pressure plot see figure 5). During and after baking no indications

of a leak at the PV could be detected. Due to the high number of new components installed inside the PV during MP2.1, more outgassing had to be handled in comparison to previous baking processes. The vessel pressure after cool-down is slightly lower than in previous campaigns and promises a good base for upcoming experiments.

For a more robust working process and a higher throughput in the boronisation process in OP2.1, a 3rd diborane-decomposer has been integrated in one of the present vacuum units of the PV. The new decomposer has been successfully tested during a boronisation test run in He at 9th September 2022. First boronisation is foreseen for mid of November 2022.

In 2021/22 a detailed maintenance of the components and sub-assemblies of the central gas supply system has been performed. Finally, the interaction between the gas supply and the segment control system of W7-X has been checked in collaboration with CoDaC. In addition, the divertor gas supply has been integrated in the central gas supply system.

2.2 Magnets and Cryo Systems

2.2.1 Superconducting Magnet System

The superconducting magnet system, the associated power supplies and the magnet protection system worked reliably during the first campaigns between 2015 and 2018. Nevertheless, aging effects required more and more effort in terms of maintenance and repair. Due to the age of more than 20 years the procurement and stocking of spare parts, the qualification of new components and system maintenance were the main focus of the work in this operation break. It was still possible to stock up on some discontinued spare parts, but more and more redesign solutions were necessary to replace out dated components.

The commission of the superconducting magnet system for OP2.1 started in July 2022. The current in the seven coil circuits was increased step by step, finally reaching the required magnetic configurations. Associated high voltage tests at room temperature as well as at cryogenic temperature confirmed the required voltage strengths of the insulation. New magnetic configurations will be commissioned according to the needs of the experimental program.

Control Coils

Updates and upgrades: The power supplies for the control coils can deliver DC currents of up to 2.5 kA and in addition ac currents of up to 625 A with frequencies between 1 and 20 Hz. Based on experiences during the first three operation phases, substantial modifications and improvements of the performance of the control coils power supplies have been implemented.

Commissioning for OP2.1: In preparation for the experimental phase of W7-X the power supply was tested with a dummy load and later on together the real control coils. Some adjustments had to be made.

Trim Coils

For the commissioning of the trim coil system, a dummy load and associated cooling system has been designed and installed in order to gain more flexibility for the operation of the power supplies. The commissioning of the trim coils with full power for the first time was 2.1 successfully.

2.2.2 Cryo Supply Refrigeration Plant Maintenance

Maintenance work on the refrigeration plant was continued. The two screw compressors had to be realigned on the concrete foundations. The aim here was to minimize vibrations and bearing loads by precisely aligning the compressors with the electric motors. Afterwards, the functionality of the compressors was checked by means of a test run.

After the complete reassembly of all components, which were disassembled during maintenance, the helium circuits were cleaned by evacuating and refilled with helium for several times. In the last step, 7500 Nm³ of helium gas were refilled into the gas storage tanks.

Operation Scenarios with Cryo Pumps in Cooperated

The helium refrigeration system needs to be operated differently when cryo pumps are in use. The cooling of the CVP and the cooling of the W7-X cryostat (with magnet system) are closely connected: Cool-down as well as the warm-up of the cryo pump takes place when the cryostat is cold. The return gas quantity and return gas temperature from the cryo pump must be limited during cool-down such that the temperature profiles in the refrigeration system are not shifted. Therefore a new procedure was developed and commissioned successfully.

The thermal shield for the CVP is cooled with liquid nitrogen (LN2). In order to be able to set the desired temperature for the cooling process, the liquid nitrogen flow from the LN2-tank will be evaporated. The heat exchanger used for evaporation, also connects the helium circuit in the cold box. Therefore, the helium and the nitrogen temperatures connected. This requires a balanced operation and therefore limits the available evaporation rate for the nitrogen gas. The optimization process is ongoing for the refrigerator operation. The goal is to minimize the impact on the organization of an operating day when using the cryogenic pump.

Commissioning Cryo System and Cool Down

The cryo system was put back into operation 2022. The new components (transfer lines, valve box and cryo pumps) were first purged with nitrogen and then with helium. Then the components were evacuated several times and refilled with helium. After cleaning of all cooling circuits, cooling of the W7-X cryostat was started. Cool down proceeded without major problems within four weeks. In a next step, the 10 cryo pumps with connected supply lines and valve box were

cooled down. In contrast to the cryostat cooling, the thermal shield of the cryogenic pumps is cooled with liquid nitrogen at 80 K, while the pump panels are operated at 4.4 K. The first cooling of the entire CVP circuit required two days. The process was then optimized such that the cryo pumps cool down to operating temperature within 24 hours. Warm-up to room temperature was achieved within 24 hours as well. The thermal cycle for regeneration requires 1 h for warm-up to 30 K and 2 h for cool-down to 4.4 K.

2.3 Codac

IT Security and Data Handling for OP2.1

The long completion phase before OP2.1 was used to implement a comprehensive IT security plan in order to find the appropriate balance between operability and IT Security. The experiment network is now fully separated from the internet, as well as from the other network zones of the institute. Per design, access to the experiment network is only possible from the control room. The IT infrastructure is predominantly based on virtualization. This means, that in all instances where this is possible, virtual machines run on the centralized infrastructure of the datacenter, benefiting from both central management as well as the flexibility that this kind of infrastructure offers. In order to facilitate the daily life of the operators and scientists in the control room, a split architecture has been derived that allows independent access to both virtual experiment machines as well as to virtual office machines (with internet access) from the same workstation inside the control room without allowing direct communication between them.

The data handling requirements for OP2.1 made a second extension of the data archive system necessary. It became clear that the originally foreseen data rate of 20 GB/s would be significantly exceeded in reality, primarily due to the new camera systems installed to protect the actively cooled divertor. The IT completed a project which doubled the streaming capacity of the network to 40 GB/s and tripled the data storage capacity. In combination with the real-time data compression, which will become standard for most high bandwidth systems at W7-X, this should be sufficient for the next few years.

Systems Integration

The central safety and interlock systems were completely re-designed during CP 2. A significant number of new requirements had to be implemented. One of the lessons from the previous campaign that influenced the final design was that the use cases of machine commissioning and scientific operation are very different and require a number of different operating regimes for the safety system in order to support parallel commissioning activities as best as possible. The fast interlock system nearly doubled in scope due to the actively cooled divertor and inner wall. This required both a significant enhancement in terms of functionality as well as a complete change in hardware architecture. All these projects were completed on budget and on time. The CoDaC division integrated more than 30 new or

significantly enhanced diagnostic systems, nearly doubling the previously supported systems. In previous experimental campaigns, a number of diagnostics could not be integrated into the central infrastructure and ran on a parallel control and archiving system based on MDSplus. Now an interface to the central infrastructure has been implemented, which allows a full integration of the component in terms of control, archiving and timing but leaves the data acquisition to the individual diagnostic. This will greatly facilitate experimental operation in OP2.1., and the use of the MDSplus parallel infrastructure is discontinued. Divertor protection was one of the major tasks for the CoDaC division in CP2. More than 20 high-speed cameras of four different types had to be integrated. In order to propose a standardized solution, an MTCA-based standardized camera interface was developed. This will allow the integration of any industry standard camera without the need for bespoke hardware and software. This is also the ITER preferred solution for cameras. In order to address the high data rates produced by state of the art cameras, a lossless video compression algorithm was developed together with collaborators from the Google company and integrated into the W7-X software infrastructure. The algorithm allows for a 50 % data rate reduction and is transparent to the user. Compression happens at the source and decompression is done within the API while reading data. Hence, the user does not even realize that data was compressed without loss during transport and storage.

CoDaC Infrastructure

The real-time control system had to be re-designed as well. The original VxWorks based architecture was re-worked and ported to a real-time linux infrastructure. This makes the implementation of the current requirements possible and furthermore provides enough flexibility to cope with future real-time control requirements. Another major task of was the re-design of a core component of the heart of the CoDaC infrastructure, the segment control system. The original design dating back 20+ years did not take into account the number of segment-controlled components required for a discharge in OP2.1. This made significant changes in the underlying database architecture as well as the business processes (e.g. parameter transformations, consistency checks or distributed experiment preparation) of the segment control system necessary. As these changes affect the fundamental components, significant effort was required to propagate them through all components of the segment control system.

2.4 Device Operation

2.4.1 General Control Room

The control-room for W7-X was modified to have more seating places (86 instead on 60), and to have additions info screens. Due to the Corona pandemics, only 53 seats are allowed to be used. Also, the operation team in the control room had to be reduced.

Electronic Documentation

As the, 2004 introduced, documentation system (Agile PLM) is not state of the art anymore and the demands of W7-X have changed, it was decided to change to IDM. The ITER IDM was tailored to the specific needs of W7-X.

1.1.1 Operational Plans and Procedures

Magnetic Field Scenarios

W7-X has 70 superconducting coils of seven types. For operating W7-X, all ten coils of each type are connected in series. Seven independent power supplies offer a wide range of magnetic configurations (characterized by iota, shear, magnetic well/hill, inward-/outward-shift, and toroidal mirror ratio). A new database has been developed for requesting, reviewing and releasing new magnet configurations to be used during experiments.

Session Planning

For each campaign, a large number of physics proposals is usually submitted. These proposals are boiled down and grouped to half-day sessions, during which a specific plasma program is conducted. Also for this purpose a new database was developed. This database provides a central platform for submitting, reviewing and releasing the half-day sessions. It enables the operation team to review upcoming sessions regarding requirements for pulse length, heating power and magnetic configurations and assess their feasibility.

Increasing the Heating Energy in the Plasma

The specification for OP2.1 foresees an integrated input energy into the plasma ($\int P_{\text{heat}} dt = W_{\text{input}}$) of W7-X of up to 1 GJ. As in previous campaigns, for increasing W_{input} , an organizational and formal process is implemented for the increase in well-defined steps. This has to be conducted for each magnetic configuration separately, as the wall loads and their distribution depend very strongly on the shape and the position of the plasma. The limiting criteria to get to a higher level of W_{input} are temperature levels of the divertor components (observed by IR thermography) and of the heat sinks on target, baffle and heat shields, NBI beam-dumps and on diagnostics, as well as the occurrence of hot spots on the plasma vessel.

Device Safety

The central safety system (cSS) of the Wendelstein 7-X is designed to follow the safety life cycle according IEC 61511. Based on the individual safety analyses of each component and the safety analysis for the W7-X, safety integrated functions (SIF) were defined. After OP1.2b a full re-design of safety instrumented functions (SIFs) was performed. To protect diagnostics and components inside the plasma vessel a central fast interlock system (cFIS) was developed and already in operation during OP1.2. For OP2 (actively cooled first wall components) the cFIS was expanded in terms of functionality as well as a complete

change of the hardware architecture. Additional thermal sensors and IR observation were included in the cFIS logic to provide suitable first wall protection during plasma operation.

Wendelstein 7-X Science

Heads: Prof. Dr. Thomas Klinger, Prof. Dr. Thomas Sunn Pedersen, Prof. Dr. Robert Wolf

The focus of the last years was on the completion of Wendelstein 7-X, implementing actively cooled in-vessel components and, in particular, an actively cooled high heat flux divertor for steady-state power exhaust. In parallel to this major intervention, the scientific results achieved during the first operational campaigns (OP1) were consolidated. This included a better understanding of the ion-temperature clamping, the mechanisms for overcoming it by means of density peaking, plasma exhaust and divertor detachment and transport and stability studies. In a strategy process further upgrades of Wendelstein 7-X were defined. Main elements are the extension of the heating power and the development of a tungsten divertor concept. In addition to the upgrade of diagnostic and heating systems, the expansion of the ECRH power already started. Moreover, the coverage of the first wall with tungsten was significantly increased for the up-coming campaign.

1 Stellarator Heating and Optimization (E3)

Head: Prof. Dr. Robert Wolf

1.1 Core Plasma Performance and Characteristics

During the period between the end of the first operation campaigns (OP1) and the beginning of this year's plasma operation scientific results and their initial interpretation were consolidated. The most prominent result was the discovery that in gas fuelled ECRH plasmas the ion temperature is clamped, while peaked density profiles via pellet injection lead to a breaking of this temperature limitation. Although achieved transiently, these plasmas showed the highest triple product achieved in stellarators so far and were instrumental in verifying the optimization of the neoclassical transport [1] underlying the W7-X design. Comparing typical gas fuelled ECRH plasmas with those exhibiting peaked density profiles, it becomes evident that typical ECRH discharges show a high level of anomalous transport, while in those with peaked density profiles the ion transport is reduced to neoclassical levels in the plasma core [2]. The strong anomalous transport and the clamped ion temperatures can be characterized by stiff ion temperature profiles in the central part of the plasma. The normalized ion temperature gradient decreases with increasing heat flux, which is explained by ITG turbulence and its dependence on T_e/T_i in the electron heated plasmas [3].

First neutral beam experiments on W7-X revealed a distinctly different behaviour compared to ECRH plasmas [4]. Most striking was the continuous increase of the central plasma density with NBI, which was stopped or even reversed by adding low levels of ECRH power. The density increase was accompanied by steep density gradients at half radius similar to a transport barrier and an increase of the carbon impurity content. In these NBI plasmas the spatial and temporal evolution of the carbon concentration is consistent with neoclassical predictions, not requiring any anomalous contributions to describe the behaviour during the density rise (see figure 1).

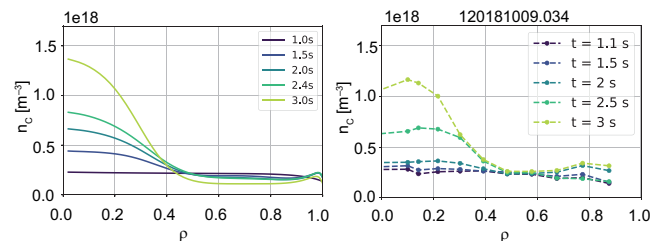


Figure 1. Simulated carbon densities assuming neoclassical transport (using the STRAHL code, left) and corresponding experimentally obtained carbon densities for a plasma heated purely with NBI (right).

The design features of the W7-X optimized configurations include low magnetic shear, low toroidal plasma currents, and a low order edge resonance giving rise to the edge island structure of the island divertor. One disadvantage of such configurations is their sensitivity to plasma currents, such as the bootstrap current or external current drive. In order to investigate the possibility to compensate the effect of the bootstrap current on the divertor topology, electron-cyclotron current-drive (ECCD) was investigated. Sawtooth-like oscillation of the electron temperature were observed. The ECCD drives a core current density resulting in a core crossing of $\iota = 1$ which is accompanied by $(n/m = 1/1)$ mode activity. In cases where the sawtooth oscillations are particularly strong, they lead to a significant confinement degradation or even to a complete loss of the plasma [5]. In order to better understand the underlying mechanism of these events, a Motional Stark Effect (MSE) diagnostic is being developed to provide measurements of the ι -profile.

An underlying goal of the W7-X project is to establish the extrapolation of W7-X results to fusion power plant. For the better understanding of the integral characteristics of a fusion power plant, the systems code PROCESS was adapted to include the features of a stellarator reactor based on a direct extrapolation from W7-X. In a more recent modification of the code, the description of stellarators was extended to a more general class of stellarators [6]. More details about this work are given in the chapter DEMO Design Activities.

1.2 Core Diagnostics Development towards Steady-state Plasma Control

Profile diagnostics are continuously developed for discharge control, eventually providing radial profiles of electron density, and electron- and ion-temperatures in real-time. The Thomson scattering system was upgraded to three YAG lasers resulting in nearly 10 ms time resolution in standard operation. A fourth YAG laser with longer wavelength but using the same optics was prepared [7]. With this addition, two-frequency Thomson scattering will be evaluated in the upcoming campaign. Advantages are an extended accuracy at higher values of T_e using the same set of detection filters and the possibility of an in-situ calibration of the T_e measurement.

Moreover, in particular the large scatter of the Thomson density measurements of the past campaigns should be reduced by a new active control of mechanical drifts over the long transmission lines and a new method of laser beam position dependent Raman calibration taking the jitter of the beam pointing direction into account [8].

Regarding already recorded density data, the scatter could be reduced significantly assuming that it can be attributed to systematic movements of the laser position crossing the plasma vessel. In-situ spectral calibration, including the observation windows, was implemented using a tuneable laser. The use of the Thomson sightlines for bremsstrahlung measurements is being prepared in a collaboration with the Akademia Morska Szczecin. Moreover, a project for real-time Thomson scattering was launched together with the Princeton Plasma Physics Laboratory (PPPL).

Real time control of density profiles will be addressed by supplementing the successful dispersion interferometry by a multichannel interferometer with four additional channels in a first stage. For high-resolution edge density measurements a density profile reflectometer integrated into the ICRH antenna was prepared together with Research Centre Jülich (FZJ).

Plasma operation in W7-X is aiming at plasma densities above 10^{20} m^{-3} , where the neoclassical transport optimization is most effective. For this purpose, W7-X is equipped with an elaborate multi-pass ECRH scheme for using the 2nd harmonic O-mode with low single pass-absorption to access densities above the X2 cut-off in the range of $1.2 - 1.8 \times 10^{20} \text{ m}^{-3}$. Long-pulse operation O2-ECRH requires qualification of windows, as they will be exposed to higher levels of non-absorbed microwave stray radiation.

For operation at densities above the $1.2 \times 10^{20} \text{ m}^{-3}$, where the optically thick X2-ECE is running into cut-off, a radiometer for measuring T_e is in preparation, using the optically grey 3rd harmonic. This will be supplemented by the now permanently installed Martin-Puplett interferometer simultaneously scanning the 2nd and 3rd harmonics of the ECE spectrum with a lower frequency / spatial resolution [9].

For the X-ray imaging system, providing continuous line integrated T_i and impurity information, an absolute wavelength calibration will allow to derive improved measurements of the Doppler shift and subsequently the radial electric field. Also the question of the accuracy of the inferred plasma parameters was further investigated [10].

Steady-state capable cooled observation systems were installed for core charge-exchange-recombination spectroscopy (CXRS), observing the heating neutral beams (NBI). The combination of these sightlines provides beam emission and CXRS spectra, measuring profiles of T_i , E_r and various low-Z impurities [11].

An assessment on the improved fast ion confinement necessary for a reactor and one of the optimization criteria of W7-X must be addressed with a variety of diagnostics probing the phase space of fast H-ions created by NBI or ICRH. Measurement of the fast ion birth profiles, distribution function, and wall loads are key to this assessment.

Required are in particular the fast ion birth profile, slowing down and finally the resulting localized wall loads. Aside the fast ion H-alpha spectroscopy, a steady state capable very flat Faraday cup detector was built as a prototype. At a later stage, arrays of these are planned to be integrated in wall tiles at critical locations. A scintillator-based detector being developed by PPPL will be installed nearby for cross comparison [12]. A prototype for an infrared wall observation of critical locations is under design. Altogether, the fast ion physics relies on comparison with code calculations as a full coverage of plasma and vessel components is beyond the capabilities.

Finally, a modular data-analysis-scheduler software was developed, aiming at an automated inter-shot or overnight analysis of the most important plasma parameter and profile data. The upcoming experiments (OP2) will be used to commission and test these further developed systems, approaching on the one hand, long-pulse operation and, on the other hand, advanced plasma control. For efficient profile analysis in OP2, a WEB-based profile-fitting tool (Profile-Cooker) was constructed, which automatically builds a database of profile fits of n_e , T_e , T_i etc. with elaborate error analysis. These profile fits provide an input for a new WEB-based power-balance tool enabling neoclassical heat flux calculations and subsequently the calculation of the anomalous transport component on the spot, which helps control room decision making and further detailed transport analysis.

1.3 An Electron-Cyclotron-Resonance Heating (ECRH) System for High-power Steady-state Operation

Achieving the scientific goals of W7-X requires an increase of the heating capacity. For the ECRH, a gradual increase of the output power from now $\sim 8 \text{ MW}$ to ultimately 18 MW until 2030 is planned [13]. The first step is the development of a 1.5 MW gyrotron in collaboration with KIT and Thales Electron Devices. Based on the existing 1 MW design, a 1.5 MW prototype gyrotron was built, preceded by successful tests of a short-pulse version at KIT with the new design features [14]. If the higher power can be verified also for long-pulse operation, the plan foresees the gradual replacement of the older gyrotrons by the more powerful ones. 18 MW can only be achieved if a further increase of the unit power can be realized. The installation of additional gyrotrons at W7-X also required the expansion of the ECRH plant from 10 to 12 positions, which was realised by building the new (so-called F5 gyrotron) position and a new beam line for microwave transmission to the plasma vessel. The installation of the 12th position (F1) is ongoing.

The experiences from the previous experiments and the perspective of higher gyrotron power require an improvement of the microwave transmission. For this purpose, a high-performance air-drying system was installed in the last section of the quasi-optical transmission line, reducing the relative humidity down to 10 %. This resulted in a reduction of atmospheric absorption and a higher electrical breakdown strength, which was already demonstrated in a dedicated high-power transmission experiment.

As a further upgrade with regard to the efficient use of the available installed gyrotron power for plasma heating, the O2 multi-pass scenario for operation at densities beyond 10^{20} m^{-3} was improved. To avoid holographic gratings with finite efficiency and limited polarization matching capabilities, slightly off-axis beam passes were chosen for 8 of the 12 possible beamlines realizing again a triple beam-path scenario in combination with the original surface geometry opposite to the ECRH launchers. For this reason, polarization gratings could be used on the flat reflector tiles at the inner side of the plasma-facing wall, avoiding the generation of X-mode components after the first pass, which would be in cut-off for the envisaged densities.

A high-resolution CTS diagnostic, which is supposed to be particularly sensitive to fast ions, does not work with the high background of thermal ECE at 140 GHz, because the ECE intensity is up to two orders of magnitude higher than the intensity of the scattering signal. Therefore, the scattering frequency is placed in the minimum of the ECE spectrum at approximately 175 GHz between the second and third harmonic ECE. In addition to changing the detector frequency from the former 140 GHz to the 175 GHz range, the scattering gyrotron in particular must be tuned to the 175 GHz frequency range. In collaboration with KIT, the corresponding operational parameters were determined [15], although the selected gyrotron initially was not designed for this parameter range. As part of the replacement of an outdated gyrotron magnet with a high LHe consumption, a modern cryo-free 7.1 T magnet was procured, meeting the resonance condition for the excitation of the corresponding gyrotron modes around 175 GHz. With this, the predicted mode (TE_{34,10}) at 174 GHz could be excited with 300 kW output power.

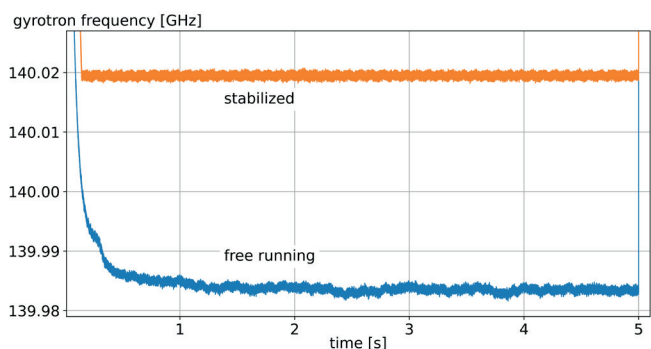


Figure 2. Time traces of the frequency of a high power gyrotrons with and without frequency stabilization showing clear the effect of the phase-locked-loop without any visible drift of the gyrotron frequency.

Furthermore, in cooperation with KIT, a frequency stabilisation and control of the high-power gyrotrons based on a phase lock loop (PLL) was realised for the first time (figure 2). While the frequency of the freely running gyrotron changes by 40 MHz, stabilizing the frequency no longer indicates any shift within the noise level. An important application of this result is an improved CTS diagnostic, which has both

a favourable signal-to-noise ratio and gives access to the scattering spectrum very close to the scattering frequency [15].

Preparing long-pulse operation in W7-X and ITER, stray radiation exposure experiments were carried out with the MISTRAL facility, mimicking the effect of non-absorbed microwave power on in-vessel components and diagnostic interfaces such as vacuum windows. Stray radiation losses in vacuum windows can now be computed accurately using permittivity and loss tangent values as measured in low-power experiments. The stray radiation response of microwave absorbing coatings was measured and modelled as a function of thickness. ITER-developed stray radiation windows sensors, that use such coatings, were characterized [16, 17].

1.4 New Ion-Cyclotron-Resonance-Heating (ICRH) System for Wendelstein 7-X

In a larger collaboration with FZJ and the École Royale Militaire, Brussels, (ERM/KMS) a new ICRH system was designed, constructed and installed at W7-X [18]. For this purpose, two RF generators, formerly used at TEXTOR, were refurbished and upgraded. The installation of the transmission lines and the matching system for the initial operation of one generator was completed. A new two-strap antenna was designed, fitting in one of the larger W7-X ports and matching the 3D shape of the plasma boundary. After successfully testing the antenna at FZJ, all the components were delivered to W7-X. Meanwhile, the ICRH system is fully integrated into the W7-X infrastructure, including water-cooling, high voltage and gas supplies, and data acquisition and control. Installed on a rail system outside the plasma vessel, the antenna head can be moved radially, allowing the adjustment with respect to the actual plasma boundary and thus optimization of the wave coupling to the plasma.

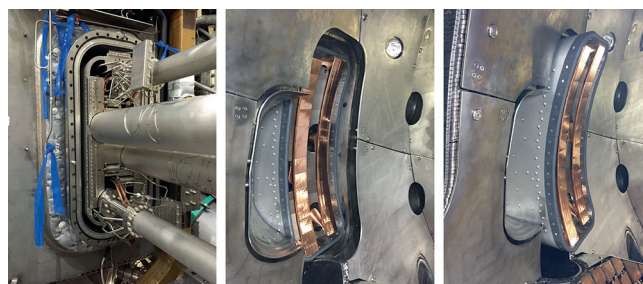


Figure 3. ICRH antenna head, seen from outside the cryostat/plasma vessel (left), from inside the plasma vessel in a retracted position (middle), and in a position moved radially towards the plasma (right).

Figure 3 shows the installed antenna head. In the picture on the left, the view is towards the cryostat/plasma vessel. In the middle picture, the antenna can be seen in a retracted position, which is taken when ICRH is not needed. For applying ICRH, the antenna can be moved towards the plasma, as seen in the picture on the right. This system is expected to generate $\sim 1.5 \text{ MW}$ of ICRH at frequencies between 25 and 38 MHz.

1.5 Increase of Neutral Beam Injection (NBI) Power

Already during the first operational phase, (OP1) NBI heating was successfully applied, using one injector box and two beams with 55 keV hydrogen injection. For the upcoming campaign (OP2) the NBI system was extended to two boxes and four beams, together delivering ~ 7 MW of heating power. The extension of the NBI system was accompanied by a complete revision of the safety system, the integration of the second beam box in the control, gas supply and high voltage subsystems. Meanwhile the re-commissioning of the previous injector box and the new commission of the second injector box is well underway. To prevent damage to the inner wall of W7-X, which is where the beam not absorbed by the plasma is deposited (beam dump area), a two-colour pyrometer based safety system was redesigned, newly built, installed and integrated into the new, cwcapable NBI safety system for the plasma vessel protection.

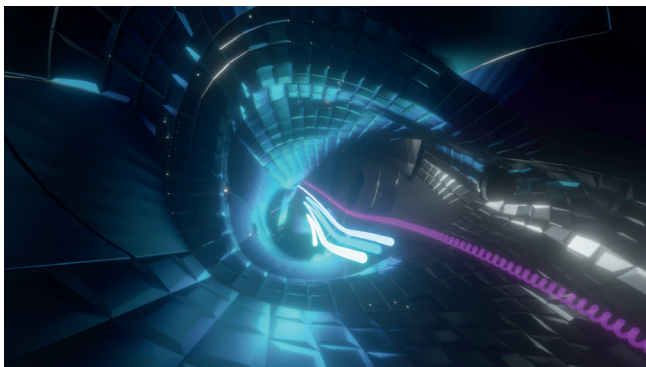


Figure 4. Visualization of a NBI fast ion gyro orbit in Wendelstein 7-X as simulated by ASCOT5/BEAMS3D. The trace shows how a passing particle can transition into a trapped orbit and begin precessing poloidally.

One of the scientific goals of W7-X is to demonstrate the increasing quasi-isodynamic behaviour of fast ions with increasing plasma beta. As plasma beta increases in the high-mirror configuration collisionless drift surfaces are predicted to close, enhancing the confinement of deeply trapped particles [19]. Work to develop an array of fast ion loss detectors for W7-X showed that the NBI generated fast ions do not exhibit this behaviour [20] (see also figure 4). The NBI system on W7-X does not populate the deeply trapped orbits necessary to assess this effect. Modelling work is underway to assess the possibility of couple ICRH and NBI for this purpose. Simulations suggest NBI fast ion losses to the ICRH antenna are within acceptable limits. Experimental fast ion wall loads were shown to be significantly smaller than those predicted by simulations [21]. Two proposed mechanisms for the lack of wall loads are the neglect of a scrape-off layer and the neglect of charge exchange in simulations. Work is underway at Aalto University to assess the effect of including a SOL in the fast ion simulations. Complimentary work at CIEMAT is helping to better

understand the role of charge exchange losses in the calculations. Both works are part of ongoing collaborations between the W7-X and the ASCOT team. Still it should be noted that the NBI system on W7-X has proven itself as a reliable source of ion heating in W7-X, allowing achievement of the highest plasma densities yet achieved in the experiment [4]. Work is currently underway to provide post shot fast ion density, heating, and current profiles for experimental purposes.

2 Stellarator Edge and Divertor (E4)

Head: Prof. Dr. Thomas Sunn Pedersen

2.1 Pellet Injection

Deep particle fuelling is a pre-requisite to accomplish good energy confinement, and it can provide the access to fusion relevant discharge scenario, as for instance detachment of the edge plasma with reduced core turbulence and minimized heat load to plasma facing components. A new continuous pellet injector is now installed on W7-X, having the capability of injecting high-speed pellets (of up to 1000 m/s) deep into the core plasma, even for discharges of up to 30 minutes length [22]. The pellet particle fuelling rate of up to 10^{22} particles/s is chosen high enough to guarantee for the ability of rapid density built-up, even if the envisaged enhanced divertor pumping capability of up to 106,000 l/s is taken into account. This high pumping speed is obtained by the use of new cryo-pumps inside the divertor pumping chambers. Only injection from the magnetic low-field side will be realized, because earlier experiments showed that the benefit of magnetic high-field side injection is only marginal, taking the enhanced technical efforts into account which are required for the high-field side. In order to specify the technical requirements for this new pellet injector appropriately in synopsis with the plasma requirements in W7-X, numerical code calculations for the pellet ablation and subsequent particle deposition are performed. This is done for a vast variety of plasma discharge conditions and pellets parameters. Hence, the optimum specifications for the new pellet injector could be revealed, which was built within the framework of an international partnership between the Princeton Plasma Physics Lab, the Oak Ridge National Lab, the Japanese National Institute for Fusion Science and the Max-Planck Institute for Plasma Physics.

2.2 Edge Spectroscopy

Coherence Imaging Spectroscopy (CIS) monitored the C^{2+} flow velocity and line-emission intensity throughout the entire OP1.2b campaign. Analysis of a large fraction of the experiments shows strong relationships of the measured quantities with varying plasma parameters. Both the impurity velocity and emission intensity are influenced by the SOL densities and are not directly affected by the input power, in both attached and detached conditions. The CIS diagnostic has been updated to meet the new technical requirements of OP2, e.g. the toroidal observation system has been moved to another port.

Additional CIS hardware at the vertical view is being developed for OP2.1 for the measurement of ion temperatures in the SOL. Two of four planned divertor spectroscopy endoscopes have been installed at two inner diagnostic ports AEL30 and AEL51. The systems will provide vertical view on the horizontal and tangential view on the vertical divertor targets close to the position of the helium beam injection. Plasma emission will be recorded by five filter cameras and several spectrometers at each endoscope. Spectroscopic observation at four additional perpendicular ports AEI30/51 and AEF30/51 was already setup in the last campaign OP1.2 and is being extended by additional spectrometers for the upcoming campaign OP2.1. Tomographic reconstruction of CIII emission in the divertor using Gaussian Process Tomography in the Bayesian modeling framework Minerva shows strong localization of the radiation at the separatrix and close to the X-point location in detached plasma conditions (see figure 5).

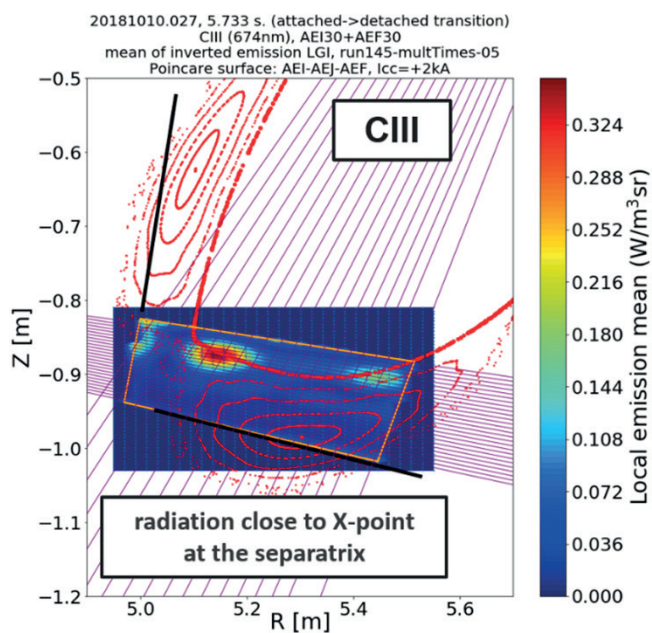


Figure 5. Tomographic reconstruction of CIII emission in front of the divertor for detached conditions.

Collisional radiative model for atomic helium has been implemented in Minerva to study the impact of several uncertain atomic model parameters on the inferred n_e and T_e values in the divertor plasma: of the recently calculated new set of the electron-collision excitation and ionization rate coefficients, proton and charge exchange collisions as well as the magnetic field effect on level mixing. Analysis of highly resolved spectral lines of hydrogen and some impurity lines (e.g. CIII) was done with consideration of Zeeman and Stark splitting effects. At least three populations with different temperatures of atomic hydrogen as well as some capabilities of the emission localization by utilizing

the map of magnetic field strength at the emission zone were demonstrated. Minerva Bayesian inference model has been developed to infer Z_{eff} profiles from the visible and near IR spectra recorded with the single and multichannel diagnostic systems. For the next campaign OP2.1 few new lines of sight have been added to sample the visible bremsstrahlung tangentially and slightly inside of the separatrix in order to improve the Z_{eff} inference accuracy at the separatrix.

2.3 Magnetic Topology and Edge Profiles

With the integration of the new HHF divertor starting with OP2 a new Langmuir probe system had to be prepared as well. The new system consisting of in total 36 fast reciprocating probes, stellarator symmetrically distributed in the upper/lower horizontal targets in module No. 5, was simultaneously installed in that divertor module. For OP2.1 a preliminary operation of the diagnostic is foreseen, applying other measuring principles and full CoDaC support are anticipated for later operation campaigns. At the alkali metal beam diagnostic some initial spectral investigations were carried out in the OP1.2b campaign with the aim of identifying line transitions suitable for the local determination of T_i via CXRS at the ion beam. After evaluating the data, a second system for the observation of CIII transitions was proposed and constructed by the Hungarian colleagues from EK-CER, suitable for the determination of radial T_i profiles in the plasma edge. The light is focused on a fibre array with a total of 136 fibres and then directed to a high-resolution spectrometer. The system allows also the future integration of additional optical diagnostics. In addition a new quasi-Bayesian linearized reconstruction algorithm for fast density reconstruction has been developed.

For the magnetic flux surface diagnostic, some in-vessel repair was required. Furthermore, the planned connection of the in-vessel frontend and shutter to the cooling water supply was finalized. For future observation of the manipulator AEV30 the camera has to be moved from port AEQ21 to AEA21 for which an additional mechanical adapter was manufactured.

For the divertor manipulator project MATEO, which is a cooperation with Forschungszentrum Jülich (FZJ), the 3D models of the manipulator, the port adapter and vacuum barrier as well as the media supply, the location of the control cabinets and the cable routes were created and the installation concept was discussed. On the part of FZJ, a sample manipulator including the associated control system is currently being set up. Preparatory work in the torus hall, such as the measurement of the port and the procurement of a transport platform, is planned for maintenance phase MP2.2. However, due to resource constraints the installation of the manipulator with uncooled head is now planned for OP2.3.

2.4 Concept Development W Divertor

The ambition of W7-X to prove that a stellarator is a viable path towards a nuclear fusion reactor requires the demonstration of high performance plasma operation with plasma facing components with minimal tritium retention, i.e. carbon free in-vessel components.

In 2021, a temporary working group delivered a roadmap towards an exchange of the current CFC based divertor with a new tungsten based divertor. Alternative strategies like coating the existing CFC divertor with tungsten or coating and re-use of the TDU were rejected. Following this roadmap, a new team was established in E4 starting in 2022, dedicated to make a concept of a new water cooled divertor including baffles with a detailed schedule and resource estimate as a basis for a major go / no go decision for such exchange in 2026. In the framework of installing a completely new divertor, the team aims for an optimization of the plasma facing geometry to improve the exhaust, reduce thermal overloads and simplify manufacturing and installation. It means that besides a new design for the divertor and baffles, also pumping gap panels, and if needed poloidal and toroidal closures, will be redesigned. Other in-vessel components like the cryopumps, control coils and water supply infrastructure are assumed to remain unaffected.

For the optimization of the plasma facing geometry and the shape of the pumping gap, a tool is being developed to describe the magnetic flux surfaces of the core and islands for vacuum and non-vacuum fields in Fourier components, which can be directly transformed into a CAD file. With these CAD models of the magnetic field, the intersection between the plasma and the target geometry can be directly determined. In addition, tools are under development to enable a two-way exchange between CAD and plasma physics models like EMC3-light, which allow for a fast modification of geometry in CAD as input for EMC3 and vice versa, a direct plot of heat load output from EMC3 onto components in CAD. Also, simplified geometries of the sub-divertor room have been established to enable a fast and parametric modelling of the neutral gas flow.

The structural design of the target aims at a flat tile technology existing of a CuCrZr heat sink with a tungsten based top surface and a steady state heat load capacity of 10 MW/m^2 , similar to the existing CFC divertor. As an improvement, a design load of 10 MW/m^2 is also pursued on the middle part of the divertor (target modules TM5h and TM6h) and on the end tiles of the target elements near the pumping gap ("Dach- und Stirnziegel").

To allow for this design heat load, a welded or brazed connection between a tungsten based plasma facing material and copper based heat sink is required as the thermal resistance of a bolted connection is too large and would cause to too high temperatures in the plasma facing material. The welded or brazed connection, however, results in not only a nearly perfect thermal contact, but also a nearly perfect mechanical contact. As a result, high thermal stresses are inevitable due to the thermal expansion mismatch between tungsten and copper (alloys). Therefore, a soft copper interlayer is required to reduce these thermal stresses and avoid fatigue failure.

In addition, a tungsten alloy (notably W95NiFe) is under investigation as plasma facing material, because it is ductile at room temperature and easier to machine than pure tungsten. As a result, it could even be used

a structural material and the team investigates if a target element can be made completely out of this alloy, thus avoiding the thermal stresses. Also, the impact of the slight magnetic susceptibility of W95NiFe onto the occurrence of magnetic field errors is being checked. First results show that the impact is negligible. To simplify manufacturing, it is pursued to maximize the size of target elements, ideally making a target module out of a single target element only, thus significantly reducing the pipework and number of leak tight weld seams. For that purpose, additive manufacturing of CuCrZr heat sinks is under investigation as well as diffusion welding and hot isostatic pressing (HIP) to join the heat sinks to the tungsten (alloy) tiles with soft copper interlayer. The soft copper interlayer is either directly diffusion welded or HIP-ed onto both sides or alternatively first cast or galvanized onto the tungsten tile.

2.5 Particle Balance and PWI

For OP2, tungsten PFCs have been installed at different positions in W7-X to investigate the effect of tungsten erosion, transport and possible accumulation on the overall plasma performance during the upcoming campaign. Heat shield tiles coated with tungsten are used in the ECRH beam reflection areas (see figure 6) promoting also an improved microwave reflectivity.

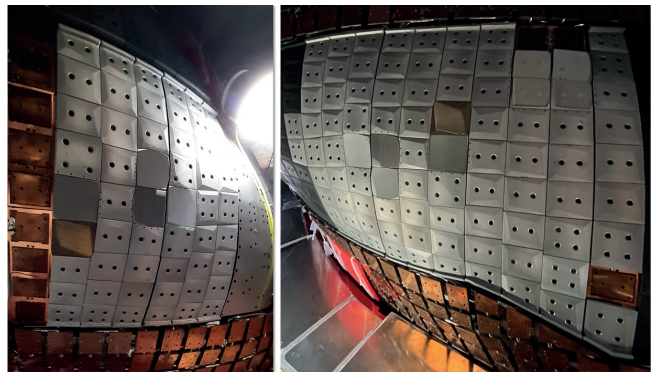


Figure 6. Tungsten coated heat shield tiles in module 1 (left) and 5 (right).

The installation of thin W/WCuNi tiles ($\sim 5 \text{ mm}$ thick) together with modified graphite tiles in the area of the vertical baffle is expected (see figure 7) to reduce the heat load, especially when using the high-mirror configuration, where severe limitations of the plasma operation were encountered in the last experimental campaign.



Figure 7. Tiles from baffle module BM1v: middle four tiles are thin tungsten/tungsten-alloy tiles.

Neutral Gas Exhaust and Plasma-wall Interaction Studies

The development of robust pressure gauges using LaB6 crystal emitters enabled reliable neutral gas pressure measurements in the plasma vessel of W7-X and allowed characterization of the particle exhaust performance of the island divertor. Neutral particle compression of about 30 in the standard magnetic configuration and about 80 in the high iota configuration was achieved in the experiment campaign OP1.2b. The lower compression in the standard configuration was due to the low efficiency of particle exhaust: only 0.44 % of the particles hitting the divertor targets were pumped out at a maximum exhaust gas flow of 9.4 mbar l/s. In the high-iota configuration, the exhaust efficiency was 2.9 % and the maximum exhaust flow was 17.7 mbar l/s, i.e., twice as high despite the lower pumping speed over the AEP ports in this divertor section. The reason for this large differences is probably the low particle collection efficiency in the standard magnetic configuration.

Only 0.69 % of the particles that encountered the divertor targets entered the sub-divertor volume through the pump gap. Two conclusions can be drawn from this [23]: The performance of the island divertor is good in the high-iota configuration in terms of particle removal. However, the poloidal divertor of a tokamak is superior in this respect. The extrapolation to steady-state operation shows that the high-iota configuration appears particularly promising, while the standard configuration could be critical for operation with heavy particle fuelling, as with NBI heating and pellet injection.

The concept of the diagnostic residual gas analyzer (DRGA) was developed for ITER, focusing on the detection of fast helium and hydrogen isotopes. The first operation of the prototype DRGA (P-DRGA) at the Wendelstein 7-X stellarator showed potential for improvement in terms of magnetic sensor shielding, automation of data acquisition, and possible new additions to the sensor cluster at the p-DRGA. Recently, a Monte Carlo simulation of the outflow of the mixed gas species from the pressure-reduction port through the approximately 8-m-long sampling tube into the analysis area of the sensors was performed, which was in general agreement with previous calculations and measurements, but revealed potential backflow effects for light gases that affect the detection limits of both the prototype and the ITER-DRGA under design. For the upcoming prototype campaign, an improved soft iron shield will protect the instrumentation from stray magnetic field effects. The newly introduced shielding was tested for its effect on stray magnetic fields and found to reduce the residual internal field by about two orders of magnitude [24].

First attempts have been undertaken to understand the carbon balance in W7-X, which was operated with inertially cooled divertor units in OP1.2. Both regions of high net erosion and regions dominated by deposition are observed at the divertor targets, with net erosion clearly predominating. In particular, the strike-line regions are the dominant source of carbon impurities in the plasma. Thick deposition layers with thicknesses $>1 \mu\text{m}$ were observed on some baffle tiles near the divertor targets. Only very thin deposits with thicknesses of a few tens of

nanometers were found on the heat shield tiles and in remote areas, e.g., on the plasma vessel surfaces behind the divertor targets. This behaviour, which is particularly pronounced in OP1.2a, is fundamentally different from divertors in tokamaks with carbon plasma facing components, where the eroded material (from the divertor, but also due to erosion on the wall surfaces in the main chamber by charge exchange neutrals) is typically redeposited on the divertor targets as well as in remote divertor regions. This could be due to the fact that the divertor in W7-X is not toroidally closed as in tokamaks, and higher particle losses may occur during parallel transport between the different divertor units. This behaviour was established on the basis of surface analyses in which various selected plasma-facing components were taken out for these ex-situ measurements. In addition, the divertor and PFCs were not actively cooled, and cumulative effects were observed after OP1.2a with high C and O impurities and OP1.2b with reduced impurities due to boronizations. Therefore, it would be too early to draw a general picture of carbon migration in W7-X. For OP2, a new actively cooled CFC divertor will be used. The energy supplied to the plasma will be gradually increased to 18 GJ in successive campaigns, and the carbon balance will be monitored by in situ spectroscopic measurements and post-mortem analyses of the first wall panels [25].

2.6 Divertor Physics Scenarios

The island divertor geometry was found to support full magnetic flexibility with exhaust at the level near the requirements of W7-X. Of all particles neutralized in the divertor, a fraction of 4 % is collected into the sub-divertor under attached conditions. The fraction is determined by the pump gap opening angle to the strike line. Of all the particles in the sub-divertor, ca. 6 % are removed by the turbo molecular pumps. To increase the pressure, one can increase the collected particle fraction, or increase the neutral source in general. An increase in the particle collection is achieved by shifting the strike line towards the pumping gap. In a steady-state regime, W7-X will operate with continuous pellet fuelling. It has been found that particle balance in pellet-fuelled discharges is close to the requirements of the steady-state operation. A sum of divertor fuelling rate and pellets could be reduced to the level below the total pumping rate of the turbo-molecular pumps.

3 Stellarator Dynamics and Transport (E5)

Head: Prof. Dr. Thomas Klüger

A number of diagnostic systems were significantly improved and extended, several new instruments were designed, constructed and installed; all in time and in budget. Turbulence and the related transport of particles and energy is the main factor determining the plasma performance of Wendelstein 7-X. The radiation physics connects impurity transport with a better understanding of sources. Magnetohydrodynamics prepares for future high- β operation.

3.1 Turbulence Group

3.1.1 Microwave Diagnostics

During Operational Phase 1 (OP1), several Doppler reflectometry and correlation microwave diagnostics were commissioned and used to perform initial studies of plasma density and electron temperature fluctuation intensity, localization, and propagation on Wendelstein 7-X. For Operational Phase 2 (OP2), diagnostic extension and upgrades to each system are underway to continue these studies and to provide additional capabilities that are necessary for studying the relationship between fluctuation measurements and turbulence which drives plasma transport in Wendelstein 7-X. The focus of the Doppler and correlation reflectometry measurements is on the perpendicular propagation, from which the radial electric field can be deduced. Here, for various different plasma scenarios and magnetic configurations, the comparison with neoclassical transport predictions shows good agreement.

Using full-wave modelling, the nonlinear instrument response is addressed in order to assess quantitatively the fluctuation level. Comparisons with nonlinear gyrokinetic simulation results have started with a focus on the role of the radial electric field in the turbulence evolution. For OP2, two V-band (50–75 GHz) Doppler reflectometers, measuring in two toroidally displaced positions, will be used for zonal flow and turbulence saturation studies. A steerable mirror has been installed for one of these systems, allowing wavenumber spectra measurements and turbulence localization studies. An additional E-band (60–90 GHz) system has also been installed in the same port, alongside a new 7-channel comb system in the W-band (75–110 GHz) to access higher plasma densities and perform radial correlation studies. During OP1, the poloidal correlation reflectometer (PCR) consisted of a single Ka-band (26–40 GHz) reflectometer with four receiving antennas. It was used to determine the structure and propagation of coherent plasma density fluctuations in the plasma edge and scrape-off layer region of Wendelstein 7-X. This system has been extended by adding a U-band (40–60 GHz) reflectometer that allows access to plasma densities up to $4 \times 10^{19} \text{ m}^{-3}$ and measurements of the radial and poloidal correlation lengths of plasma density fluctuations. The correlation radiometry (CECE) diagnostics on Wendelstein 7-X were operated in a test configuration throughout OP1, and a dedicated CECE diagnostic is now under development for OP2. This new system has a focusing antenna with a beam width of less than 2.5 cm allowing for radial correlation studies of electron temperature fluctuations. A secondary CECE antenna has overlapping measurement volumes with the reflectometry diagnostics. It allows one to study correlations between electron temperature and plasma density fluctuations in the near-edge region of Wendelstein 7-X. Additionally, a conceptual design study for an electron cyclotron emission imaging (ECE imaging) diagnostic has been started with the purpose of developing a non-invasive microwave diagnostic, capable of measuring the electron temperature in a two-dimensional plane at high temporal and spatial resolution.

This would provide a passive measurement of the core electron dynamics spanning from small-amplitude, high-frequency fluctuations driven by turbulence to large-scale MHD events.

3.1.2 Multi-purpose Manipulator

After successful initial operation in OP1 involving 11 different probes for various physics objectives, the multi-purpose manipulator (MPM) was further improved for OP2. The probe electronics were upgraded to improve signal quality and reduce electronic noise in the 100 kHz range. New probe biasing options enable us to operate swept probes up to 100 kHz. Furthermore, the MPM has been prepared to cope with radio frequency noise to enable probe measurements in ICRH plasmas. Most of the probe heads from OP1 have been either upgraded or replaced by improved versions. As a particular highlight, a new probe head containing 29 electrodes in a 2D radial-poloidal array was developed with carefully optimized geometry. This will simultaneously provide fundamental plasma parameters as density, electron and ion (via ball-pen probes) temperatures, potentials and electric fields together with two-dimensional measurements of turbulent particle transport by capturing the spatiotemporal evolution of plasma fluctuations.

3.1.3 Phase Contrast Imaging

Phase contrast imaging (PCI) has been operated throughout OP1.2a/b. It has continuously delivered poloidally resolved, absolute line-integrated density fluctuation spectra for most discharges throughout these campaigns. PCI is based on small angle scattering of an infrared laser beam that passes through the magnetic axis and is subsequently imaged onto a detector array by purpose-built optical elements. The absolute calibration of both the wavenumber and fluctuation amplitude enable a comparison across various experimental situations, as well as to gyrokinetic simulations, which is extended by newly developed synthetic diagnostic tools. PCI represents the only dedicated core turbulence diagnostic. It has already revealed important physics mechanisms, for instance the stabilization of predominantly ion temperature gradient driven (ITG) turbulence in response to scenarios with central density peaking. Here, the experimental results are in good agreement with linear and nonlinear gyrokinetic simulations, underlining that turbulence reduction is due to ITG suppression by a core density gradient without a significant destabilization of trapped electron modes (TEMs). In preparation for OP2, the beam path has been redesigned in response to new space constraints. The modified system is currently being commissioned and will be operational in time for OP2. In addition to the new beam path, the modified system includes several new diagnostic features. One of those is the use of improved spatial filtering masks to enable radial resolution of the PCI measurements by only permitting beam components scattered from a limited range of magnetic field pitch angles to reach the detector arrays. Another feature, expected to be available during the latter part

of OP2, is the heterodyne detection scheme for high-frequency fluctuations close to the ICRH frequency, which will allow for the study of mode conversion of the ICRH waves and ion cyclotron emission.

3.1.4 Gas Puff Imaging

The gas puff imaging diagnostic has completed the design review process and has been installed in time for OP2. Its two-dimensional field of view includes the separatrix and near to mid scrape-off layer and will allow for imaging and subsequent statistical analysis of the spatio-temporal dynamics of turbulent filamentary density structures. The system consists (I) of an optimized supersonic nozzle that enables collimated propagation of the gas puff through the wide magnetic island zone, and (II) a lens and shutter mirror system within an immersion tube, designed to handle the large cumulative heat loads during steady-state operation. Image acquisition is done by a high-speed avalanche photo diode array camera, which has a rectangular field of view aligned with the last closed flux surface for filament tracking, predominantly along the poloidal direction.

3.1.5 Heavy Ion Beam Probe

The heavy ion beam probe (HIBP) diagnostic is a unique tool for the measurement of plasma parameters critical for turbulence characterisation. Simulations, based on the finalized conceptual design for Wendelstein 7-X, show that the HIBP would provide measurements of electrostatic potential over a large range of plasma radii as well as fluctuations of density, potential and their cross-phase, along most of the minor radius on the outboard side. The conceptual design study is completed and ready for a design review and possible progression towards the detailed design phase.

3.1.6 Key Scientific Achievements

Core Turbulence

Turbulent fluctuations and associated anomalous heat transport dominate the dynamics of electron-cyclotron-resonance-heated (ECRH) plasmas in Wendelstein 7-X [3, 26, 27]. A profound understanding of the fundamental mechanisms behind turbulence in this type of discharge and collecting experimental evidence is required, in particular for long pulse discharges with ECRH in Wendelstein 7-X. It is also necessary to find actuators for reducing turbulence. The core plasma density fluctuations in Wendelstein 7-X ECRH plasmas arise predominantly due to ion-temperature-gradient (ITG) driven turbulence. ITG fluctuations are radially localised in the outer half of the plasma. This was investigated experimentally via phase contrast imaging (PCI) and combined with numerical gyrokinetic simulations using the code GENE [28]. Due to the radial localisation of fluctuations, measured wave-number-frequency spectra exhibit a dominant phase velocity, directly related to the rotation velocity at the respective radial position. The experimentally found radial position agrees well with findings for density fluctuations and ion heat flux in non-linear gyrokinetic simulations.

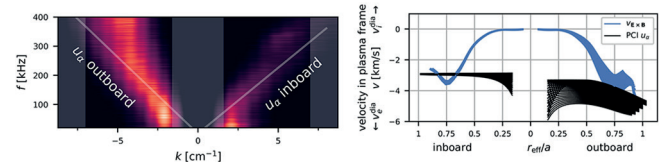


Figure 8. Wavenumber-frequency spectrum with dominant velocity bands of line-integrated density fluctuation measurements with PCI (left) and comparison to ExB rotation velocity along the PCI line of sight showing a match at $r_{\text{eff}}/a \approx 0.75$ (right).

Furthermore, they exhibit typical features of ITG driven turbulence, and the radial location coincides with the region of the strongest gradient. Linear gyrokinetic simulations confirm that ITG modes are the most dominant mechanism driving turbulence, in particular in this radial region.

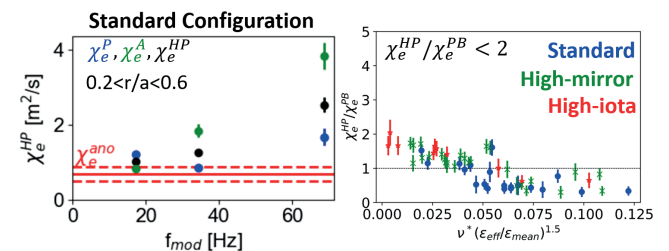


Figure 9. Heat pulse electron thermal diffusivity measured at multiple harmonics of the ECRH modulation frequency during a transient transport experiment (black; result from the amplitude in green and phase in blue) compared to the anomalous electron thermal diffusivity inferred from a power balance analysis (red line; uncertainties dashed lines) in the standard magnetic configuration for a typical ECRH heated plasma (left). Stiffness in the electron heat flux as a function of collisionality in W7-X for three magnetic configurations (standard configuration in blue, high-mirror in green, and high-iota in red) (right).

The shape of the kinetic profiles is well-known to have a strong impact on the growth (linear) and saturation (nonlinear) of turbulence and transport in magnetically confined devices. In tokamak devices, the magnetic curvature can drive an inward pinch of particles that is associated with the ITG mode, while at high electron-to-ion temperature ratios (T_e/T_i) thermo-diffusion can drive an outward particle flux that is associated with electron temperature gradient (ETG) and trapped electron modes (TEMs) [29]. Similarly, all three drift wave types can drive an apparent stiffness in the electron heat flux in tokamaks, parameterized as the ratio of the electron thermal diffusivities from a transient and steady-state analysis ($\chi_e^{\text{HP}}/\chi_e^{\text{PB}}$), where the electron temperature profile is resilient to changes in heating power and deposition location and $\chi_e^{\text{HP}}/\chi_e^{\text{PB}} < 10$ [30]. During OP1, the plasma density profiles in Wendelstein 7-X were typically observed to be flat or slightly peaked with normalized plasma density gradient scale lengths less than 1 in plasmas heated by ECRH, $0 < a/L_{ne} < 1$.

The neoclassical particle flux is directed outward and driven by thermo-diffusion in Wendelstein 7-X, and the slight peaking in the plasma density profile is thought to be produced by a convective inward particle pinch driven by turbulence. The stiffness in the electron heat flux in Wendelstein 7-X has been measured to vary between approximately 2 and 0.5 as a function of collisionality, which is similar to measurements in other stellarator devices [31]. This can be indicative of convective particle transport and/or a plasma parameter dependence of the transport coefficients.

To study this effect, the diffusive and convective contributions to the electron heat flux have been separated using transient transport measurements at multiple harmonics of the ECRH modulation frequency. The convective contribution, when associated with the particle flux, is significantly larger than that expected from neoclassical thermodiffusion; however, it is of the correct order of magnitude to reproduce the experimental plasma density profiles measured during the first operational phase of Wendelstein 7-X ($V_e^{\text{HP}} \sim 1\text{--}2$ m/s). This result is quantitatively similar to previous measurements of an anomalous impurity pinch in laser blow-off experiments on Wendelstein 7-X [32]. Differentiating the heat transport driven by the particle flux from a plasma parameter dependence of the diffusivity is not possible without further model refinement and additional measurements in the particle transport channel, such as those from gas puff modulation experiments (planned for OP2). Comparisons to nonlinear gyrokinetic calculations are currently underway.

SOL Turbulence

Turbulent transport is a major contribution to perpendicular transport in the SOL of fusion plasmas. In tokamaks in particular, isolated blob-filaments are observed to carry a significant part of the total turbulent transport from their birth region around the LCFS into the far SOL, where they lead to high relative fluctuation levels (“turbulence spreading”). In OP1.2b, data from more than 200 reciprocating probe measurements in the SOL of Wendelstein 7-X was used to survey the relation of turbulent particle flux and the local pressure gradient, where both quantities were obtained simultaneously using a multi-pin probe head. The result of this survey is presented in figure 10 for different magnetic configurations. It is observed that in most configurations there is a roughly linear relation between the turbulent particle flux and the pressure gradient, indicating the absence of turbulence spreading. Examining the “high mirror”, “high iota” and “low iota” configurations in more detail, a dependence of the slope of the roughly linear relation is observed (i.e. the turbulent transport magnitude for a given gradient depends on the magnetic configuration) which is not yet fully understood. The “standard” configuration reveals a less clear picture, particularly for the blue data points resembling experiments with unmodified magnetic islands (no use of island control coils I_{cc}). It is the current hypothesis that this is due to the additional transport effects in the magnetic islands, which are particularly prominent in the standard configuration.

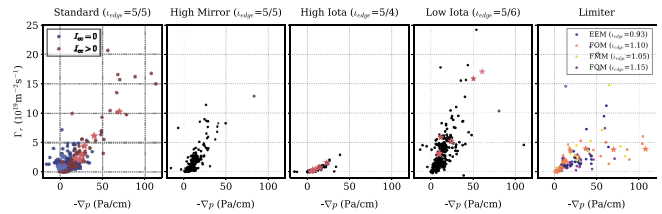


Figure 10. Scatter plot of turbulent radial particle flux as a function of radial plasma pressure gradient distinguished by magnetic configuration in the SOL of W7-X, taken by reciprocating probes. Each dot represents a 5 ms time slice of probe data, covering a wide range of heating and fueling scenarios.

3.2 Impurity Transport and Radiation Physics

Core impurity transport in non-axisymmetric configurations, such as stellarators, is most often unfavorable with an inward pinch in reactor-relevant conditions. This leads to impurity profile peaking and accumulation, which can result in performance degradation, dilution or even radiative instabilities. In previous campaigns of Wendelstein 7-X, it was demonstrated that the impurity transport is largely dominated by turbulence, resulting in flat impurity profiles and impurity transport times well below the neoclassical level. Inferred transport coefficients in dedicated laser blow-off (LBO) experiments are in line with numerical simulations on ITG-type turbulent transport. In addition, theoretical expectations of stabilizing effects from kinetic profile parameters, such as T_e/T_i or increased $(1/n_e)dn_e/dr$, can be qualitatively recovered by turbulence modelling and are seen to reduce the transport as shown in figure 11.

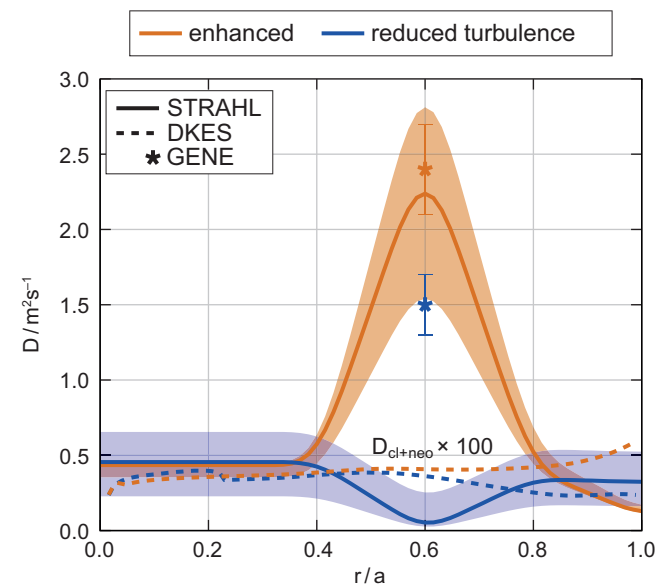


Figure 11. Transport coefficient profiles inferred from an LBO injection experiment with different density gradients in the radial region where ITG is expected to be maximum. For comparison, the predicted diffusion coefficients from flux tube turbulence simulations with the GENE code are shown as well.

Under special conditions, such as purely NBI-heated plasmas, low power or low-density ECRH plasmas, the turbulent impurity transport was observed to be suppressed significantly. Peaking of the impurity and radiation profiles and impurity accumulation were measured by a number of diagnostics, such as bolometry, CXRS and XMCTS. Transient conditions with suppressed impurity transport are created with boron-dropper, massive LBO, massive TESPEL and pellet fuelling. The impurity transport analysis for a purely NBI-heated scenario implies almost pure neoclassical impurity transport ($D_{\text{turb}} < 0.3 D_{\text{neoclassical}}$) for C and Ar. Application of additional ECRH to such scenarios lowers the impurity accumulation in the center, which is believed to be due to turbulent transport driven by steeper gradients in the kinetic profiles.

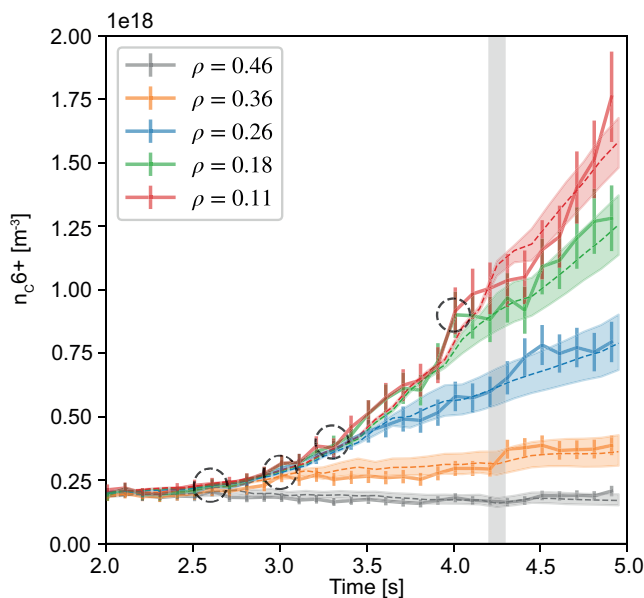


Figure 12. Time evolution of modelled (dashed) and measured (solid lines) impurity densities. Purely neoclassical transport coefficient are used for the modelling.

Edge impurity transport is equally important to allow the assessment of the radiative limits, the impurity control and the helium-exhaust capabilities of the boundary plasma. Spectroscopic measurements of impurity concentrations in the divertor of Wendelstein 7-X showed first indications of impurity enrichment in line with expectations from EMC3-Eirene modelling. The modelling showed that for regular Wendelstein 7-X conditions the parallel impurity transport is deep in the friction-force dominated regime and impurities are very well retained at the target plates. In the simulations, small parallel flows in the region across the island O-point lead to long residence times of impurities. Consequently, impurities accumulate locally and a significant cross-field diffusive flux towards the separatrix along the stagnation region of the island is caused. Validation experiments with different seeding locations for impurities are planned for OP2.

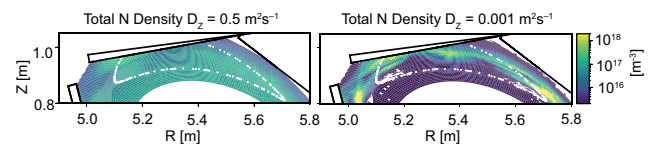


Figure 13. Impurity density distributions for an impurity diffusion coefficient parameter scan in EMC3-Eirene show that the suppression of perpendicular transport leads to almost perfect retention of the impurities in the vicinity of the target.

Last, but not least, bolometric measurements showed strong asymmetries of X-point radiation in detached conditions, especially at high-collisionality. These radiation asymmetries and their dynamics imply the importance of impurity transport (parallel & drifts) for the radiation in the SOL and at the separatrix.

3.3 MHD Group

3.3.1 Magnetic Diagnostics

The data acquisition systems (DAQs) of all magnetic sensors, i.e. Rogowski coils, diamagnetic coils, saddle loops and Mirnov coils have been updated and embedded within the upgraded central segment control system of Wendelstein 7-X. Since new and improved heating systems (ECRH, ICRH and NBI) will be operated in the upcoming experimental campaign, the machine safety relevant interlock signal, which is generated based on the diamagnetic energy measurement, has been adapted. Commissioning is planned for the first part of OP2. The generation of an additional trigger signal, which will activate a fast magnet discharge in case of a fast plasma collapse has been implemented and successfully tested in the laboratory. It will be part of the magnetic diagnostic system. The amplitude and phase calibration of the Mirnov coils has been finished and results are taken into account in the respective data analysis software.

3.3.2 X-ray Pulse Height Analysis System

An issue in the pulse height analysis (PHA) X-ray spectral measurement could be resolved: A source for falsely detected peaks could be permanently removed from the detection system. High-amplitude reset pulses, produced by a reset-type preamplifier, were identified to generate false peaks. Several measures to improve the shielding between the three channels eliminated the interference between the channels. This will allow for better accuracy in the estimation of carbon and oxygen line intensities in the future. The preamplifier settings were also optimized in terms of increased photon flux for OP2 (amplitude and reset interval).

3.3.3 Soft X-ray Tomography System (XMCTS)

During an in-vessel inspection after OP1.2, many beryllium filters inside the XMCTS pinhole cameras exhibit a coating. For OP2 the beryllium filters of affected cameras have been exchanged. To avoid

sightline shadowing, which required additional modelling efforts, the shutters have been clamped to fix the camera apertures in a fully open position. In preparation of high power plasmas, foreseen in OP2, the slit aperture widths have been decreased for 18 of 20 cameras to reduce the signal intensity reaching the detectors. Newly measured edge frequencies of 100 kHz indicate that the long signal cables have a minor effect on the bandwidth.

3.3.4 Key Scientific Achievements

The analysis of the data acquired in operational phase OP1.2 was continued. The dependence of the bootstrap current on a comprehensive set of parameters was investigated. Intrinsic, diffusion-driven toroidal (bootstrap) currents between -7 and 17 kA were measured for several magnetic configurations at line-integrated plasma densities between 2×10^{19} and $1.6 \times 10^{20} \text{ m}^{-2}$ and heating powers between 0.5 and 6 MW. The sign of the bootstrap current changes with field reversal, and its magnitude decreases with the increase of the mirror term and the rotational transform of the magnetic configuration, as well as the line-integrated plasma density and increases with the heating power. Both the absolute values and the above-described parameter dependencies agree with neoclassical calculations within the uncertainties, which confirms the neoclassical optimization of Wendelstein 7-X for small bootstrap currents [33]. For faster equilibrium reconstruction, the VMEC code has been substantially improved. This will allow the analysis of plasma dynamics, specifically for upcoming high beta experiments.

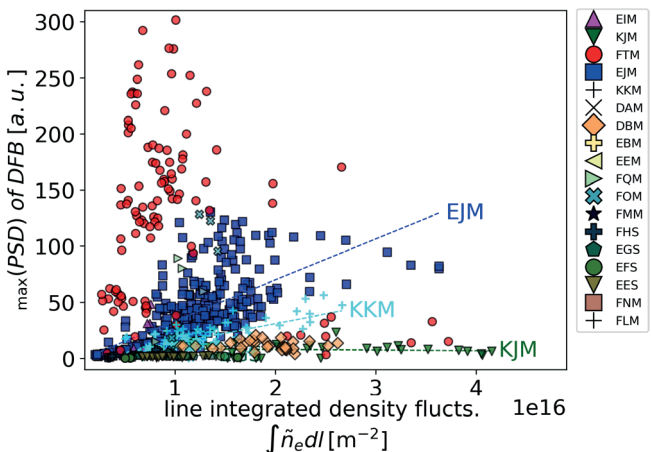


Figure 14. The measured magnetic fluctuation amplitude of the dominant frequency band (DFB) around 200 kHz scales linear with the line integrated density fluctuations, which are measured by the PCI diagnostic and proportional to the core turbulent density fluctuations. A clear magnetic configuration dependency is visible.

The analysis methods of magnetic fluctuations, which were measured with 125 in-vessel Mirnov coils, have been substantially improved. The typically observed broad-band fluctuations around 200 kHz

have been studied within a large data set comprising of almost 1000 experimental programs. The dependency of the mean frequency and amplitude of the bands on global plasma parameters (like density, temperatures, heating power, magnetic configuration, etc.) was investigated. The clear correlation to turbulent density fluctuation levels, as measured by the PCI system, suggests that the dominant driving mechanism of the magnetic fluctuations is strongly linked to ITG turbulence (figure 14). This hypothesis is supported by numerical simulations using EUTERPE, which were accompanied by detailed pre-evaluations carried out with CONTI and CKA-EUTERPE. Data analysis methods providing toroidal and poloidal mode numbers for the identification of associated frequency regimes have been further developed and benchmarked against the results of other machines (e.g. TJ-II).

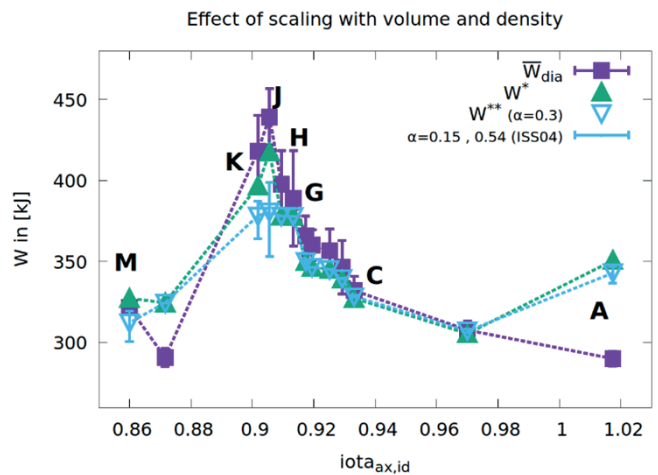


Figure 15. Configuration scans changing the rotational transform ι . Plotted is the diamagnetic energy W_{dia} (violet), energy W^* which is scaled to a norm-volume of 31.5 m^3 (green filled triangles) and energy W^{**} which is additionally scaled to a norm-line-density of $3.5 \cdot 10^{19} \text{ m}^{-2}$ (blue, open, upside-down triangles). Labels (A to M) indicate magnetic configurations in the scan.

The main focus of the Wendelstein 7-X data analysis was on electron cyclotron current drive (ECCD) and high performance experiments. The results contribute to the understanding of fast saw-tooth-like crashes and reveal evidence to theoretically predicted kinetic ballooning modes during high beta plasmas. Ballooning mode activity has been observed during phases, where the stored plasma energy W_{dia} approaches 1 MJ. The activity has been analyzed using XMCTS sightline data and a poloidal mode forward model. Poloidal modes in the range $m=8-11$ in a radial region close to the core ($r \sim 0.15 \text{ m}$) could be identified [34]. Investigations using mode decomposition tools directly on tomographic data are also indicating poloidal mode number regions of $m > \sim 8$, in mid range radial regions [35,36]. Configuration scans conducted in OP1.2b [36] explored magnetic configurations

between high-iota- and standard-configuration by means of planar coil current change covering a range in central $\iota(0)$ from 0.854 to 1.012 corresponding to ι -values at the boundary of 5/5 and 5/4, respectively. Analysis of the influence of the rotational transform variation revealed an increase of the plasma energy and thus implicitly of the confinement time in the intermediate limiter configurations. The confinement improvement persists when accounting for effects of volume changes in the different configurations and when scaling the energy data to the same line density (figure 15).

It is striking that this improvement relates to the presence of the 5/5-islands close to the plasma boundary. First investigations in this direction have been started [37]. A bursty MHD-activity has been observed by several diagnostics in the configurations with improved confinement. The mode, termed island-localized mode (ILM), is related to the presence of the 5/5-island chain and its amplitude correlates with the size of the internal 5/5 islands: it becomes larger with island enlargement and decreases with the reduction of the island size. However, the change of the island size seems to have no effect on the diamagnetic energy. Typically up to 3% of the stored plasma energy is lost within a few milliseconds during those ILM events. Analysis of SX sightline data indicates a correlation of ILM activity to the magnetic island chains located in the edge region. Tomographic inversion reveals a sudden onset of low mode number ($m \sim 1$) activity in the edge, which decays rapidly after the event.

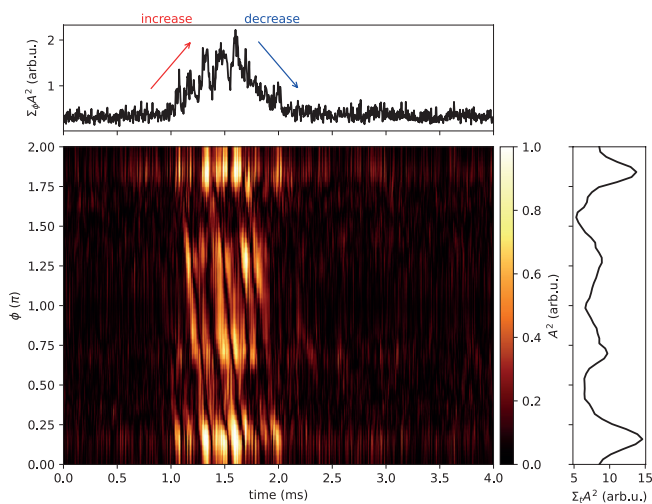


Figure 16. ILM MHD event showing an $m = 1$ mode in space-time SX fluctuation data along a flux surface contour (extracted from a time series of tomograms). The quantity A is the fluctuation amplitude, A^2 denotes the energy.

Figure 16 shows soft X-ray fluctuations obtained from extraction of space-time data of a poloidal array extracted from tomograms. An $m = 1$, mode develops swiftly within ~ 0.25 ms, stays for ~ 0.5 ms and decays within 0.25 ms.

3.4 Engineering

The central engineering group supports the topical groups of the division in the development, production and operation of diagnostics. Five engineers, four technicians and one electrician are available for this purpose. During the completion phase 2 (CP2) in the years 2019–2022, it was thus possible to work on nine diagnostics projects, of which six were completely new developments and another three required major modifications. In addition to development and manufacturing, another focus point is servicing and maintenance of existing diagnostics. At present, there are 17 diagnostics operated by the division E5. They are continuously improved and adapted. Besides uninstalling and reinstalling already running diagnostics (PHA, TESPEL, reflectometers) for accessibility to the torus during CP2, it was taken over the task of hardening the already existing diagnostics. For example, the horizontal core bolometer needed a cooled protection for the port wall and its welds to the plasma vessel, due to the higher power in the plasma in OP2. For that purpose it was equipped with a 3d-shaped cooling tube, the currently largest cooled 3d printed part on Wendelstein 7-X. After intensive testing conducted by the quality management department, this component is now in operation. Further, the phase contrast imaging (PCI) system had to be adapted, as the expansion of the cooling circuits for Wendelstein 7-X took up the previously occupied space. For this, a new beam path had to be found together with a new position for an optical table and its control cabinet. In OP1.2, operating the laser blow-off (LBO) system was only possible using the multipurpose manipulator (MPM). To avoid that a new dedicated manipulator was built specifically for the LBO system. Other new developments during CP2 include the divertor bolometers: Based on the concepts of the core bolometers, two additional camera immersion tubes were designed, manufactured and installed. Finally, an infrared observation system was converted into an infrared bolometer for test purposes.

Wendelstein 7-X – Scientific Staff

W7-X Team: P. Aleynikov, K. Aleynikova, A. Ali, T. Andreeva, J. Baldzuhn, M. Banduch, S. Bannmann, C. D. Beidler, A. Benndorf, C. Biedermann, M. Blatzheim, T. Bluhm, D. Böckenhoff, D. Bold, M. Borchardt, H.-S. Bosch, S. Bozhenkov, M. Beurskens, R. Brakel, C. Brandt, T. Bräuer, H. Braune, K.-J. Brunner, R. Burhenn, R. Bussiahn, B. Buttenschön, V. Bykov, A. Carls, N. Chaudhary, D. Cipciar, M. Cole, M. Czerwinski, H. Damm, S. Degenkolbe, C. P. Dhard, A. Dinklage, M. Drevlak, P. Drewelow, P. van Eeten, G. Ehrke, M. Ender, J. Fellinger, Y. Feng, E. R. Flom, O. Ford, G. Fuchert, Y. Gao, J. Geiger, D. Gradic, M. Grahl, O. Grulke, J. F. Guerrero Arnaiz, D. Hartmann, D. Hathiramani, B. Hein, P. Helander, S. Henneberg, F. Henke, M. Hirsch, U. Höfel, A. Hölting, Z. Huang, M. Jakubowski, T. Jesche, J.-P. Kallmeyer, U. Kamionka, C. Killer, R. Kleiber, T. Klinger, J. Knauer, M. Khokhlov, A. Könies, R. König, P. Kornejew, J.-P. Koschinsky, R. Krampitz, T. Kremeyer, M. Krychowiak, P. A. Kurz, S. Kwak, A. Langenberg, H. Laqua, H. P. Laqua, R. Laube, S. Lazerson, C. Li, J. Lion, J.-F. Lobsien, J. Loizu, A. Lorenz, S. Marsen, M. Marushchenko, P. McNeely, S. Vaz Mendes, A. Mishchenko, B. Missal, A. Mollen, T. Mönnich, D. Moseev, M. Nagel, D. Naujoks, U. Neuner, H. Niemann, C. Nührenberg, J. Nührenberg, J. W. Oosterbeek, M. Otte, N. Panadero, G. Partesotti, E. Pasch, A. Pavone, T. S. Pedersen, V. Perseo, D. Pilopp, S. Pingel, G. Plunk, P. Pölöskei, S. Ponomarenko, A. Puig Sitjes, F. Purps, K. Rahbarnia, F. Reimold, J. Riemann, K. Risse, T. Romba, D. Rondeshagen, P. Rong, L. Rudischhauser, K. Rummel, T. Rummel, A. Runov, N. Rust, J. Schacht, J. Schilling, G. Schlisio, M. Schneider, P. Scholz, M. Schröder, T. Schröder, R. Schroeder, F. Sciortino, B. Shanahan, C. Slaby, H. Smith, A. Spring, T. Stange, J. Svensson, H. Thomsen, H. Trimino Mora, Y. Turkin, I. Vakulchik, S. Valet, L. Vano, H. Viebke, R. Vilbrandt, A. von Stechow, F. Wagner, Z. Wang, L. Wegener, Th. Wegner, G. M. Weir, J. Wendorf, U. Wenzel, T. Windisch, M. Winkler, A. Winter, V. Winters, R. C. Wolf, P. Xanthopoulos, M. Zanini, D. Zhang, J. Zhu, A. Zocco

Other IPP Divisions, Garching: M. Balden, B. Böswirth, J. Boscary, M. Dibon, S. Elgeti, H. Frerichs, H. Greuner, B. Heinemann, P. Junghanns, D. Kulla, P. Lang, M. Mayer, B. Mendelevitch, R. Neu, R. Nocentini, S. Obermayer, G. Orozco, R. Riedl, V. Rohde, R. Stadler, J. Tretter, A. J. van Vuuren, M. Zilker

University of Greifswald, DE: A. Dinklage, P. Helander, T. Klinger, H. P. Laqua, T. S. Pedersen

Leibniz Institute for Plasma Science and Technology (INP), Greifswald, DE: K. D. Weltmann, J. Berger

Technical University of Berlin, DE: H.-S. Bosch, F. Köster, R. C. Wolf

Physikalisch-Technische Bundesanstalt (PTB), DE: A. Lücke, M. Zboril, A. Zimbal

Forschungszentrum Jülich, Institute of Energy and Climate Research – Plasma Physics (IEK-4), Jülich, DE: J. Assmann, S. Brezinsek, R. Caspers, J. Coenen, G. Czymek, T. Dittmar, P. Drews, G. Esser, A. Freund, U. Habrichs, X. Han, K. P. Hollfeld, D. Höschen, M. Hubeny, M. Knaup, A. Knieps, A. Krämer-Flecken, Th. Krings, Y. Liang, C. Linsmeier, O. Marchuk, O. Neubauer, D. Nicolai, G. Offermanns, G. Satheeswaran, B. Unterberg, K. Von Bovert, E. Wang, Sh. Xu

Karlsruhe Institute of Technology (KIT), Karlsruhe, DE: L. Feuerstein, G. Gantenbein, S. Illy, J. Jelonnek, J. Jin, L. Krier, A. Marek, T. Ruess, T. Rzesnicki, S. Stanculovic

IGVP, University of Stuttgart, DE: W. Kasperek, M. Krämer, C. Lechte, B. Plaum, F. Remppe, H. Röhlinger, B. Roth, K.-H. Schlüter, S. Wolf, A. Zeitler

Technical University of Denmark, Lyngby, DK: O. Grulke, T. Jensen, M. R. Larsen, S.K. Nielsen, R. Ragona, M. Salewski, B. S. Schmidt, A. Tancetti

Aalto University, Espoo, FI: T. Kurki-Suonio, S. Sipliä

Eindhoven University of Technology, Eindhoven, NL: H. Brand, J. Howard, P. T. Mullholland, S. Paqay, J. H. E. Proll, E. Sweerts, F. Warmer, M. Zuin

Laboratorium for Plasma Physics of the Ecole Royale Military, Brussels, BE: D. Castano-Bardawill, K. Crombe, F. Durodie, A. Gorjaev, Y. O. Kazakov, D. Lopez, F. Louche, J. Ongena, B. Schweer, I. Stepanov, M. van Schoor, M. Vergote, M. Verstraeten, M. Vervier

KU Leuven, BE: R. de Wolf, M. Jacobs, W. Dekeyser, T. Baelmans, G. Samaey

Culham Centre for Fusion Energy, Abingdon, GB: S. Schmuck

CEA Cadarache, Saint-Paul-lez-Durance, FR: A. da Silva, H. Fernandes, B. Goncalves, A. Grosman, M. Houry, V. Moncada, T. Ngo, S. Renard, J. M. Travere

Instituto de Plasmas e Fusao Nuclear, Lisboa, PT: B. Carvalho

CIEMAT, Madrid, ES: A. Alonso, E. Ascasibar, E. Blanco, I. Calvo, A. Cappa, D. Carralero, F. Castejon, A. de la Pena, H. Esteban, T. Estrada, J. Fontdecaba, M. I. Garcia Cortes, J. Garcia Regaña, C. Guerard, J. Hernandez, C. Hidalgo, D. Loesser, K. McCarthy, D. Medina Roque, L. Pacios Rodriguez, N. Panadero Alvarez, E. Sanchez, B. van Milligen, J.-L. Velasco, H. Zhang

Universidad Carlos III de Madrid, Madrid, ES: A. Gogoleva, L. Vela

University of Cagliari, Cagliari, IT: B. Cannas, F. Pisano

Universidad de Cordoba, Cordoba, ES: J. A. Alcúson

Consorzio RF X, Padova, IT: L. Carraro, L. Giudicotti, F. d'Isa, M. Spolaore, N. Vianello

University of Salerno, Fisciano SA, IT: R. Citarella, V. Giannella

ENEA Centro Ricerche Frascati, Frascati RM, IT: G. Claps, F. Cordella

University of Milano-Bicocca, Milano, IT: A. da Molin

Istituto di Fisica del Plasma Piero Caldirola, Milano, IT: M.-E. Puiatti, M. Romé

Austrian Academy of Science, Wien, AT: F. Köchl, R. Schrittwieser

Centre for Energy Research, Budapest, HU: G. Anda, A. Buzás, G. Cseh, B. Csillag, D. Dunai, G. Kocsis, D. Nagy, D. Réfy, T. Szabolics, T. Szepesi, M. Szűcs, M. Vécsei, S. Zoletnik

Institute of Plasma Physics and Laser Microfusion, Warsaw, PL: T. Fornal, A. Galkowski, M. Gruca, M. Jabłczyńska, S. Jablonski, J. Kacmarczyk, N. Wendler, M. Kubkowska, G. Pelka, L. Ryc

University of Szczecin, Szczecin, PL: M. Slecza, B. Zamorski

University of Opole, Opole, PL: I. Książek, K. Książek, E. Pawelec

Institute for Nuclear Research, Kiev, UA: Y. Kolesnichenko, V. Lutsenko

Institute of Plasma Physics, National Science Center, Kharkov Institute of Physics and Technology, Kharkov, UA: M. Dreval, A. Beletskii

Ioffe Physical-Technical Institute of the Russian Academy of Sciences, St Petersburg, RU: F. Chernyshev

Illinois State University, Normal, IL, US: A. Harris

Princeton Plasma Physics Laboratory, Princeton, NJ, US: D. Gates, B. Israeli, A. LeViness, D. Mikkelsen, J. Mittelstaedt, N. Pablant, A. Reiman, M. Sibilina, M. Zarnstorff, R. Lunsford

Massachusetts Institute of Technology, Cambridge, MA, US: S. G. Baek, J.-P. Böhner, S. Ballinger, S. K. Hansen, M. Porkolab, J. Terry, A. White, B. Wiegel

SUNY Cortland, Cortland, NY, USA: E. M. Edlund

University of Wisconsin-Madison, Madison, WI, US: D. Boyaert, A. Demby, B. J. Faber, H. Frerichs, B. Geiger, C. C. Hegna, G. Held, J. Hoffman, O. Schmitz, S. Sereda

Oak Ridge National Laboratory, Oak Ridge, TN, US: L. Baylor, M. Cianciosa, M. J. Cole, J. H. Harris, J. Lore, A. Lumsdaine, S. Meitner, D. A. Spong

Auburn University, Auburn, AL, US: D. Ennis, T. Gonda, M. Kriete, D. Maurer, J.C. Schmitt

University of Maryland, MD, US: M. Landreman

Los Alamos National Laboratory, Los Alamos, NM, US: G. Wurden

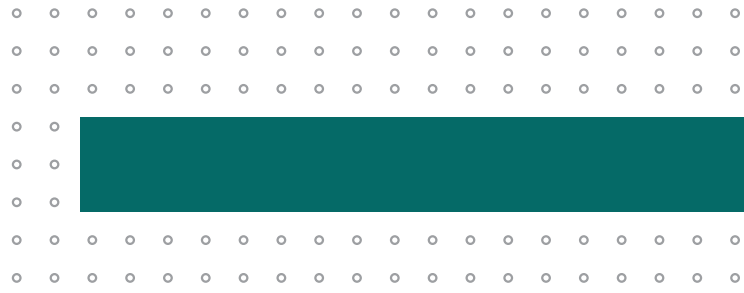
National Institute for Fusion Science, Toki, JP: T. Funaba, X. Huang, K. Ida, H. Kasahara, G. Kawamura, N. Kenmochi, M. Kobayashi, S. Masuzaki, T. Morisaki, K. Ogawa, S. Ohdachi, B. Peterson, S. Ryosuke, R. Sakamoto, S. Satake, C. Suzuki, N. Tamura, H. Tsuchiya, T. Tsujimura, H. Yamada, I. Yamada, R. Yasuhara, M. Yokoyama

Kyoto University, Yoshidahonmachi, Sakyo Ward, Kyoto, JP: K. Nagasaki, S. Ohshima, R. Matoike, A. Miyashita

Hiroshima University, Higashihiroshima JP: Y. Suzuki

Xantho Technologies, LLC: T. P. Crowley, D. R. Demers, P. Fimognari

The Australian National University, Canberra, AU: B. Blackwell, J. H. Matthew, A. Wright



DEMO

DEMO Design Activities

Head: Prof. Dr. Hartmut Zohm

The 'DEMO Design Activities' project focuses on aspects of physics and technology relevant for tokamak and stellarator designs, in line with the unique position of IPP following both lines. Many of the activities are carried out under the EUROfusion PPP&T Programme, where substantial EU collaborations exist. On the national level, the German DEMO Working Group, chaired by IPP, joining scientists from FZJ, IPP and KIT serves to strengthen collaboration and strategic planning.

Technology for DEMO Plants

IPP continues to contribute to the development of technology for DEMO plants on both sites in the areas of diagnostics, heating and current drive, fueling, PFCs and, more recently, plant electrical systems. Measurements of divertor thermo-currents by a target plate with shunt have proven to be a reliable diagnostic for divertor detachment control. Transferring this technique to DEMO requires development of a HHF PFC that is electrically isolated but thermally well connected and can survive the harsh DEMO environment. A promising concept using alumina/zirconia bushes has been designed and has passed initial tests. A back-up solution using Rogowski coils around the divertor cassette is also considered. An interface to SOLPS/EIRENE to calculate the level of thermo-current expected is being developed. FEM simulations of a recently proposed alternative DEMO divertor design with high temperature are also under way.

IPP is also responsible for developing the interferometer, which, due to the absence of a robust concept for a retro-reflector, is now employing toroidal sightlines, as shown in figure 1. While this concept rules out the use of polarimetry for vertical plasma position measurement, it still contributes to its determination using a vertical array of sightlines above and below the plasma center.

In the area of PFC development, the successful development of HHF target elements has been reported in the previous report has been continued. The ITER-like PFC has been shown to withstand severe overload conditions of 1500 pulses at 25 MW/m^2 without loss of performance in the GLADIS teststand at IPP.

In the area of ICRF heating, the antenna with toroidally arranged halves (see previous SR) was now adapted to full toroidal and poloidal geometry, and the design improved to increase the coupled power and minimize the near fields which is important for minimizing impurity production. The study of the influence of the propagating slow wave on the near fields was started for the case of low plasma density in the scrape-off layer. Also, new vacuum lines with vacuum window are being designed and optimized which meet the DEMO requirements in size and electrical fields. The lines will be tested with ASDEX Upgrade antennas.

For a DEMO NBI system IPP's focus was on assessing the feasibility of a beam-driven plasma neutraliser. In this concept the passing beam ionises the neutraliser gas and the presence of charged particles enhances the stripping of the beam's D^- ions, increasing neutralisation yield. Introducing particle and energy losses neglected in the previous

zero-dimensional model [1] reduced the prediction for the neutralisation yield from $\geq 80\%$ to $\approx 68\%$ [2], still attractive compared with 55% in a gas neutraliser. A proof of principle experiment to test the model predictions for the achievable plasma density at relevant parameters is in the design phase.

Recovery of the residual ions' kinetic energy by electrostatic deceleration was also investigated for a realistic conceptual design. It was shown that deceleration down to 5% of the beam energy is possible, but the net efficiency gain crucially depends on beamline pressure.

In a tokamak, the fluctuating reactive power in the PF coil system can easily reach values of the order of 100 MVar , which calls for efficient electrical storage that can buffer the fast changes. Supercapacitors offer a new route to solve this problem, and are being explored at IPP. A full topology of a large storage consisting of more than 2000 individual sub-modules has been designed [3], and an individual sub-module was tested to full specification [4]. Also, parallel operation of four modules was demonstrated and followed well the theoretical expectation in terms of balanced current sharing and temporal response [5].

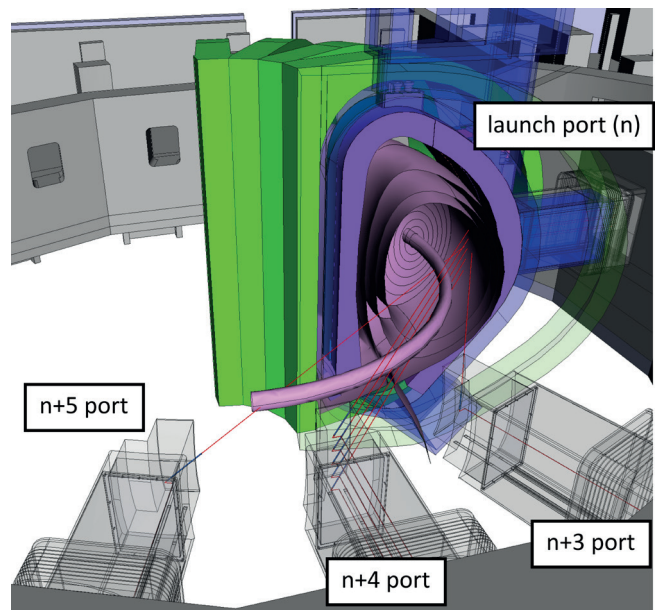


Figure 1. Conceptual design of a toroidally viewing interferometry diagnostic for EU DEMO.

Studies on a Stellarator FPP

In the context of evaluating stellarators as future fusion power plants, one important question is to which degree the large 3D design space can be leveraged to find optimal economical stellarator reactor design points.

The recent development of the stellarator version of the systems code PROCESS allows to quantify the relative importance of several

optimization parameters with respect to the economics of the plant in an integrated way. For example, it is now possible to model how much more economical a reduction of the neutron wall load (NWL) compared to an improvement of the confinement factor is, for a certain set of physics and technological assumptions (e.g. for a fixed upper NWL and for a fixed machine).

An example of such a comparison of the sensitivity of several key optimization parameters obtained with stellarator-PROCESS that could be design for is shown in figure 2.

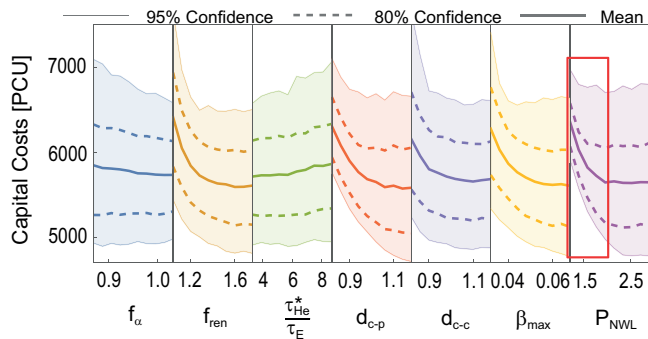


Figure 2. Sensitivity of characteristic stellarator parameters with respect to capital costs of a HELIAS power plant with 1 GWe. From Left: Fast particle confinement fraction, ISS04 confinement factor, thermal helium confinement time ratio, min. coil-plasma distance, min. coil-coil distance, maximal allowable beta, max. allowable NWL. Capital costs are provided in PROCESS Cost Units (PCU) and should serve as relative comparison only.

One of the conclusions of such an exercise is the importance of easing the NWL requirements in a HELIAS design. This can be seen in figure 2 as indicated by the red box, which points at a strong correlation between the maximum imposed NWL limit and economics of the plant. It is thus likely worth exploring methods to decrease the peak NWL. If not taken care of, stellarators suffer from inhomogeneities of neutron loads at the first wall and in the blanket volume, due to their typically irregular plasma geometries. One approach to overcome this issue and thus at the same time to reduce the peak NWL, is an optimization of the first wall geometry with respect to the peak neutron loads, which was recently demonstrated in a HELIAS-5 design.

EU Tokamak DEMO Scenario

IPP is strongly involved in the newly established DEMO Central Team of EUROfusion, leading the Plasma System Division. In the reporting period, a tentative plasma scenario has been identified, consisting of

- ‘hybrid’ core with central $q(r) > 1$ clamped by flux pumping
- ELM-free edge in the QCE regime (see AUG part of this SR), with RMP ELM suppression as back-up
- conventional detached divertor relying on high core radiation fraction such that $P_{sep} = 1.2 P_{LH}$

For these three elements, critical knowledge gaps have been identified and research is carried out over the whole EUROfusion experimental and theoretical programme to close these. In addition, missing technical capabilities, such as 3-D coils for ELM suppression) were identified and are being implemented together with the engineering division of the DCT.

A development originating from the ASDEX Upgrade Control Group is the flight simulator Fenix. After kinetic (burn) control was already studied under flattop conditions, Fenix-DEMO has now been upgraded, in a collaboration with CREATE, to include self-consistent control of the magnetic equilibrium using a newly developed free boundary solver for use with the ASTRA transport code. This allows to study dynamic phases such as ramp-up or down of the plasma in a realistic way, which is needed e.g. for evaluation of control margins or the total poloidal flux consumption.

Using the ASTRA code, we also studied the possibility of heating the DEMO plasma to burn with ECRH only [7]. These studies show that for a broad range of assumptions on transport and impurity concentrations, it should be possible to access H-mode operation since in the large DEMO plasma, the majority of the heat flux is transferred to the ion channel at the plasma edge. This can be seen in figure 3. Once this is achieved, the combination of ECRH and α -power provides a path to a stationary burn point.

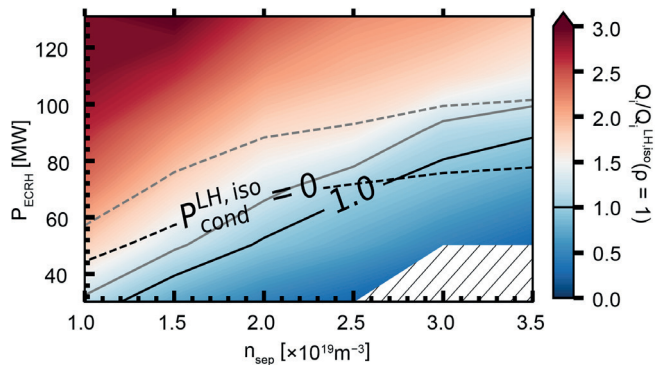


Figure 3. Contour plot of ion heat flux at the separatrix normalized to the requirement predicted by the L-H scaling in [6], as function of separatrix density and ECRH power. The dashed line indicates the LH power threshold from the Martin scaling. In this case, realistic impurity concentrations of 8 % He and 0.1 % Ar were assumed. It can be seen that within the planned installed ECRH power of 130 MW, there is a large operational window to access H-mode.

Scientific Staff

C. Angioni, M. Beurskens, V. Bobkov, K.-J. Brunner, P. David, E. Fable, U. Fantz, H. Faugel, T. Franke, L. Giannone, O. Girka, T. Härtl, C. Hopf, P. T. Lang, J. Lion, A. Kallenbach, A. Magnanimo, R. Neu, R. Ochoukov, B. Plöckl, E. Poli, M. Teschke, M. Siccino, J. Stober, G. Suarez-Lopez, W. Treutterer, M. Usovltceva, T. Vierle, F. Warmer, M. Weissgerber, R. Wolf, J.-H. You, I. Zammuto, H. Zohm



Plasma-Wall Interactions and Materials

Plasma-Wall Interaction

Head: Prof. Dr. Rudolf Neu

Within the project "Plasma-Wall Interaction" the areas of plasma-surface-interaction studies, material modification under plasma exposure, development of new plasma-facing materials and their characterisation have been merged to form a field of competence at IPP. The work supports exploration and further development of the fusion devices at IPP and generates basic expertise with regard to PFC-related questions in ITER, DEMO and future fusion reactors.

Surface Processes on Plasma-Exposed Materials Influence of Displacement-damage on Helium Penetration into Tungsten

Helium (He) will be produced in the fusion reaction and finally impinge on the walls surrounding the fusion plasma. Implanted He will change the behavior of wall materials in particular with respect to hydrogen retention properties. One open question is whether or not the penetration of He into larger depth of the material depends on the local defect density. To study these effects the influence of preexisting displacement damage on the early stages of He interaction with tungsten (W) and the resulting defect creation was investigated experimentally. Displacement-damaged samples were exposed to a He plasma applying a He ion energy of 100 eV at a sample temperature of 300 K.

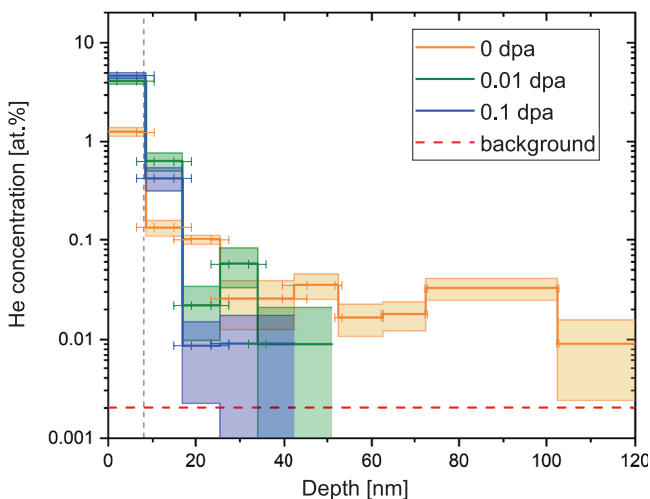


Figure 1. Helium depth profiles in polycrystalline W samples after exposure to 10^{21} He/m². The orange line shows the depth profile of the undamaged sample, the green and blue lines refer to samples damaged to 0.01 dpa and 0.1 dpa, respectively. The faded colored areas indicate the range of uncertainty. The dashed vertical grey line shows the calculated maximum implantation depth of the impinging 100 eV He ions. The red line indicates the sensitivity limit of the ERDA measurements.

Elastic recoil detection analysis (ERDA) shows that the He retention in the damaged samples is one order of magnitude larger than in the

undamaged sample. Detailed He depth distributions were derived by stepwise removal of nearsurface layers and subsequent ERDA measurements of the remaining He content. Pre-damaged samples show a significantly faster decrease in He retention with depth than the undamaged sample (see figure 1), indicating that pre-existing defects substantially decrease the diffusion of He into deeper regions. The undamaged sample exhibits a lower He concentration in the near surface region and a flatter distribution of He up to a depth of 100 nm [1].

Sputtering of Steel Grades Developed for Fusion Applications

Various grades of Reduced Activation Ferritic Martensitic (RAFM) steel grades were developed around the globe as structural material for future fusion power plants. The behavior of the three RAFM steels EUROFER, RUSFER and CLAM – developed in Europe, Russia and China, respectively – was thoroughly investigated and compared after bombardment with energetic deuterium in the IPP SIESTA facility. Quantification of the sputter yield was accompanied by thorough investigation of changes of the surface morphology with Scanning Electron Microscopy. Furthermore, Nuclear Reaction Analysis and Thermal Desorption Spectrometry were employed to analyze deuterium retention in all the samples. The erosion behavior of all three steels under deuterium bombardment was confirmed to be similar. The measured sputter yield was comparable for all three steels, and significantly lower than that of pure Fe. Likewise, all steels develop a needle-like surface morphology under the given exposure conditions and a W- and Ta-enriched layer in the range of a few nanometers, while the Fe sample remained smooth. Retained deuterium amounts were also comparable among the steel samples, and were overall larger than the retention measured for the pure Fe sample. From these results it can be concluded that all three steel grades behave comparably under exposure to boundary plasmas [2].

Arc Behaviour on Different Materials in ASDEX Upgrade

Arcs, a source of dust particles and a localized erosion mechanism of the plasma-facing components, are found in all major fusion plasma devices. To allow extrapolation to future fusion devices different materials are used to study the influence of the material properties on arcing. In AUG, inserts were installed at the inner baffle region to quantify erosion. The use of polished inserts allows an accurate determination of the arc traces by depth maps obtained by laser profilometry. It turned out that the melting temperature of the materials is the main parameter for erosion. For tungsten mounted at the inner baffle, a region that is deposition dominated, an erosion rate by arcing of 1.2×10^{13} at $\text{cm}^{-2} \text{s}^{-1}$ was measured. For Beryllium, 9.5×10^{13} at $\text{cm}^{-2} \text{s}^{-1}$ is extrapolated from its thermal properties. As martensitic-ferritic low-activation steel is under discussion for the use in DEMO, magnetic steels were also investigated. Comparing stainless steel with magnetic steel, much deeper and wider craters are found in the latter one: they reach an erosion depth of up to 80 μm .

The erosion of magnetic steel by arcs is 40 times higher compared with stainless steel, which has almost the same physical properties [3].

Erosion and Redeposition Patterns after Exposure in WEST

The net erosion and deposition patterns in the inner and outer divertor of WEST were determined after different experimental campaigns (C3 and C4) of the first operational phase using ion beam analyses and scanning electron microscopy techniques. The analyses were performed on four entire tiles from inertially cooled, W-coated divertor units with an additional Mo marker coating covered with a further W coating. Strong erosion occurred at the expected location of the inner and outer strike line area with a campaign-averaged net erosion rate of $> 0.1 \text{ nm s}^{-1}$. On the high field side of the inner strike line area, thick deposited layers were found ($> 10 \mu\text{m}$; growth rate $> 1 \text{ nm s}^{-1}$), mainly composed of B, C, O, and W. Additionally, strong arcing was observed in this region. At the end of the C4 campaign, He discharges were performed to study the He-W interaction. Although the conditions for nanotendrils, i.e. fuzz formation, were fulfilled around the outer strike line position, neither nanotendrils nor He bubbles ($> 10 \text{ nm}$) were observed at this area [4].

WallDYN-3D Predictions for Tritium Co-deposition in ITER

The retention by co-deposition of fuel species in Beryllium (Be) layers, forming due to migration of Be eroded from the 3D-shaped main chamber wall in ITER, was modelled with WallDYN-3D. The influence of the 3D shaping of the first wall on the locations of Be layer formation was compared with previous 2D calculations for a perfectly toroidally symmetric main chamber Be wall. The 3D shaping results in a large number of partially plasma-shadowed regions in the main chamber, where Be can deposit and form layers. Depending on the main chamber plasma solution, this results in a shift of the primary Be layer deposition location from the divertor in 2D to the main chamber in 3D calculations. The deposition location is important because the higher average hydrogen isotope (HI) particle energy in the main chamber affects HI content in the co-deposited layers. However, for the currently available HI/Be scaling laws the resulting increase in HI/Be is small. A comparison of the 3D-shaped Be main chamber erosion calculated recently by ERO2.0 and by WallDYN-3D in this work, shows very similar erosion patterns. However, differences exist in the deposition locations because, in contrast to ERO2.0, WallDYN-3D takes re-erosion of deposited Be into account. To match the absolute amount of Be erosion the Be-sputter yields used by WallDYN-3D have to be increased by a factor of 1.5, due to a different erosion yield database used by ERO2.0 which results in higher yields at oblique impact angles. This uncertainty in the sputter yield, but also in the HI/Be scaling laws, make an uncertainty quantification necessary. Applying polynomial chaos expansion to the Be layer growth rate and HI-retention rate by co-deposition, yields an uncertainty of about 100 % in both quantities, due to the uncertainties in the sputter yields and the fit parameters of the HI/Be scaling laws [5].

Tritium Inventory – Understanding and Control Hydrogen Isotope Trapping and Release from Cavities in Tungsten

Plasma-facing components (PFCs) in future fusion power plants will be subjected to high fluxes of 14 MeV neutrons. This will result in the production of displacement damage. Furthermore, PFCs will operate at elevated temperatures. Such conditions will favour the formation of nm-sized cavities in metallic PFCs. Cavities will act as trapping sites for hydrogen (H) isotopes. Contrary to other lattice defects (vacancies, small vacancy clusters, dislocations, etc.), H_2 gas precipitation can take place in the cavity volume. So far, a rigorous description of the kinetics of H trapping and release from cavities in metals is missing.

First, 3D simulations of H interaction with a single nm-sized spherical cavity in tungsten (W) were performed [6]. The simulations considered diffusive transport of H in W with the boundary condition at the cavity surface provided by the kinetic model of H_2 gas interaction with metal surfaces. It was shown that the previously used approaches based on local thermodynamic equilibrium between H_2 gas in the cavity and the surrounding solute H are inadequate for simulating thermal desorption spectra (TDS) from cavities. The features of TDS spectra from cavities are different compared with TDS spectra from point defects described by the conventional reaction-diffusion models. In particular, H release from a gas-filled cavity at a fixed temperature (below the TDS peak) stays constant for some time, in contrast to exponential decay observed for point defects. Concurrently, a constant release rate is also found during equilibrium decomposition of metal hydride precipitates. Therefore, constant release rate at a fixed temperature cannot serve as an exclusive proof of the presence of gas-filled cavities or hydride precipitates. A simplified analytic model allowing to explain the features of TDS spectra from cavities was developed.

Next, a novel reaction-diffusion model describing H trapping and release from an array of cavities in a metal was developed [7]. It considers the kinetics of H atom trapping in chemisorption sites at the cavity surface and H_2 molecule precipitation in the cavity volume. In the case of low cavity number density $N_c \ll 1/(4\pi R L^2)$ (R is the cavity radius and L is the width of the region containing cavities), there is a negligible effect of re trapping on H transport during TDS. The features of TDS spectra are identical to the previously considered case of a single cavity. At high cavity number densities $N_c \gg 1/(4\pi R L^2)$ re trapping effects are significant. This results in broadening of the TDS peak and its shift to higher temperatures. In contrast with the case of low cavity number density, constant desorption rate at a fixed temperature is not observed. Furthermore, the dependence of the TDS peak position on the heating rate is different compared with the case of low cavity number density. A simplified analytic model that allows to explain the observed features was developed.

The dynamics of H transport and trapping in a metal containing cavities differs significantly from the case of point defects. The difference is especially pronounced at low temperatures, when the local thermodynamic equilibrium between the solute H and H_2 gas is not reached on a practical time scale. Such non-equilibrium effects are particularly important for metals with low H solubility, such as W and Be. Unlike the TDS spectra described by the conventional model for point defects, the TDS spectra from cavities exhibit a sharp rising edge. Such spectra cannot be fitted using the conventional model for point defects, unless *ad hoc* assumptions like reduced re trapping, surface-limited release, etc. are imposed. Overall, for making reliable predictions of H isotope transport, trapping, and release during baking in fusion devices, cavities have to be treated rigorously in reaction-diffusion models.

Influence of Oxygen on Hydrogen Retention in and Release from Tungsten

For practical reasons the overwhelming majority of experiments studying HI retention in W is carried out “ex situ” meaning that the W samples have contact with ambient air before and in between experimental steps, e.g., between D plasma loading and ion beam analysis. Due to its affinity for oxygen, W readily forms a thin natural oxide film on the sample surface under ambient conditions. Due to its low thickness of only 1–2 nm, the influence of such natural oxide films has been considered to be negligible. Recently, however, it has been found that natural oxide films on W may have a significant effect on the release of HIs from W. This is an important point, as these natural surface oxide films are present in all ex situ laboratory experiments (and also in most in situ experiments if not great efforts are undertaken to remove them) but not in a fusion reactor, where they would most likely be reduced by the fusion plasma, at least for directly plasma-exposed surfaces. Therefore, any effects the natural oxide films might have would represent an unaccounted difference between laboratory studies and reactor-relevant conditions.

In a first set of experiments the uptake of deuterium (D) into tungsten (W) through thin W oxide films after exposure to low-temperature D plasma was studied. A defect-rich layer of self-damaged W underneath the oxide was used as a getter layer to enable the detection of D that penetrates the oxide film. Depth-resolved concentration profiles of D and oxygen (O) measured by ion beam analyses revealed that oxygen is partially removed from the uppermost atomic layers (≈ 13.5 nm) creating a W-enriched near surface region. Furthermore, D accumulates in the oxide film to concentrations of up to 1.3 at. %, but does not penetrate into the underlying W. Sufficiently thick surface oxide films on W effectively block D uptake into metallic W. However, this is not limited by the transport in the oxide film itself – D diffuses fast throughout the oxide but is stopped at the interface to the metallic W – but due to the difference in the heat of solution for D in W oxide and metallic W. D cannot overcome this barrier once it is thermalized within the W oxide film [8].

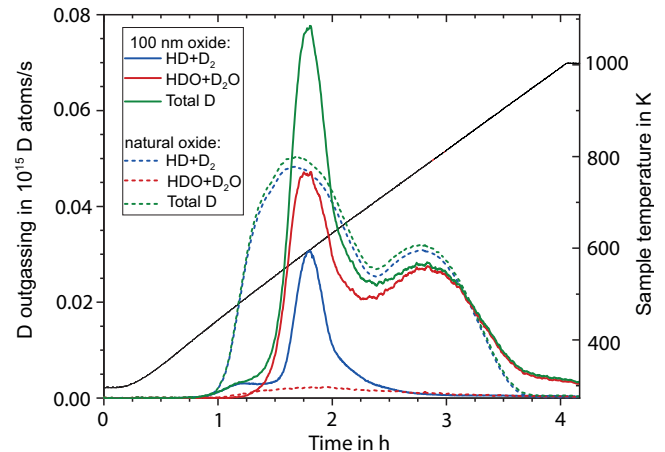


Figure 2. Comparison of the released deuterium amounts from tungsten with a natural oxide layer and with a 100 nm thick oxide layer as measured by TDS (3 K/min ramp to 1000 K). The straight black line shows the temperature ramp of 3/K min, with units on the right y-axis. Plotted are the total released amounts and the fractions released in form of molecular hydrogen (D_2 and HD) and heavy water (HDO and D_2O). The thick oxide layer causes a shift of the main desorption peak to higher temperature and a dramatic change of the release spectrum. In the sample with the natural oxide, release is dominated by molecular hydrogen (blue lines), while the sample with the thick oxide layer releases dominantly heavy water (red lines). In particular, the peak at higher temperature is only due to released heavy water.

In a second series of experiments the influence of oxide layers with thicknesses ranging from 5 to 100 nm on the release of HIs was studied. The outgassing of D through the oxide film was analysed with thermal desorption spectroscopy (TDS). Thin oxide films significantly influence the release behaviour. The first D release peak (at 560 K) is shifted towards higher temperature with increasing oxide thickness. This indicates that the oxide film acts as both a D reservoir and a transport barrier that delays D release at temperatures above 475 K. At this temperature, D also starts to interact chemically with the oxide film and is released not only as HD or D_2 but also in the form of heavy water (HDO and D_2O). Above 700 K, D is released only in form of heavy water as long as enough oxide is available. Our results indicate that the oxide film becomes relevant for the D release during TDS if the ratio of O atoms at the surface to D atoms in the sample is larger than 5–10 %. Consequently, even the natural oxide film (1–2 nm) that forms on W upon contact with air may significantly influence the D release spectra from TDS for experiments with low D retention [9].

Deuterium Retention in Tungsten Fibre-Reinforced Tungsten Composites

Tungsten fibre-reinforced tungsten (W_f/W), a tungsten matrix containing drawn tungsten fibres, was developed to mitigate the intrinsic brittleness problem of W by using extrinsic toughening mechanisms

to achieve pseudo-ductility. The deuterium (D) retention in W_f/W manufactured by chemical vapor deposition (CVD) has been investigated using W_f/W single layered model systems consisting of a single plane of unidirectional tungsten fibres embedded in a tungsten matrix produced by CVD. Various parameters with potential influence on the D retention, such as the choice of an interface and potassium doping, have been included in the investigation. The samples were exposed to a low-temperature D plasma at 370 K to a total fluence of 10^{25} D/m². The D retention of all samples was measured by nuclear reaction analysis (NRA) and TDS revealing that it is higher than in reference samples made from hot-rolled W by factors between 2 and 5. In addition, a comparison of NRA and TDS data indicates that D penetrates faster into the depth of W_f/W material than into hot-rolled tungsten [10].

Tritium Permeation and Retention in DEMO

Tritium self-sufficiency presents a critical engineering challenge for DEMO, requiring efficient breeding and extraction systems, as well as minimizing tritium losses to the surrounding systems, such as plasma-facing components, vacuum vessel, cooling system, etc. Structural and plasma-facing components will act as a tritium sink, as tritium will be accumulated in the bulk of these components due to energetic particle bombardment and may permeate out of the vacuum system. The design of the plasma-facing components will consequently directly influence the plant lifetime, operational safety and cost of any future power plant. Therefore, modelling of tritium retention and permeation in these components is required for the engineering designs of the tritium breeding and safety systems. In this respect, the diffusion-transport code TESSIM-X was benchmarked against the well-established TMAP7 code and a comparison with a simplified DEMO-relevant test case was performed. Following this, TESSIM-X was applied to provide a preliminary assessment of tritium permeation and retention in the DEMO first wall, based on the current WCLL (Water Cooled Lithium Lead) and HCPB (Helium Cooled Pebble Bed) breeding blanket designs [11].

Materials and Components

Behaviour of DEMO PFC Mock-Ups under Cyclic Load

A reliable high-heat-flux (HHF) technology is one of the crucial requirements of power exhaust strategy for a fusion reactor. The baseline HHF technology of the EU-DEMO, which inherited mostly the ITER technology, is based on the tungsten monoblock design and hot radial pressing joining technique. Thermal resilience and structural integrity under all off-normal transient events foreseen are essential prerequisites for validation of the technology towards demonstration of full-scale prototype manufacture. Therefore, the HHF performance of the baseline technology needs to be evaluated also in the transient overload regime. To this end, an extensive HHF testing campaign was

pursued at IPP's neutral beam high heat flux test facility GLADIS using small-scale test mock-ups of the tungsten monoblock target for two slow (10 s) overloads at 20 MW/m² (up to 2000 pulses) and 25 MW/m² (1000 pulses), and for a short (0.4 s) overload at 40 MW/m² (5000 pulses). Finally, excessive heat loads (35 MW/m²) were applied beyond the armour melting event to test the structural stability. IR thermography, ultrasonic inspection and electron microscopy (EBSD) delivered direct information and insight on the structural integrity and the impact on the armour microstructure. It was found that the tungsten monoblock target remained fully intact at least up to 1000 heating cycles at 20 MW/m² and survived 2000 cycles without any major failure. At 25 MW/m², the mock-ups remained nearly intact at least up to 500 heating cycles and survived 1000 cycles without critical failure. However, the armour surface showed substantial deformation and roughening with the height of 1000 µm after 1000 cycles. At 40 MW/m² with short pulses, the mock-ups remained fully intact without any serious damage at least up to 5000 cycles. The mock-ups even withstood the limit heat load of 32 MW/m² at least for several pulses [12].

Additively Manufactured Plasma-Facing Components

The term additive manufacturing (AM) describes fabrication processes with which three-dimensional objects are realised by means of sequential layerwise deposition of material under computer control. With respect to plasma-facing components (PFC), AM could be very beneficial and allow further unexploited PFC performance enhancements. Recently, substantial progress regarding the AM of pure W was achieved by the project in collaboration with Fraunhofer IGCV through the use of laser powder bed fusion (LPBF) processes. In recent investigations several aspects were highlighted: There is a strong influence of the powder characteristics on the built part quality and, as expected, spheroidised W powders are best suited for LPBF processing.



Figure 3. Tungsten lattice builds additively manufactured by the laser powder bed fusion method (sample dimensions: 10×10×10 mm³, 15×15×15 mm³, 20×20×20 mm³).

Specifically, thin-walled test parts exhibited distinct differences in built part quality in terms of porosity and surface quality depending on the type of raw powder material used. With these preparatory investigations, it was possible to fabricate complexly shaped W lattice structure samples (see figure 3). In a further step, additively manufactured W structures were used as a preform for Cu infiltrated W-Cu composites for complete high-heat flux PFCs which potentially could solve issues of joining the Cu heat sink to the W armour material [13].

DEMO Limiter Armour for Extreme Heat Fluxes

Off-normal global plasma instabilities possibly occurring in a fusion power plant represent the most critical operational accidents and pose a serious risk to economically viable exploitation of fusion power. During such an instability, the plasma energy is rapidly deposited onto the first wall which can cause severe damages or a fatal failure of the first wall even by a single event. To cope with this issue, a limiter concept is developed within the European DEMO project under IPP's leadership. The limiters shall be installed at those wall areas where plasma contact is expected and its front face shall be covered with sacrificial tungsten armour. To implement the limiter concept, comprehensive engineering efforts were pursued including conceptual design study and technology R&D to manufacture the armor material and joint. The sacrificial armour should have a reduced thermal conductivity to mitigate the impact of extreme heat flux pulses for protecting the heat sink. The R&D focus was put on the advanced additive manufacturing technology based on the powder bed fusion laser printing technique. A novel lattice-type tungsten armor material was developed and fabricated (see figure 3). These materials were tested under extreme heat flux loads at a QSPA facility at KIPT in Kharkov showing a similar response of the tungsten lattice material as dense tungsten for the modest absorbed energy density range of up to 1.2 MJ/m^2 [14].

Resilience of Tungsten Fibres Against Irradiation Effects

The effect of the fusion environment on the mechanical properties of tungsten fibre-reinforced composites, e.g. the embrittlement by neutron irradiation, plays a key role for its use in future fusion reactors. To simulate this effect, high-energy ions are used as a substitute for the displacement damage by neutrons. The use of very fine tungsten wires allows studying the influence of irradiation damage on the mechanical properties because a full-depth irradiation of almost the entire volume is possible despite the limited penetration depth of ions. Geometrical size effects are mitigated due to the nanoscale microstructure of the wire. W wires with an initial diameter of $16 \mu\text{m}$ were electrochemically thinned to $5 \mu\text{m}$ and irradiated with 20.5 MeV W^{6+} ions and the mechanical properties were subsequently determined by macroscopic tensile testing. Irradiation to 0.3, 1 and 9 dpa did not lead to any change of the mechanical behaviour. Both strength and ductility, the latter indicated by the reduction of area, were similar to the as-fabricated state pointing to a substantial resilience against radiation damage [15].

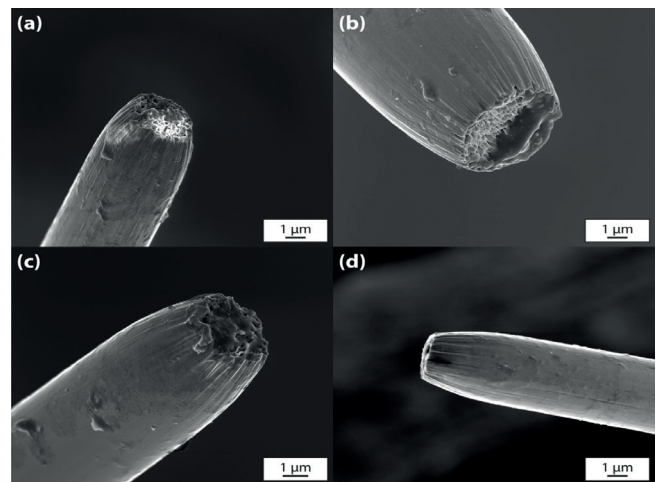


Figure 4. Typical fracture surfaces of tensile tests on drawn tungsten wire with a diameter of $5 \mu\text{m}$ in (a) non-irradiated state and after irradiation to (b) 0.3 dpa, (c) 1 dpa and (d) 9 dpa. All samples show pronounced necking pointing to the retained ductility.

Interlayer Properties of Tungsten Fibre-Reinforced Composites

In tungsten fibre-reinforced composites the interlayer between the tungsten fibre and tungsten matrix enables the activation of extrinsic mechanisms to improve the toughness similar to ceramic fibre-reinforced ceramics. In addition, the evaluation of the interlayer parameter is necessary to model the composite behaviour. Therefore, single fibre model systems with Er_2O_3 and Y_2O_3 as interlayer were evaluated by push-out and pull-out tests. The results were used to determine the interfacial shear strength, the interfacial frictional shear stress and the fracture energy of the interlayer. In addition, tensile tests on the composite material were performed to evaluate the interfacial frictional shear stress. It became evident that there is a strong influence of the testing method and that pull-out tests are superior to push-out. Both interlayer systems provide the interfacial properties to allow for the necessary fibre-matrix debonding necessary to reach the pseudo-ductile behaviour of the W composite [16].

Charpy Impact Tests of Tungsten Fibre-Reinforced Composite from $-150 \text{ }^\circ\text{C}$ to $1000 \text{ }^\circ\text{C}$

Tungsten fibre-reinforced composites have the potential to overcome brittleness at room temperature and the potential embrittlement during operation. Charpy impact tests ranging from $-150 \text{ }^\circ\text{C}$ to $1000 \text{ }^\circ\text{C}$ have been performed in order to identify the ductile-to-brittle transition temperature (DBTT). For the W fibre a DBTT between $-100 \text{ }^\circ\text{C}$ to $-50 \text{ }^\circ\text{C}$ has been found whereas the matrix behaves ductile only from $1000 \text{ }^\circ\text{C}$ on. The low DBTT of the fibres is caused by their special microstructure resulting from wire drawing. The high DBTT of the W matrix might be caused by fluorine impurities (stemming from the

chemical vapour deposition), which could possibly be suppressed by an optimization of the deposition process [17].

Cold Spray Tungsten Coatings for Plasma-Facing Applications

Cold spray for the production of thick tungsten (W) coatings has been investigated for use at plasma-facing components. Since the brittle nature of W strongly impedes its deposition, a systematic study was performed using mixtures of tungsten and tantalum (Ta) powders. Whereas the use of 100 % W powder was not successful yet, 2 mm thick coatings on steel were produced by using a W/Ta powder mixture with 90 vol. % W, yielding a W content in the coating of 70 vol. %. The coatings show negligible porosity and very good adhesion to the substrate. High heat flux experiments have been performed in GLADIS on samples with the size 80 × 80 mm² in order to investigate the behaviour under low (≤ 4 MW/m²) steady state loads and high power (~ 40 MW/m²) transients. During the pulses with low-power density, being typical for applications at the main chamber first wall, no defects were observed and a thermal conductivity close to that of the bulk materials was found. During the high-power transients lasting for 200 ms cracks parallel to the surface appeared inside the coating [18].

Integration of and Collaboration in the EU Programs

Within the new EUROfusion work programme under Horizon 2020 and Horizon Europe (from 2021 on) some members of the project are involved in the scientific exploitation of the European tokamaks under the Taskforces WPJET1 and WPMST1/WPTE, but the project's main activities under EUROfusion are centred within the work packages WPPFC/WPPWIE, WPDIV, WPMAT, WPJET2 and WPLMD/WPPRD.

Work Package Plasma-Facing Components / Plasma-Wall Interaction and Exhaust (WPPFC/WPPWIE)

The work within WPPFC/WPPWIE (from 2021 on) comprises several subprojects dealing with subjects centred around investigations on plasma-material interaction in linear and laboratory devices as well as fusion devices. IPP is strongly involved in five of the subprojects and provides the subproject leader for 'Retention and Release'.

Work Package Divertor (WPDIV)

The scope of the Divertor Project (WPDIV) covers all elements of conceptual design for the whole divertor system of the first DEMO reactor. From 2021 WPDIV also coordinates investigations for the divertors of DTT, JT-60 SA and W7-X (W PFCs). IPP provides the project leader as well as one of the subproject leaders of WPDIV and is involved in all 4 subprojects for development and testing and analysis of high heat flux components. Within the work package IPP's high heat flux facility GLADIS is operated as a 'technology hub'.

Work Package Materials (WPMAT)

Within WPMAT materials for a Demonstration Fusion Power Plant are developed. The work of IPP concentrates on the development of high heat flux materials namely as tungsten copper composites as well as tungsten alloys as an armour for plasma-facing components.

Work Package Liquid Metal Divertor / Perspective Research (WPLMD/WPPRD)

The work package LMD (WPLMD) investigated the possibility of using liquid metal as armour material for plasma-facing components. Until 2020 IPP performed detailed investigation on the behaviour of (solid/liquid) tin under low-energy plasma irradiation. From 2021 the PWI project is involved in investigations for the test of liquid tin in divertor of AUG within WPPRD. The development of W_f/W performed within WPMAT until 2020 is now performed within WPPRD.

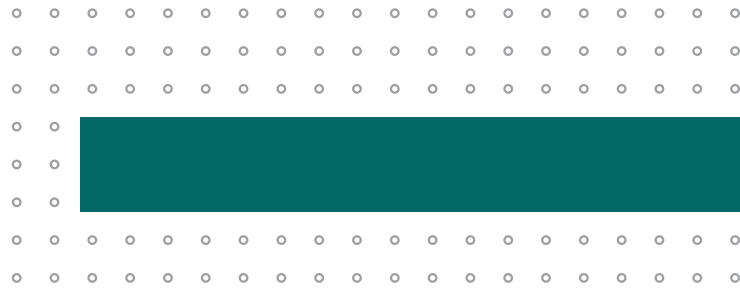
Work Package JET2 (WPJET2)

The work package JET2 (WPJET2) aimed at the exploitation of the JET ITER-Like Wall (ILW) in view of the erosion/deposition pattern and fuel inventory of the plasma-facing components. IPP was responsible for the nuclear reaction analysis of specific tungsten components. The work package has been integrated into WPPWIE from 2021 on.

Scientific Staff

R. Arredondo Parra¹, M. Balden¹, J. Boscary¹, M. Bösser¹, B. Böswirth¹, D. Brida¹, A. Castillo Castillo¹, B. Curzadd¹, R. de Luca^{1,7}, C. P. Dhard^{1a}, J. Dörner¹, T. Dürbeck¹, R. Dux¹, G. Ehrke^{1a}, S. Elgeti¹, M. Faitsch¹, A. Feichtmayer¹, M. Fuhr¹, M. Fußeder¹, H. Greuner¹, A. Herrmann¹, T. Höschen¹, K. Hunger¹, W. Jacob¹, P. Junghanns¹, A. Kärcher¹, K. Kremer¹, K. Krieger¹, N. Kwak⁸, R. Lürbke¹, H. Maier¹, A. Manhard¹, M. Mayer¹, D. Naujoks^{1a}, N. Nemati¹, R. Neu^{1,3}, U. Potoschnik¹, J. Riesch¹, V. Rohde¹, P. Sand¹, K. Schlüter¹, K. Schmid¹, J. Scholte⁹, T. Schwarz-Selinger¹, J. Skrotzki^{1,10}, U. Stroth^{1,2}, A. von Müller¹, U. von Toussaint¹, B. Wielunski^{1,6}, M. Wischmeier^{1,5}, J.-H. You^{1,3}, I. Zammuto¹, K. Zhang¹, M. Zibrov¹

¹ IPP Garching, DE – ^{1a} IPP Greifswald, DE – ² Department of Physics E28, Technical University of Munich, DE – ³ Department of Mechanical Engineering, Plasma Material Interaction, Technical University of Munich, DE – ⁴ Faculty of Natural Sciences, Ulm University, DE – ⁵ Faculty of Mathematics, Natural Sciences, and Materials Engineering, Experimental Plasma Physics, Augsburg University, DE – ⁶ Warsaw University of Technology, Warsaw, PL – ⁷ Department of Economics, Engineering, Society and Business Organization, University Tuscia, Frascati, IT – ⁸ College of Engineering, Department of Materials Science and Engineering, Seoul National University, KR – ⁹ Dutch Institute for Fundamental Energy Research (DIFFER), Eindhoven, NL – ¹⁰ Leipzig University of Applied Sciences (HTWK), Leipzig, DE



Plasma Theory

Theoretical Plasma Physics

Heads: Prof. Dr. Sibylle Günter, Prof. Dr. Per Helander, Prof. Dr. Frank Jenko, Prof. Dr. Eric Sonnendrücker

The project "Theoretical Plasma Physics" is devoted to the development of theories and advanced simulations for laboratory and astrophysical plasmas based on first principles. It combines the efforts within the divisions Tokamak Theory, Stellarator Theory, and Numerical Methods in Plasma Physics (including an Advanced Computing Hub supported by EUROfusion). It is also a major partner in the Max Planck / Princeton Center for Plasma Physics.

1 Tokamak Theory

Head: Prof. Dr. Frank Jenko

The research activities within Tokamak Theory Division (TOK) at Garching span a wide range of topics and methodologies. In fusion physics, both analytical and computational are used in tandem to explore various aspects of plasma behavior, from turbulent and neo-classical transport to heating and current drive to edge and scrape-off layer physics. While most of these efforts are focused on tokamaks, extensions to stellarators are also pursued. Moreover, many members of TOK are actively involved in various experiments, including ASDEX Upgrade, JET, and Wendelstein 7-X. A recent new emphasis has been to apply machine learning techniques to the analysis of experimental data and the acceleration of computer simulations, mainly in the context of the Munich School for Data Science (MuDS). In addition to all of this, there exists a growing effort in plasma astrophysics, in particular within the framework of the Excellence Cluster ORIGINS, which involves both large universities as well as several Max Planck Institutes (IPP, MPP, MPA, MPE) at Munich. In this context, Prof. Jenko also serves as a member of the Research Board and the Council, and as coordinator of Connector CN-6 on Cosmic Accelerators. Embedded within TOK is a Young Investigator Group led by Dr. Daniel Told which bridges fusion-related and astrophysics-related plasma theory. TOK's research activities in the area of plasma astrophysics are described elsewhere in this report.

1.1 Analytical Calculations, Advanced Simulations, and Scientific Machine Learning

Methodologically, our analytical and computational studies are deeply intertwined. More recently, rather extensive analytical calculations have been used, e.g., to gain a deeper understanding of ion-orbit loss effects [1], to develop advanced quasilinear models of turbulent transport [2], to improve multi-component fluid models for the plasma edge [3], to construct reduced models of fast-particle effects on turbulent transport [4], and to shed new light on the complex behavior of Geodesic Acoustic Modes [5]. Such analytical calculations are essential, among other things, for putting computational studies on a firm mathematical basis, for providing fundamental insights into the physical processes under investigation, and for creating reduced models which can be used to interpret and guide experiments. Meanwhile,

state-of-the-art simulation tools are developed and deployed. In this context, our flagship effort is the continuous evolution of the GENE family of gyrokinetic turbulence codes, with a world-wide user base. Besides the flux-tube and full-torus tokamak versions of GENE, we have recently added the full-torus stellarator version GENE-3D and the full-f edge and scrape-off layer version GENE-X. The latter leverages the mathematical and computational infrastructure originally developed for the fluid edge turbulence code GRILLIX. It is based on a Flux Coordinate Independent (FCI) approach that allows to naturally treat a wide range of toroidal magnetic configurations, including those involving open field line regions, stochastic regions, and magnetic islands. Other important simulation codes further developed and employed at TOK (and beyond) include the gyrokinetic PIC codes ORB5 and PICLS, as well as codes like SOLPS, TORBEAM, and TORIC. Complementing the traditional pillars of analytical and computational approaches, we have started to explore various opportunities offered by scientific machine learning. Respective techniques have been applied to the analysis of experimental data and the acceleration of computer simulations [6, 7, 8, 9]. In the following, we will focus on some recent research highlights obtained by combining all of the approaches just mentioned.

1.2 Quantum Mechanical Methods for GAMs and Electron Cyclotron Waves

Applying approaches developed in different fields of physics to fusion-plasma problems opens the way to a deeper insight into the physics under consideration and to the possibility of profiting from known techniques and results. Due to the similarities of the underlying equations, methods originally developed in the field of quantum mechanics were successfully applied to the description of Geodesic Acoustic Modes (GAMs) and of high-frequency wave beams [10, 11, 12].

Linear and nonlinear dynamics of GAMs. GAMs are plasma oscillations caused by the compression of the so-called zonal flows and play a fundamental role in the regulation of tokamak turbulence. In linear numerical simulations, they are often initialized in the form of (e.g., Gaussian) packets that evolve in time. Wigner-function methods developed in the frame of non-Hermitian quantum mechanics were applied to (linear) damped geodesic oscillations, which satisfy a Schrödinger equation (SE) with complex coefficients. Through a comparison between the results obtained from a paraxial solution of the SE and gyrokinetic simulations performed with the code ORB5, it was possible to show that dispersive and dissipative effects can be efficiently predicted without resorting to large-scale numerical calculations, while at the same time gaining a deeper physical insight.

If a nonlinear response of the plasma to the GAM oscillation is allowed for, the system exhibits a behavior that can be described by a nonlinear Schrödinger equation (NLSE). Also in this case, solution approaches of the NLSE borrowed from nonlinear-fiber optics (e.g. variational method) show an excellent agreement with gyrokinetic simulations for moderate nonlinearities (see figure 1).

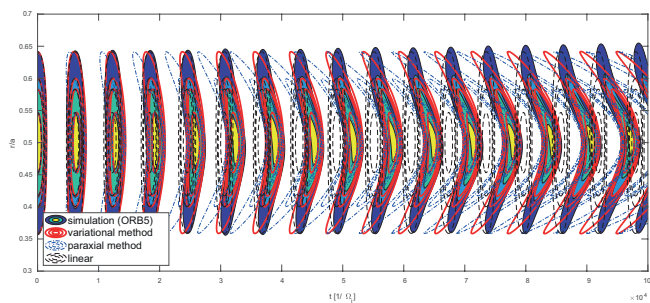


Figure 1. Contour levels of the absolute value of the radial electric field of a GAM packet including the nonlinear plasma response, as a function of time (x-axis) and plasma radius (y-axis).

Scattering of high-frequency wave beams by density fluctuations.

Wigner-function methods can be applied also to the description of the scattering of wave beams (employed e.g. for electron cyclotron heating) by density fluctuations. For the first time, it was possible to successfully validate the implementation of this approach in the Monte Carlo, ray-based WKBeam code against experimental (TCV) data. Moreover, exploiting explicitly the paraxial limit in the underlying wave kinetic equation shows that a significant reduction of the computational burden with respect to WKBeam might be achieved, as demonstrated in simplified setups. A generalization to experimental tokamak geometries will follow.

1.3 GENE Simulations of Turbulence Suppression by Energetic Particles

Mechanisms of turbulence suppression by energetic particles.

In recent years, it has become increasingly clear that supra-thermal particles can have a strong effect on plasma turbulence. This led to the identification of different physical mechanisms which could be invoked to improve the performance of future fusion devices. In particular, (i) a multi-scale nonlinear coupling between marginally stable, energetic-particle-driven modes and ITG turbulence was identified in references [13, 14], reducing the bulk ion free energy content and enhancing zonal flow activity; (ii) a resonant interaction between supra-thermal particles and ITG modes was recently discovered when the fast ion magnetic drift frequency is close to the ITG frequencies [15, 16]. These theoretical and numerical results have recently been applied to design a discharge at ASDEX Upgrade, where these effects were optimized beforehand via global gyrokinetic GENE simulations predicting the formation of a new type of transport barrier via energetic particle effects. In particular, this ASDEX Upgrade experiment showed the expected features of transport reduction and the formation of a central region of improved confinement with no degradation of the energy confinement during the external heating power ramp-up [17, 18]. This led to a strong increase in the on-axis ion temperature and hence a large increase in plasma performances.

Applications to Stellarators. These results are particularly promising for reducing turbulent transport in conditions where ion-scale turbulence limits the development of the central ion temperature in experiments. This has been a major obstacle in the recent W7-X experimental campaign, where the ion temperature was clamped at 1.3 keV regardless of the external ECRF heating power. In reference [19], we showed that by properly exploiting the wave-particle resonant interaction between energetic particles and ITGs, a significant turbulence reduction of roughly 65% is observed in the GENE numerical simulations. These predictions will be tested in the next experimental campaign at LHD and W7-X.

Self-consistent profile predictions. In addition to these results, we have worked in coupling the radially global version of the gyrokinetic code GENE to the transport solver TANGO. This is a major result allowing for the first time high-fidelity gyrokinetic simulations up to the transport time scale, including kinetic electrons, collisions, electromagnetic effects and, more recently, supra-thermal particles. This newly developed tool has allowed us to perform simulations as ASDEX Upgrade and correctly compute the plasma profiles in conditions where TGLF-ASTRA fails in reproducing the peaking of the ion temperature as observed in the experiment [20]. Moreover, by retaining different physical effects in the GENE simulations, e.g., collisions, toroidal rotation and electromagnetic effects, we demonstrate that the ion temperature profile's peaking is due to electromagnetic effects of submarginal MHD instability.

1.4 Interaction of Electromagnetic Turbulence and MHD Modes with ORB5

Electromagnetic turbulence.

The challenge to develop robust electromagnetic gyrokinetic PIC codes has persisted over more than two decades. In recent years, further developments of ORB5 have led to breakthroughs along these lines. For instance, we were able to compare low-beta ion-temperature-gradient driven (ITG) turbulence with the higher beta kinetic ballooning mode (KBM) turbulence in the same magnetic configuration and for the same plasma profiles [21]. Strong profile relaxation has been observed in the case of KBM dominated turbulence for a large-aspect-ratio tokamak.

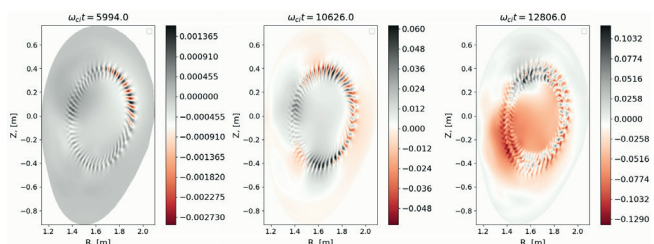


Figure 2. Evolution of the electrostatic potential in ASDEX-Upgrade for the KBM dominated regime, $\beta = 4.8\%$. Left: linear phase; Center: early nonlinear phase; Right: saturation phase.

In this case, the mode saturation is due to the flattening of the temperature profile caused by an outward transport of the turbulent fingerlike structures. We have also considered an ASDEX Upgrade (AUG) equilibrium, where a transition to a KBM dominated turbulence regime has been obtained by artificially increasing the value of beta. The profile relaxation is weaker in this scenario (as compared to the large aspect ratio case), and the observed KBM saturation is due to an interplay between profile evolution, linear stability, and zonal flow generation.

Energetic particle (EP) driven modes. ORB5 successfully participated in an international benchmark effort of gyrokinetic and MHD-hybrid codes for an NBI-heated AUG discharge [22]. A remarkable agreement is observed among the codes, obtaining for all of them an Alfvén mode localized close to the magnetic axis when off-axis NBI heating is applied. Moreover, we have addressed one of the hot topics in the EP community, namely the development of EP transport models based on the time evolution of phase space zonal structures (PSZS). To validate transport model results against nonlinear gyrokinetic simulations, diagnostics for the time evolution of PSZSs has been successfully implemented in ORB5 [23]. In addition, ORB5 has been used to investigate nonlinear processes in AUG discharges, focusing, in particular, on the saturation properties of EP driven modes like TAEs, EPMs, and EGAMs, demonstrating the coupling of EPMs and EGAMs [24] and of EPMs and TAEs [25] via EP phase-space nonlinearities. To quantitatively reproduce experimental results, ORB5 has been adapted to simulate experimental NBI distribution functions produced by the RABBIT code. We have studied the dependence of the EGAM resonance condition on the details of the velocity space dependence of the distribution functions. It has been shown that linear physics is not enough to explain the presence of unstable EGAMs in the experiment [26].

1.5 Towards a Better Understanding of Outer-core and Edge Turbulence

Comprehensive code validation. While gyrokinetic simulation has become a workhorse in turbulence studies over the last several years, the question remains if it is able to reliably and comprehensively describe experimental observations. This question has been addressed by facilitating the excellent and recently further improved fluctuation diagnostic coverage installed at ASDEX Upgrade which – for technical reasons – is currently best for L-mode plasmas. Here, outer-core GENE simulations have been compared with electron temperature fluctuation measurements from the upgraded Correlation Electron Cyclotron Emission (CECE) both in hydrogen and deuterium L-mode plasmas [27] exhibiting good agreement and substantially improving on previous attempts validating GENE with CECE measurements. An even more ambitious validation involving scale-resolved Doppler reflectometry, CECE and cross phase comparisons at two radial positions and for two different L-mode heating scenarios has been

tackled as well [28], generally confirming a high realism of gyrokinetic simulations in these scenarios and further populating the still rather scarce world-wide knowledge base with respect to strict validation beyond simple transport flux comparisons.

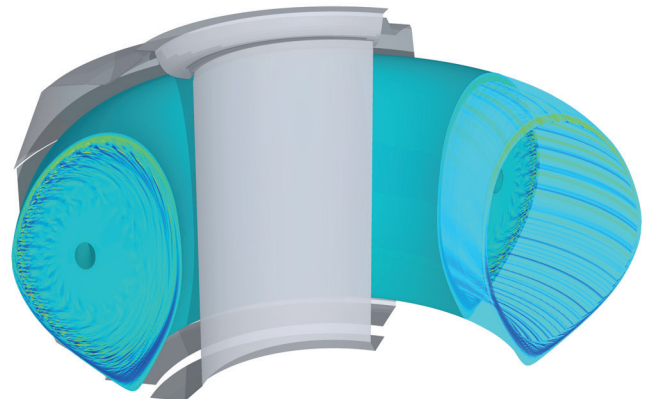


Figure 3. Example of edge fluctuation data – here density fluctuations – obtained from global GENE simulations

Edge turbulence in ELM-free scenarios. Pushing GENE towards the edge and hence closer to its formal limits, dedicated analyses could, e.g., show that the ASDEX Upgrade I-mode pedestal is dominated by microtearing modes (MTM) and that the heat fluxes are determined by ion-scale electrostatic turbulence [29]. Also, first pedestal top simulations have been conducted for an argon-seeded ASDEX Upgrade EDA H-mode discharge revealing trapped electron modes (TEMs)/ electron temperature gradient (ETG) driven modes as dominant ion-/electron-scale modes. Nonlinearly, the ETG contribution turns out to be surprisingly small and the majority of the transport is hence expected on ion scales where global electrostatic simulations could approach experimental heat flux levels [30]. Comprehensive global nonlinear electromagnetic gyrokinetic simulations, supported by a detailed characterization of gyrokinetic instabilities at pedestal top, center, and foot with linear local simulations have also been performed for the full pedestal up to the separatrix of a well-diagnosed ASDEX-Upgrade H-mode [31]. Both, experimental measurements [32] and the global GENE simulations reveal a complex heat flux structure with different radial transport regimes. At the pedestal top MTMs and TEMs are found to cause ion-scale heat fluxes in the electron and ion channel while only very small turbulent heat flux levels are observed. In the steep gradient region, neoclassical transport appears to be dominant. From the pedestal center to foot, fine-scale ETG driven turbulence takes over the electron heat flux that was driven by TEM/MTM on the pedestal top.

Unravelling L-H transition physics. In addition to the traditional delta-f gyrokinetic codes like GENE, ORB5, GYRO, GKW, and others which

often employ field-aligned coordinates to exploit the high anisotropy of plasma core turbulence, a new class of full-f gyrokinetic codes with flux coordinate independent coordinates is currently evolving which allow flux-driven simulations crossing the separatrix and including scrape-off-layer physics. Very first applications to ASDEX Upgrade along these lines have been performed with the full-f, long-wavelength gyrokinetic GENE-X code which could already validate the SOL power falloff length according to the Eich fit function [33].

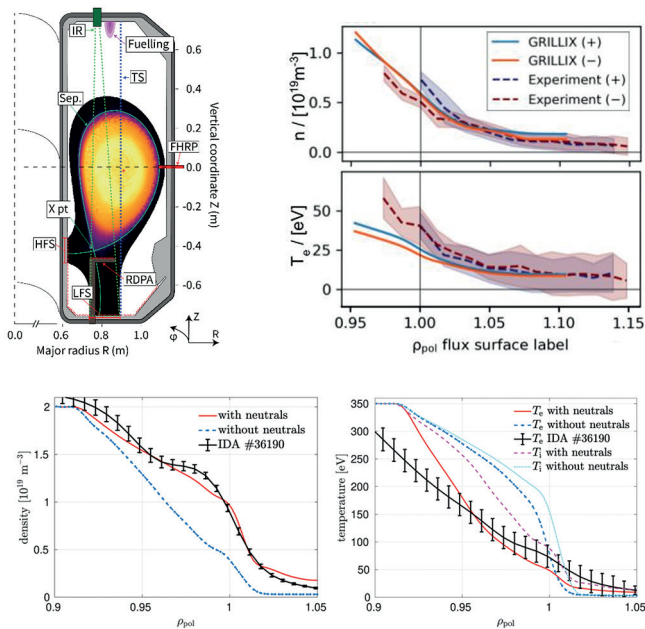


Figure 4. Left: Poloidal cross section of TCV-X21 scenario with density-snapshot from GRILLIX simulation. Center: Outboard midplane profiles of TCV-X21 simulation for forward (+) and reversed (-) configuration. Right: Outboard midplane density profile for AUG L-mode simulation.

The combination of these two complimentary approaches appears to be particularly promising for a theoretical ASDEX Upgrade edge and pedestal turbulence description including the large-scale coupling between edge and SOL on the one hand, and the multi-scale character involving electron-scale turbulence on the other.

1.6 State-of-the-art Fluid Turbulence Simulations with GRILLIX

Detailed experimental comparisons. In recent years, the edge and scrape-off layer fluid turbulence code GRILLIX has become one of the premier tools of its kind. Currently, it is being actively developed towards performing reactor-relevant simulations of the edge and scrape-off-layer. To improve the model accuracy, a campaign of rigorous validations has been performed against TCV and ASDEX Upgrade. Within the TCV-X21 [34] project specifically designed TCV experiments

were performed for a first-of-a-kind validation of several edge fluid turbulence codes (GBS, TOKAM3X, GRILLIX). The simulation results were compared qualitatively and quantitatively to the experimental measurements, and the whole validation data set (experiment and simulations) was published in a FAIR public repository. In the corresponding flux driven GRILLIX simulations the plasma profiles, turbulence and transport were evolved self-consistently at realistic parameters and in realistic diverted geometry. Overall, a very good match at outboard midplane for both mean profiles and fluctuations was obtained. On the other hand, the divertor targets showed a poorer match in some respects, which directly motivated further dedicated model extensions, e.g., sheath boundary conditions and development of a neutral gas model. Another validation focused on an ASDEX Upgrade L-mode discharge [35, 36], which constitutes a considerably larger case than the TCV-X21 scenario. A significant improvement was obtained with the newly developed neutral gas model resulting in an overall good match of the simulation data with the experiment.

Model improvements towards ITER simulations. In addition to further model improvements, i.e., electromagnetic flutter terms, Landau-fluid closure and ion-orbit loss effects, GRILLIX underwent a major refactoring, employing state-of-the-art software engineering design concepts. Besides improved robustness, flexibility and modularity of the code, a significant computational performance gain was obtained. Altogether this enabled routine turbulence simulations of AUG size experiments and the feasibility of an ITER scale reactor relevant scenario was shown.

1.7 Towards a Gyrokinetic Description of the L-H Transition with GENE-X

A novel full-f gyrokinetic edge turbulence code. The development of GENE-X [37] started in 2018, based on many years of experience with GENE. It is the first grid-based full-f and electromagnetic gyrokinetic turbulence code that is able to treat the edge and scrape-off layer regions of a fusion device. In 2020, the first proof-of-principle edge simulations became feasible – but only for simplified test cases. Since then, we have taken the necessary steps to advance the code to a point where it can be compared quantitatively with actual experimental observations. For this purpose, the physics model was extended to include electromagnetic field equations, adding the self-consistent solution of magnetic field fluctuations.

First applications to tokamaks and stellarators. In the first simulations in diverted geometry, the code was validated against an ASDEX Upgrade L-mode discharge, resulting in an overall good agreement between simulation and experiment [38]. On top of the electromagnetic extension, the physics model was further improved by including a Fokker-Planck-like collision model [39]. A second validation against TCV experiments was done to assess the overall impact of collisions, with the result that the more realistic collision model improves the agreement with the experiment significantly (see figure 1) [40].

So, since 2020, it was progressively shown that GENE-X is able to perform realistic simulations of edge and scrape-off layer turbulence in tokamak devices. Ongoing work on GENE-X includes the extension of the code to simulate edge and scrape-off layer turbulence in stellarator devices. This will make GENE-X one of only a few codes capable of exploring plasma turbulence in complex 3D magnetic fields, which can include open field lines, islands, and stochastic regions. One key goal in the next phase of development and application is to address the physics of the L-H transition.

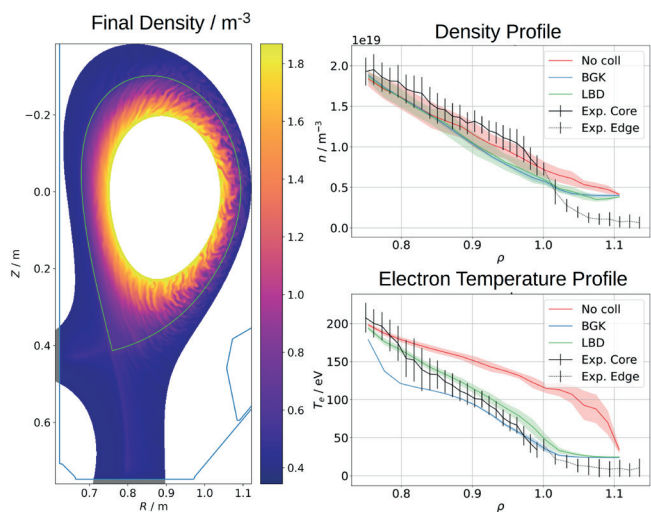


Figure 5. Left: Snapshot of a GENE-X simulation in diverted geometry (TCV validation case) that shows the final density. Right: Improved agreement of outboard-midplane plasma profiles by using improved collision models. No collisions vs. BGK (very simple) vs. LBD (most realistic)

1.8 First-principles Based Profile Predictions for W7-X

Full-torus simulations of stellarator turbulence with GENE-3D. As stellarators continue to gain attention as an alternative reactor concept, we put constant effort into extending our simulation tools to keep up with the increased numerical complexity that arises due to the complicated magnetic field structure in such machines. Our efforts are spearheaded by GENE-3D, the member of the GENE family of codes that is specifically optimized to simulate global plasma dynamics in non-axisymmetric fusion devices. Over the past two years, we have extended the capabilities of GENE-3D to efficiently describe the turbulent transport in a stellarator plasma, including kinetic electron dynamics as well as electromagnetic effects. Due to these advances, we were able to perform the world's first global, electromagnetic turbulence simulation of a stellarator plasma [41]. In this context, we have seen that even a moderate level of electromagnetic field perturbations can have a substantial influence on the strength of ion-temperature-gradient (ITG) turbulence. Capturing such effects will be of significant importance for the upcoming experimental campaign of

W7-X in which electromagnetic effects are expected to play a major role and even trigger new types of turbulent modes.

Profile predictions for W7-X. To date, all gyrokinetic stellarator codes were limited to relatively short time scales (of the order of a ms), not allowing for reliable predictions of plasma performance. To overcome this limitation, a recent effort has been made to push GENE-3D simulations from turbulent to transport time scales. For this purpose, we have developed a new coupling framework involving GENE-3D, the neoclassical code KNOSOS, and the 1D transport solver TANGO [42]. The result is the first high-fidelity model in the stellarator community that can compute plasma profiles based on the combined effects of neoclassical transport, turbulent transport, and external particle/heat sources in three-dimensional magnetic equilibria. By performing first-principle-based simulations within this framework, we were able to capture the ion temperature profile evolution in W7-X for the first time and reproduced the experimentally observed degradation of confinement in electron-heated plasmas, where the central ion temperature was “clamped” to approximately 1.5 keV, regardless of the external heating power (see figure 1). The mechanism responsible for this clamping was found to be a destabilization of ion-scale turbulence due to the ratio between electron and ion temperature being increased with external power in electronheated plasmas [42].

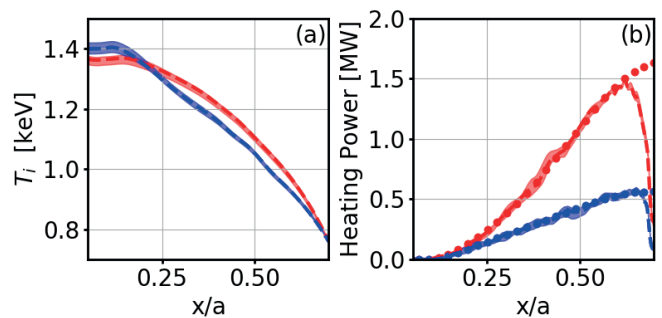


Figure 6. Comparisons of the converged ion temperature profiles (a). Both simulations lead to the same on-axis temperature, despite the large difference in ion heating power (factor of 3 at $x/a = 0.7$) (b).

1.9 Significant AI-based Acceleration of Turbulence Simulations

Scientific machine learning. Currently, there are several ongoing projects exploring the potential of scientific machine learning for fusion research. Building on recent advances in AI-related techniques, we have started to analyze experimental data in novel ways, but also to seek ways to significantly accelerate large-scale simulations – as exemplified through a project in which we replace small-scale dynamics in Hasegawa-Wakatani-based turbulence simulations by data which is generated via machine learning. More recently, we were able to make great strides in this direction. Our approach combines

standard numerical simulations at low resolution with a learned nonlinear correction from a neural network. By chaining iterations of this hybrid predictor-corrector assembly, we expose the network to the data it has generated, and as a result successfully eliminate the natural positive-feedback loop that often makes these approaches unstable. All physical checks indicate that the neural network has learned the physics itself rather than an estimation of it. After seeing intervals of just 3 frames, the network produces practically unconditionally stable simulations tested up to 106 steps – 75x longer than any reference paper. This process allows us to capture the relevant statistical properties of the turbulent system under consideration. Theoretical speedups are almost four orders of magnitude for this rather simple model, suggesting that an application of this technique into state-of-the-art codes (like GENE) is very promising.

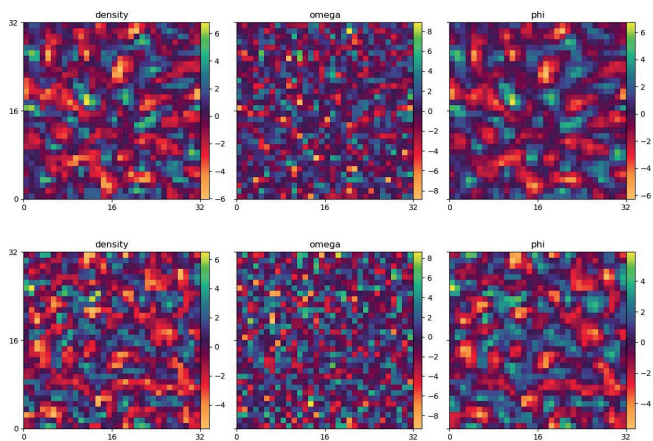


Figure 7. Typical snapshots of down-sampled ground truth (top) and simulated state (bottom).

Scientific Staff

V. Artigues, A. Banon Navarro, A. Bergmann, M. Bergmann, R. Bilato, T. Body, M. Bösl, A. Bottino, A. Chankin, D. Coster, A. Di Siena, C. Gahr, T. Görler, J. Graw, R. Greif, F. Jenko, J. Lakhilili, L. Leppin, O. Linder, S. Makarov, J. Martin Collar, F. Matos, D. Michels, A. Mustonen, I. Novikau, N. Oliveira Lopes, G. Papp, G. Pautasso, C. Pitzal, E. Poli, K. Pommois, B. Rettino, M. Smedberg, A. Stegmeier, K. Stimmel, D. Told, J. Trilaksono, P. Ulbl, F. Vannini, E. Walter, M. Weidl, M. Weiland, F. Wilms, Y. Yudin, K. Zhang, W. Zholobenko, R. Zille

Guest

F. Widmer (NINS, Japan)

2 Research Unit MHD and Fast Particles

Head: Prof. Dr. Sibylle Günter

Within the group a hierarchy of different models and numerical implementations is developed and used in order to address various open issues in the field of MHD and energetic particles physics for present day and future burning fusion plasmas. Special attention is given to challenging multi-spatio-temporal scale problems in the view of extrapolating to ITER parameters and beyond.

2.1 MHD Transients – Studies of Large Scale Violent Plasma Instabilities

Several codes are developed and used in the group to study large scale plasma instabilities. CASTOR3D allows for linear tokamak and stellarator studies including 3D conducting structures. It includes non-ideal effects and was recently extended for pedestal physics. TM1 is a non-linear extended MHD code allowing for efficient two-fluid simulations in simplified circular toroidal geometry. JOREK is a non-linear extended MHD code for realistic divertor tokamak geometries. IPP is one of the main hubs developing and using JOREK, coordinates the code development in the international community and is leading the EUROfusion TSVV project on MHD transients that addresses in particular disruption, SOL and pedestal physics. A comprehensive overview of the code was recently published [43]. Large improvement of the solver and preconditioner were performed jointly with NMPP and MPCDF providing a speed-up by a factor of 2–3 for many highly-nonlinear production cases [44]. The development is crucial both for the simulation of large-scale devices like ITER and DEMO but also for future stellarator simulations where non-linear mode coupling is particularly pronounced. An option for higher order B-splines was implemented (lead by our collaborators from UKAEA) [45]. TRIMEG is a gyro-kinetic full-f and delta-f PiC code for electromagnetic full device simulations that is developed in the group. The present focus lies on exploring numerical techniques like a fully implicit PiC method [46] and an E&B gyrokinetic model for toroidal geometries [47], which are considered also for implementation in other codes such as JOREK eventually.

2.1.1 The Physics of Disruptions

JOREK was used to simulate benign beam termination in JET [48]; results were compared to the dynamics and timescales of the experiment [49], and put into context with observations from DIII-D [50]. The model is now applied to predictive ITER simulations as reported separately in the chapter tokamak collaborations. One strategy considered for runaway electron (RE) mitigation lies in a dilution of the plasma prior to the thermal quench (TQ). Simulations show that pre-existing MHD activity can either accelerate or decelerate the TQ onset after massive deuterium injection depending on the relative phase between injection location and magnetic island [51].

Dedicated experiments on AUG were carried out for so-called hot vertical displacement events (hot VDEs) with different plasma current and magnetic field amplitude. This represents a worst-case scenario for ITER in terms of halo currents and electromagnetic forces in which the vertical position control is lost while the plasma confinement is still intact. First simulations for one of the cases show good matches in terms of vertical motion, halo current magnitude and toroidal asymmetries as well as the edge safety factor at which the TQ sets in; simulations of further cases with different plasma parameters are on the way. Hot VDE experiments were now repeated, but with neon SPI applied at different points in time showing that the halo current amplitude can be strongly mitigated even with an injection just before the natural TQ onset. In direct collaboration with ITER, systematic simulations of such cases and of other AUG SPI scenarios are started for validation in view of ITER predictions. For the formation of halo currents, scrape-off layer parameters play an important role; COMPASS experiments and simulations show that the ion saturation current is an essential ingredient to capturing the full physics and describing the halo width correctly [52]. Preliminary analysis seems to confirm this finding also on AUG. First of a kind 3D simulations of a mitigated current quench (CQ) in ITER were performed with fully realistic parameters (starting the simulation after the TQ) allowing to assess the expected vertical and horizontal forces, which seem tolerable for this mitigated scenario [53]. Test particle RE studies in this case, taking into account newly implemented Coulomb collisions and the radiation reaction force, investigate particle losses including a detailed study of trapped particle loss mechanisms [54]. In this scenario, RE beam formation would be prevented by strong losses in the stochastic magnetic topology. As uncertainty for these predictive simulations results from the assumed plasma state after the TQ used as initial condition for the simulation, future studies lead by ITER focus on simulating the full disruption process (at scaled parameters) and are closely connected to the ongoing model validation on AUG.

For a high fidelity assessment in particular of horizontal forces, a detailed 3D model of the walls is necessary. In view of that, JOREK is presently being coupled to the CARIDDI code. The no-wall limit has already been benchmarked successfully and the eddy current coupling is nearly complete while halo current coupling will require further derivations and developments.

RE beam formation can potentially be mitigated by externally applied perturbation fields. One option for this is to excite such perturbations by a passive helical coil in which current is induced during the CQ. For such coils planned for DIII-D and SPARC, test particle simulations were carried out with ASCOT5 to assess RE losses predicting beneficial effects [55, 56]. For AUG, simulations are presently on the way to assess whether installing a passive helical coil could be of interest in AUG, or whether the existing active B-coils could be a more flexible alternative (if enhanced for higher currents).

As neoclassical tearing modes (NTMs) are often the cause of disruptive behaviour, the effect of resonant magnetic perturbations (RMPs)

on NTMs was studied with TM1. A moderate applied RMP below the penetration threshold is found to significantly change the local flux-surface-averaged plasma current density gradient at the resonant surface; the effect increases with the electron temperature. As a result, the growth of small 2/1 NTMs is found to be stabilized by moderate static 4/2 or 6/3 RMPs if the local electron fluid velocity is in the ion drift direction or sufficiently large in the electron drift direction [57]. Also magnetic reconnection during sawtooth crashes in AUG was studied; the radial velocity of the plasma core agrees well with experimental measurements indicating that two-fluid effects are sufficient to capture the dynamics [58].

2.1.2 Pedestal Physics

Simulations of a small-ELM scenario at low triangularity were now published including a demonstration of the transition to the large-ELM regime [59]; simulations for the EDA H-mode scenario have started to assess whether extended MHD models can capture all relevant aspects and whether the regime could be ITER relevant. Detailed simulations of natural and pellet-triggered ELMs were published [60]. Previously performed type-I ELM simulations are used for studies of parametric decay instabilities [61], scattering of ion cyclotron range of frequency waves by filaments [62, 63], ELM induced fast ion losses [64], and virtual reflectometry [65]. Simulations for QH-mode recently obtained experimentally in the all-metal AUG show the formation of a saturated edge instability that prevents the temperature build-up and leads to a nonsinusoidal oscillation of the edge density. Like in the experiment, this saturated mode collapses when the density increases, marking the transition of the QH-mode into an ELM regime. The critical density is in quantitative agreement to the experiment. RMP penetration was studied with free boundary treatment, fully realistic plasma parameters, and taking into account realistic $E \times B$ and diamagnetic plasma flows. Simulations show an excellent match with the experimentally observed corrugation of the plasma boundary. Based on this validation, simulations for RMP-ELM interaction are on the way aiming to reproduce the bifurcation between mitigation and suppression regimes depending on the plasma density. CASTOR3D was extended taking into account gyroviscosity in the momentum equation, as well as pressure and Hall terms in Ohm's law using drift approximations. The effects onto ideal and resistive modes were studied individually for the terms showing, as expected, that the diamagnetic drift effects strongly influence stability properties. While the ion diamagnetic drift effect plays the dominant role for ideal modes, both, ion and electron diamagnetic drift effects are important for resistive instabilities. This development strongly increases the applicability of CASTOR3D to high fidelity edge stability studies.

2.1.3 Stellarator Physics

The research on stellarator physics by the group was conducted within the framework of the Max Planck Princeton Center and is described in the corresponding section.

2.1.4 Energetic Particle (EP) Physics

After successfully comparing the gyrokinetic (GK) hybrid LIGKA/HAGIS model with the self-consistent global non-linear ORB5 code for ITER parameters [66], and benchmarking with MHD-hybrid codes (XHMGC, amongst others) for an AUG case [67], each of the three code packages was further developed and applied to problems they are particularly suited for.

Porting the LIGKA code into the ITER IMAS framework facilitated the automated, time-dependent stability analysis of various global Alfvén-type perturbations (AEs) in AUG, TCV, JET, JT-60SA and ITER. In particular, a fully IMAS based workflow for AUG shot data has been established and verified. It enables a transparent and reproducible way of following the linear properties of various perturbations throughout the interesting phases (typically 1–3 seconds) of a discharge [see figure 8]. It captures the sensitivity of the global mode properties on equilibrium profile changes and thus allows one to perform an uncertainty quantification of mode structure, frequency and damping rate based on AUG IDA (integrated data analysis) data [68, 69]. Also, ITER scenario projections based on various transport models were analyzed, showing that often the least damped AEs are found at the end of the power ramp-up phases due to the complex interplay of temperature, density and safety factor profile evolution [69].

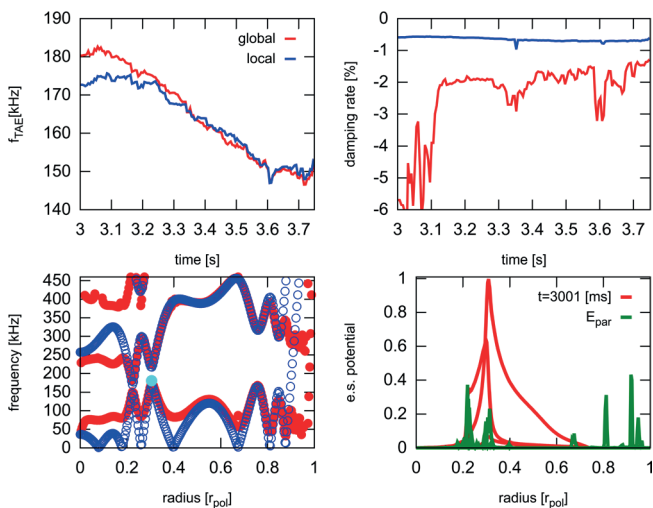


Figure 8. IMAS based, automated analysis of AUG discharge 39681 between $t = 3$ and 3.7 s for an $n = 2$ toroidal Alfvén eigenmode. The top row shows the time-dependent evolution of the TAE frequency and damping rate during the L-H transition for both global and local LIGKA models. The bottom row shows the shear Alfvén continuum (ideal MHD in blue, kinetic in red) and global mode structure at $t = 3.7$ s, whose interaction is responsible for the strong sensitivity of the damping rate (top right).

In order to determine if these weakly damped modes deteriorate the EP confinement as seen in many present day experiments, an EP transport

analysis is needed. Since many time slices need to be investigated and eventually optimization calculations need to be carried out, the application of reduced, albeit still global kinetic models is indispensable, a problem not solved so far within the EP community. To this end a new, fully IMAS based EP transport model has been developed that technically builds on the LIGKA/HAGIS framework and conceptually on the general EP transport theory of phase space zonal structures (PSZS) [70]. First encouraging results of this ATEP code (advanced EP transport model) demonstrate the practical feasibility of this novel ansatz and its versatility to recover simplified transport models in appropriate limits, such as the kick-model. Furthermore, the concept of PSZSs is key to compare the transport model results with non-linear codes such as ORB5, XHMGC and HAGIS. Thus, following XHMGC, PSZS diagnostics have been successfully implemented in ORB5 and HAGIS.

Whereas for the ATEP code simple saturation rules for the mode amplitudes are presently used, in the future much more sophisticated models will be needed to account for the influence of non-linearly generated zonal structures, mode-mode coupling processes and the cross-scale interactions with small scale turbulence. ORB5 has been used to shed light on various aspects of these non-linear processes: the saturation properties of TAEs and EGAMs in an AUG scenario with strong EP-driven activity have been investigated, demonstrating the coupling of the two instabilities via EP phase space non-linearities. The saturation amplitudes of both modes are considerably modified in simulations where both modes are present compared to single-mode runs, in agreement with analytical models for 3-wave interaction [71, 72]. Furthermore, increasingly realistic distributions functions were implemented and used for this case. In particular an interface to the RABBIT code has been established meaning that now experimental NBI distribution functions can be used in ORB5. As expected, interesting modifications to the AUG NLED case were found [73]: the EGAM, previously investigated with a bump-on-tail distribution, is driven by the anisotropy in pitch angle. Detailed comparisons with AUG discharges using different beam injection angles confirm the sensitive dependence on the alignment of the EGAM resonance condition and the gradients in velocity space. Interestingly, the nominal experimental EP density is not enough to destabilize the EGAM. In addition to profile and distribution function uncertainties, also the nonlinear interaction with the co-existing TAE/EPM bursts, as seen in the experiments, could explain this remaining discrepancy. Whereas experimental modeling for AUG was focused on low toroidal mode numbers n , ORB5 was also used to perform a multi-scale analysis for an ITER pre-fusion-power operation scenario [74]. Three classes of instabilities were found: weakly damped TAEs in the range $n = [10 - 25]$ that can be potentially destabilized by EPs, meso-scale unstable bulk-plasma driven AITGs in the range $n = [45 - 60]$ and micro-instabilities in the range $n = [150 - 200]$. The scale separation obtained in this linear study demonstrates the challenges for non-linear simulations

that need to address the cross-scale coupling via various channels such as mode-mode interaction and (phase space) zonal structures.

Extending the phase space diagnostics capability of the XHMGC code made it possible to identify the details of resonant structures contributing to mode drive during the evolution of chirping AEs, i.e. a mode that rapidly changes its frequency during its lifetime [75]. If the frequency were constant, saturation would occur as the density flattening reaches the inner and outer limit of the resonance region. With decreasing frequency, however, this region drifts further inwards and keeps the inner gradient within the region where the particle-wave power transfer is effective, helped by a significant resonance widening. The phase-space island then grows around the new resonance radius, by trapping new particles on its inner boundary, while other particles get de-trapped from the outer one. The process continues as long as the frequency change is effective in causing an inward shift of the resonance region that is able to recapture the density gradient. This fundamental investigation sheds light on the detailed non-linear wave-trapping/detrapping mechanism and highlights the important role of radial non-uniformity for the modes' non-linear evolution and saturation. Based on this understanding, AE chirping simulations with ORB5 have been started that add new physics elements to the picture, e.g. non-linear damping, zonal structure physics and the influence of background turbulence on the chirping processes [76].

The ability of AEs to expel runaway electron (RE) seed particles is explored in the pursuit of a passive, inherent RE mitigation scenario for ITER. Due to the different slowing down times of thermal and energetic α -particles during the thermal quench, the free energy linked to radial gradient of α -particles can overcome the vanishing ion Landau damping of AEs in a certain time window of a disruption. It was found that the mode amplitudes are predicted to be sufficiently large to permit the possibility of significant radial transport of runaway electrons [77]. However, this transport is not always beneficial, since depending on the modes' radial spectrum, additional seed electrons can be transported in regions where runaway currents form [78].

The JOREK code was extended to allow EP simulations with both the full and reduced MHD models. An anisotropic pressure coupling was implemented and successfully benchmarked for the ITPA-TAE case in simple geometry and a more realistic scenario based on the AUG-NLED experiments. Further linear and non-linear studies using a realistic full-f fast-ion distribution function are ongoing and show reasonable agreement to the experimentally observed mode spectra.

Scientific Staff

F. J. Artola, F. Atour, V. Bandaru, H. Bergström, A. Cathey Cevallos, S. Günter, T. Hayward-Schneider, F. Holderied, M. Hölzl, K. Lackner, Ph. Lauber, A. Lieber, Z. Lu, G. Meng, V. Mitterauer, N. Nikulsin, V.-A. Popa, R. Ramasamy, K. Särkimäki, N. Schwarz, E. Strumberger, W. Tang, F. Vannini, X. Wang, F. Wieschollek, Q. Yu

3 Stellarator Theory

Head: Prof. Dr. Per Helander

The central challenge in stellarator theory is to understand how the geometry of a magnetic field affects the properties of the plasma it confines. This question is explored in the Stellarator Theory Division, where fundamental theory of plasmas confined by non-axisymmetric magnetic fields is developed and theoretical support for W7-X is provided.

3.1 Demonstration of Reduced Neoclassical Energy Transport in Wendelstein 7-X

Neoclassical energy transport in stellarators scales very unfavourably with the plasma temperature. This will lead to prohibitive energy loss at the temperatures required in a reactor unless the stellarator's magnetic field has been optimised to reduce strongly the geometrical factor associated with this transport. Such a reduction was therefore one of the principal goals of the W7-X optimisation. As noted in the IPP Scientific Report 2017–2020, record values of the fusion triple product achieved in W7-X high-temperature plasmas confirm the successful achievement of this goal, as such results would be impossible for stellarators lacking a comparable degree of neoclassical optimisation. These results have since been documented in a Nature article [79].

3.2 Gyrokinetics

Most of the energy losses from W7-X plasmas come from plasma turbulence, and for this reason much effort is being devoted to the study of gyrokinetic turbulence, including fundamental theory, such as a novel linear and non-linear stability theory, the advancement of code capabilities to open otherwise inaccessible physical regimes, simulation work interpreting central experimental findings in W7-X, and the development of gyrokinetic turbulence models that lay the foundation for optimisation of stellarators for turbulent transport. Highlights of these works are given below.

3.2.1 Energetic Stability Bounds

While traditional gyrokinetic linear instability analysis forms the foundation of transport modelling and turbulence theory for magnetic fusion plasmas, it is notoriously complicated due to the large number of distinct instability types and sensitivity to the inclusion of new physical effects (magnetic fluctuations, kinetic species, etc). Furthermore, it is far too expensive numerically to prove useful in stellarator optimisation. A method has been developed to derive rigorous upper bounds linear and non-linear instability growth, which overcomes these limitations. In a series of papers [80, 81, 82], the idea has been systematically developed, starting from compact, approximate forms for these bounds, and then proceeding to 'tight' realisable bounds that give the theoretical maximum of the growth of the Helmholtz free energy.

The solutions that achieve optimal growth are termed ‘optimal perturbations’, and are valid in the fully electromagnetic gyrokinetic limit. The direct comparison of the bounds with gyrokinetic simulations shows how they capture well the dependence of linear growth rates on plasma parameters, and come quite close quantitatively in some key limits. Work is ongoing to extend the optimal mode analysis to include more effects of magnetic geometry, so that it may be applied to stellarator optimisation for reduced turbulence.

3.2.2 Progress with EUTERPE

Recent work on the gyrokinetic code EUTERPE addresses the need for pointwise consistent pressure equilibria in global studies, especially those involving variation of instability parameters (e.g. gradient scale lengths and wavenumbers) [83]. The procedure enables clearer theoretical comparisons and physical interpretation of global simulations, for instance revealing a sensitivity to density gradients for the transition from temperature- to density-gradient dominated instabilities. Since this phenomenon is believed to underlie the ion-temperature clamping observed in W7-X (see below), it will be further addressed in future research, in conjunction with activities on MHD stability.

For stellarators, the global numerical treatment of electromagnetic turbulence, still generally in its infancy, is also the subject of recent advances with EUTERPE. Such turbulence, involving fluctuations in both the electric and magnetic fields, arises at sufficiently high plasma pressure and is expected to be important in W7-X, but its numerical treatment remains challenging in part due to computational complexity and the technical issues associated with magnetic fluctuations. One important physics problem here is the transition between ITG and kinetic ballooning mode (KBM) driven turbulence, for which large-scale modes are improperly treated by local gyrokinetic codes, sometimes resulting in a failure of the turbulence to saturate.

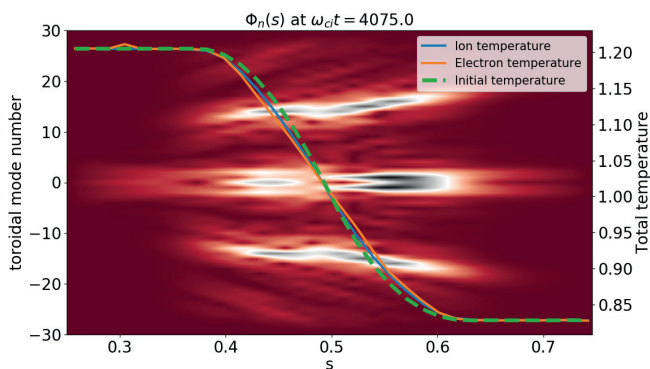


Figure 9. Radial structure of electrostatic potential fluctuations overlaid with initial and final temperature profiles in EUTERPE simulations.

A fully electromagnetic extension of EUTERPE has been developed, which includes all components of the electromagnetic field perturbations.

For the first time, results have been obtained showing saturated KBM turbulence in stellarator plasmas, even for plasma equilibria that have large-scale MHD instability; see figure 9. The parallel component of the magnetic field, known to be important for KBMs, especially the large-scale modes that plague local simulations, has been included in the long-wavelength approximation. Nonlinear saturation of the KBM turbulence was observed as a consequence of zonal-flow excitation and profile relaxation. An interesting feature of these simulations is that energy is transported outward by the turbulence whereas the particle flux is inward. This particle pinch may explain why hollow density profiles and impurity accumulation are usually not observed in the plasma core of W7-X, as expected from neoclassical transport theory.

3.2.3 Turbulent mechanisms of enhanced performance in Wendelstein 7-X

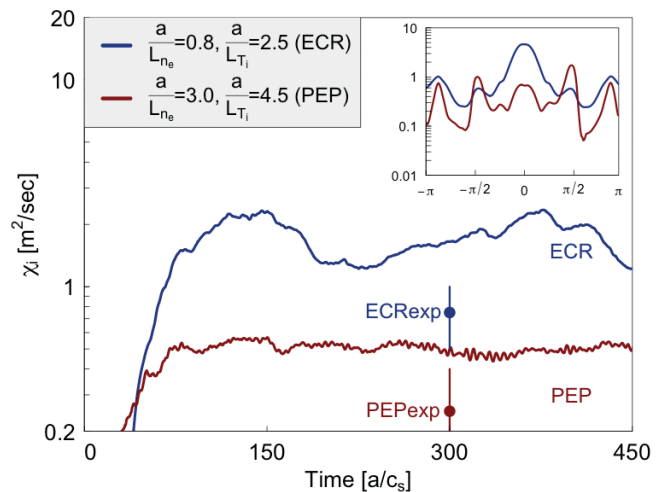


Figure 10. Heat diffusivity from gyrokinetic turbulence simulations before (ECR, blue) and after (PEP, red) pellet injection.

The most successful discharges from the last W7-X campaign involve the injection of pellets. Using gyrokinetic theory, two possible effects have been examined and compared which are thought to be responsible for the observed reduction of turbulence driven by the ion temperature gradient (ITG) [84]. These effects are: i) the neoclassical radial electric field, which is known to reduce ITG turbulence, and ii) the strong density gradient formed by the injected fuel. Whereas the ion-root electric field causes some reduction of the turbulent ion heat flux, it is found to be insufficient to explain the experimental heat diffusivity. On the other hand, the density gradient was observed to robustly suppress ITG turbulence. This effect is related to the specific optimisation of W7-X, and would otherwise produce stronger turbulence due to the excitation of trapped-electron modes as, for instance,

happens in a tokamak. The strong density gradient produced shortly after the injection of pellets is thus able to reduce turbulence, thus improving the performance of such plasmas. Figure 10 shows the result of these gyrokinetic simulations compared with experimental ion heat diffusivities, using the gyrokinetic code GENE. The “ECR” simulation (blue) corresponds to the experimental phase prior to the pellet injection, whereas the “PEP” simulation (red) corresponds to the experimental phase shortly after the pellet injection. Clearly, a notable reduction of the ion heat diffusivity is found, which is attributed to the transition from ITG turbulence to Ion driven-Trapped Electron Mode (ITEM) turbulence, due to the formation of a strong density gradient. ITEM turbulence has been known to be relatively benign in optimised stellarators that have the maximum-J property. In the same figure, experimental heat diffusivities are also presented, including error bars, as compared to the simulated heat diffusivities. Differences could be explained by the lack of inclusion of the neo-classical radial electric field in the flux tube approach used for these simulations. Despite these differences, the simulations are able to capture the experimental trends.

3.2.4 Ion Temperature Clamping in Wendelstein 7-X

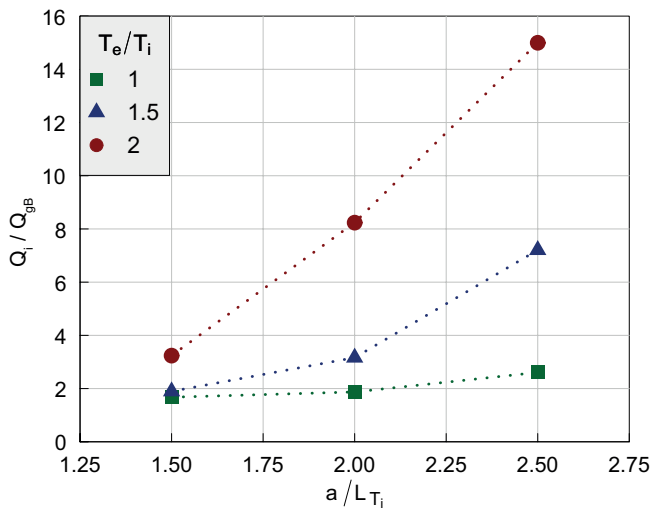


Figure 11. Dependence of ITG-turbulence-driven energy transport fluxes on temperature ratio.

In the last experimental W7-X campaign, numerous plasmas with electron cyclotron resonance heating (ECRH) were produced which demonstrated poorer energy confinement than predicted from neo-classical transport alone, indicating a relatively large turbulent heat transport for the ions. This resulted in an ion temperature clamped at around 1.5 keV, despite an electron temperature reaching up to 10 keV for input powers up to 7 MW. To explain this behaviour, a theoretical analysis based on nonlinear gyrokinetic simulations with the

GENE code was performed, showing a sensitivity of ion turbulence to the ratio T_e / T_i . As shown in figure 11, the ion heat flux increases both for larger ion temperature gradient (at fixed T_e / T_i) and for larger T_e / T_i (at fixed gradient). As a result, the ion transport becomes gradually stiffer with increasing T_e / T_i , as also observed in tokamaks. In these simulations, the electrons are treated gyrokinetically, while the density gradient is set to zero and electromagnetic effects are neglected [7].

3.2.5 Modelling the ITG Threshold in Stellarators

ITG-driven turbulence is thought to be linked to significant thermal losses in the W7-X [85]. A theory has been developed for the linear instability threshold, based on an understanding of resonant ITG modes near marginal stability, using a coarse-graining procedure to obtain smoothed geometric profiles of arbitrary stellarator configurations [86, 87]. The result is an expression for the critical gradient in terms of an effective, coarse-grained magnetic field-line curvature, with a correction for stabilisation by a finite parallel correlation length set by global magnetic shear. The model accurately produces the behaviour of a wide range of stellarators (figure 12), and has been applied successfully to stellarator optimisation. A small-aspect-ratio version of W7-X, called W7-K for Kompakt, was created to demonstrate the impact of smaller aspect ratio and increased magnetic field line curvature on the critical gradient. Relative to the high-mirror (KJM) W7-X configuration, W7-K was found to have twice the linear stability threshold, an increased nonlinear critical gradient, and weaker turbulent heat losses for experimentally relevant values of the temperature gradient above the marginal stability point. Optimisation work is now underway to produce new configurations with improved ITG critical gradients, as compared with existing designs.

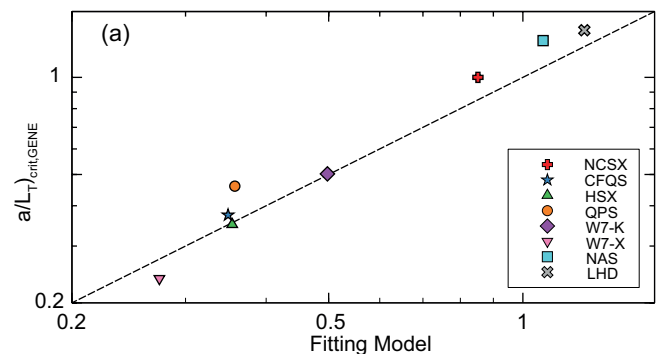


Figure 12. Observed linear ITG stability threshold obtained by gyrokinetic simulation, compared with model prediction.

3.2.6 Predictive Model of the Dimits Shift

In toroidal fusion plasmas, it has long been noted that the linear stability threshold is generally not equal to the actual onset of appreciable plasma turbulence. The discrepancy, the so-called “Dimits shift”, is widely understood to result from nearly complete suppression of

turbulence by nonlinearly driven zonal flows. Despite its obvious importance for understanding plasma confinement, a detailed and predictive understanding of the Dimits shift has not yet been achieved. Using the GENE code, nonlinear simulations have been run to study the phenomenon in collisionless Z-pinch entropy mode-driven turbulence, as a step towards general toroidal systems. Simulations are also performed of the corresponding “tertiary instability”, i.e. the mode that arises when a drift wave is subjected to zonal flows, quantifying the stabilising properties of different zonal flow profiles. Observing that zonal flows nonlinearly evolve toward stable configurations, an efficient prediction of the Dimits shift was proposed, based on the tertiary threshold with a maximally stabilising zonal profile, which proved accurate over a wide parameter range. This is the first such predictive theory for a gyrokinetic system [88].

3.2.7 Near-marginal Turbulence and Dimits Shift in Wendelstein 7-X

Just above the linear threshold, ITG modes extend far along the magnetic field, even in the presence of kinetic electrons, providing a drive that results in finite turbulent transport. In simulations of such turbulence, a Dimits shift is not observed. The reason has been identified as due to the peculiar radial structure of marginal turbulence, which is more localised in the radial direction than in the fluid case and therefore less likely to be stabilised by shearing flows [89].

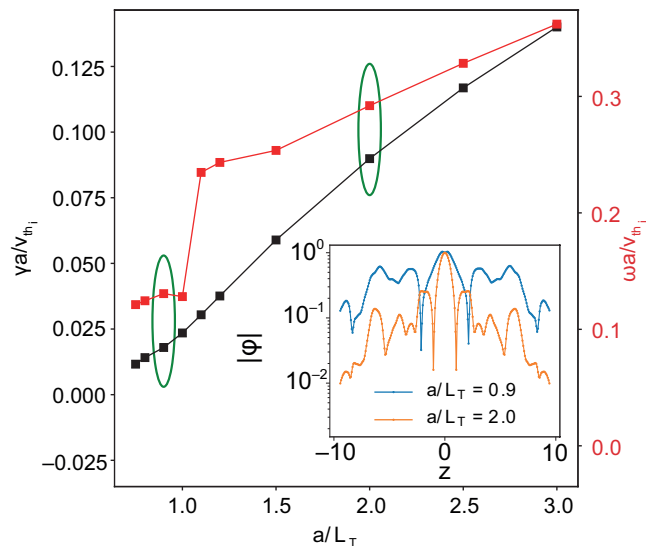


Figure 13. Growth rate and frequency for the most unstable ITG mode as a function of the temperature gradient. Inset: linear eigenfunctions. Fluid-like modes ($a/L_T > 1$), Floquet-type modes ($a/L_T < 1$).

3.2.8 Trapped-electron-mode Turbulence

The best energy confinement in W7-X was achieved in plasmas where ITG modes were stabilised by a density gradient resulting from

pellet injection. Such gradients can drive trapped-electron-mode (TEM) turbulence, but this is relatively benign in W7-X thanks to the fact that most trapped particles mostly reside in regions of good curvature. In order to quantify this effect, the “available energy” of trapped electrons (a thermodynamic concept of wide interest) has been calculated and been found to correlate well with the energy flux from gyrokinetic simulations of density-gradient-driven turbulence in a range of stellarator and tokamak plasmas [90].

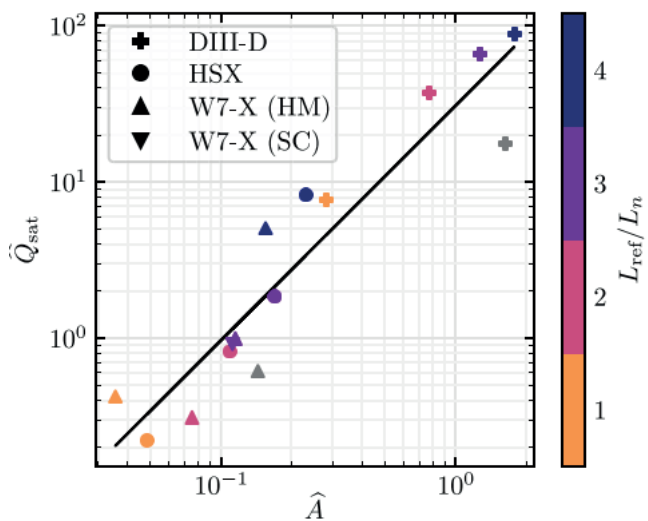


Figure 14. Normalised energy flux from gyrokinetic turbulence simulations vs “available” energy of trapped electrons in various stellarator and tokamak plasmas. These simulations were carried out in plasmas without a temperature gradient and with a density gradient indicated by the colour code.

3.3 Plasma Equilibria, MHD and Large-scale Stability

3.3.1 Databases W7-X Equilibria

The calculation of magnetic plasma equilibria has always been a key issue of stellarator research. It is essential to ensure accurate predictions for experiments and is required for the interpretation of data from plasma diagnostics. The equilibrium-configuration database containing possible W7-X configurations is steadily growing. A suite of codes is used to produce equilibrium data and neoclassical transport coefficients for use in transport analysis.

An important point for the preparation of the upcoming W7-X campaign is the search for configurations that are MHD unstable already for currently achievable plasma parameters, so that the importance of MHD optimisation for confinement and transport can be investigated experimentally. The procedure of identifying such equilibria was technically demanding and involved the construction of fit functions to operate in a data base of almost 7000 W7-X equilibria in 1700 magnetic configurations. The critical values for the plasma- β above which the plasma becomes unstable were calculated with the CAS3D code.

3.3.2 Sawtooth Instabilities

As described above, the EUTERPE code was developed for studying global gyrokinetic instabilities, but the code can also be used to calculate large-scale instabilities, thus making contact with MHD. Thanks to the layered structure of EUTERPE, it is possible to treat different particle species with different equations. Using hybrid calculations, where the electrons are treated as a fluid, magnetic reconnection in W7-X has been analysed in a series of models of increasing complexity [91]. The investigation focused on W7-X plasmas with electron cyclotron current drive (ECCD) causing the rotational transform to exceed unity in a certain radial domain. For suppressed temperature and density gradients, a kink instability arises in this region. This was shown first with a collisionless, fully gyro-kinetic, cylindrical model. A full-geometry electron-fluid model with uniform resistivity (η), (numerical) viscosity, and a term accounting for the electron inertia revealed that the most unstable mode is $(m,n) = (-4,4)$ in agreement with earlier work, with a growth rate proportional to $\eta^{1/3}$. Adding a gyro-kinetic ion species was found to have a stabilising effect. For collisionalities relevant to W7-X, the growth rate scales linearly with the electron skin depth.

This investigation of linear stability was supplemented by nonlinear calculations with the resistive MHD code MEGA (developed at NIFS, Japan). The linear phase of the simulations was also found to be dominated by a $(m = 4, n = -4)$ activity, which in the non-linear phase evolves into a spatially more extended $(m = 1, n = -1)$ structure, as observed in W7-X discharges with sawtooth crashes [92].

3.3.3 MHD of Rotating Plasmas

Due to their neo-classical transport properties, stellarators are not intrinsically ambipolar but have a radial electric field and an equilibrium mass flow. This field had not earlier been considered in the calculation of frequencies and growth rates of MHD modes in stellarators but has now been accounted for in the CAS3D code. The Mach number is generally small, and the Frieman-Rosenbluth equations could therefore be implemented in the subsonic approximation. Apart from an expected Doppler shift of stable modes, unstable flow-induced continua and a novel type of global, flow-induced, stable modes have been found. The unstable continua relate to an interaction between Alfvén and sound branches with the same poloidal mode number. The novel global modes reside above the maxima or below the minima of the flow-distorted Alfvén and sound continua [93].

The calculation of Alfvén and sound continua (usually done with the CONTI code for W7-X) is a standard means to analyse experimental data and identify modes, because continuum modes are radially local and therefore much easier to calculate than the full global stability with CAS3D. In order to use CONTI with flow, a radial electric field was added to the continuum equations derived from the corresponding gyrokinetic equations with flow implemented in the EUTERPE code [94]. For W7-X, coupled sound and Alfvén continua have

been calculated and show that the continua are distorted and can even disappear.

It has also proved possible to compare MHD continua with global, electromagnetic, gyrokinetic simulations. Figure 15 shows a tokamak benchmark of results from CONTI and the EUTERPE code using state-of-the-art signal processing (DMUSIC).

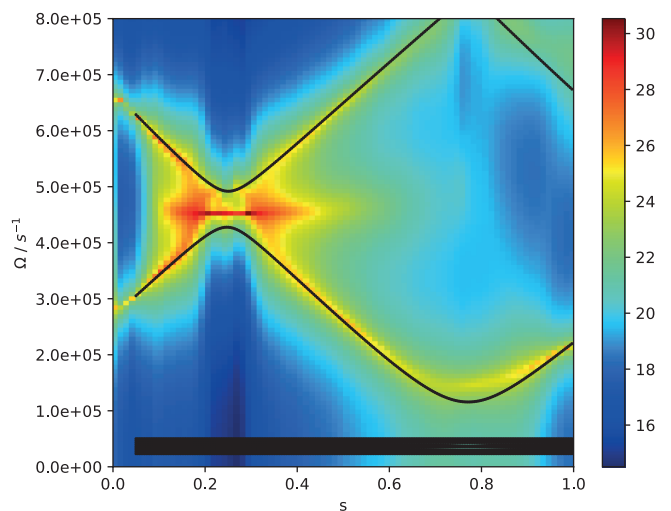


Figure 15. Fully gyro-kinetic continuum with a radial electric field in a tokamak calculated with the EUTERPE code (colour code) in comparison with an ideal MHD calculation with CONTI (black curves).

3.3.4 Non-neutral Plasmas

Experience in generating equilibria on the one side and gyrokinetic theory on the other has also proved useful in a quite different context. A non-neutral plasma can be confined in a stellarator, but it is not easy to calculate the resulting equilibria since the electric potential is given by a nonlinear integro-differential equation. Using the EUTERPE code, a kinetic ensemble of positrons was followed in time with collisions until an equilibrium state was reached. The charge and potential contours can thus be calculated for the positron experiment EPOS, a quasi-axial symmetric stellarator being developed at IPP Garching. Previous attempts to solve for such equilibria were plagued by convergence and numerical problems, limiting them to systems smaller than about 10 Debye lengths. With the kinetic method, these problems do not occur and solutions can be found for much larger plasmas.

3.4 Stellarator Optimisation

Wendelstein 7-X has convincingly demonstrated the practical value of stellarator optimisation. Its success has sparked a significant number of new design efforts as well as increased theoretical research activity in the fusion science community. There is consensus that any future stellarator fusion device will need to be based upon an optimised design.

3.4.1 Axis Expansion

Expansion of the magnetic field around the magnetic axis is an important tool in stellarator optimisation and can be used to generate quasi-isodynamic (QI) stellarators [95]. In the last year, this technique has been used to create single-period configurations with properties setting them apart from traditional QI stellarators [96]. The formalism can also be used for QI stellarators with an arbitrary number of field periods. Figure 16 shows an example with three field periods exhibiting low plasma elongation, torsion and curvature [97]. Its effective neoclassical ripple is similar to that of W7-X at the boundary and is lower in the region close to the axis.

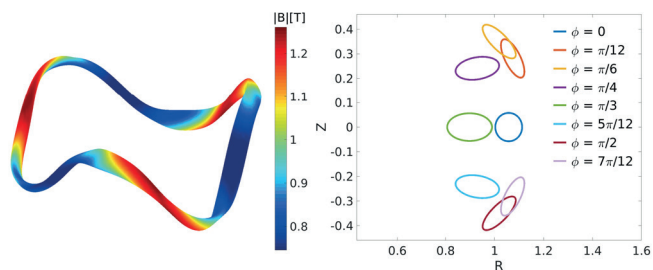


Figure 16. 3-period Quasi-Isodynamic MHD equilibrium obtained by axis expansion.

In a second research project using the same formalism, the parameters describing the axis shape are subjected to a nonlinear optimisation seeking configurations promising good fast-particle confinement. This approach has resulted in configurations exhibiting extremely small effective ripple.

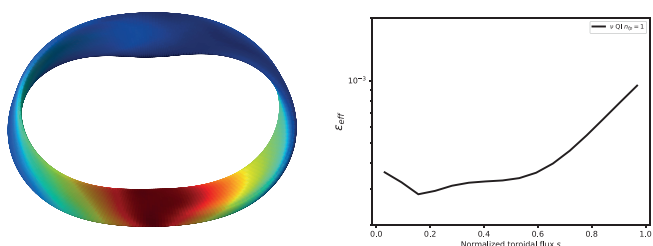


Figure 17. 1-period QI configuration found by axis expansion with optimised axis parameters.

3.4.2 Conventional Optimisation

Conventional stellarator optimisation does not rely on the near-axis expansion but on the numerical computation of equilibria in an optimisation loop involving the evaluation of metrics characterising plasma performance. The figure below shows an example of a novel QI configuration obtained in this way. It is one example in a series of optimisation campaigns seeking equilibria with good fast particle confinement at relatively high aspect ratio. The field strength mapped

on the plasma boundary shows very good poloidally closed areas of constant field. Neoclassical and fast-particle losses are significantly smaller than in W7-X.

This type of optimisation is facilitated by a novel mathematical representation of the plasma boundary. The conventional representation is not unique, which leads to an unnecessarily large number of dimensions of the optimisation space and the appearance of spurious local optima therein. The novel technique improves both the speed and outcome of the optimisation [98].

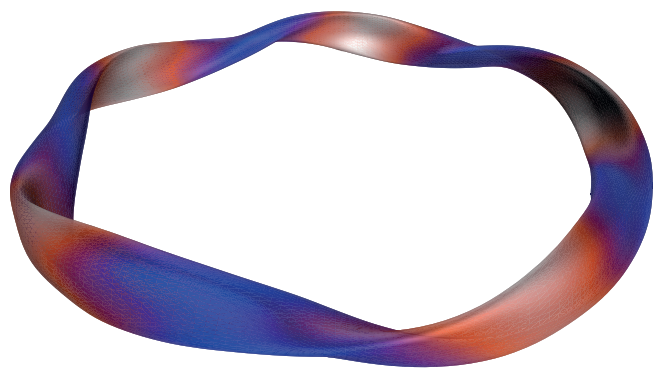


Figure 18. 5-period QI-stellarator with improved confinement properties.

3.5 Detachment Physics of the Wendelstein 7-X Divertor

The exhaust of particles and energy from an ignited plasma is an issue of critical importance for any fusion reactor. W7-X island-divertor plasmas have demonstrated great success in accessing and stabilising detachment – a SOL plasma scenario that is highly reactor relevant thanks to very low heat loads onto the divertor plates. Detachment in W7-X exhibits many features that differ from those observed in its predecessor, W7-AS, and in tokamaks. With the help of EMC3-Eirene, and in conjunction with the experimental results, it is possible to clarify how the W7-X island-divertor plasma self-regulates to maintain particle, momentum and energy balance under detached conditions [99].

Compared to the “partial” character of W7-AS detachment, that achieved in Wendelstein 7-X is “complete”, in the sense that the heat flux on individual divertor targets decreases much more uniformly with rising radiation. The reduction of recycling flux observed at high radiation levels may be understood as a constraint on the total power balance, which in W7-X is mainly related to a drop of the plasma pressure at the last-closed-flux-surface (LCFS) and a steepening of the pressure gradient there. Viscous momentum transport into the confinement region plays a supporting role, while plasma-neutral friction (which is crucial for tokamak detachment) causes only a small reduction of the recycling flux in the island divertor. The decrease in the upstream plasma pressure is primarily a temperature effect resulting

from an interplay between cross-field conduction and an inward shift of the radiation zone; this is further supported by a density profile steepening at the edge, as the edge density is reduced at deep detachment.

Both experimental results and EMC3-Eirene modelling consistently show that the W7-X divertor provides good compatibility of particle and heat exhaust. For example, the maximum divertor neutral pressure is obtained under deeply detached conditions with a radiated-power fraction of roughly 80%, and where the recycling flux has significantly decreased. This comes about, first, thanks to intense carbon radiation cooling the downstream plasma to an ionisation-inactive state, thereby opening up an ionisation-free channel for the recycling neutrals toward the divertor gap. Second, momentum transfer between neutrals and ions through charge-exchange or elastic collisions generally hinders the neutrals from penetrating the ionisation zone, which is shifted away from the target and is usually located near the last closed flux surface for the high radiation levels of interest. These scattering processes tend to retain the recycled neutrals in the near-target region, increasing their probability of being captured by the divertor chamber.

3.5.1 Pellet Physics

Pellet fuelling of W7-X plasmas, and a resultant steepening of the density gradient, has been observed to reduce ITG turbulent transport and has been instrumental for obtaining high-performance experimental conditions in W7-X. The physics of pellet ablation and subsequent assimilation in the plasma presents a challenging multi-scale problem to describe the transformation of solid material into an expanding plasmoid and is being investigated theoretically and numerically to support the enhanced experimental capabilities offered by the advent of a new steady-state pellet injector.

A detailed analytical study of plasmoid expansion dynamics has shown that the expansion is insensitive to the profile of the gas cloud that supplies the plasmoid and details of the ionisation of the gas. This is due to the self-similar nature of the expansion [100]. These analytical results have been confirmed with a newly developed hybrid fluid and kinetic Lagrangian code, which offers higher-fidelity physics models of the plasmoid assimilation [101].

Full-wave Modelling of Over-dense Electron Cyclotron Heating

ECRH provides the predominant means of heating W7-X plasmas and represents the only “steady-state” option, with the 140 GHz gyrotrons capable of providing continuous wave power for up to 30 minutes. X2- and O2-mode heating, which have been successfully used for a variety of W7-X operation scenarios, are nevertheless subject to density ceilings. For X2 heating, a density limit of 10^{20} m^{-3} has been enforced (to remain safely below the X2 cutoff at $1.2 \times 10^{20} \text{ m}^{-3}$), while for the O2-mode, densities up to $1.5 \times 10^{20} \text{ m}^{-3}$ have been attained (O2 absorption worsens well below the O2 cutoff at $2.4 \times 10^{20} \text{ m}^{-3}$).

Using ECRH at higher densities will require an over-dense plasma heating scenario. One such possibility involves a double mode-conversion, from O- to slow X- and then to Bernstein-mode. Such a scenario cannot be adequately described within the ray-tracing approximation, however. Therefore, the 3D full-wave code CUWA has been employed, which makes use of sophisticated numerical techniques and massive parallel computations with GPUs to significantly accelerate its calculations, thereby allowing large parametric scans over a broad range of parameters. The physics of O- to X-mode wave conversion in W7-X plasmas having densities in excess of $2.5 \times 10^{20} \text{ m}^{-3}$ has been investigated with CUWA and the feasibility of a viable mode conversion scenario has been assessed. A maximum O-X conversion efficiency of approximately 50% is predicted for the scenario expected in W7-X. All possible O-X “conversion windows” in the device have been quantified. These results will help guide experimental efforts to demonstrate O-X-B heating in the coming campaign.

3.5.2 ICRH Physics

Ion cyclotron resonance heating (ICRH) will hopefully become available for the first time at W7-X during the upcoming operation phase. ICRH is foreseen primarily for the production of fast ions, to allow the experimental investigation of improved fast-particle confinement for which W7-X was optimised. In preparation, numerical simulations with the SCENIC code package have been performed, a self-consistent combination of the equilibrium code ANIMEC, the full-wave code LEMan, and the particle-following code VENUS-LEVIS. Initially, the ICRH antenna will undergo testing in helium plasmas with a small minority of hydrogen ions. Such plasmas typically offer good power absorption, but are not favourable for the generation of long fast-ion tails in the distribution function. SCENIC simulations of this scenario confirm that most of the RF-power is indeed directly absorbed by the hydrogen minority (the second largest power fraction goes to the electrons) for a wide range of minority concentrations and background-plasma densities, and that this heating scheme is not well suited for the generation of very energetic ions. At most, the ions can be accelerated to an energy of about 50 keV. Other possibilities, such as the so-called 3-ion or NBI-ICRH-synergy schemes are known to be more advantageous for fast-ion generation. These will be investigated in the future for realistic experimental conditions.

SCENIC is able to follow fast ions only inside the confined plasma. However, the code records all relevant data when particles cross the last-closed-flux surfaces, making it possible for a more general orbit-following code, such as ASCOT, to determine whether such particles strike plasma-facing components. Such simulations provide guidance for the placement of fast-ion loss detectors around the machine. They also predict that thermal loads on the plasma-facing components are uncritical from a machine safety standpoint, which is an important prerequisite before operating the ICRH antenna in W7-X.

Future plans include the modelling of ion-cyclotron emission and looking for operating scenarios that better allow the investigation of fast-particle confinement in W7-X. The challenge here concerns the confinement of deeply trapped fast ions, as there is currently no heating system that provides such particles. Moving the ICRH power deposition away from the bean-shaped cross section (high-field region) into the triangular plane (low-field region) may alleviate this problem.

Scientific Staff

K. Aleynikova, P. Aleynikov, A. Arnold, C. Beidler, M. Borchardt, S. Buller, K. Camacho, P. Costello, M. Drevlak, Y. Feng, J. Geiger, A. Goodman, A. Hallenbert, P. Helander, S. Henneberg, A. Johansson, R. Kleiber, A. Könies, M. Kuczynski, N. Marushchenko, O. Mishchenko, A. Mutzke, Y. Narbutt, C. Nührenberg, G. Pechstein, G. Plunk, L. Podavini, J. Proll, J. Riemann, G. Roberg-Clark, A. Runov, B. Shanahan, C. Slaby, H. Smith, Yu. Turkin, P. Xanthopoulos, A. Zocco

Guests

R. Davies (Univ. of York), H. Frerichs (Univ. of Wisconsin-Madison), M. Hardman (Univ. of Oxford), S. Hudson (Princeton Plasma Physics Lab.), P. Huslage (Techn. Univ. München), R. M. Cabete de Jesus Jorge (Univ. of Maryland), Y. Kota (Nat. Inst. for Quantum Science and Technology), A. Kumar (Australian Nat. Univ.), Ro. Lunsford (Princeton Plasma Physics Lab.), R. Mackenbach (Techn. Univ. Eindhoven), P. Mülholland (Techn. Univ. Eindhoven), F. Nespola (Princeton Plasma Physics Lab.), J. Proll (Techn. Univ. Eindhoven), D. Reiter (Heinrich-Heine-Universität Düsseldorf), R. Schneider (Univ. Greifswald), S. Strotheich (Univ. Greifswald), I. Svenningsson (Techn. Hochschule Chalmers), Xing Tingjing (Univ. of Cambridge), A. M. Tschesche (Univ. Göttingen)

4 Numerical Methods in Plasma Physics

Head: Prof. Dr. Eric Sonnendrücker

The division “Numerical Methods in Plasma Physics” is devoted to the development of efficient and robust computational methods and algorithms for applications in plasma physics and more specifically for the models and problems of interest to other divisions of IPP.

4.1 Structure of the Division

The emphasis of the division lies on the development of new models suited for efficient and robust simulation, the optimization and analysis of numerical methods and is tightly coupled with the group “Numerical methods in plasma physics” at the Mathematics Center of the TU Munich. Recently an important focus has been placed on the development of simulation capabilities for physics processes beyond the gyrokinetic approximation level. In parallel research on (nonlinear) model order reduction, the derivation of new machine learning

tools based on Student-t and Gaussian Processes as well as structure preserving neural networks is pursued. In addition to inventing new methods specifically for the problem at hand, the division aims to maintain a knowledge of state of the art methods in the general area of numerical mathematics, scientific computing and machine learning in order to be able to adapt them where needed to plasma physics problems. The division consists of six research groups: ‘Kinetic and Gyrokinetic Models’, ‘Magnetohydrodynamics’, ‘Geometric Numerical Integration and Reduced Complexity Modelling’, ‘Probabilistic Data Analysis and Active Learning’, ‘Zonal Flows in Turbulent Plasmas’, and ‘Finite Element Methods’ which are closely interconnected. Moreover, one of the EUROfusion Advanced Computing Hubs (ACH) is attached to the division.

4.2 Zonal Flows and Structure Formation in Turbulent Plasmas

Zonal flows (ZF) are plasma-spanning turbulence generated large-scale flows. They exert an important effect on the overall intensity of the turbulence and the associated particle and heat transport in magnetic plasma confinement such as in tokamaks and stellarators. Their most important, yet still not understood action occurs at the boundary (or edge) of the plasma causing the low-to-high confinement transition (L/H), which is essential for the functioning of ITER and other future fusion experiments. The highly nonlinear nature of this plasma region, with fluctuation amplitudes of order of 100 %, and the influence of particle collisions lead to the breakdown of customary approximations and to the extreme difficulty to treat this boundary region.

The main angle of attack in the past period has been the development, verification of, and the study of new physics with BSL6D, a fast 6D kinetic turbulence code simulating the full gyro-motion of the particles. This approach is not as easy as it sounds, since on one hand, many new degrees of freedom appear, which need to be classified and distinguished from what is known, and on the other hand, the computational cost is much larger than previous gyrokinetic simulations. It is however a promising candidate to be adapted to future exascale computing architectures.

In addition, the matching of two-fluid and gyrokinetic turbulence simulations for the difficult plasma edge region is pursued, since the two-fluid framework is able to robustly deal with the strong nonlinearities, while gyrokinetics contains many of the kinetic effects. A difficulty for both has turned out to be the realistic treatment of collisions, which is important to get the proper level and damping rate of turbulence and zonal flows. This problem has been solved with the development of a linearised but otherwise complete Landau collision operator for the fluid and gyrokinetic simulations.

4.3 6D Kinetic Tokamak Turbulence Simulations

The novel BSL6D code developed within NMPP simulates the 6D Vlasov equation without gyrokinetic approximations using a split time-step semi-Lagrange scheme in a rotating velocity grid. That way the particle

gyration is computed particularly efficiently and the method allows to study the physics of drift time scale modes including much faster time scales and unhampered by strong nonlinearities. The code currently has been run in electrostatic mode in unsheared slab magnetic geometry using adiabatic electrons and with relatively low gradients, to be comparable to gyrokinetic runs.

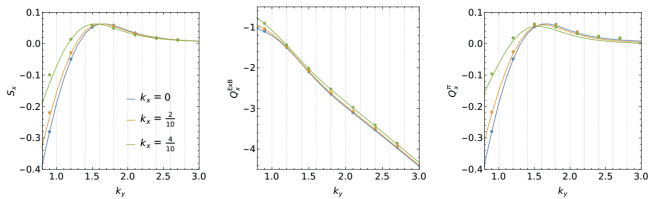


Figure 19. Quasilinear Poyniting flux (S_z), $E \times B$ heat flux $Q_x^{E \times B}$, and stress induced heat flux Q_x^{Pi} in linear slab ion temperature gradient (ITG) mode simulations (dots) and analytic theory (-) for various wavenumbers. Since the slab ITG is essentially a gyrokinetic mode, the two additional contributions are still small.

Already in the initial linear run phase, where various parameters and boundary conditions were tested, new physics emerged. While electrostatic gyrokinetics turbulence is described by a single convective energy flux – the $E \times B$ induced heat flux – it turned out that the 6D simulations require three different types of fluxes, which together make up the complete energy flux (figure 19). This study was aided by the derivation of a novel representation of the convective fluxes, which made it particularly easy to filter out superposed spurious fluxes due to fast ion Bernstein oscillations (which are part of the new physics in the 6D code).

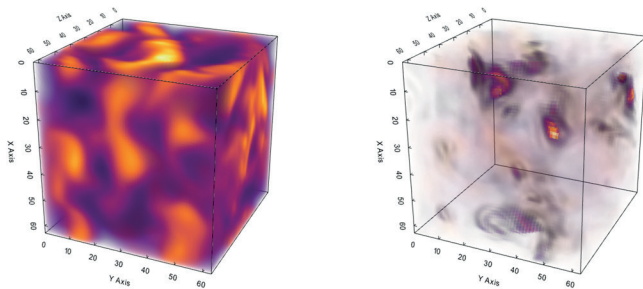


Figure 20. Snapshot of density fluctuations of saturated slab ITG turbulence (left) simulated using a 6D-space-velocity grid of dimensions $64^3 \times 32^3$ and associated cyclotron resonance mode intensity from time/frequency transform (right). The magnetic field points in z-direction, the temperature gradient in negative x direction.

In the subsequent nonlinear turbulence runs the gyrokinetic slab ion temperature turbulence could be reproduced, but already at the smallest gradients significant ion Bernstein/ion cyclotron waves appeared (figure 20) as secondary instabilities. These modes have frequencies

close to harmonics of the ion cyclotron frequency and require non-gyroaveraged distribution functions. They are therefore ignored in the customary gyrokinetic simulations and represent another new piece of physics in the code. It was discovered that those modes can indeed be driven unstable by purely gyrokinetic distribution functions (i.e. distribution functions which are constant along a Larmor orbit) and in fact are practically always unstable – although normally at low growth rate.

For the near term, it remains to quantify exactly how much the overall convective flux is influenced by the non-gyrokinetic modes, and to expand the geometry and electromagnetic degrees of freedom of the 6D simulations.

For the longer term, the 6D code is demanding exascale computing power. Since the architecture of those future systems cannot be known at present and may be quite complex, we are in the process of porting the code to C++ using Kokkos, a performance portability library. Kokkos renders the hardware largely transparent, so that the source code is independent of the node level implementation based on various combinations of processors (CPU) and graphics cards (GPU). Figure 21 shows a comparison of the computer time used for the ported fundamental semi-Lagrangian time step on comparable CPU and GPU systems, much in favor of the GPU architecture.

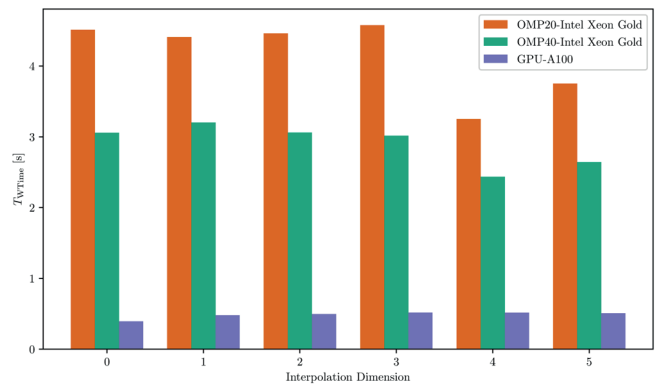


Figure 21. 6D advection step time tests; OMP20: 20 threads on 1 CPU (COBRA, 0.1TB/s peak bandwidth); OMP40: 40 threads on 2 CPUs (0.2TB/s BW); A100: 1 GPU (RAVEN, 1.6TB/s peak BW); a single GPU is much faster than even two CPUs with overall 40 cores.

Further development of the code in the direction of exascale readiness will have to target methods to exploit extra parallelism and to reduce the communication of boundary values even at increased computational cost, such as by parallel-in-time and discontinuous Galerkin methods.

4.4 3D MHD Equilibrium

The computation of the ideal MHD equilibrium is a basic modelling step to describe the confined plasma state of a tokamak and a stellarator. Nestedness of flux surfaces is guaranteed only for axisymmetric domains (tokamak), and not for 3D fields in general.

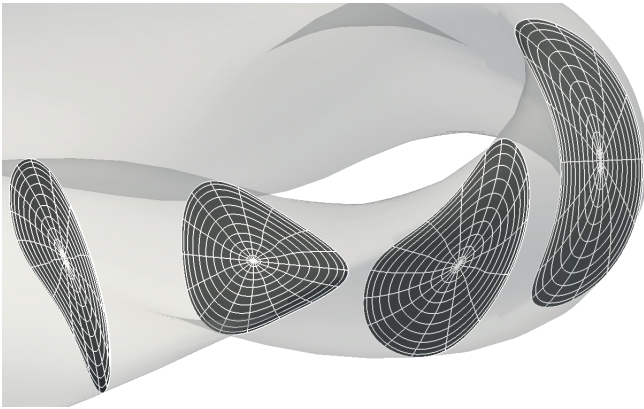


Figure 22. Visualisation of the straight-field line grid (PEST coordinates) of a W7-X equilibrium solution computed with GVEC using a radial grid of 11 P4 elements.

However, the assumption of closed nested flux surfaces allows finding 3D MHD equilibria with good confinement properties, as shown by the well-established equilibrium code VMEC. Adopting the same strategy as VMEC, a new 3D MHD equilibrium code GVEC (Galerkin Variational Equilibrium Code) was developed from scratch at NMPP over the last years. A main difference to VMEC is the radial discretisation, using B-Splines on a non-uniform grid spacing, which allows local refinement and includes the magnetic axis. As B-Splines are high order with a high continuity, less radial grid points are needed for a certain accuracy, and they provide smooth radial derivatives, needed for evaluating equilibrium quantities, such as metrics and magnetic field. A W7-X solution with 11 radial elements of degree 4 is visualised in figure 22.

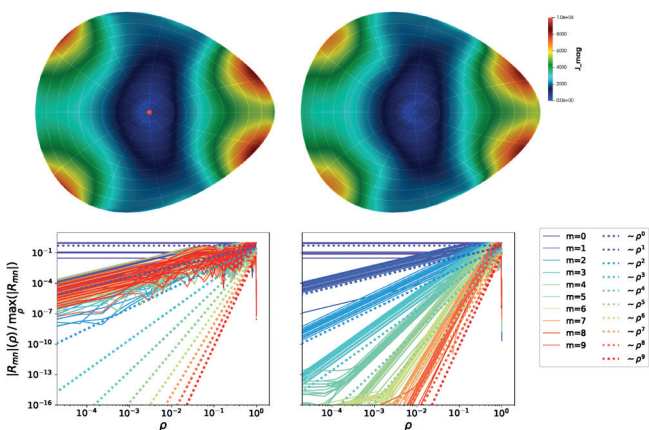


Figure 23. Effect of GVEC smoothness constraint at magnetic axis. Top line: magnitude of the current in a poloidal plane of a stellarator, numerical artefact appears without smoothness constraint (left) and is removed with smoothness constraint (right). Bottom line: Fourier mode of solution R over radial coordinate, numerical behaviour towards the axis is correct only with the smoothness constraint (bottom right).

GVEC has been benchmarked against VMEC fixed boundary solutions of tokamak and stellarator configurations. GVEC is already used within IPP to provide the final equilibrium solution to other codes via specific interfaces: At NMPP, a python interface to the STRUPHY code is available, and in collaboration with TOK, different interfaces exist to the linear 3D MHD stability code CASTOR3D, the newly developed non-linear 3D MHD code JOREK-3D and the gyro-kinetic turbulence code GENE-3D. It was found recently that numerical artefacts can appear at the magnetic axis, producing for example a unphysical local current spike. The magnetic axis is the singular point of the flux-aligned coordinate system. Due to the B-Spline discretisation, it is now possible to control radial derivatives at the axis and thus avoid the singular behaviour, yielding a smoothness constraint that effectively removes the artefacts at the axis, as shown in figure 23.

4.5 Metriplectic Relaxation for Calculating Equilibria

In the past years, we have pursued the idea of using metriplectic relaxation for the calculation of equilibria with specific focus on (but not limited to) magnetohydrodynamic equilibria. Specifically we construct artificial metriplectic dynamical systems that relax a given initial condition to an equilibrium. Here “metriplectic” refers to a particular algebraic structure, which generalizes Hamiltonian dynamics in order to include dissipative mechanisms. Numerical schemes have been designed for various metriplectic structures. In one particular case in which metriplectic relaxation is applied to a magnetic field, the method reduces to the known magnetic relaxation method, for which we obtained a new structure-preserving discretization in the framework of finite-element exterior calculus. Magnetic relaxation consists essentially in the push-forward of the magnetic field with the flow of an effective velocity. Therefore, the magnetic field lines are “frozen into the flow”. One important property, which is exactly preserved by the numerical scheme, is the conservation of magnetic helicity, a quantity which is related to the topology of magnetic-field lines.

4.6 Data Science and Machine Learning

Novel methods of data science and machine learning have an enormous potential to process and better understand a large variety of data from simulations and experiments at IPP. During the reporting period, members of the NMPP division participated in several interdisciplinary projects targeted at these developments: The MIT Global Seed Fund (MISTI) project on surrogate data and disruption prediction, the Helmholtz Foundation grant on Reduced Complexity models, the VECMA project for verified exascale computing and the Munich School for Data Science. Furthermore, there has been active involvement in the Helmholtz Information and Data Science Academy and Incubator.

4.7 Data Augmentation and Disruption Prediction

Disruptions pose serious challenges to the operation and design of tokamaks. Due to rapidly growing instabilities, thermal and magnetic

energy is rapidly lost during a disruption, the magnetic confinement of the plasma is destroyed, and energy is deposited into the confining vessel, potentially causing serious damages. Hence, to maintain a reliable fusion operation, disruption mitigation mechanisms should be triggered with sufficient warning time prior to the disruption.

Disruption prediction is a challenging task for various reasons. One of them is the imbalanced data situation; for some disruption classes, only a few measurements are available, making it difficult to obtain robust results. This is challenging, especially when working with neural networks, as they require a large training data set in order to give satisfying results and to avoid overfitting. However, generating such an amount of training data from additional discharges is expensive and also potentially harmful for the reactor. Particularly with regard to future reactors such as ITER or SPARC, a sufficient data set will not be available at the time these reactors will start operating.

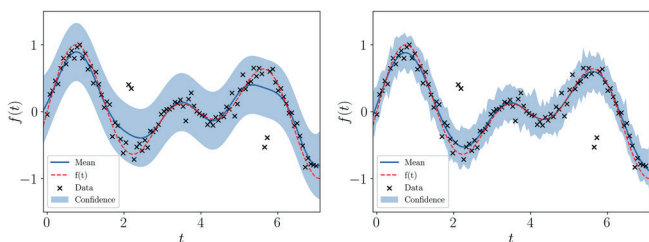


Figure 24. Predicted mean and 95 % confidence band with for a Gaussian process (left panel) and a Student-t process (right panel) trained on $N = 100$ training data points following $f(t) = \sin(2t)\cos(0.4t)$ corrupted by additive Gaussian noise and superimposed with several outliers.

Data augmentation is one possibility to balance the training data set by creating rare disruption events and thereby improve the prediction performance of machine learning models. The aim of data augmentation is to produce an arbitrarily large amount of artificial samples that have the same statistical properties as the original small data set. However, many commonly used methods are not expedient for the task at hand, as time-dependencies and the causal structure of physical signals are destroyed by such transformations. More elaborate methods for multivariate time series generation using e.g. neural networks or mixture autoregressive models require substantially more samples per class than usually available for disruption prediction. The above-mentioned challenges were addressed within a collaboration with DIII-D and MIT by exploiting a non-parametric Bayesian approach to design the multivariate surrogate model based on Student-t process regression to generate additional data. This model improves upon the more commonly used Gaussian process regression because one drawback of standard Gaussian processes regression is the assumption of Gaussian noise, which is inaccurate due to outliers in the present application case. This results in unreliable uncertainty estimates. In contrast, the chosen approach builds on Student-t processes with

analytic inference schemes that also allow for a heavy tailed noise distribution and give robust results even for noisy data corrupted by outliers as illustrated in figure 24. Please note that the Student-t based regression does not only follow the true mean closer than the GP-based regression but exhibits also a smaller uncertainty.

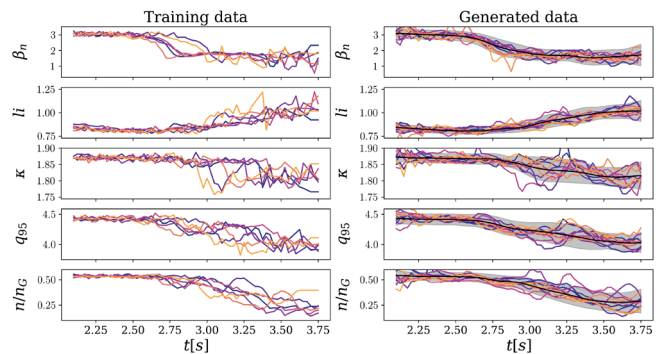


Figure 25. Training data (left panel) and 10 generated data sets (right panel) from the state space Student-t surrogate model together with the estimated mean (black solid line) and 95 % confidence (grey shaded region) for a test case of time traces of disruptive plasma discharges.

Another challenge imposed by high-resolution time series data is the computational complexity of multivariate Gaussian or Student-t process regression of $O(N^3)$, where N is the number of training data points given by the product of dimensions D and time steps T of the multivariate time series. For typical values of $N > O(5000)$, traditional process regression requires unbearable computing time. Here the use of a state space formulation of the Student-t process as a linear time invariant stochastic differential equation, which can be solved using a corresponding filter and smoother reduces the computational complexity to $O(N)$, making it also suitable for high-resolution time series. To account for signal interdependencies in the plasma signals, correlations and cross-correlations are introduced via coloring transformations in a post-processing step. As can be seen in figure 25 even with a few time-traces as input (left panel) the surrogate time traces (right panel) are almost indistinguishable. Moreover, use of the surrogate data for disruption data augmentation resulted in an improved prediction performance by ANNs. In ongoing studies, the optimal mixing ratio of real and surrogate data as function of the number of available training data and its fluctuation level is being studied.

4.7.1 Scientific Machine Learning

Scientific machine learning is an emerging research area that uses machine learning techniques to address problems across all sciences. In plasma physics, hybrid approaches where physics-based methods are combined with data-driven methods e.g. to solve differential equations (physics informed machine learning) are particularly promising.

Here the design of neural network architectures for the construction of surrogate models is studied. The neural network shall by design encode important properties of the equations being approximated. Geometry guides the design process to facilitate networks that are specifically tailored to the solution of a specific problem.

One of the objectives was the construction of Hamiltonian Autoencoders (HAEs). Autoencoders are an established tool for dimension reduction and feature extraction in data science and can be used in a very similar fashion as a reduced basis (see above). The main difference is, that standard reduced basis methods define (linear) vector spaces, while autoencoders define (nonlinear) manifolds. Thus theoretically, autoencoders can reach the same or better expressiveness than reduced basis using a much smaller number of degrees-of-freedom. The training of these HAEs requires novel gradient descent methods, that leverage the differential-geometric structure emerging from the network design. For evolving the low-dimensional system in time, neural network-based integrators as well as traditional symplectic ones can be used. The new architecture has been found to significantly outperform existing designs in accuracy.

4.7.2 Reduced Complexity Modelling and Model Reduction of Stochastic Systems

Reduced complexity modelling aims to capture the dominant behaviour of a complex system while at the same time saving computational cost. A prominent family of reduced order models employ a reduced basis that is constructed by identifying dominant modes from the results of sample ‘training’ simulations for select parameter values. The reduced basis can then be used to simulate the system for numerous other parameters using a cheaper reduced model. This approach is often beneficial in many-query applications, where the reduced model has to be evaluated many times, for example inside an optimisation loop, the solution of inverse problems or real-time control problems. Recently a combination of three fields of computational mathematics, namely geometric integration, stochastic integration, and data-driven model reduction, has been applied to plasma physics simulations, specifically the construction of reduced models for collisional Vlasov equations.

To this end a geometric description of collisional Vlasov equations has been developed. The collisional Vlasov-Maxwell and Vlasov-Poisson equations were recast as systems of coupled stochastic and partial differential equations, and the stochastic variational principles which underlie such reformulations have been derived. Also, a stochastic particle method for the collisional Vlasov-Maxwell equations was proposed and a variational characterization provided. This variational characterization is currently used as a basis for the development of stochastic structure-preserving particle-in-cell integrators for collisional Vlasov equations.

Ongoing work addresses the design of data-driven geometric model reduction strategies to reduce the high computational costs of

particle-in-cell simulations of collisional Vlasov equations. To this end, it was demonstrated that reduced basis methods based on singular value decomposition (SVD) known for ordinary differential equations, such as the proper orthogonal decomposition, can be extended to stochastic differential equations. This allows to reduce the computational cost arising from both the high dimension of the considered stochastic system and the large number of independent Monte Carlo runs. Also the proper symplectic decomposition method was extended to stochastic Hamiltonian systems, both with and without external forcing, and argued that preserving the underlying symplectic or variational structures results in more accurate and stable solutions that conserve energy better than when the non-geometric approach is used. The proposed new techniques were validated with numerical experiments for a semi-discretization of the stochastic nonlinear Schrödinger equation and the Kubo oscillator. Current research focusses on the application of these methods to collisional Vlasov equations.

4.8 Quantifying Uncertainties in Simulation and Experiment

Uncertainty quantification in the results of not only experiments, but also simulations is a topic that has received an increasing amount of attention in the recent years. Complex numerical models in plasma physics and other areas depend on a number of input parameters that are often subject to uncertainties. On the one hand this includes parameters derived from measurement data which may deviate from an exact value due to limited accuracy, fit uncertainties or inherent statistical nature. On the other hand, discretization errors and statistical noise in numerical computations directly introduce additional uncertainty in simulation results.

To tackle these issues, the strategy during the recent years has been the development of tools for automatic construction of data-driven response models that leverage information from computationally expensive simulations in an efficient way. The principle consists in estimation of the relation between input parameters and simulation output based on point samples in parameter space. One way to realize uncertainty quantification uses a polynomial expansion that leads to spectral accuracy in the estimation of statistical errors and sensitivity analysis within the framework of polynomial chaos expansion (PCE). In the last years several approaches have been implemented as Open Source Python and HPC-Fortran toolkits which are now shared with various project partners within and also outside of the fusion community.

4.9 A General Framework for Variational Hamiltonian EM Particle Schemes

A few years ago the Geometric Electromagnetic Particle-in-Cell (GEMPIC) method has been developed by combining point particles with B-spline finite elements that preserve the de Rham structure at the discrete level. The resulting scheme possesses a Hamiltonian

structure with discrete Casimirs preserved on long times, including the discrete Gauss laws. We have extended this work by devising a general variational derivation of structure-preserving particle schemes for the Vlasov-Maxwell equations, resulting in gauge-free Hamiltonian schemes with fairly general particle smoothing.

The strength of our derivation is that it applies to a wide variety of field solvers and particle coupling techniques. Indeed it is based on a discrete Action principle which only assumes that (i) the field solver relies on a discrete de Rham sequence and that (ii) the particle-field coupling operators commute with the exact differential operators. In particular this approach applies to field solvers based on polynomial elements, compatible spline spaces, Fourier modes, or a combination of those. It also handles Fourier filtering and is easily applied to curvilinear coordinates, since mapped finite elements defined via standard push-forward and pull-back transforms preserve the de Rham structure.

Future directions of research consist in studying efficient implementation of these schemes in relevant configurations, and extension to reduced models such as drift-kinetic or gyrokinetic equations.

4.10 Structure-preserving Finite Elements on Fully Discontinuous Spaces

A parallel body of work has been to devise structure-preserving discretizations with broken (fully discontinuous) finite elements spaces that provide stable, high-order and efficient solvers for Maxwell's equations in complex domains. This framework extends the original conforming/nonconforming Galerkin (CONGA) scheme developed for Maxwell's equations and builds upon the Finite Element Exterior Calculus (FEEC) theory. In particular preserves at the discrete level the de Rham geometric structure of the exact problems. In particular, it represents a new class of field solvers on which Hamiltonian particle schemes can be derived, following the generic variational derivation described above. The fully discontinuous nature of the spaces then allows for a greater locality in the computations (in particular the derivatives and coderivatives are all local discrete operators, which is not the case with typical structure-preserving finite elements) and a greater modularity in the implementation.

These generic field solvers have been shown to give good results on several electromagnetic problems on multi-patch curvilinear domains, such as magnetostatic problems on domains with holes. Because such domains possess non-trivial harmonic fields, magnetostatic problems are a priori ill-posed without a proper characterization of the harmonic parts, which makes structure-preserving schemes particularly appealing.

4.11 PSYDAC Finite Element Library

PSYDAC is a Python 3 library for the solution of partial differential equations, which combines the convenience of a domain specific language with the speed of a high-performance parallel engine. Its

current focus is on isogeometric analysis using tensor-product B-spline finite elements, but extensions to other methodologies are under consideration. The library supports multi-patch mapped geometries, and finite element exterior calculus (FEEC). In order to use PSYDAC, the user defines the weak form of the model equations using SymPDE, an extension of Sympy that provides the mathematical expressions and checks their semantic validity. Simple mappings can be defined analytically, while multi-patch NURBS geometries can be imported from a geometry file. Once a finite element discretization has been chosen, PSYDAC maps the abstract concepts onto concrete objects, the basic building blocks being MPI-distributed vectors and matrices. Python code is automatically generated for all the computationally intensive operations (matrix and vector assembly, matrix-vector products, matrix transpositions, etc.). Finally, the generated code is accelerated using either Numba or Pyccl.

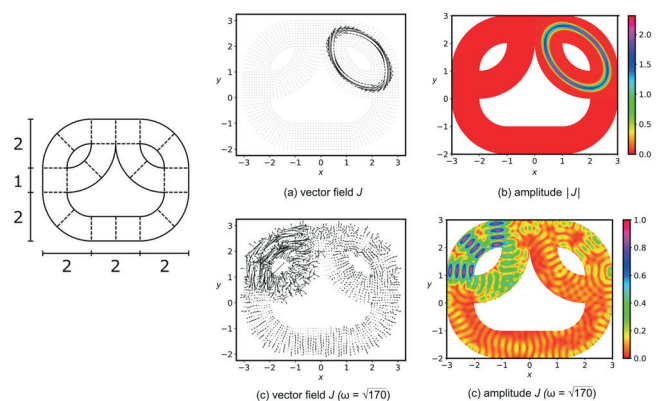


Figure 26. (left panel) Non-contractible domain consisting of 18 patches, each defined through a smooth mapping from a reference unit square. Solid and dashed lines are used to represent the domain boundaries and the patch interfaces, respectively. (right panel) Time harmonic Maxwell's equations with PEC (perfect electric conductor) boundary conditions. Top row: vector field (a) and magnitude (b) of the current source. Bottom row: vector field (c) and magnitude (d) of the electric field computed with Psydac. All quantities are in arbitrary units. The solution is obtained with 20×20 cells per patch and tensor-product splines of degree (6, 6).

In the last two years complete support for FEEC was added to the library, and extensively tested. On single-patch mapped domains a discrete de Rham sequence is exposed to the user in terms of conforming finite element spaces, commuting projection operators, differential operators, and appropriate push-forward and pullback operators. These features will be used by the Struphy code, which has recently been interfaced to Psydac. On multi-patch domains the CONGA approach has been successfully employed to define a discrete de Rham sequence based on the patch-local sequences: spectral correctness and convergence has been proven, and numerically verified, for the solution of electrostatic, magnetostatic, and electromagnetic problems in non-contractible domains (c.f. figure 26).

4.12 STRUPHY

STRUPHY (STRUcture-PReserving HYbrid codes) is a Python package for simulating energetic particles in plasma fluids, developed at NMPP since 2019. STRUPHY aims to provide easy access to partial differential equations (PDEs) used in plasma physics, by abstracting away tasks like array allocation, marker initialization or MPI communication. The Python language leads to an intuitive access to plasma physics equations, and the provided abstraction layers enable the streamlined implementation of new model equations or physics features. The current focus of the development team is on kinetic-fluid hybrid models, which couple a thermalized bulk plasma (MHD equations) to energetic particle (EP) species (kinetic or drift-kinetic). An example of this is the current-coupling model between linear, ideal MHD equations and the full-orbit 6d Vlasov equation for energetic ions. The STRUPHY implementation of this model has recently performed the ITPA TAE benchmark with success (c.f. figure 27). The expected growth of the TAE induced by the presence of energetic particles after $t = 250$, seen in the middle plot, is clearly reproduced. Remark that this was a full-f, full-orbit simulation, which required the resolution of the EP cyclotron period by the time step, and featured exact conservation of the total discrete energy, due to the use of geometric methods. In recent months, the STRUPHY code has been upgraded to feature MPI parallel field solvers, and the capability of distributing finite element coefficients with MPI. This represents a major step towards a fully CPU-parallel Python PIC library, which can be applied to a variety of physics models in the future

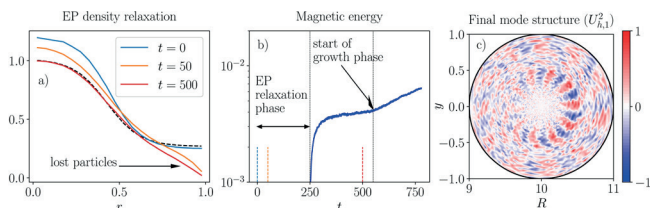


Figure 27. ITPA TAE case. Left: evolution of the EP density profile with respect to time and comparison to the benchmark distribution (black dashed line). Middle: evolution of the magnetic field energy after switching on the coupling terms between MHD and EP Vlasov equations at $t = 250$. Right: final mode structure that developed out of particle induced noise.

Scientific Staff

C. Albert, T. Blickhan, B. Brantner, C. Bressan, M. Campos Pinto, V. Carlier, B. Dingfelder, A. Dodhy-Würsching, J. Dominguez, E. Franck, F. Fambri, M. Gaja, I. Garnelo Abellanas, L. Guidi, Y. Güçlü, S. Hadjout, K. Hallatschek, F. Hindenlang, O. Hoenen, R. Köberl, K. Kormann, M. Kraus, J. Lakhilili, N. Legouy, Y. Li, O. Luk, O. Maj, L. Mendoza, M. Mazza, M. Musch, B. K. Na, D. Nille, H. Oberlin, F. Patrizi, B. Perse, S. Possanner, R. Preuss, S. A. Raiesi, A. Ratnani, M. Räth, M. Restelli, K. Röck, B. Scott, N. Schild, F. Schnack, U. von Toussaint, C. Tronci, T. Tyranowski, A. Yurova, E. Zoni

4.13 Advanced Computing Hub

Head: Dr. Roman Hatzky

4.13.1 The High Level Support Team

Already with the start of the EFDA HPC for Fusion (HPC-FF) project in 2009, it became clear that it is insufficient to only provide a dedicated HPC machine for the European fusion community. Therefore, the High Level Support Team (HLST) was established to make an optimal use of the hardware possible. Until the middle of 2021, the HLST has provided support to scientists from all EUROfusion Research Units (RUs) for the development and optimisation of their codes on the dedicated HPC machines of EUROfusion. The current machine is MARCONI-FUSION, which is hosted by CINECA in Bologna, Italy. It consists of a conventional partition of 2848 Intel Skylake (SKL) nodes and a GPU partition of 99 nodes. Its total compute power accumulates to about 12 petaflop/s. Furthermore, the HLST had a bridging function between the users on the one side and the system and vendor personnel on the other side, to guarantee an efficient handling of the users' support requests on EUROfusion HPC machine issues.

The HLST support covered the following tasks:

- Parallelise codes using e.g. OpenMP and/or MPI standards for massively parallel computers;
- Improve the performance of existing parallel codes, both at the single node and inter-node levels;
- Provide support for high performance parallel I/O;
- Support the transfer of codes to new multiprocessor architectures like MIC and GPU;
- Choose or, if necessary, adapt algorithms and/or mathematical library routines to improve applications on targeted computer architectures;
- Give feedback to the community based on experience gained from specific project work;
- Provide guidance to young scientists on available training activities in HPC, including upcoming new computer architectures;
- Provide consultancy to scientists within the RUs working on HPC;
- Assess the "MARCONI-FUSION" tickets submitted by the users to the user support of CINECA;
- Monitor and improve the performance of the "MARCONI-FUSION" supercomputer.

Over its operational time of twelve years, the HLST provided support through more than 130 projects with principle investigators from 14 countries. This enabled RUs from all over Europe to get access to HPC support. Especially the smaller RUs benefited from this opportunity, as it is more difficult for them to obtain high quality HPC support using local resources. The success of the HLST proved that it is not sufficient to only provide access to HPC resources. Additionally, it is necessary to provide access to high quality HPC support to the scientists of EUROfusion.

From 2020 to mid of 2021, the HLST core team had been involved in eight different projects submitted by scientists from all over Europe.

As an example, we present an overview of the work being done for two of these projects.

4.13.2 CINCOMP Project

A suite of different benchmarks and tests were performed in order to determine the performance of Fugaku. As of March 2021, the Fugaku supercomputer was the leading system on the Top500 list, which ranks the most powerful supercomputers in the world. The supercomputer is housed at the RIKEN Center for Computational Science (R-CCS) in Kobe, Japan. The STREAM benchmark shows a high node memory bandwidth of 831 GB/s (81 % of the theoretical value). This is higher by a factor of four than the corresponding value of the Marconi SKL partition (203 GB/s).

A maximum node performance of 1.869 TFLOPS was reached on Fugaku with the HPL benchmark (61 % of the theoretical value). With the support of the HPCI helpdesk it was possible to improve this result up to 2.15 TFLOPS (70 % of the theoretical value). However, this achievement is still lower in comparison to what was reached in the HPL benchmark for the Top500 list (82 %).

The Fujitsu TofuD inter-node connection between two distinct nodes was tested using the Intel MPI Benchmarks. A maximum bandwidth of 6.2 GB/s and 12.1 GB/s were reached for the uni- and bi-directional data transfer, respectively. These values are 91.2 % and 89 % of the theoretical peak bandwidth of one Tofu network interface.

The intra-node data transfer was tested using both the OSU Micro-Benchmarks and Intel MPI Benchmarks. A maximum saturated unidirectional bandwidth of 223 GB/s was achieved on Fugaku, which is 87.1 % of the theoretical peak memory bandwidth. This bandwidth is higher by a factor of three in comparison to the Marconi SKL intra-node connection.

4.13.3 MULTIKIN Project

The HLST project MULTIKIN investigated the potential benefits of a multi-language solution for performance portability using the Kokkos framework. Performance portability is an important feature for large-scale simulation codes, due to the fragmented nature of current and future HPC platforms.

From these investigations, which were coupled with many implementation examples and tests, it can be concluded that Fortran is not well suited to solve this important challenge. Coupling Fortran with C++, with the hope of bringing some of the modern capabilities over, proved to not be worthwhile. The restrictions, imposed by Fortran, do not leave a lot of the desired functionalities intact.

Nonetheless, these investigations led to a collection of important conclusions and guidance in relation to performance portability with Fortran. A host of sample implementations was presented and strategies, which can help make Fortran codes more performance portable or port them over to C++ in their entirety.

Finally, the electron pusher of EUTERPE was ported to Nvidia GPUs

using OpenACC. This required a lot of careful modifications and changes to the code. The full evaluation of correctness and performance benefits were finally performed.

4.13.4 The Advanced Computing Hub

After HLST ceased operation, the Advanced Computing Hub (ACH) of MPG started seamlessly its operation on 1st July 2021. The initial team consisted of six persons based at IPP Garching plus one person situated at the EUROfusion consortium associate at Dublin City University (DCU). The team members are HPC experts with a background in developing large scientific applications. They are specialists in numerical algorithms and parallel computing. The work force of the ACH will increase up to eight persons in 2024. Currently, the project duration is limited until the end of 2025.

The main task of the ACH is to give support for the entire E-TASC initiative with their Theory, Simulation, Verification and Validation (TSVV) Tasks and the EUROfusion Theory and Simulation programme. In addition to classical High Performance Computing (HPC) support, which was provided by the HLST, the ACH will give support in the following fields:

- Support for code development of EUROfusion users;
- Long-term collaborations on code development with the TSVV Tasks;
- Comprehensive state-of-the-art algorithmic support;
- Performance-engineering support;
- Development and maintenance of EUROfusion standard software.

From the middle of 2021 to 2022, the ACH had been involved in sixteen different projects submitted by scientists from all over Europe. As an example, we present an overview of the work being done for one of these projects.

4.13.5 GENEX Project

Our objective in this project was to optimise GENEX's usage of the multicore architecture. We carefully benchmarked the performance of specific hotspots of the application using the Raven and Cobra clusters of the Max Planck Computing and Data Facility (MPCDF), which are representative of powerful modern clusters. We performed small, localized tests involving single Raven and Cobra nodes as well as medium-sized tests using 32 Raven nodes (2304 cores) and observed a consistent performance gain of about 30 % of the optimised code compared to the original.

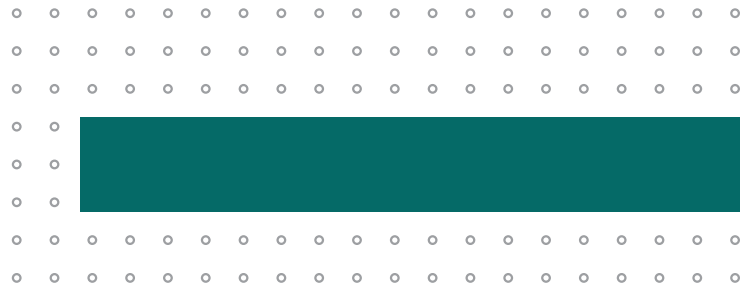
We compared the performance of several different implementations of the loops involving all five dimensions concluding that implicit loop collapsing is the strategy delivering the best performance, between 13 % (for small problems) and 40 % (for larger problems) better than the non-optimised implementation. Whenever implicit index collapsing is not possible, manual index collapsing delivered best performance and showed to be more robust (i.e. automatically collapsing using OpenMP's intrinsic pragmas may result in an error for specific compiler flags). For the non-rectangular six-dimensional loops within

the collision operators, we proposed the precomputing of terms depending on the species into arrays, resulting in a simplified rectangular four-dimensional loop (which was then collapsed using OpenMP intrinsics) with a nested two-dimensional loop.

Furthermore, we also investigated the effect of using PARALLAX's implementation of Morton's Z-order curve on some operators, more notably the operator to compute the time-dependent terms of the right hand side of the Vlasov equation. These preliminary tests revealed a performance gain of up to 45 % just for the reordering itself. This performance benefit can be further improved by the previously discussed OpenMP optimisations, leading to a total of 58 % performance gain.

Scientific Staff

M. Borchardt, I. Holod, K. S. Kang, R. Lago, M. Mazzeo, S. Mochalskyy, N. Moschüring, P. Nair, T. Ribeiro, P. S. Verma



Max Planck Princeton Cooperation

Max Planck Princeton Research Center for Plasma Physics

Heads: Prof. Dr. Sibylle Günter, Prof. Dr. Per Helander

The Max Planck Princeton Research Centre for Plasma Physics has since 2012 provided a platform for scientific collaboration between three Max Planck Institutes (for Plasma Physics, Astrophysics and Solar System Research, respectively) and Princeton University (Dept. of Astrophysical Sciences and Princeton Plasma Physics Laboratory). It has resulted in many common projects and publications over the years. The most recent ones are described here.

Anisotropic Heat Conduction in Chaotic Magnetic Fields

In collaboration with PPPL, the problem of anisotropic heat conduction in a plasma embedded in a magnetic field with irregular, possibly chaotic, field lines has been analysed. The heat conductivity is usually much larger along the field lines than across them, and this enhances the transport across a domain where good flux surfaces do not exist.

For this reason, the confining quality of a magnetic field is very sensitive to the question of whether the field lines trace out magnetic surfaces. If they do not, e.g. if the magnetic field lines are chaotic, the dominant heat conduction along the field can significantly enhance the energy losses from the plasma. There is a large body of literature discussing the extent of this enhancement and the underlying physical mechanisms in chaotic magnetic fields. In these works, scalings for the effective cross-field diffusion coefficient are derived in terms of local diffusion coefficients and the statistical properties of the magnetic field lines, such as Kolmogorov or correlation lengths. Such information is meaningful insofar as these properties are approximately constant over the region under consideration. But chaotic magnetic fields often contain an astonishing amount of structure, such as remnant flux surfaces, magnetic islands and partial transport barriers, which impart a similar structure, or variability, on the transport. Figure 1 illustrates this point, showing a Poincaré plot of field lines in an incompletely chaotic magnetic field, upon which isotherms from a heat conduction equation with very anisotropic conductivity are superimposed in the left half of the figure. The distance between the isotherms is highly variable, and it is clear that the net transport cannot be described by anything like a constant “effective” heat conductivity.

In a novel approach to the problem, rigorous upper and lower bounds have been derived on the overall enhancement of the transport and on the temperature variation along the magnetic field. These bounds are derived on the basis of a variational formulation of the anisotropic heat conduction equation, by constructing increasingly sophisticated trial functions that are based on invariant and almost-invariant structures under the magnetic field-line flow. In this way, remarkably accurate approximations for the temperature can be rapidly constructed without solving the diffusion equation, even in the small perpendicular-diffusion limit when the solution for the temperature is dominated by the fractal structure the magnetic field lines [1, 2].

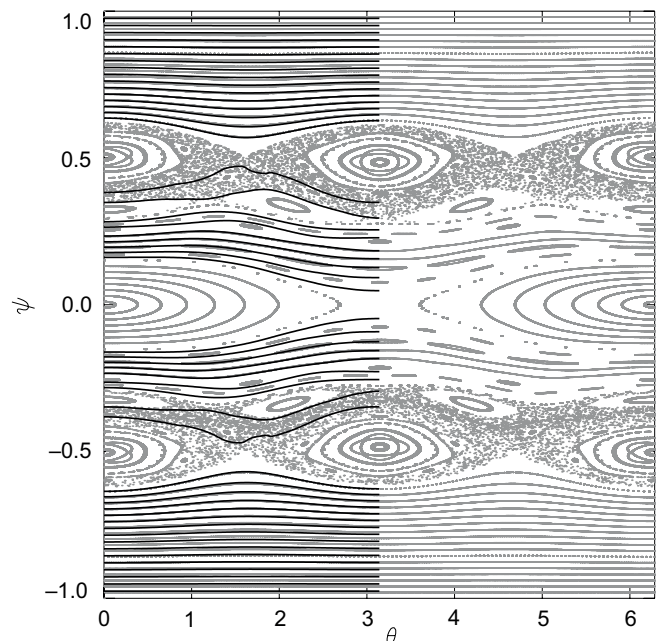


Figure 1. A Poincaré puncture plot of a partially chaotic magnetic field and, in the left panel, isotherms of a solution of the anisotropic heat conduction equation.

Kinetic Ballooning Modes in W7-X High-performance Plasmas

Wendelstein 7-X aims to demonstrate operation at high β (ratio of kinetic to magnetic pressure), which necessitates high plasma densities up to $2 \cdot 10^{20} \text{ m}^{-3}$ since energy confinement improves with density. In recent W7-X experiments, injection of hydrogen pellets was successfully applied for core fuelling [3].

During high- β phases of these discharges, MHD-like events were observed, which may indicate a stability limit. In addition, linear gyrokinetic simulations suggest that the density and temperature gradients were large enough to destabilise kinetic ballooning modes (KBMs). Although these plasmas are stable to ideal-MHD instabilities, including ballooning modes, gyrokinetic effects on the latter render them unstable [4]. Figure 2 shows a typical fluctuation structure in the plasma obtained from a tomographic analysis of soft X-ray emission.

The possibility of KBMs limiting plasma performance motivates a study of different W7-X configurations [2, 4, 5] with regard to, first, electromagnetic effects on the microinstability landscape and, second, the connection between stability properties in global MHD and local gyrokinetics. In particular, the effects of the vacuum rotational transform, ι , and the mirror ratio have been considered. KBMs appear to be more unstable in configurations with lower mirror ratio and lower ι [5], which are also generally more unstable with respect to ideal-MHD ballooning modes. The identification of these trends is useful for planning W7-X experiments.

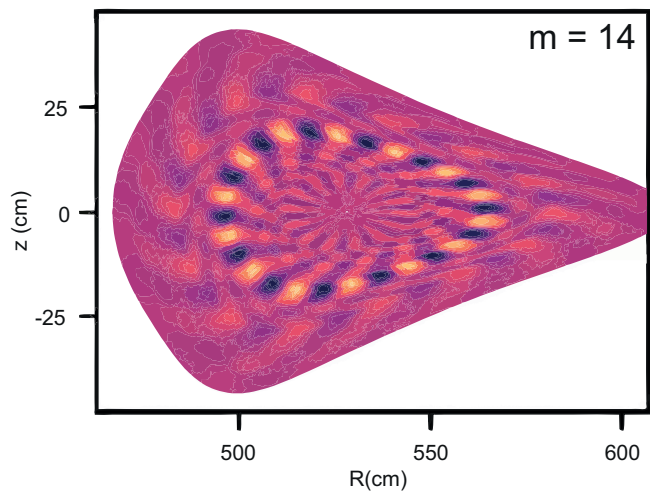


Figure 2. Tomographic reconstruction of soft X-ray emission from a high-performance W7-X discharge.

Model for Current Drive Induced Crash Cycles in W7-X

In W7-X discharges with strong ECCD, phenomena resembling tokamak “sawtooth” instabilities are observed, with periodic collapses of electron temperature occurring in the core of the plasma. The onset of these instabilities can probably be explained by long-wavelength modes in the vicinity of resonant magnetic surfaces. Since the deposition profile of ECCD is usually radially localized, it results in a strong distortion of the rotational transform, which may then cross a low-order rational value.

A mathematical model that combines resistive current diffusion with a recipe for fast magnetic relaxation conserving the corresponding helical flux [6] was proposed [7] to describe plasma evolution during sawtooth cycles in W7-X. As observed in the experiments [8], the mixing area associated with the sawtooth crashes grows gradually as the discharge proceeds, and the toroidal current saturates earlier than expected from resistive diffusion of the ECCD current alone. The model further predicts toroidal current evolution qualitatively similar to the observations, and also provides a prescription for the mixing area. Moreover, the toroidal current is forced to saturate at a lower value (figure 3) due to the continual dissipation of magnetic energy associated with the crashes. In addition, the model explains why there are different types of crashes (“small” and “medium-sized” ones) and why these occur at different frequencies (see figure 3). The small ones affect only the centre of the plasma and occur in several cycles between medium-sized ones. Finally, there is a relatively long time gap between the first medium-sized crash and the first small one, and these two types of crashes affect the total plasma current differently. All these results of the model are in line with experimental observations.

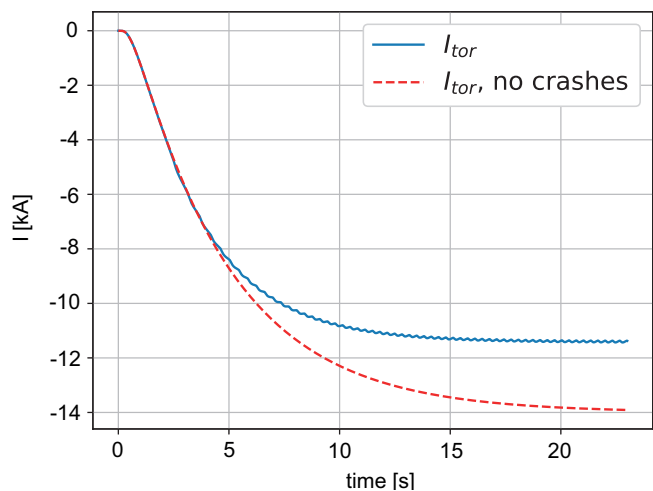


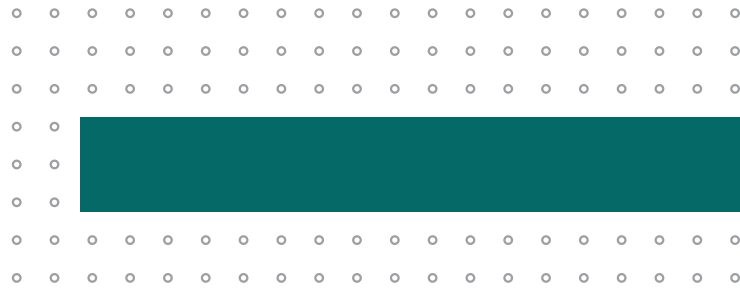
Figure 3. Resistive current evolution in a W7-X sawtooth discharge modelled with (blue) and without (red, dashed) sawtooth crashes.

Non-linear MHD Instabilities

Saturated external modes for several experimentally motivated tokamak cases were compared between the VMEC equilibrium code and JOREK showing generally good agreement, but also clear differences where the ideal MHD assumptions of VMEC become invalid [9]. This was done in preparation of the ongoing effort of applying the same techniques to saturated instabilities in stellarator geometry. Studies of violent external modes in quasi-axisymmetric stellarator geometry and a comparison to the equivalent tokamak configuration were published [10]. An extension of JOREK code to stellarators was implemented and benchmarked successfully to CASTOR3D for simplified W7A like geometry [11, 12]. Growth rates of $n = 10$ ballooning modes agree within a few percent between both codes. In a joint effort between researchers at IPP in Garching and Greifswald as well as collaborators at PPPL, the models are now being tested for complex stellarator geometries, which requires further numerical optimisation in terms of performance, boundary treatment, and numerical stability. Ongoing nonlinear MHD simulations will also help to clarify the nature of the sawtooth crashes observed in W7-X experiments. Future plans also include the study of instabilities encompassing the entire W7-X plasma. Understanding their mechanism would be helpful for ensuring safe operation of the device.

Scientific Staff

K. Aleynikova, S. Günter, P. Helander, F. Hindenlang, M. Hölzl, N. Nikulin, R. Ramasamy



Plasmas beyond Fusion

Plasma for Gas Conversion

Head: Prof. Dr.-Ing. Ursel Fantz

The usage of low temperature plasmas (non-equilibrium or thermal) for conversion of abundant molecules into value-added chemicals is a promising emerging alternative technology to the classical conversion by electrochemical or thermochemical processes. Since the establishment of the group at IPP in 2017, the focus has been on CO₂ conversion into CO using microwave plasmas (syngas route). Currently, it is expanded towards hydrogen (production and storage) technology, using other gases in combination with catalysts for which dielectric barrier discharges are envisaged.

The challenges associated with the energy transition are opening up opportunities for novel energy conversion technologies that harness the surplus power from renewable energy sources. Among the emerging and promising technologies for the conversion of abundant molecules like CO₂, CH₄, H₂O and N₂ into value-added chemicals for syngas production or hydrogen production and storage, or nitrogen fixation, the plasma conversion technology is ideally suited for its fast response time to intermittent energy sources [1]. The activities of the P4G group started in 2017 and are embedded in the PoF IV program (2021–2027) of the HGF within the research field Energy. The consortium contributing to the chemical energy carriers via the plasma route is led by IPP and consists of collaborations among IGVP at University of Stuttgart, IHM and IMVT at KIT, IEK-1 and IEK-4 from FZJ, and IPP including activities at EPP, University of Augsburg. The milestone incorporated into the research program targets the integration of microwave-induced CO₂ plasma splitting with oxygen separation to deliver a gas suitable for fuel synthesis, as well as a benchmark with electrochemical CO₂ reduction in terms of energy efficiency and cost. The milestone is envisaged to be achieved in December 2022, which means the work done so far has been focused on CO₂ conversion into CO, on the separation of oxygen by membranes, for which suitable materials needed to be identified, and on the definition of suitable parameters for a meaningful comparison between the plasma and electrochemical technologies.

Among the plasma discharges investigated so far for CO₂ conversion, microwave discharges showed the best performances in terms of energy efficiency and conversion [2]. Therefore, two microwave experiments (2.45 GHz, max. power 3 kW) were chosen. The plasma torch covering the pressure range from 30 mbar to atmospheric pressure has the goal to achieve best performance at atmospheric pressure for industrial applicability. The surfguide experiment is operated at lower pressures (1 to 60 mbar) and enables fundamental studies of plasma processes. As shown in the last Annual Report, the transition from a non-equilibrium plasma, where electron collisions determine the plasma chemistry, to a thermal plasma can give important insights in the underlying conversion mechanisms.

The main limitation for high CO₂ (CO₂ → CO + O) conversion in the plasma torch is the slow cooling of the plasma gas in the effluent allowing the CO recombination with O back to CO₂. To enhance the

cooling of the plasma gas (quenching), two methods were investigated: use of a nozzle in the effluent (which enhances the mixing of the hot plasma gas and the surrounding colder gas), and use of a reverse vortex configuration with cooled narrow channels in the effluent. For both methods, a strong increase of the conversion and energy efficiency was observed at atmospheric pressure as shown in figure 1. At atmospheric pressure and with a gas flow of 10 slm, the conversion increases by a factor of 2.5 to 35 % at an energy efficiency of 26 %, whereas an energy efficiency of 42 % could be achieved at 10 % conversion [3]. Changing the gas flow from vortex to a reversed vortex configuration enlarges the stable operation regime of the plasma torch at atmospheric pressure, meaning that higher microwave powers can be coupled into the plasma. With these modifications, the operation of the plasma torch at atmospheric pressure yields performances comparable to those during low pressure operation, which is an important step towards industrial applicability. In an ongoing collaboration with the University of Antwerp, a fluid model is being developed to gain insights in the gas mixing processes.

For the milestone, the IPP setup with the nozzle will be combined with oxygen separation membranes. IGVP together with IEK-1 identified the most suitable ceramic materials to manufacture hollow fibers withstanding the temperatures in the effluent of the plasma (800 to 1200 °C) such that oxygen separation in a plasma environment could be demonstrated [4]. The common experimental campaign at IPP to determine the parameters relevant for the comparison with electrolysis is planned for October 2022; discussions with electrolysis experts within HGF to define the figures of merit are ongoing.

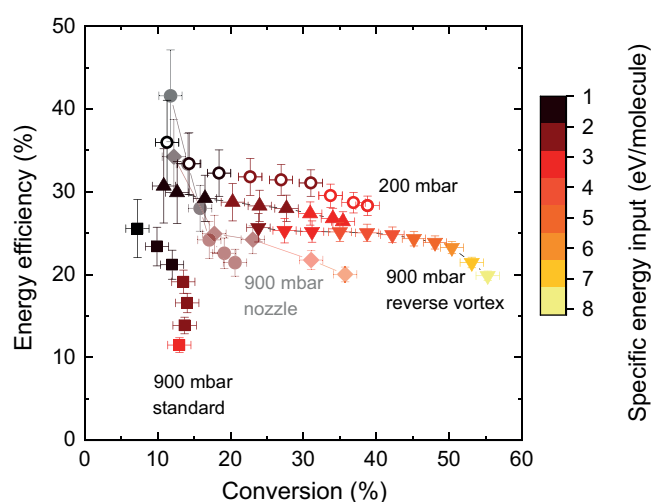


Figure 1. The energy efficiency and conversion at atmospheric conditions (900 mbar, full symbols) and at pressure of 200 mbar (hollow symbol), where the highest conversion and energy efficiency in standard configuration have been achieved so far. Specific energy input is calculated as ratio of the microwave power deposited in the plasma over the input CO₂ gas flow.

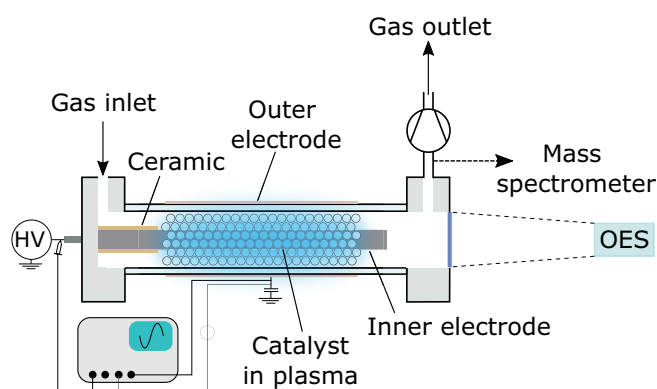


Figure 2. Schematic of a cylindrical DBD reactor powered by a high-voltage (HV) power supply and characterized by electrical and optical means (e.g. Optical Emission Spectroscopy, OES).

For the surfaguide plasma source, used to investigate fundamental aspects of (electron-impact driven) CO_2 conversion at low pressures, conversion values up to 90 % (however at energy efficiencies below 10 %) are measured. Moreover, the plasma is characterized via optical emission spectroscopy as well as absorption measurements utilizing laser-induced fluorescence. Two-photon absorption laser-induced fluorescence (TALIF) measurements of atomic oxygen number densities and translational temperatures are carried out simultaneously along a 15 cm long section in the effluent of the plasma source's resonator. The first results demonstrate almost constant temperatures but complex atomic oxygen density profiles. Complementary work is performed at the University of Augsburg where the surfaguide is used to investigate nitrogen and hydrogen plasmas with the aim of determining the rotational and vibrational temperatures over a broad pressure range (0.03–20 mbar), thus contributing to the fundamental understanding towards (catalytic) NH_3 synthesis from $\text{N}_2 + \text{H}_2$ plasmas.

As the plasma performances are mainly driven by volume reactions and cooling effects, additional decomposition pathways might appear if catalytic surfaces are placed either in contact with the plasma (in-plasma catalysis) or in the effluent (post-plasma catalysis). Due to the large temperatures (2000–6000 K) in the plasma volume, only post-plasma catalysis is possible with the microwave plasmas (at atmospheric conditions). At these conditions, heat from the plasma combined with catalyst properties (e.g., bandgap, oxygen vacancies) might promote additional CO_2 dissociation. Promising commercially available catalysts such as Al_2O_3 , ZrO_2 , TiO_2 , as well as 10 wt % Ni-TiO_2 prepared within the ongoing collaboration with the National Institute of Chemistry (Ljubljana, Slovenia) were positioned in the effluent of the plasma. First experiments in standard and nozzle configurations led to no improvements in CO_2 conversion. The results suggest that electrons and photons from the plasma could be necessary for sufficient activation of the catalysts.

Owing to the significantly lower gas temperatures (≤ 200 °C) in a plasma generated with a Dielectric Barrier Discharge (DBD) at atmospheric pressures, catalytic surfaces can be directly placed in the plasma region. Thus, electrons, photons, radicals, excited species can be in direct contact with the material's surface that is beneficial for NH_3 synthesis from $\text{N}_2\text{-H}_2$ mixtures. The first plasma in a cylindrical DBD (figure 2 shows the concept) is planned for the second half of 2022 in a new P4G laboratory dedicated to plasma catalysis. This is accompanied by developments at the University of Augsburg for in-situ diagnostics using the same setup. At IPP, the chemistry of the plasma-exposed surface will also be studied using high-resolution X-Ray Photoelectron Spectroscopy (XPS). To this end, a dedicated reactor chamber featuring a planar DBD is currently under development. This chamber will be attached to the XPS at E2M for in-vacuo studies of plasma-exposed samples.

Further extensions of the activities target towards green hydrogen technologies, such as using methane (CH_4) or biogas for H_2 production, either through dry reforming of methane ($\text{CH}_4 + \text{CO}_2 \rightarrow 2\text{H}_2 + 2\text{CO}$) or methane pyrolysis ($\text{CH}_4 \rightarrow 2\text{H}_2 + \text{C(s)}$) preferably in the plasma torch where the challenge is to cope with soot (C(s)) formation. To that point the use of the reverse vortex configuration, or differential gas inlets for different gases might mitigate the accumulation of soot particles.

Scientific Staff

U. Fantz, A. Hecimovic, R. Antunes, S. Buchberger, C. Kiefer, A. Meindl, W. Zhang (Guest), A. Brydon (Bachelor Thesis), M. Mühlmeier (Bachelor Thesis), D. Rauner (Univ. Augsburg), V. Wolf (Univ. Augsburg)

Astrophysical Plasmas

Head: Prof. Dr. Frank Jenko

In 2021, several new positions were created at IPP to enable the establishment of a permanent concerted effort in plasma astrophysics, building on a long tradition at IPP to investigate basic plasma physics. Important activities along these lines are also pursued in the context of the Excellence Cluster ORIGINS and in a Young Investigator Group associated with the TOK division.

Helmholtz Young Investigator Group on Weakly Magnetized Plasmas

(Dr. Daniel Told et al.)

Many plasmas in nature (such as the solar wind) and in the laboratory (like the edge of fusion plasmas) are weakly magnetized. Ordering assumptions made in gyrokinetic theory – like low frequency or moderate gradients – may be then challenged, particularly for the heavier ions. To overcome these limitations, the group derived equations for a hybrid model that includes fully kinetic physics for the ions, but gyrokinetic physics for the electrons. Thereby, only the slower ion gyration needs to be followed, while still benefitting from a faster treatment of the electrons. To obtain consistent model equations, both the equations of motion as well as the field equations were derived following a variational approach. The numerical implementation of the hybrid model equations proceeded in two steps: First, a dispersion solver FIDEL was developed to allow the comparison of wave solutions against other models. Second, the hybrid model was implemented into the existing simulation code ssV, developed in the department of Theoretical Physics I at Ruhr-Universität Bochum. The ssV code is based on advanced Semi-Lagrangian-type methods (e.g. the PFC scheme [1]). For the implementation of the hybrid model, ssV was extended with a standard-Semi-Lagrangian drift-kinetic electron solver, as well as solvers for the field equations. This implementation was successfully used to simulate 2D-3V electrostatic turbulence (as in [2]), demonstrating the ability of the code to capture the higher order $E \times B$ physics while retaining fully kinetic effects. In addition, electrostatic wave modes were successfully matched to solutions obtained from the FIDEL dispersion solver, which in turn compare well against fully kinetic solutions. The study of instabilities and turbulence relevant to tokamak edge turbulence, has driven significant further enhancements to ssV: In particular when evolving the full particle distribution (“full-f”), it is challenging to preserve accurate long-term physics while resolving the gyration timescale. Both existing and novel higher-order schemes had to be implemented and tested as a remedy: For example, at least a 5th order scheme is needed in velocity space to gain sufficient accuracy for ion-temperature-gradient driven instability (ITG) simulations. Figure 1 shows the time evolution of a 3D-3V full-f drift-kinetic ITG turbulence test. Ongoing work on ssV and FIDEL involves the addition of electromagnetic capabilities, which will enable application to space and astrophysical plasmas.

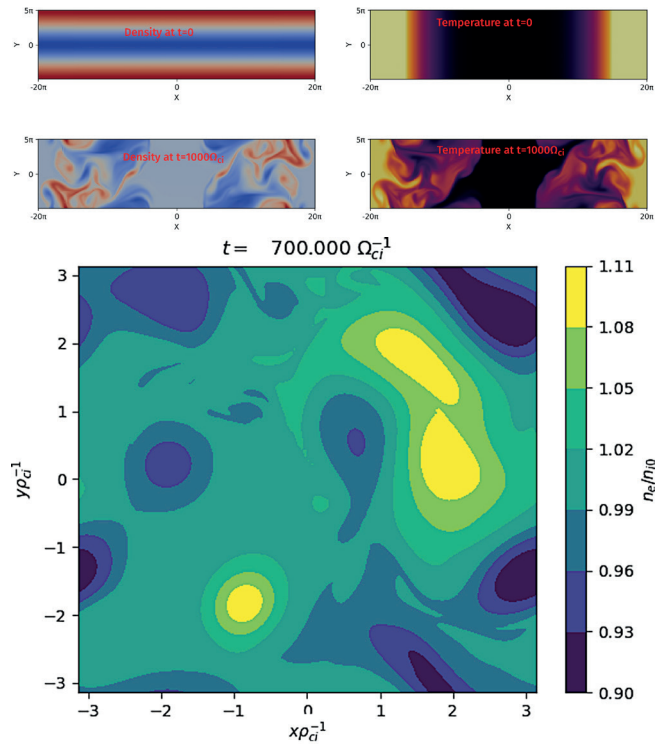


Figure 1. Snapshot of a 3D-3V “full-f” drift-kinetic ITG simulation.

Shock Waves in Gamma-ray Bursts

In the jets of gamma-ray bursts, the temperature is so high that α particles are created, resulting in a plasma consisting of electrons, protons, and α particles. Perpendicular shocks form in these jets, and they have been analyzed via the fully kinetic PIC code OSIRIS. Characteristic multiple-ion shock features are obtained, such as alternating-peak structures: A proton shock front is followed by an α particle shock front, which is followed by a proton and then by an α particle peak (see figure 2). The electron acceleration efficiency ϵ_e shows a lot of variability. While out-of-plane magnetic fields show values in the range of $\epsilon_e \approx 0.04 - 0.05$, in-plane simulations exhibit values of $\epsilon_e \approx 0.12 - 0.13$. The electron acceleration efficiency changes only mildly with the ionic fraction of α particles. When analyzing the proton and α particle acceleration efficiency, it can be found that α particles lose energy on average when entering the downstream regardless of the amount of α particles simulated with. The proton acceleration efficiency ϵ_p is, however, strongly dependent on the amount of α particles. When the ionic fraction of α particles is low, protons will lose energy on average when they enter the downstream, while when the ionic fraction of α particles is high, they will gain energy. This can be explained by the fact that α particles also transfer energy to the lighter protons. Protons, hence, are heated due to the heavier α particles and the heating is greater the more α particles there are.

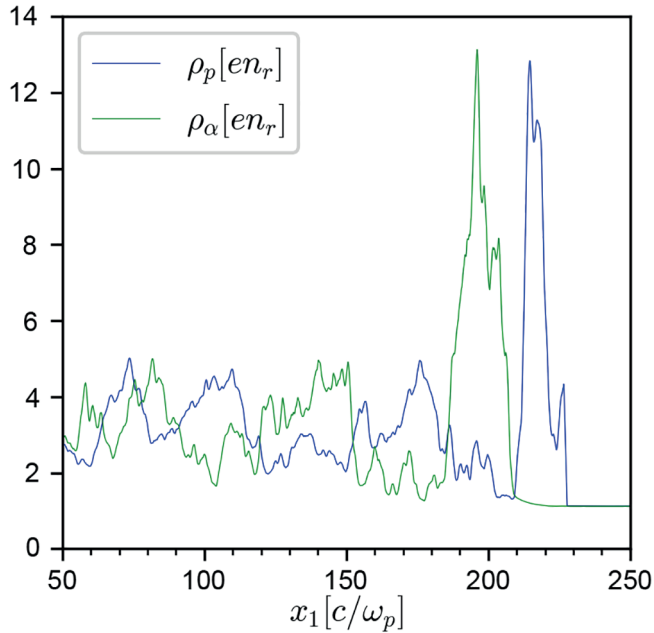


Figure 2. Characteristic bi-ion shock structures showing alternating peaks of proton and alpha particle charge densities.

Current Filamentation Instabilities in Proton-driven Wakefield Accelerators

A beam propagating in a plasma is subject to the Weibel-like current filamentation instability (CFI), splitting the beam and plasma into filaments and generating a perpendicular magnetic field. The instability is highly relevant for astrophysical phenomena such as gamma-ray bursts, where it is likely a mechanism for the generation of collisionless shocks and particle acceleration. Further, it is a potential limiting factor in proton-driven wakefield acceleration as it greatly disturbs the accelerating electric field gradient generated by the beam. For this work, we collaborate with the Advanced Proton Driven Plasma Wakefield Acceleration Experiment (AWAKE) at CERN. CFI has not been observed in the current AWAKE runs, and the goal of this work is to investigate for which achievable parameters in the future of the experiment CFI may be investigable. The work mainly consists of numerical simulations using fully electromagnetic and quasistatic PIC codes. Due to the large size of the beam and its high relativistic factor requiring a long propagation distance, electromagnetic PIC simulations are complicated. Quasistatic codes are good candidates for simulating relativistic beams in cold plasma as they greatly reduce computational resources. To compare the filamentation instability between electromagnetic and quasistatic codes, a fireball beam consisting of positrons and electrons is used. As it is short, quasi-neutral and dense, CFI is dominant and computational resources are greatly reduced. Figure 3 shows the filamentation of the fireball beam and the corresponding perpendicular magnetic field using a quasistatic code.

This work has the potential to pave the way to higher acceleration gradients in such acceleration schemes, as well as to provide insight into analogous astrophysical scenarios.

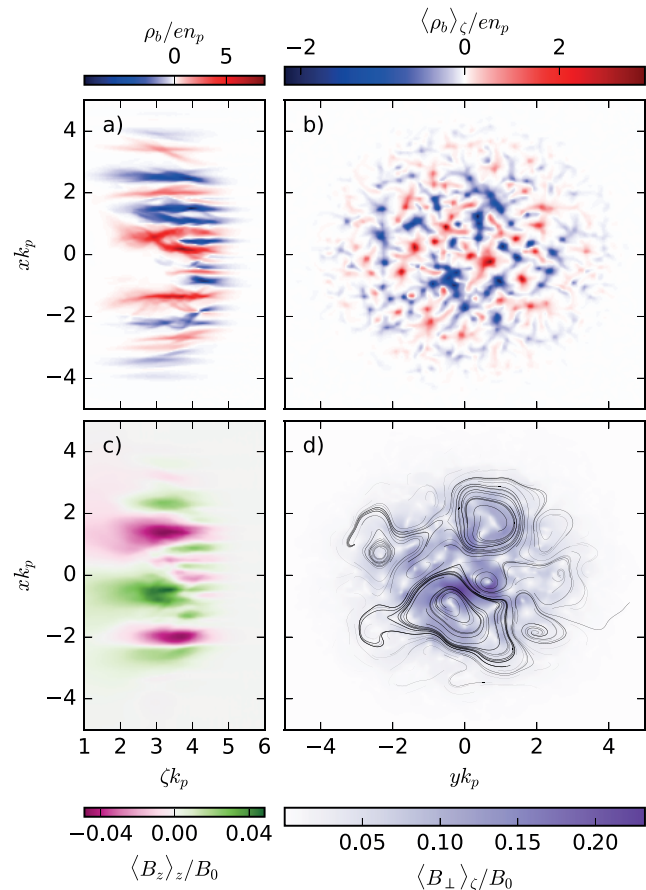


Figure 3. Fireball beam density and magnetic field after the linear stage of the instability. a) Axial slice and b) transverse projection of the net charge density. c) Axial and d) transverse projection of the perpendicular magnetic field.

Scientific Staff

J. Graw, F. Jenko, A. Mustonen, K. Pommois, D. Told, E. Walter, M. Weidl

Electron-Positron Plasmas

Heads: Dr. Eve V. Stenson, Prof. Dr. Thomas Sunn Pedersen

Laboratory studies of matter-antimatter “pair” plasmas are a compelling frontier in fundamental plasma physics research. Among the APEX Collaboration’s latest progress toward this goal are notable milestones such as positron injection into significant electron space charge, as well as the commissioning of the high-temperature superconducting coils for the levitated dipole trap.

Overview

The APEX (A Positron Electron eXperiment) Collaboration is based at the Max Planck Institute for Plasma Physics but includes essential partnerships with colleagues at universities in Germany, the U.S., and Japan. Its primary goals are the generation and investigation of confined, strongly magnetized, electron-positron plasmas in the laboratory. The mass symmetry of such plasmas simplifies many aspects of their physics, according to more than four decades of theory/simulation predictions.

The collaboration’s “road map” to experimental pair plasma studies [1] involves unifying and advancing state-of-the-art physics and engineering in several areas, including: extended accumulation and high-capacity storage of large numbers of positrons, originating from a world-class positron source; two superconducting, tabletop-sized, toroidal confinement devices with complementary magnetic topologies (a dipole and a stellarator), in which the positrons will be combined with electrons and their plasma properties studied; and the development and verification of a number of essential enabling techniques – e.g., efficient transport of positrons across magnetic flux surfaces and subsequent trapping.

Non-neutral Plasma Accumulation & Storage

The NEutron-induced POSitron source MUniCh (NEPOMUC) in Garching, one of the most intense antimatter sources in the world, is capable of producing $>10^9$ positrons per second. In order to capture and collect these positrons in large numbers, we will be installing at NEPOMUC a series of linear, non-neutral plasma traps. A “buffer-gas trap” (BGT) is the standard method to accumulate positron beams into cold, dense, tailorable positron plasmas, but this has not been done yet with a reactor-based beam (which offers a uniquely high rate of positrons, as well as adjustable spatial and velocity distributions [2]). In preparation for pioneering this combination, our BGT (figure 1a) has undergone extensive overhauls and upgrades; it is currently being tested and optimized with electrons, in preparation for installation on NEPOMUC after the next reactor cycle (planned for early 2024).

To reach the $10^{10} - 10^{11}$ cold (~ 1 eV) positrons needed to ensure plasma densities in the toroidal traps, multiple positron plasma pulses from the BGT will need be transferred, combined, and stored for hundreds of seconds in another, higher-capacity trapping stage. This involves a nested array of several non-neutral traps in ultra-high vacuum in a high-field (currently 3.1-T) magnet. A “master cell” is designed to transport

plasmas into and out of the storage cells by means of controlled auto-resonant excitation or damping, respectively, of the $m=1$ diocotron mode. Essential trap alignment and plasma manipulation techniques [3], enabling extended confinement in the master cell and near-unity transfer efficiency into multiple off-axis cells, have been successfully developed with electrons (figure 1b&c).

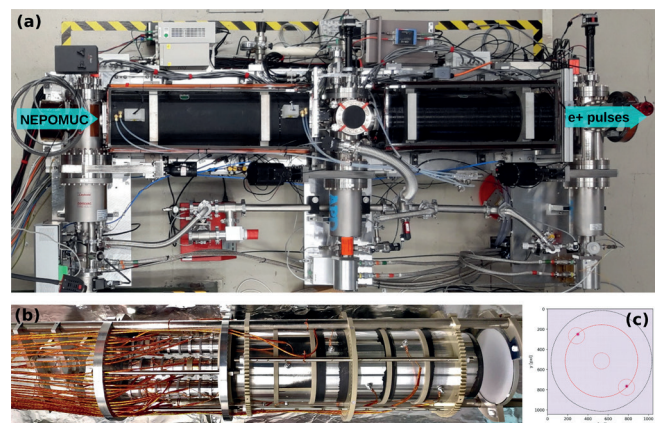


Figure 1. Linear traps for positrons. (a) “bird’s eye view” of the ~ 2.5 -meter-long, upgraded and overhauled BGT system (b) the ~ 0.5 -m-long electrode structure for the multi-cell trap, showing the master cell and three storage cells (c) a phosphor screen image showing two electron plasmas that were confined simultaneously in the off-axis storage cells.

Electrons and Positrons Combined in a Prototype Dipole Trap

To demonstrate the proofs-of-principle needed for design decisions regarding the pair plasma traps, we have been using a prototype dipole trap based on a supported permanent magnet [4], combined with full-orbit trajectory simulations to guide and interpret the experimental data. We had previously determined that the electrostatic potential landscape in a select region of the trap can be strategically tailored to transport positrons (via $E \times B$ drifts) from open field lines (connecting to the NEPOMUC beam line) onto closed field lines (connected only to the magnet), where they are then transiently confined (for ~ 1 toroidal transit). This drift injection process can be highly efficient [5], and when the injection potentials are switched off, positrons that were transiting the confinement region become captured, persisting in the trap for hundreds of thousand of toroidal transits, limited only by diffusion due to elastic scattering off residual gas [6, 7]. Most recently, we established that this single-particle manipulation technique could also be used when there was already a significant population of electrons in the trap [8]. This was the first time plasma densities were measured in the prototype trap (for the electrons; reaching positron plasma trap densities will require the installation of the linear traps), as well as the first time we reported a combined system of electrons and positrons.

Development of Toroidal Traps

In order to confine positrons and electrons simultaneously, with both species at plasma densities, toroidal magnetic flux surfaces with excellent confinement properties are required. Furthermore, the flux surfaces need to be generated without plasma current, as the densities of our pair plasmas will be very low (limited by the rate of available positrons and reasonable accumulation times). There are two configurations that emerge as obvious top candidates for this purpose, a levitated dipole trap and an optimized stellarator, and both have received third-party funding. Once both traps are in operation, this will allow us to compare and contrast the behavior of strongly magnetized pair plasmas in two very different magnetic topologies, taking advantage of the shared positron accumulation systems, diagnostic techniques and tools. In turn, the pair plasmas (which, due to being half anti-matter, can be very sensitively diagnosed with gamma detectors) will provide new insights into equilibria and transport in these two very different geometries.

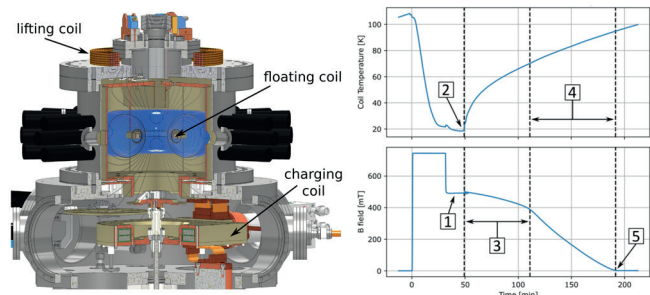


Figure 2. The left panel shows the final CAD design of the levitated dipole trap, including the coldhead-cooled HTS “floating” (F) and “charging” (C) coils (THEVA) and the water-cooled copper “lifting” (L) coil. The right panel plots measurements of temperature (top) and axial magnetic field (bottom) during a cool/charge/quench test of the F coil. After being cooled below T_c and inductively charged, the F coil generates 0.5T on axis (1). After the F coil is thermally disconnected from the cooling system (2), the persistent current gradually decays over an hour as the coil warms (3), then undergoes a gentle, 80-minute quench (4) until the field is back to 0T at a coil temperature of 95K (5).

The assembly of the levitated dipole trap (figure 2, left) is nearing completion, the culmination of several years of physics and engineering development. Key components are the two high-temperature superconducting (HTS) coils, the systems for cooling and energizing those coils, and the levitation system. A novel method has been developed for repeatedly and reproducibly making/breaking the thermal connection between the “floating”/“F” coil (which radiatively warms over the duration of an experiment cycle) and the coldhead used to cool it. Involving a “sub-chamber” within the experiment that is temporarily filled with helium gas, this approach has been successfully deployed with the F coil (figure 2, right). Commissioning of the entire

trap as a whole is ongoing and has been highly successful to date; levitation of the F coil is expected by the end of 2022.

The design of the stellarator (EPOS, for Electrons and Positrons in an Optimized Stellarator) is underway, with a dozen different candidate magnetic configurations currently being evaluated; these have been supplied by collaborators in ST and the Simons “Hidden Symmetries” collaboration. Considerations include compatibility with HTS coil windings, as well as coil sets that include deliberate “stray field” with which to guide positrons from the NEPOMUC beam line, up to an injection region spatially proximate to the flux surfaces; these must be balanced with a desire for low aspect ratio and high quasi-symmetry. Meanwhile, engineering proof-of-concept tests are planned for the coming year.

Outlook

In addition to the work described in more detail above, there has also been significant progress in terms of preparations to properly diagnose and interpret the plasmas we will be creating. Suitable next-generation diagnostics are being developed, as are theory predictions for the properties of both quasi-neutral e^+e^- pair plasmas and intermediary non-neutral (pure e^-) plasmas in our specific magnetic geometries and regime. The collaboration’s next couple years, when the systems which to date were developed independently will be completed and brought together, are expected to be exciting.

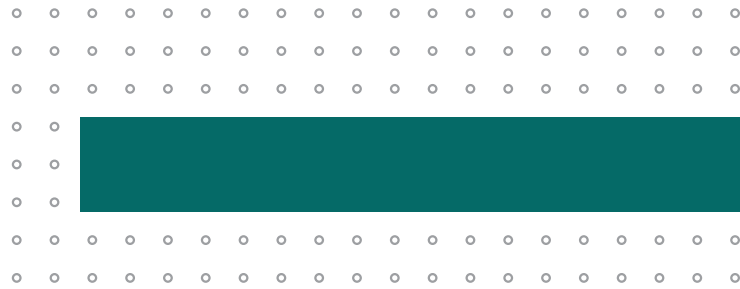
Scientific Staff & Collaborators

A. Card¹, P. Costello¹, J. R. Danielson², A. Deller^{1,2}, M. Drevlak¹, P. Helander^{1,5}, U. Hergenhanh³, J. Horn-Stanja¹, C. P. Hugenschmidt⁴, P. Huslage^{1,4}, D. Kennedy¹, J. von der Linden¹, A. Mishchenko¹, S. Nißl^{1,4}, T. Sunn Pedersen^{1,5}, C. W. Rogge^{1,4}, H. Saitoh⁶, L. Schweikhard⁵, M. Singer^{1,4}, M. Singer^{1,5}, J. Smoniewski¹, P. Steinbrunner^{1,5}, E. V. Stenson¹, M. R. Stoneking⁷, C. M. Surko², D. Wittman²

¹ IPP – ² University of California, San Diego, CA – ³ Fritz Haber Institute of the Max Planck Society, Berlin, DE – ⁴ Technical University of Munich, DE – ⁵ University of Greifswald, DE – ⁶ University of Tokyo, JP – ⁷ Lawrence University, Appleton, WI

Funding Acknowledgements

The APEX collaboration receives/has received support from IPP/MPG; the Helmholtz Association Young Investigator Group program; the European Research Council (ERC) under the European Union’s Horizon 2020 research and innovation programme; the Deutsche Forschungsgemeinschaft (DFG); the Helmholtz Postdoc Programme; the Humboldt Foundation; the UC San Diego Foundation; the United States Department of Energy; the Japan Society for the Promotion of Science (JSPS); and the National Institute for Fusion Science (NIFS).



Publications, Figures and References

Publications

2021–2022

Bibliography

The bibliography – articles, books and inbooks, conference papers, theses, PhD theses, habilitations, laboratory reports, lectures – can be found under the link

<https://www.ipp.mpg.de/publications>

Patents

G. Birkenmeier, K. Kaunert, V. Rohde and M. Sochor: Vakuum-kompatible regenerative Bildleiterheizung. Invention disclosure dated 08.12.2021. The invention was claimed by IPP. Currently drafting a German patent application.

K. Kaunert and B. Kurzan: Laserlichtschanke. Invention disclosure dated 11.08.2020. The invention was claimed by IPP. Submission of a German patent application No. 10 2021 124 548.6 on 22.09.2021.

A. Manhard, U. von Toussaint and M. Stienecker: Lateral hochaufgelöster Wasserstoffdiffusionsnachweis durch optische Indikatormethode. Invention disclosure dated 06.06.2019. The invention was claimed by IPP. Submission of a German patent application No. 10 2020 111 959.3 on 04.05.2020. Submission of a PCT subsequent application No. PCT/EP2021/061391 on 30.04.2021. Currently preparing a nationalisation of the PCT application in Europe and the USA.

T. S. Pedersen and N. Paschkowski: Anordnung elektrischer Leiter und Verfahren zur Herstellung einer Anordnung elektrischer Leiter. Release of the patent on 07.10.2021.

Electronic Report

For a complete electronic version of this report follow the link www.ipp.mpg.de/report_en

Figures

Science

Fig. 1: L. Vano, Carbon content and transport investigations on Wendelstein 7-X with Charge Exchange Recombination Spectroscopy (PhD Thesis)

Fig. 9 (left): G. M. Weir et al., presented at 23rd ISHW Conference (2022)

Fig. 9 (right): G. M. Weir et al., Nucl. Fusion 61, 056001 (2021),
<https://doi.org/10.1088/1741-4326/abea55>

Theoretical Plasma Physics

Fig. 10: P. Xanthopoulos et al., Phys. Rev. Lett. 125, 075001 (2020),
<https://doi.org/10.1103/PhysRevLett.125.075001>

Fig. 11: M. N. A. Beurskens et al., Nucl. Fusion 61(11), 116072 (2021),
<https://doi.org/10.1088/1741-4326/ac1653>

Fig. 12: G. T. Roberg-Clark et al., Phys. Rev. Res. 4, L032028 (2022),
<https://doi.org/10.1103/PhysRevResearch.4.L032028>

Fig. 13: A. Zocco et al., Phys. Rev. E 106, L013202 (2022),
<https://doi.org/10.1103/PhysRevE.106.L013202>

Fig. 14: R. J. J. Mackenbach et al.: Phys. Rev. Lett. 128, 175001 (2022),
<https://doi.org/10.1103/PhysRevLett.128.175001>

Fig. 15: A. Könies et al., Phys. Plasmas 27, 122511 (2020),
<https://doi.org/10.1063/5.0023961>

References

ASDEX Upgrade

- [1] D. Stieglitz et al., Nucl. Fusion, submitted (2022)
- [2] G. Birkenmeier et al., Fusion Eng. Des. 168, 112644 (2021), <https://doi.org/10.1016/j.fusengdes.2021.112644>
- [3] J. Rueda-Rueda et al., Rev. Sci. Instrum. 92, 043554 (2021), <https://doi.org/10.1063/5.0043768>
- [4] P. Radecker, Concept Development and Testing of an Invesssel Articulated Arm for Remote Handling in ASDEX Upgrade – IVAR, Master Thesis, TU München (2022)
- [5] A. Redl et al., Talk, 25th PSI Conf. (2022)
- [6] T.-O. Hohmann et al., Fusion Eng. Des., submitted (2022)
- [7] P. T. Lang et al., Fusion Sci. Technol. 77(1), 42–50 (2021), <https://doi.org/10.1080/15361055.2020.1842713>
- [8] A. Kallenbach et al., Nucl. Fusion 62, 106013 (2022), <https://doi.org/10.1088/1741-4326/ac888a>
- [9] K. C. Behler et al., Fusion Eng. Des. 159, 111873 (2020) <https://doi.org/10.1016/j.fusengdes.2020.111873>
- [10] M. Teschke et al., Fusion Eng. Des. 146, Pt. A, 1181–1185(2019), <https://doi.org/10.1016/j.fusengdes.2019.02.036>
- [11] M. Teschke, Fusion Eng. Des. 171, 112541 (2021), <https://doi.org/10.1016/j.fusengdes.2021.112541>
- [12] A. Magnanimo et al., Fusion Eng. Des. 171, 112574 (2021), <https://doi.org/10.1016/j.fusengdes.2021.112574>
- [13] A. Magnanimo et al., IEEE Trans. Plasma Sci. 50(7), 2178–2184 (2022), <https://doi.org/10.1109/TPS.2022.3179624>
- [14] A. Magnanimo et al., Fusion Eng. Des., submitted (2022)
- [15] M. Teschke, Fusion Eng. Des., submitted (2022)
- [16] T. Happel et al., Nucl. Fusion, accepted (2022)
- [17] M. Siccino et al., Fusion Eng. Des. 176, 113047 (2022), <https://doi.org/10.1016/j.fusengdes.2022.113047>
- [18] A. Polevoi A. et al., Nucl. Fusion 60, 096024 (2020), <https://doi.org/10.1088/1741-4326/aba335>
- [19] A. Bock et al., Proc. 47th EPS Conf. Plasma Phys., P1.1053 (2021)
- [20] J. Stober et al., Plasma Phys. Control. Fusion 62, 024012 (2020), <https://doi.org/10.1088/1361-6587/ab512b>
- [21] M. Reisner et al., Nucl. Fusion 60, 082005 (2020), <https://doi.org/10.1088/1741-4326/ab8b32>
- [22] HPC resources from CINECA Marconi-Fusion (Project FUA35_STATS)
- [23] M. Reisner et al., Proc. 48th EPS Conf. Plasma Phys., O4.103 (2022)
- [24] F. Ryter et al., Nucl. Fusion 52, 114014 (2012), <https://doi.org/10.1088/0029-5515/52/11/114014>
- [25] M. Willensdorfer et al., Phys. Plasmas 29, 032506 (2022), <https://doi.org/10.1063/5.0073841>
- [26] W. Suttrop et al., Nucl. Fusion 58, 096031 (2018), <https://doi.org/10.1088/1741-4326/aace93>
- [27] M. R. Wade et al., Nucl. Fusion 55, 023002 (2015), <https://doi.org/10.1088/0029-5515/55/2/023002>
- [28] W. Suttrop et al., Plasma Phys. Control. Fusion 59, 014049 (2017), <https://doi.org/10.1088/0741-3335/59/1/014049>
- [29] O. Samoylov et al., Nucl. Fusion 62 074002 (2022), <https://doi.org/10.1088/1741-4326/ac6617>
- [30] Q. Yu et al., Nucl. Fusion 55, 113008 (2015), <https://doi.org/10.1088/0029-5515/55/11/113008>
- [31] F. Klossek, Master Thesis, LMU München (2020),
- [32] P. Dular and C. Geuzaine, <http://getdp.info>
- [33] M. Lehnen et al., J. Nucl. Mater. 463, 39-48 (2015), <https://doi.org/10.1016/j.jnucmat.2014.10.075>
- [34] T. Peherstorfer, Master Thesis, TU Wien (2022)
- [35] G. Tardini et al., Nucl. Fusion 61, 036030 (2021), <https://doi.org/10.1088/1741-4326/abd3eb>
- [36] E. Fable et al., Nucl. Fusion 62, 024001 (2022), <https://doi.org/10.1088/1741-4326/ac3e81>
- [37] N. Bonanomi et al., Nucl. Fusion 61, 054001 (2021), <https://doi.org/10.1088/1741-4326/abebeb>
- [38] C. Angioni et al., Nucl. Fusion 62, 066015 (2022), <https://doi.org/10.1088/1741-4326/ac592b>
- [39] N. Bonanomi et al., Phys. Plasmas 28, 052504 (2021), <https://doi.org/10.1063/5.0040247>
- [40] N. Bonanomi et al., Proc. 48th EPS Conf. Plasma Phys., O5.101 (2022)
- [41] P. A. Schneider et al., Nucl. Fusion 61, 036033 (2021), <https://doi.org/10.1088/1741-4326/abd95e>
- [42] P. A. Schneider et al., Plasma Phys. Control. Fusion 63, 064006 (2021), <https://doi.org/10.1088/1361-6587/abf540>
- [43] T. Luda et al., Nucl. Fusion 61, 126048 (2021), <https://doi.org/10.1088/1741-4326/ac3293>
- [44] T. Luda T. et al., Proc. 48th EPS Conf. Plasma Phys., I4.102 (2022)
- [45] G. Tardini et al., Nucl. Fusion 61, 126045 (2021), <https://doi.org/10.1088/1741-4326/ac301e>
- [46] P. Mantica et al., Nucl. Fusion 61, 096014 (2021), <https://doi.org/10.1088/1741-4326/ac146e>
- [47] A. Mariani et al., Nucl. Fusion 61, 116071 (2021), <https://doi.org/10.1088/1741-4326/ac1fa9>
- [48] F. Janky et al., Fusion Eng. Des. 146, Pt. B, 1926–1929 (2019), <https://doi.org/10.1016/j.fusengdes.2019.03.067>
- [49] E. Fable et al., Plasma Phys. Control. Fusion 64, 044002 (2022), <https://doi.org/10.1088/1361-6587/ac466b>
- [50] M. Muraca et al., Proc. 48th EPS Conf. Plasma Phys., O4.102 (2022)
- [51] D. Fajardo et al., Plasma Phys. Control. Fusion 64, 055017 (2022), <https://doi.org/10.1088/1361-6587/ac5b4d>
- [52] R. Bilato R. et al., 24th Topical Conf. on Radio-frequency Power in Plasmas (TCRFPP) (2022), in preparation
- [53] R. Ochoukov et al., Nucl. Fusion 60, 126043 (2020), <https://doi.org/10.1088/1741-4326/abb79f>
- [54] M. Usoltceva et al., Rev. Sci. Instrum. 93, 013502 (2022), <https://doi.org/10.1063/5.0074838>
- [55] W. Tierens et al., Plasma Phys. Control. Fusion 64, 035001 (2022), <https://doi.org/10.1088/1361-6587/ac3cfe>

References

- [56] W. Tierens et al., *J. Plasma Phys.* 87, 905870405 (2021), <https://doi.org/10.1017/S002237782100074X>
- [57] A. Kostic, *Electric Field Measurements in the Vicinity of an ICRF Antenna*, PhD Thesis, LMU München (2021), <https://doi.org/10.5282/edoc.28672>
- [58] T. Nishizawa T. et al., *Nucl. Fusion* 62, 076021 (2022), <https://doi.org/10.1088/1741-4326/ac60e8>
- [59] R. McDermott et al., *Nucl. Fusion* 62, 026006 (2022), <https://doi.org/10.1088/1741-4326/ac3cd9>
- [60] D. J. Cruz-Zabala et al., *Plasma Phys. Control. Fusion* 64, 045021 (2022), <https://doi.org/10.1088/1361-6587/ac5917>
- [61] D. Wendler et al., *Plasma Phys. Control. Fusion* 64, 045004 (2022), <https://doi.org/10.1088/1361-6587/ac49f8>
- [62] T. Nishizawa et al., *Rev. Sci. Instrum.* 92, 103501 (2021), <https://doi.org/10.1063/5.0062436>
- [63] U. Plank et al., *Rev. Sci. Instrum.*, in preparation
- [64] U. Plank et al., *Phys. Plasmas*, submitted (2022)
- [65] P. Cano-Megias et al., *Nucl. Fusion* 62, 076005 (2022), <https://doi.org/10.1088/1741-4326/ac579f>
- [66] L. Gil et al., *Nucl. Fusion* 60, 054003 (2020), <https://doi.org/10.1088/1741-4326/ab7d1b>
- [67] K. Stimmel et al., *J. Plasma Phys.* 88(3), 905880315 (2022), <https://doi.org/10.1017/S0022377822000484>
- [68] G. F. Harrer et al., *Nucl. Fusion* 58, 112001 (2018), <https://doi.org/10.1088/1741-4326/aad757>
- [69] G. F. Harrer et al., *Phys. Rev. Lett.* 129, 165001 (2022), <https://doi.org/10.1103/PhysRevLett.129.165001>
- [70] L. Radovanovic et al., *Nucl. Fusion* 62, 086004 (2022), <https://doi.org/10.1088/1741-4326/ac6d6a>
- [71] A. Cathey et al., *Plasma Phys. Control. Fusion* 64, 054011 (2022), <https://doi.org/10.1088/1361-6587/ac5b4b>
- [72] C. U. Schuster et al., *Nucl. Fusion* 62, 066035 (2022), <https://doi.org/10.1088/1741-4326/ac6072>
- [73] T. Eich et al., *Nucl. Fusion* 61, 086017 (2021), <https://doi.org/10.1088/1741-4326/ac0412>
- [74] T. Eich et al., *Nucl. Fusion* 60, 056016 (2020), <https://doi.org/10.1088/1741-4326/ab7a66>
- [75] K. Krieger et al., 24th PSI Conf. (2021)
- [76] S. Ratynskaia et al., 25th PSI Conf. (2022) / *Nucl. Mater. Energy*, submitted (2022)
- [77] S. Ratynskaia et al., *Phys. Scr.* 96, 124009 (2021), <https://doi.org/10.1088/1402-4896/ac1cf4>
- [78] K. Krieger et al., *Nucl. Fusion*, submitted (2022)
- [79] K. Krieger et al., 25th PSI Conf. (2022) / *Nucl. Mater. Energy*, submitted (2022)
- [80] M. Cavedon et al., *Nucl. Fusion* 62, 066027 (2022), <https://doi.org/10.1088/1741-4326/ac6071>
- [81] M. Bernert et al., *Nucl. Fusion* 61, 024001 (2021), <https://doi.org/10.1088/1741-4326/abc936>
- [82] M. Bernert et al., 25th PSI Conf. (2022) / *Nucl. Mater. Energy*, submitted (2022)
- [83] E. Viezzer et al., 25th PSI Conf. (2022) / *Nucl. Mater. Energy*, submitted (2022)
- [84] M. Bernert M. et al., *Nucl. Fusion*, in preparation (2022)
- [85] T. Lunt T. et al., *Phys. Rev. Lett.*, submitted (2022)
- [86] U. Stroth et al., *Nucl. Fusion* 62, 076008 (2022), <https://doi.org/10.1088/1741-4326/ac613a>
- [87] Ou Pan et al., *Nucl. Fusion*, submitted (2022)
- [88] M. Maraschek et al., *Plasma Phys. Control. Fusion* 60, 014047 (2018), <https://doi.org/10.1088/1361-6587/aa8d05>
- [89] D. Silvagni et al., *Nucl. Fusion* 60, 126028 (2020), <https://doi.org/10.1088/1741-4326/abb423>
- [90] D. Silvagni et al., *Nucl. Fusion* 62, 036004 (2022), <https://doi.org/10.1088/1741-4326/ac4296>
- [91] T. Eich et al., *Nucl. Mater. Energy* 12, 84–90 (2017), <https://doi.org/10.1016/j.nme.2017.04.014>
- [92] F. Jenko et al., *Phys. Plasmas* 7, 1904 (2000), <https://doi.org/10.1063/1.874014>
- [93] C. Lechte et al., *IEEE Trans. Plasma Sci.* 37(6), 1099–1103 (2009), <https://doi.org/10.1109/TPS.2009.2019651>
- [94] K. Höfler et al., *Plasma Phys. Control. Fusion* 63, 035020 (2021), <https://doi.org/10.1088/1361-6587/abd896>
- [95] K. Höfler, *Turbulence measurements at the ASDEX Upgrade tokamak for a comprehensive validation of the gyrokinetic turbulence code GENE*, PhD Thesis, TU München (2022)
- [96] A. Frank, *Impact of the Plasma Curvature and the Probing Beam Geometry on Doppler Reflectometry Velocity Measurements*, Master Thesis, TU München (2021)
- [97] T. Happel et al., *Plasma Phys. Control. Fusion* 59, 054009 (2017), <https://doi.org/10.1088/1361-6587/aa645b>
- [98] C. Lechte et al., *Plasma Phys. Control. Fusion* 59, 075006 (2017), <https://doi.org/10.1088/1361-6587/aa6fe7>
- [99] S. Freethy et al., *Phys. Plasmas* 25, 055903 (2018), <https://doi.org/10.1063/1.5018930>

International Tokamak Collaborations

- [1] J. Mailloux et al., *Plenary Talk, 48th EPS Conf. Plasma Phys.*, I1.004 (2022)
- [2] C. Challis et al., *Proc. 48th EPS Conf. Plasma Phys.*, 01.101 (2022)
- [3] A. Kappatou et al., 64th Annu. Meet. APS Div. Plasma Phys. (2022)
- [4] J. Hobirk et al., *Proc. 48th EPS Conf. Plasma Phys.*, P2a.113 (2022)
- [5] E. Righi et al., *Nucl. Fusion* 39, 309–319 (1999), <https://doi.org/10.1088/0029-5515/39/3/302>
- [6] G. Birkenmeier et al., *Nucl. Fusion* 62, 086005 (2022), <https://doi.org/10.1088/1741-4326/ac6d6b>
- [7] Y. R. Martin et al. (the ITPA CDBM H-mode Threshold Data Group), *J. Phys. Conf. Ser.* 123, 012033 (2008),

- <https://doi.org/10.1088/1742-6596/123/1/012033>
- [8] G. Birkenmeier et al., Plasma Phys. Control. Fusion, submitted (2022)
- [9] P. A. Schneider et al., Nucl. Fusion 62, 026014 (2022), <https://doi.org/10.1088/1741-4326/ac3e82>
- [10] P. A. Schneider et al., Nucl. Fusion 61, 036033 (2021), <https://doi.org/10.1088/1741-4326/abd95e>
- [11] T. Luda et al., Nucl. Fusion 61, 126048 (2021), <https://doi.org/10.1088/1741-4326/ac3293>
- [12] T. Luda et al., Nucl. Fusion 60, 036023 (2020), <https://doi.org/10.1088/1741-4326/ab6c77>
- [13] C. K. Kiefer et al., Nucl. Fusion 61, 066035 (2021), <https://doi.org/10.1088/1741-4326/abfc9c>
- [14] D. Wunderlich et al., Nucl. Fusion 59, 084001 (2019), <https://doi.org/10.1088/1741-4326/ab246c>
- [15] D. Wunderlich et al., Rev. Sci. Instrum. 90, 113304 (2019), <https://doi.org/10.1063/1.5127832>
- [16] D. Wunderlich et al., Nucl. Fusion 61, 096023 (2021), <https://doi.org/10.1088/1741-4326/ac1758>
- [17] M. Peglau et al., in preparation
- [18] R. Nocentini et al., Rev. Sci. Instrum. 92, 023504 (2021), <https://doi.org/10.1063/5.0022465>
- [19] D. Wunderlich et al., AIP Conf. Proc. 2373, 030003 (2021), <https://doi.org/10.1063/5.0057534>
- [20] N. den Harder et al., Fusion Eng. Des. 173, 112837 (2021), <https://doi.org/10.1016/j.fusengdes.2021.112837>
- [21] N. den Harder et al., J. Phys. Conf. Ser. 2244, 012053 (2022), <https://doi.org/10.1088/1742-6596/2244/1/012053>
- [22] D. Wunderlich et al., J. Appl. Phys. 130, 053303 (2021), <https://doi.org/10.1063/5.0054949>
- [23] M. Lindqvist et al., Nucl. Fusion, submitted (2022)
- [24] F. Merk et al., Talk, 25th Europhys. Conf. At. Mol. Phys. Ionized Gases (ESCAMPIG) (2022)
- [25] A. Heiler et al., AIP Adv. 12, 035339 (2022), <https://doi.org/10.1063/5.0078380>
- [26] S. Jahanbakhsh et al., to be submitted
- [27] F. Penzel et al., Poster, Combined 23rd IEEE Pulsed Power Conf. (PPC) and 29th IEEE Symp. Fusion Eng. (SOFE) (2021) / Fusion Eng. Des.
- [28] F. Penzel et al., 4th Eur. Conf. Plasma Diagn. (ECPD) (2021)
- [29] H. Meister, et al., Poster, 32nd Symp. Fusion Technol. (SOFT) (2022)
- [30] F. Mackel et al., Poster, 4th Eur. Conf. Plasma Diagn. (ECPD) (2021)
- [31] F. Mackel et al., Poster, 32nd Symp. Fusion Technol. (SOFT) (2022)
- [32] A. Castillo et al., Fusion Eng. Des. 181, 113194 (2022), <https://doi.org/10.1016/j.fusengdes.2022.113194>
- [33] G. T. A. Huijsmans et al., Nucl. Fusion 47(7), 659 (2007), <https://doi.org/10.1088/0029-5515/47/7/016>
- [34] M. Hoelzl et al., Nucl. Fusion 61, 065001 (2021), <https://doi.org/10.1088/1741-4326/abf99f>
- [35] V. Bandaru et al., Phys. Rev. E 99, 063317 (2019), <https://doi.org/10.1103/PhysRevE.99.063317>
- [36] L. Hesslow et al., Nucl. Fusion 59, 084004 (2019), <https://doi.org/10.1088/1741-4326/ab26c2>
- [37] O. Vallhagen et al., J. Plasma Phys. 86, 475860401 (2020), <https://doi.org/10.1017/S0022377820000859>
- [38] R. Fischer et al., Nucl. Fusion, ITER Special Issue, to be published
- [39] P. Lang et al., Fusion Sci. Technol., 78, 1–9 (2021), <https://doi.org/10.1080/15361055.2021.1940034>
- [40] M. Dibon et al., Rev. Sci. Instrum. 88, 033508 (2017), <https://doi.org/10.1063/1.4978805>
- [41] Ph. Lauber et al., Proc. 28th IAEA Fusion Energy Conf., TH/P1-20 (2021)
- [42] N. Bonanomi et al., Proc. 48th EPS Conf. Plasma Phys., 05.101 (2022) / Nucl. Fusion, in preparation (2022)
- [43] G. M. Staebler et al., Nucl. Fusion 61, 116007 (2021), <https://doi.org/10.1088/1741-4326/ac243a>
- [44] T. Luda et al., Nucl. Fusion 61, 126048 (2021), <https://doi.org/10.1088/1741-4326/ac3293> / 48th EPS Conf. Plasma Phys., I4.102 (2022)
- [45] P. Vincenzi et al., Proc. 47th EPS Conf. Plasma Phys., P3.1057 (2021)

W7-X Construction and Operations

- [1] IPP Scientific Report 2017–2020

W7-X Sciences

- [1] C. D. Beidler et al., Nature 596, 221 (2021), <https://doi.org/10.1038/s41586-021-03687-w>
- [2] S. Bozhnikov et al., Nucl. Fusion 60, 066011 (2020), <https://doi.org/10.1088/1741-4326/ab7867>
- [3] M. N. A. Beurskens et al., Nucl. Fusion 61, 116072 (2021), <https://doi.org/10.1088/1741-4326/ac1653>
- [4] S. A. Lazerson et al., Nucl. Fusion 61, 096008 (2021), <https://doi.org/10.1088/1741-4326/ac121c>
- [5] M. Zanini et al., Nucl. Fusion 61, 116053 (2021), <https://doi.org/10.1088/1741-4326/ac2870>
- [6] J. Lion et al., Nucl. Fusion 61, 126021 (2021), <https://doi.org/10.1088/1741-4326/ac2dbf>
- [7] E. Pasch et al., Rev. Sci. Instrum. 89, 10C115 (2018), <https://doi.org/10.1063/1.5038422>
- [8] G. Fuchert et al., J. Instrum. 17, C03012 (2022), <https://doi.org/10.1088/1748-0221/17/03/C03012>
- [9] N. Chaudhary et al., Plasma Phys. Control. Fusion 64, 055016 (2022), <https://doi.org/10.1088/1361-6587/ac5df3>
- [10] N. Pablant et al., Rev. Sci. Instrum. 92, 043530 (2021), <https://doi.org/10.1063/5.0043513>
- [11] O. Ford et al., Rev. Sci. Instrum. 91, 023507 (2020), <https://doi.org/10.1063/1.5132936>

- [12] A. J. van Vuuren et al., *IEEE Trans. Plasma Sci.* 50(11), 4114–4119 (2022), <https://doi.org/10.1109/tps.2022.3183890>
- [13] H. P. Laqua et al., 21st Joint Workshop ECRH & ECE (2022) / EPJ Web of Conferences, accepted (2022)
- [14] K. A. Avramidis et al., *Fusion Eng. Des.* 164, 112173 (2021), <https://doi.org/10.1016/j.fusengdes.2020.112173>
- [15] L. Krier et al., 46th Int. Conf. IRMMW-THz, 2 p. (2021), <https://doi.org/10.1109/IRMMW-THz50926.2021.9566847>
- [16] J. W. Oosterbeek et al., *Fusion Eng. Des.* 183, 113256 (2022), <https://doi.org/10.1016/j.fusengdes.2022.113256>
- [17] J. W. Oosterbeek et al., 21st Joint Workshop ECRH & ECE (2022) / EPJ Web of Conferences, accepted (2022)
- [18] D. A. Castaño Bardawil et al., *Fusion Eng. Des.* 166, 112205 (2021), <https://doi.org/10.1016/j.fusengdes.2020.112205>
- [19] J. L. Velasco et al., *Nucl. Fusion* 61, 116059 (2021), <https://doi.org/10.1088/1741-4326/ac2994>
- [20] D. Kulla et al., *Plasma Phys. Control. Fusion* 64, 035006 (2022), <https://doi.org/10.1088/1361-6587/ac43f1>
- [21] M. Cornelissen et al., *Plasma Phys. Control Fusion*, submitted (2022)
- [22] S. Meitner et al., *IEEE Trans. Plasma Sci.* 48 (6), 1585–1590 (2020), <https://doi.org/10.1109/TPS.2019.2949692>
- [23] U. Wenzel et al., *Nucl. Fusion* 62, 096016 (2022), <https://doi.org/10.1088/1741-4326/ac7ac4>
- [24] G. Schlisio et al., *IEEE Trans. Plasma Sci.* 50(11), 4120–4125 (2022), <https://doi.org/10.1109/TPS.2022.3183580>
- [25] C. P. Dhard et al., *Phys. Scr.* 96, 124059 (2021), <https://doi.org/10.1088/1402-4896/ac35c0>
- [26] T. Klinger et al., *Nucl. Fusion* 59, 112004 (2019), <https://doi.org/10.1088/1741-4326/ab03a7>
- [27] M. N. A. Beurskens et al., *Nucl. Fusion* 62, 016015 (2022), <https://doi.org/10.1088/1741-4326/ac36f1>
- [28] J.-P. Böhner et al., *J. Plasma Phys.* 87, 905870314 (2021), <https://doi.org/10.1017/S0022377821000635>
- [29] X. Garbet et al., *Phys. Rev. Lett.* 91, 035001 (2003), <https://doi.org/10.1103/PhysRevLett.91.035001>
- [30] N. J. Lopes Cardozo, *Plasma Phys. Control. Fusion* 37(8), 799–852 (1995), <https://doi.org/10.1088/0741-3335/37/8/001>
- [31] G. M. Weir et al., *Nucl. Fusion* 61, 056001 (2021) and references therein, <https://doi.org/10.1088/1741-4326/abea55>
- [32] B. Geiger et al., *Nucl. Fusion* 59, 046009 (2019), <https://doi.org/10.1088/1741-4326/aaff71>
- [33] U. Neuner et al., *Nucl. Fusion* 61, 036024 (2021), <https://doi.org/10.1088/1741-4326/abd61a>
- [34] M. Dreval, *Plasma Phys. Control. Fusion* 63, 065006 (2021), <https://doi.org/10.1088/1361-6587/abf449>
- [35] K. Aleynikova and C. Brandt, Talk, 23rd Int. Stellarator-Heliotron Workshop (2022)
- [36] T. Andreeva et al., *Nucl. Fusion* 62, 026032 (2022), <https://doi.org/10.1088/1741-4326/ac3f1b>
- [37] T. Estrada et al., *Nucl. Fusion* 61, 096011 (2021), <https://doi.org/10.1088/1741-4326/ac146f>

Plasma-Wall Interaction

- [1] A. Kärcher et al., Influence of Displacement Damage on Helium Uptake and Retention in Tungsten, *Nucl. Mater. Energy*, submitted (2022)
- [2] R. Arredondo Parra et al., *Nucl. Mater. Energy* 30, 101118 (2022), <https://doi.org/10.1016/j.nme.2022.101118>
- [3] V. Rohde et al., *Nucl. Mater. Energy* 29, 101083 (2021), <https://doi.org/10.1016/j.nme.2021.101083>
- [4] M. Balden et al., *Phys. Scr.* 96, 124020 (2021), <https://doi.org/10.1088/1402-4896/ac2182>
- [5] K. Schmid, An update of Tritium co-deposition in ITER using Wall-DYN3D, *Nucl. Mater. Energy*, submitted (2022)
- [6] M. Zibrov and K. Schmid: *Nucl. Mater. Energy* 30, 101121 (2022), <https://doi.org/10.1016/j.nme.2022.101121>
- [7] M. Zibrov and K. Schmid: *Nucl. Mater. Energy* 32, 101219 (2022), <https://doi.org/10.1016/j.nme.2022.101219>
- [8] K. Kremer et al., *Nucl. Mater. Energy* 27, 100991 (2021), <https://doi.org/10.1016/j.nme.2021.100991>
- [9] K. Kremer et al., *Nucl. Mater. Energy* 30, 101137 (2022), <https://doi.org/10.1016/j.nme.2022.101137>
- [10] A. Kärcher et al., *Nucl. Mater. Energy* 27, 100972 (2021), <https://doi.org/10.1016/j.nme.2021.100972>
- [11] R. Arredondo et al., *Nucl. Mater. Energy* 28, 101039 (2021), <https://doi.org/10.1016/j.nme.2021.101039>
- [12] J. H. You et al., High-heat-flux performance limit of the tungsten monoblock targets: Impact on armor materials and implications for power exhaust, *Nucl. Mater. Energy*, submitted (2022)
- [13] A. v. Müller et al., *J. Nucl. Mater.* 566, 153760 (2022), <https://doi.org/10.1016/j.jnucmat.2022.153760>
- [14] J. H. You et al., *Fusion Eng. Des.* 174, 112988 (2022), <https://doi.org/10.1016/j.fusengdes.2021.112988>
- [15] J. Riesch et al., *Nucl. Mater. Energy* 30, 101093 (2022), <https://doi.org/10.1016/j.nme.2021.101093>
- [16] H. Gietl et al., *Nucl. Mater. Energy* 28, 101060 (2021), <https://doi.org/10.1016/j.nme.2021.101060>
- [17] H. Gietl et al., *Mater. Lett.* 311, 131526 (2022), <https://doi.org/10.1016/j.matlet.2021.131526>
- [18] R. Neu et al., Investigations on cold spray tungsten coatings for plasma facing applications, *Nucl. Mater. Energy*, submitted (2022)

DEMO Design Activities

- [1] I. Turner and A. J. T. Holmes, *Fusion Eng. Des.* 149, 111327 (2019), <https://doi.org/10.1016/j.fusengdes.2019.111327>

- [2] G. Starnella et al., Nucl. Fusion 62, 066038 (2022), <https://doi.org/10.1088/1741-4326/ac5f18>
- [3] A. Magnanimo et al., Fusion Eng. Des. 171, 112574 (2021), <https://doi.org/10.1016/j.fusengdes.2021.112574>
- [4] A. Magnanimo et al., IEEE Trans. Plasma Sci. 50(7), 2178-2184 (2022), <https://doi.org/10.1109/TPS.2022.3179624>
- [5] A. Magnanimo et al., Development of a MMC demonstrator for nuclear fusion devices power supplies, Fusion Eng. Des., submitted (2022)
- [6] M. Schmidtmayr et al., Nucl. Fusion 58, 056003 (2018), <https://doi.org/10.1088/1741-4326/aaaed0>
- [7] G. Suarez-Lopez, to be published <https://doi.org/10.1103/PhysRevLett.127.025002>
- [18] A. Di Siena et al., Plasma Phys. Control. Fusion 64, 064003 (2022), <https://doi.org/10.1088/1361-6587/ac6276>
- [19] A. Di Siena et al., Phys. Rev. Lett. 125, 105002 (2020), <https://doi.org/10.1103/PhysRevLett.125.105002>
- [20] A. Di Siena et al., Nucl. Fusion 62, 106025 (2022), <https://doi.org/10.1088/1741-4326/ac8941>
- [21] A. Mishchenko et al., Plasma Phys. Control. Fusion 64, 104009 (2022), <https://doi.org/10.1088/1361-6587/ac8dbc>
- [22] G. Vlad et al., Nucl. Fusion 61, 116026 (2021) <https://doi.org/10.1088/1741-4326/ac2522>
- [23] A. Bottino et al., J. Phys. Conf. Ser., submitted (2022)
- [24] F. Vannini et al., Phys. Plasmas 28, 072504 (2021), <https://doi.org/10.1063/5.0049588>
- [25] F. Vannini et al., Nucl. Fusion, accepted (2022)
- [26] B. Rettino et al., Nucl. Fusion 62, 076027 (2022), <https://doi.org/10.1088/1741-4326/ac6680>
- [27] P. Molina Cabrera et al., to be submitted (2022)
- [28] K. Höfler, Turbulence Measurements at the ASDEX Upgrade tokamak for validation of the gyrokinetic code GENE, PhD Thesis, TU München (2022)
- [29] K. Stimmel et al., Phys. Plasmas 26, 122504 (2019), <https://doi.org/10.1063/1.5124986>
- [30] K. Stimmel et al., J. Plasma Phys. 88, 905880315 (2022), <https://doi.org/10.1017/S0022377822000484>
- [31] Cavedon et al., Plasma Phys. Control. Fusion 59, 105007 (2017), <https://doi.org/10.1088/1361-6587/aa7ad0>
- [32] Viezzer et al., Plasma Phys. Control. Fusion 62, 024009 (2020), <https://doi.org/10.1088/1361-6587/ab5b1d>
- [33] D. Michels et al., Phys. Plasmas 29, 032307 (2022), <https://doi.org/10.1063/5.0082413>
- [34] D. S. Oliveira et al., Nucl. Fusion 62, 096001 (2022), <https://doi.org/10.1088/1741-4326/ac4cde>
- [35] W. Zholobenko et al., Plasma Phys. Control. Fusion 63, 034001 (2021), <https://doi.org/10.1088/1361-6587/abd97e>
- [36] W. Zholobenko et al., Nucl. Fusion 61, 116015 (2021), <https://doi.org/10.1088/1741-4326/ac1e61>
- [37] D. Michels et al., Comput. Phys. Commun. 264, 107986 (2021), <https://doi.org/10.1016/j.cpc.2021.107986>
- [38] D. Michels et al., Phys. Plasma 29, 032307 (2022), <https://doi.org/10.1063/5.0082413>
- [39] P. Ulbl et al., Contrib. Plasma Phys., e202100180 (2021), <https://doi.org/10.1002/ctpp.202100180>
- [40] P. Ulbl et al., in preparation (2022)
- [41] F. Wilms et al., J. Plasma Phys. 87(6), 905870604 (2021), <https://doi.org/10.1017/S0022377821001082>
- [42] A. Bañón Navarro et al., Phys. Rev. Lett., submitted (2022)
- [43] M. Hoelzl et al., Nucl. Fusion 61, 065001 (2021), <https://doi.org/10.1088/1741-4326/abf99f>

Theoretical Plasma Physics

- [1] R. Brzozowski, Thermal Ion Orbit Loss in Diverted Tokamaks and its Role Approaching the L-H Transition, PhD Thesis, University of California, LA (2021)
- [2] C. D. Stephens et al., J. Plasma Phys. 87(4), 905870409 (2021), <https://doi.org/10.1017/S0022377821000763>
- [3] S. O. Makarov et al., Phys. Plasmas 28, 062308 (2021), <https://doi.org/10.1063/5.0047618>
- [4] A. Di Siena et al., Phys. Rev. Lett. 127, 025002 (2021), <https://doi.org/10.1103/PhysRevLett.127.025002>
- [5] E. Poli et al., Phys. Plasmas 28, 112505 (2021), <https://doi.org/10.1063/5.0064226>
- [6] F. Matos et al., Nucl. Fusion 60, 036022 (2020), <https://doi.org/10.1088/1741-4326/ab6c7a>
- [7] F. Matos et al., Rev. Sci. Instrum. 91, 103501 (2020), <https://doi.org/10.1063/5.0020680>
- [8] I.-G. Farcas et al., Nucl. Fusion 61, 056004 (2021), <https://doi.org/10.1088/1741-4326/abec8>
- [9] F. Matos et al., Nucl. Fusion 61, 046019 (2021), <https://doi.org/10.1088/1741-4326/abe370>
- [10] E. Poli et al., Phys. Plasmas 27, 082505 (2020), <https://doi.org/10.1063/5.0009636>
- [11] E. Poli et al., Phys. Plasmas 28, 112505 (2021), <https://doi.org/10.1063/5.0064226>
- [12] H. Weber et al., J. Comput. Electron. 20, 2199–2208 (2021), <https://doi.org/10.1007/s10825-021-01791-8>
- [13] A. Di Siena et al., Nucl. Fusion 59, 124001 (2019), <https://doi.org/10.1088/1741-4326/ab4088>
- [14] A. Di Siena et al., J. Plasma Phys. 87(2), 555870201 (2021), <https://doi.org/10.1017/S0022377821000362>
- [15] A. Di Siena et al., Nucl. Fusion 58, 054002 (2018), <https://doi.org/10.1088/1741-4326/aaaf26>
- [16] A. Di Siena et al., Phys. Plasmas 26, 052504 (2019), <https://doi.org/10.1063/1.5087203>
- [17] A. Di Siena et al., Phys. Rev. Lett. 127, 025002 (2021),

References

- [44] I. Holod et al., *Plasma Phys. Control. Fusion* 63, 114002 (2021), <https://doi.org/10.1088/1361-6587/ac206b>
- [45] S. J. P. Pamela et al., *Phys. Plasmas* 27, 102510 (2020), <https://doi.org/10.1063/5.0018208>
- [46] Z. Lu et al., *J. Comput. Phys.* 440, 110384 (2021), <https://doi.org/10.1016/j.jcp.2021.110384>
- [47] M. Rosen et al., *Phys. Plasmas* 29, 022502 (2022), <https://doi.org/10.1063/5.0079053>
- [48] V. Bandaru et al., *Plasma Phys. Control. Fusion* 63, 035024 (2021), <https://doi.org/10.1088/1361-6587/abdbcf>
- [49] C. Reux et al., *Phys. Rev. Lett.* 126, 175001 (2021), <https://doi.org/10.1103/PhysRevLett.126.175001>
- [50] C. Paz-Soldan et al., *Nucl. Fusion* 61 116058 (2021), <https://doi.org/10.1088/1741-4326/ac2a69>
- [51] F. Wieschollek et al., *Phys. Plasmas* 29, 032509 (2022), <https://doi.org/10.1063/5.0075473>
- [52] F. J. Artola et al., *Plasma Phys. Control. Fusion* 63, 064004 (2021), <https://doi.org/10.1088/1361-6587/abff620>
- [53] F. J. Artola et al., *Nucl. Fusion* 62, 056023 (2022), <https://doi.org/10.1088/1741-4326/ac55ba>
- [54] K. Särkimäki et al., *Nucl. Fusion* 62, 086033 (2022), <https://doi.org/10.1088/1741-4326/ac75fd>
- [55] R. A. Tinguely et al., *Nucl. Fusion* 61, 124003 (2021), <https://doi.org/10.1088/1741-4326/ac31d7>
- [56] V. A. Izzo, et al., *Nucl. Fusion* 62, 096029 (2022), <https://doi.org/10.1088/1741-4326/ac83d8>
- [57] Q. Yu et al., *Nucl. Fusion* 61, 036040 (2021), <https://doi.org/10.1088/1741-4326/abd197>
- [58] O. Samoylov et al., *Nucl. Fusion* 62, 074002 (2022), <https://doi.org/10.1088/1741-4326/ac6617>
- [59] A. Cathey et al., *Plasma Phys. Control. Fusion* 64, 054011 (2022), <https://doi.org/10.1088/1361-6587/ac5b4b>
- [60] A. Cathey et al., *Plasma Phys. Control. Fusion* 63, 075016 (2021), <https://doi.org/10.1088/1361-6587/abff80b>
- [61] S. K. Hansen et al., *Nucl. Fusion* 60, 106008 (2020), <https://doi.org/10.1088/1741-4326/aba802>
- [62] W. Zhang et al., *Nucl. Fusion* 60, 096001 (2020), <https://doi.org/10.1088/1741-4326/ab9a0b>
- [63] W. Zhang et al., *Nucl. Fusion* 62, 075001 (2022), <https://doi.org/10.1088/1741-4326/ac38c8>
- [64] A. Jansen van Vuuren et al., *Nucl. Fusion* 61, 046001 (2021), <https://doi.org/10.1088/1741-4326/abd4b7>
- [65] J. Vicente et al., *J. Instrum.* 16, C12024 (2021), <https://doi.org/10.1088/1748-0221/16/12/C12024>
- [66] T. Hayward-Schneider et al., *Nucl. Fusion* 61 036045 (2021), <https://doi.org/10.1088/1741-4326/abdca2>
- [67] G. Vlad et al., *Nucl. Fusion* 61, 116026 (2021), <https://doi.org/10.1088/1741-4326/ac2522>
- [68] P. Lauber et al., *Proc. 48th EPS Conf. Plasma Phys.*, P1a.105 (2022)
- [69] V.-A. Popa et al., *Talk, 4th IAEA Techn. Meeting on Fusion Data Processing, Validation and Analysis, Virtual, 2021-11-30 to 2021-12-03*
- [70] Mainly developed within the Eurofusion Enabling Research Project 'ATEP', PI Ph. Lauber
- [71] F. Vannini et al., *Phys. Plasmas* 28, 072504 (2021), <https://doi.org/10.1063/5.0049588>
- [72] F. Vannini et al., *Nucl. Fusion* 62, 126042 (2022), <https://doi.org/10.1088/1741-4326/ac8b1e>
- [73] B. Rettino et al., *Nucl. Fusion* 62, 076027 (2022), <https://doi.org/10.1088/1741-4326/ac6680>
- [74] T. Hayward-Schneider et al., *Nucl. Fusion* 62, 112007 (2022), <https://doi.org/10.1088/1741-4326/ac6f12>
- [75] X. Wang et al., *Phys. Plasmas* 29, 032512 (2022), <https://doi.org/10.1063/5.0080785>
- [76] X. Wang et al., *Invited Talk, Joint Varenna-Lausanne Int. Workshop on Theory of Fusion Plasmas(2022)*
- [77] A. Lier et al., *Nucl. Fusion* 61, 086003 (2021), <https://doi.org/10.1088/1741-4326/ac054c>
- [78] A. Lier et al., *The impact of fusion-born alpha particles on runaway electron dynamics in ITER, submitted (2022)*
- [79] C. D. Beidler et al., *Nature* 596, 221–226 (2021), <https://doi.org/10.1038/s41586-021-03687-w>
- [80] P. Helander and G. G. Plunk, *Phys. Rev. Lett.* 127, 155001(2021), <https://doi.org/10.1103/PhysRevLett.127.155001>
- [81] P. Helander and G. G. Plunk, *J. Plasma Phys.* 88(2), 905880207 (2022), <https://doi.org/10.1017/S0022377822000277>
- [82] G. G. Plunk and P. Helander, *J. Plasma Phys.* 88(3), 905880313 (2022), <https://doi.org/10.1017/S0022377822000496>
- [83] J. Riemann et al., *Plasma Phys. Control. Fusion* 64, 104004 (2022), <https://doi.org/10.1088/1361-6587/ac89ef>
- [84] P. Xanthopoulos et al., *Phys. Rev. Lett.* 125, 075001 (2020), <https://doi.org/10.1103/PhysRevLett.125.075001>
- [85] M. N. A. Beurskens et al., *Nucl. Fusion* 61, 116072 (2021), <https://doi.org/10.1088/1741-4326/ac1653>
- [86] G. T. Roberg-Clark et al., *J. Plasma Phys.* 87(3), 905870306 (2021), <https://doi.org/10.1017/S0022377821000507>
- [87] G. T. Roberg-Clark et al., *Phys. Rev. Res.* 4, L032028 (2022), <https://doi.org/10.1103/PhysRevResearch.4.L032028>
- [88] A. Hallenbert and G. G. Plunk, *J. Plasma Phys.* 88(4), 905880402 (2022), <https://doi.org/10.1017/S0022377822000587>
- [89] A. Zocco et al., *Phys. Rev. E* 106, L013202 (2022), <https://doi.org/10.1103/PhysRevE.106.L013202>
- [90] R. J. J. Mackenbach et al.: *Phys. Rev. Lett.* 128(18), 175001 (2022), <https://doi.org/10.1103/PhysRevLett.128.175001>
- [91] A. Zocco et al., *Nucl. Fusion* 61, 086001 (2021), <https://doi.org/10.1088/1741-4326/ac077d>
- [92] C. Slaby et al., *Nonlinear MHD simulations of pre-current-crash events in Wendelstein 7-X, submitted (2022)*
- [93] C. Nührenberg, *Plasma Phys. Control. Fusion* 63, 125035 (2021),

- <https://doi.org/10.1088/1361-6587/ac35ef>
- [94] A. Könies, et al., *Phys. Plasmas* 27, 122511 (2020)
<https://doi.org/10.1063/5.0023961>
- [95] G. G. Plunk et al., *J. Plasma Phys.* 85(6), 905850602
<https://doi.org/10.1017/S002237781900062X>
- [96] R. Jorge et al., *J. Plasma Phys.* 88(5), 175880504 (2022),
<https://doi.org/10.1017/S0022377822000873>
- [97] K. Camacho Mata et al., Direct construction of stellarator-symmetric quasi-isodynamic magnetic configurations, *J. Plasma Phys.*, submitted (2022)
- [98] S. Henneberg et al., *J. Plasma Phys.* 87(5), 905870503 (2021),
<https://doi.org/10.1017/S0022377821000891>
- [99] Y. Feng et al 2021 *Nucl. Fusion* 61, 086012 (2021),
<https://doi.org/10.1088/1741-4326/ac0772>
- [100] A. M. Arnold et al., *Plasma Phys. Control. Fusion* 63, 095008 (2021),
<https://doi.org/10.1088/1361-6587/ac138d>
- [101] A. Runov et al., *J. Plasma Phys.* 87(4), 905870407 (2021),
<https://doi.org/10.1017/S0022377821000714>

Max Planck Princeton Research Center for Plasma Physics

- [1] P. Helander et al., *J. Plasma Phys.* 88(1), 905880122 (2022),
<https://doi.org/10.1017/S002237782100129X>
- [2] E. J. Paul et al., *Plasma Phys.* 88, 905880107 (2022),
<https://doi.org/10.1017/S0022377821001306>
- [3] S. Bozhenkov et al., *Nucl. Fusion* 60, 066011 (2020),
<https://doi.org/10.1088/1741-4326/ab7867>
- [4] K. Aleynikova et al., *Nucl. Fusion*, to be submitted (2022)
- [5] K. Aleynikova et al., *J. Plasma Phys.*, 88(4), 905880411 (2022),
<https://doi.org/10.1017/S0022377822000745>
- [6] B. Kadomtsev, *Fiz. Plasmy* 1, 710–715 (1975)
- [7] K. Aleynikova et al., *Nucl. Fusion* 61 126040 (2021),
<https://doi.org/10.1088/1741-4326/ac2ab9>
- [8] M. Zanini et al., *Nucl. Fusion* 60, 106021 (2020),
<https://doi.org/10.1088/1741-4326/aba72b>
- [9] R. Ramasamy et al., *Phys. Plasmas* 29, 072303 (2022),
<https://doi.org/10.1063/5.0090008>
- [10] R. Ramasamy et al., *Nucl. Fusion* 61, 076017 (2021),
<https://doi.org/10.1088/1741-4326/abffdf>
- [11] N. Nikulsin et al., *J. Plasma Phys.* 87(3), 855870301 (2021),
<https://doi.org/10.1017/S0022377821000477>
- [12] N. Nikulsin et al., *Phys. Plasmas* 29, 063901 (2022),
<https://doi.org/10.1063/5.0087104>

Plasma for Gas Conversion

- [1] B. de Haart et al., *Nachrichten aus der Chemie* 69(6), 52 (2021),
<https://doi.org/10.1002/nadc.20214110510>

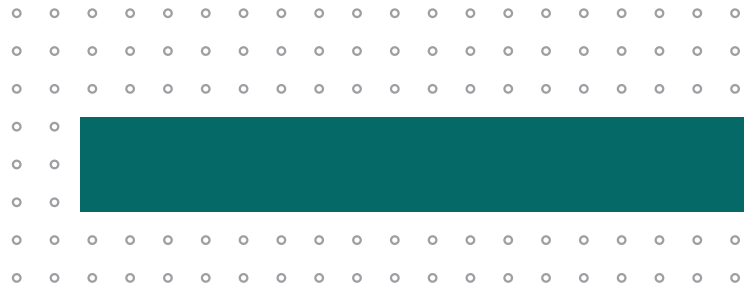
- [2] R. Snoeckx and A. Bogaerts, *Chem. Soc. Rev.* 46, 5805 (2017),
<https://doi.org/10.1039/c6cs00066e>
- [3] A. Hecimovic et al., *J. CO₂ Util.* 57, 101870 (2022),
<https://doi.org/10.1016/j.jcou.2021.101870>
- [4] F. Buck et al., *J. Ind. Eng. Chem.* 104, 1 (2021),
<https://doi.org/10.1016/j.jiec.2021.08.044>

Astrophysical Plasmas

- [1] F. Filbet et al., *J. Comput. Phys.* 172(1), 166–187 (2001),
<https://doi.org/10.1006/jcph.2001.6818>
- [2] T. Tatsuno et al., *Phys. Rev. Lett.* 103, 015003 (2009),
<https://doi.org/10.1103/PhysRevLett.103.015003>

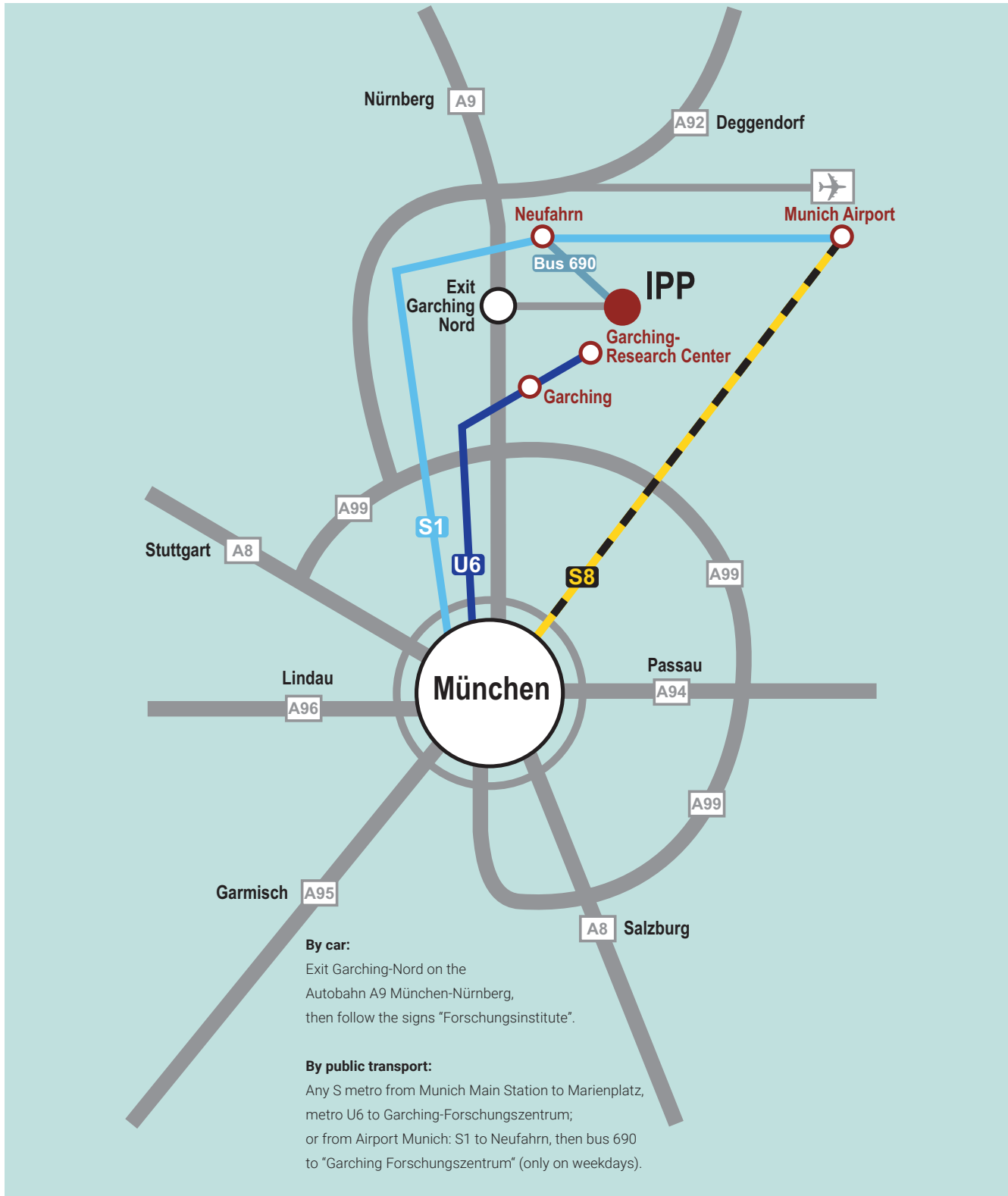
Electron-Positron Plasmas

- [1] M. R. Stoneking et al., *J. Plasma Phys.* 86(6), 155860601 (2020),
<https://doi.org/10.1017/S0022377820001385>
- [2] J. Horn-Stanja et al., *Plasma Res. Express (PREX)* 2, 015006 (2020),
<https://doi.org/10.1088/2516-1067/ab6f44>
- [3] M. Singer et al., *Rev. Sci. Instrum.* 92, 123504 (2021),
<https://doi.org/10.1063/5.0067666>
- [4] H. Saitoh et al., *New J. Phys.* 17, 103038 (2015),
<https://doi.org/10.1063/5.0050881>
- [5] E. V. Stenson et al., *Phys. Rev. Lett.* 121, 235005 (2018),
<https://doi.org/10.1103/PhysRevLett.121.235005>
- [6] S. Nissl et al., *Phys. Plasmas* 27, 052107 (2020),
<https://doi.org/10.1063/5.0007252>
- [7] J. Horn-Stanja et al., *Phys. Rev. Lett.* 121, 235003 (2018),
<https://doi.org/10.1103/PhysRevLett.121.235003>
- [8] M. Singer et al., *Phys. Plasmas* 28, 062506 (2021),
<https://doi.org/10.1063/5.0050881>

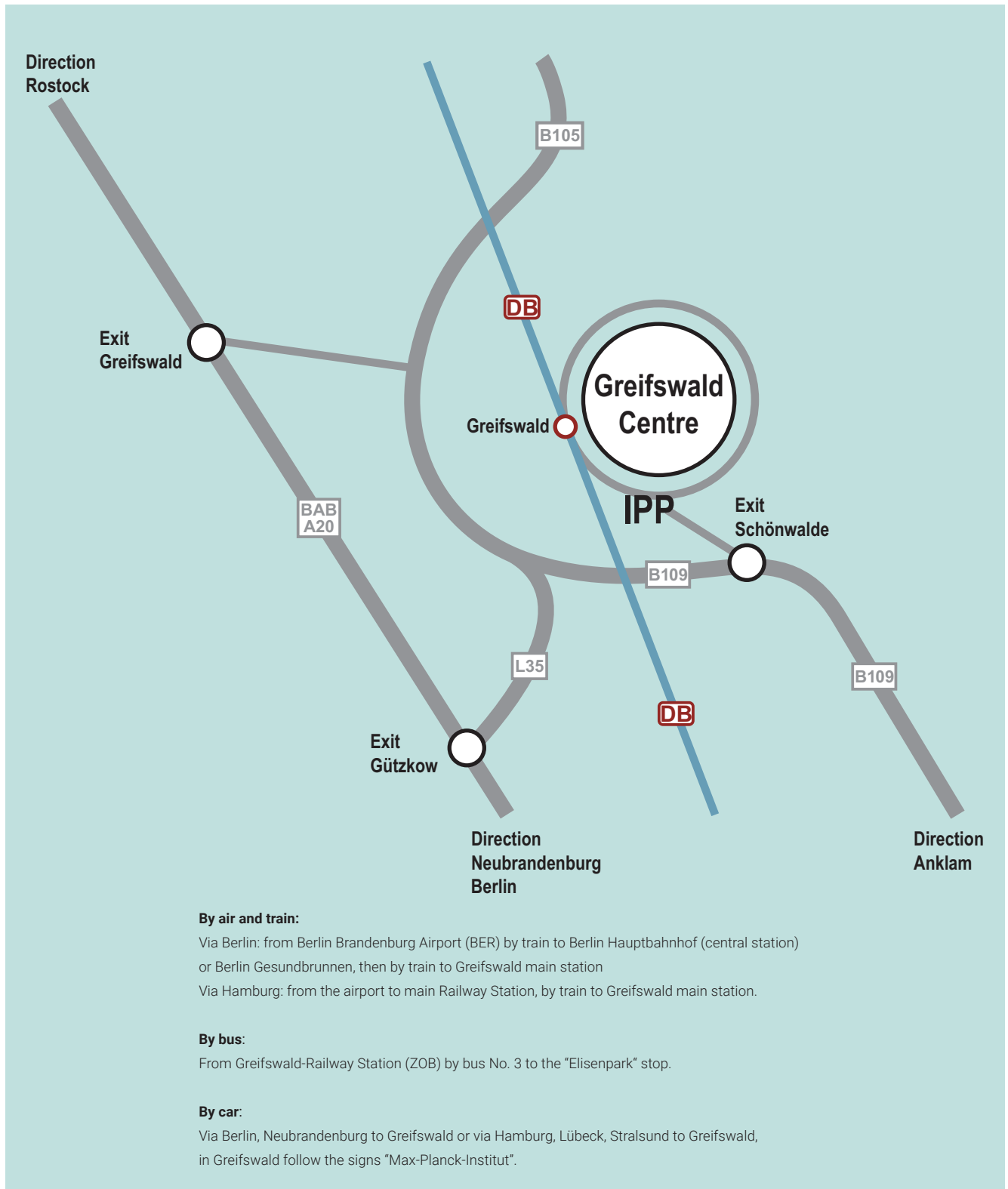


Appendix

How to reach IPP in Garching



How to reach Greifswald Branch Institute of IPP



IPP in Figures

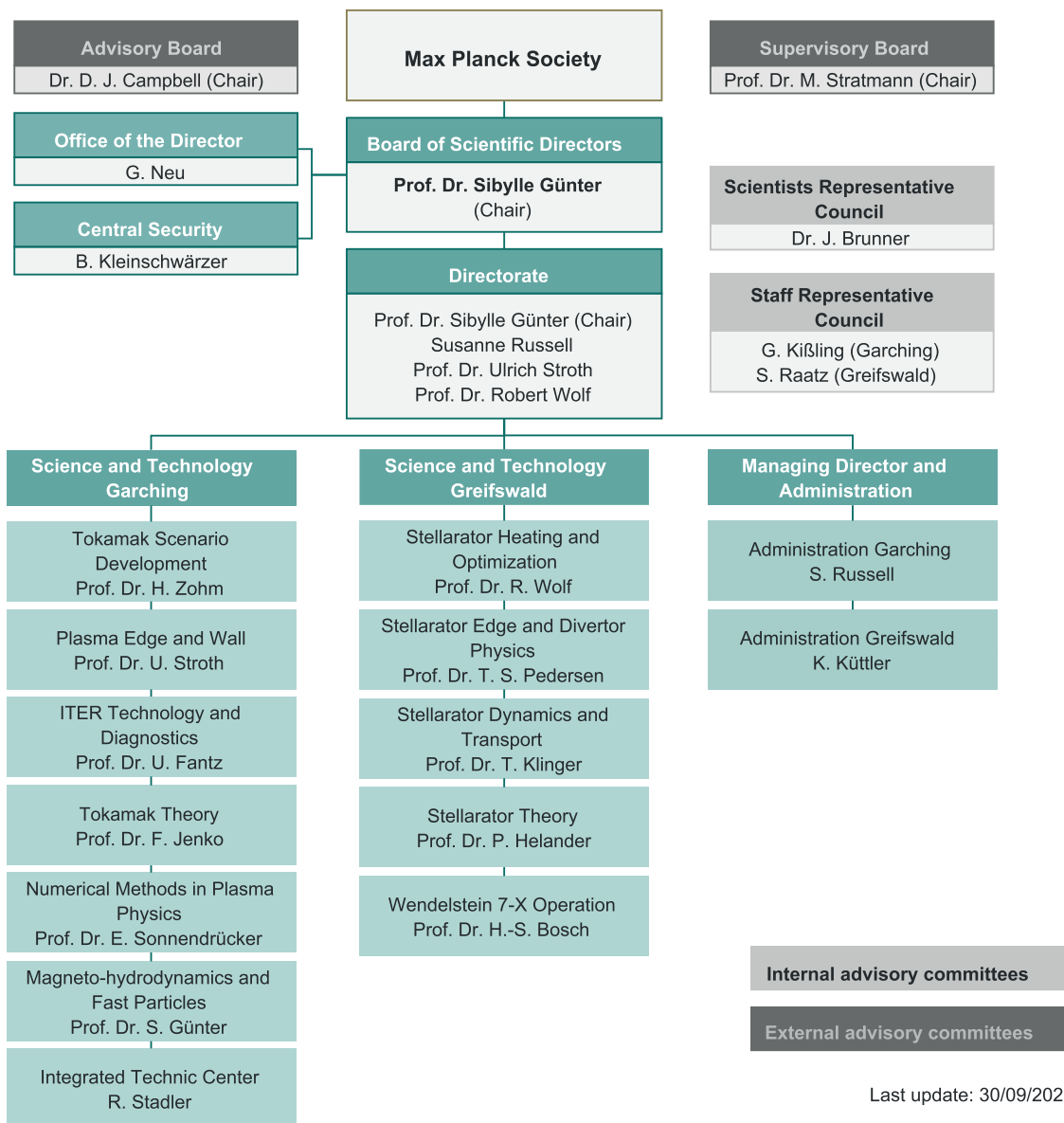
Funding

In 2021 IPP received approx. 16 % of its total funding from the European Union. Of the basic national funding 90 % is met by the Federal Government and 10 % by the states of Bavaria and Mecklenburg-West Pomerania. European and national funding amounted to approx. 143 million euros.

Scientific Staff

At the end of September 2022 IPP had a total of 1.072 members of staff, 417 of them worked at IPP's Greifswald site. The workforce comprised 269 researchers and scientists, 95 postgraduates and 63 postdocs.

Organisational Structure



Last update: 30/09/2022

Imprint

Scientific Report 2021–2022

Max-Planck-Institut für Plasmaphysik (IPP)
Boltzmannstraße 2, D-85748 Garching bei München
phone +49 89 3299-01, info@ipp.mpg.de,
www.ipp.mpg.de

Editorial Team

Andrea Henze
Julia Sieber

Further Information

Part of this work has been carried out within the framework of the EUROfusion Consortium, funded by the European Union via the Euratom Research and Training Programme (Grant Agreement No 101052200 – EUROfusion). Views and opinions expressed are however those of the author(s) only and do not necessarily reflect those of the European Union or the European Commission. Neither the European Union nor the European Commission can be held responsible for them.



All rights reserved

Reproduction – in whole or in part – subject to prior written consent of IPP and inclusion of the names of IPP and the author.

Printing

Druckerei Mang + co
2022 Copyright by IPP, Printed in Germany, ISSN 0179-9347

Cover Photo

Wendelstein 7-X presented in a CAD animation.
Detail from a Wendelstein 7-X explanatory video by tecXplain:
<https://tecxplain.de>.

MAX PLANCK INSTITUTE
FOR PLASMA PHYSICS

